Tyre Model-based Approaches for Vehicle State Estimation and Control

Vincenzo M. Arricale

Supervisor: Prof. Francesco Timpone
Prof. Aleksandr Sakhnevych
Prof. Renato Brancati

Department of Industrial Engineering
University of Naples "Federico II"

This dissertation is submitted for the degree of
Doctor of Philosophy in Mechanical Engineering

March 2022

Without data, you're just another person with an opinion.

Declaration

I hereby declare that except where specific reference is made to the work of others, the contents of this dissertation are original and have not been submitted in whole or in part for consideration for any other degree or qualification in this, or any other university. This dissertation is my own work and contains nothing which is the out come of work done in collaboration with others, except as specified in the text.

Vincenzo M. Arricale
March 2022

Acknowledgements

To the ones who inspired me... myself included

Abstract

Tyre may be one of the most critical and complex components in vehicle dynamics, it is usually the only one interfacing with the road. The pneumatic tyre has three fundamental functions: (i) generating proper forces during vehicle cornering or traction/braking, (ii) absorbing the shock and vibration caused by surface irregularity, and (iii) supporting the weight on various terrains. During the motion, due to the multi-material interaction and to the viscoelastic rubber matrix compositions, the dynamic characteristics of such part may vary considerably, even considering to modify only one parameter among inner pressure, track and ambient temperatures, pavement surface, etc. Another variable to take into account is that the structure and compound characteristics inevitably change within his life-cycle because of ageing, leading to a modification of cornering characteristics and to a decrease of the level of available grip. Therefore, starting from the earliest phases of design of the vehicle and its control systems, the understanding of tyres is critical to govern the overall dynamics. Moreover, the ability of the vehicles to drive themselves in a safe manner highly depends on their prior capability to understand the external environment and to correctly estimate the vehicle state in all the possible operating and environment conditions, which implies adverse environmental scenarios like heavy rain, snow, or ice on the road surface. Nevertheless, the current tools to estimated the vehicle state are still not designed to exploit the entire vehicle dynamics potential, preferring to assure the minimum requirements in the worst possible operating conditions instead. Furthermore, their calibration is typically performed in a pre-defined

strict range of operating conditions, established by specific regulations or OEM routines. For this reason, their performance can considerably decrease in particularly crucial safety-critical situations, where the environmental conditions, the road singularities, and the tyre thermal and ageing phenomena can deeply affect the adherence potential. Hence, in order to guarantee a greater safety-level with respect to environmental conditions [1–4], it is necessary to account for their effect since from the very beginning of the ADAS design phase, introducing advanced control strategies that could leverage both real-time measurements, coming from different in-vehicles sensors (camera, radar, lidar and combinations of those via sensor-based fusion techniques [5–8]), and on-board environmental estimation modules. Indeed, only the use of sensors' measurements could be not enough to perceive properly the external environment, since the vehicle control system has also to predict and discern how heavy rain, snow, ice condition or road singularities (e.g., oil stains, puddles, holes, or disconnected cobblestone) could impact on safety, so that the driving policy is to be tuned according to the actual environmental adversities. Moreover, in extreme scenarios vehicle dynamics may be deeply affected by the non-linearity of tyres' dynamic behavior, therefore limiting the maneuverability in terms of both longitudinal and lateral accelerations and significantly reducing drive-ability and steer-ability. This thesis is focused on the evaluation of the control strategy performance when a better estimated tyre and vehicle parameters are given to the control model take into account the variations in terms of the dynamic behavior of the tyres and of the vehicle boundary conditions. For these reasons the thesis flow is the following:

- **MULTI-PHYSICAL TYRE MODEL ANALYSIS**: starting from the study of tyre's viscoelastic properties an experimental analysis on the real tyre tread specimens has been done in order to evaluate the friction coefficient dependencies with temperature, sliding velocity and wear level. Later, a multy-physical tyre model, called MF-evo, has been presented and parametrized since data carried out by outdoor track test.

- **VEHICLE STATE ESTIMATOR**: the real-time knowledge of the correct vehicle state is needed not only to properly feed low-level control systems commonly used in commercial cars such as ABS, ESP and traction control, but also to allow the development of more accurate advanced driver assistance systems (ADAS) up to fully autonomous driving scenarios. Therefore, a benchmark on the vehicle state estimator has been presented.

- **MOTION PLANNING TO TAKE INTO ACCOUNT THE ESTIMATED PARAMETERS**: the objective of the work is to investigate the possibility of the physical model-based control to take into account the variations in terms of the dynamic behavior of the systems and of the boundary conditions. Different scenarios with specific tyre thermal and wear conditions have been tested on diverse road surfaces validating the designed model predictive control algorithm and demonstrating the augmented reliability of an advanced virtual driver aware of available information concerning the tyre dynamic limits.

- **VEHICLE FOLLOWING CONTROL STRATEGY TO EXPLOIT THE FRICTION ESTIMATION ON-BOARD**: a new model-based technique is proposed for real-time road friction estimation in different environmental conditions. The results, in terms of the maximum achievable grip value, have been involved in autonomous driving vehicle-following maneuvers, as well as the operating condition of the vehicle at which such grip value can be reached.

- **ABS CONTROL STRATEGY TO MAKE USE OF THE TYRE THERMAL DYNAMICS**: a simplified tyre thermal model has been integrated into a model predictive control technique in order to exploit the thermal dynamics dependencies in an abs system to reduce the braking distance.

This thesis is intended to highlight a necessary shift in strategy development and a solid step toward greater development of driving automation systems and physical modeling of vehicle control, capable of exploiting and taking into account multi-physical variations in tire.

Table of contents

List of figures

List of tables

Nomenclature

General Quantities

α	Slip angle	$[\mathrm{rad}]$
β	Side slip angle	$[\mathrm{rad}]$
ΔF_z	Load transfer	$[\mathrm{N}]$
δ	Steering angle	$[\mathrm{deg}]$
γ	Camber angle	$[\mathrm{rad}]$
λ_μ	Friction scaling factor	$[-]$
λ_k	Stiffness scaling factor	$[-]$
$\mu_{x_{i,actual}}$	Actual friction coefficient estimated	$[-]$
$\mu_{x_{i,refRoad}}$	Actual friction coefficient estimated on a reference road surface	$[-]$
μ_x	Longitudinal friction coefficient	$[-]$
μ_y	Lateral friction coefficient	$[-]$
Ω	Wheel angular velocity	$[\mathrm{rad/s}]$
ρ	Air density	$[\mathrm{kg/m^3}]$
$\widehat{\mu}_{x_i}$	Potential friction coefficient estimated	$[-]$

a	Front wheelbase	[m]
A_v	Master section	[m^2]
a_{lead}	Leading vehicle acceleration	[m/s^2]
B	Stiffness factor	[$-$]
b	Rear wheelbase	[m]
C	Shape factor	[$-$]
C_x	Longitudinal drag coefficient	[$-$]
C_x	Tyre braking/driving stiffness	[N/m]
$C_{y\alpha}$	Tyre cornering stiffness	[N/rad]
$C_{y\gamma}$	Tyre stiffness with respect the camber thrust	[N/rad]
C_z	Lift coefficient	[$-$]
D	Peak value	[$-$]
d	Distance lead to ego vehicle	[m]
d_0	Minimum spacing	[m]
d_{br}	Braking critical distance	[m]
d_{des}	ACC desired distance	[m]
E	Curvature factor	[$-$]
F_0	Pure interaction force	[N]
F_{ad}	Adhesive forces	[N]
F_{hys}	Hysteretic forces	[N]

F_{tot}	Resultant of the forces	[N]
F_w	Wear forces	[N]
F_x	Global longitudinal interaction force	[N]
F_y	Global lateral interaction force	[N]
F_z	Global vertical interaction force	[N]
G	Hill function	
g	Acceleration of gravity	[m/s^2]
h	Height c.o.g.	[m]
I_z	Vehicle moment of inertia about z-axis	[kgm^2]
IA	Inclination angle	[rad]
l	Wheelbase	[m]
m	Vehicle mass	[kg]
M_x	Global roll moment	[Nm]
M_y	Global pitch moment	[Nm]
M_z	Global yaw moment	[Nm]
R	Rolling radius	[m]
r	Yaw rate	[rad/s]
s_x	Longitudinal slip ratio	[−]
s_y	Lateral slip ratio	[−]
t	Vehicle track	[m]

v_{lead} Leading vehicle velocity [m/s]

v_{lead} Leading vehicle velocity [m/s^2]

$v_{x_{spindle}}$ Spindle velocity [m/s]

V_x Longitudinal Velocity [m/s]

V_y Lateral Velocity [m/s]

W_f Static load - front axle [N]

W_r Static load - rear axle [N]

State Estimator Symbols

E Residual error

K Kalman gain

P Covariance matrix

Q Process noise covariance matrix

R Measurement noise covariance matrix

v Measurement noise

w Process noise

x_k State variables

z_k Measurement variables

Optimal Control Symbols

η Switching control gain

σ Sliding surface

τ_H	headway time	
d_ω	Warning critical distance	
Hc	Control horizon	
Hp	Predicrtion horizon	
J	Objective function	
l	Limit condition	
r	Constraints	
s	Shooting points	
Ts	Sampling time	
u	Control input	
x	State system	

Thermal and Viscoelastic Quantities

ε	Strain	$[-]$
ω	Stress-strain frequency	[Hz]
σ	Stress	[Pa]
τ	Stress-strain delay	[s]
a_T	Temperature shift factor	[K]
C_i	WLF empirical constant	$[-]$
$tan\delta$	Loss factor	$[-]$
E	Relaxation modulus	[Pa]

E'	Storage modulus	[Pa]
E''	Loss modulus	[Pa]
E^*	Complex relaxation modulus	[Pa]
Tg	Glass transition temperature	[K]

Acronyms / Abbreviations

ABS Anti-Lock Braking System

ACC Adaptive Cruise Control

ADAS Advanced Driver Assistance Systems

AEB Automatic Emergency Braking

CAN Controller Area Network

CARE Community database on Accidents on the Roads in Europe

CG Center of Gravity

ECUs Electronic Control Units

EKF Extended Kalman Filter

Euro NCAP European New Car Assessment Programme

FCW Forward Collision Warning

FEM Finite element Methods

GNSS Global Navigation Satellite System

GPS Global Positioning System

GPU Graphics Processing Unit

IMU Inertial Measurement Unit

KF Kalman Filter

KKT Karush-Kuhn-Tucker

LIDAR Laser Detection and Ranging

LQR Linear Quadratic Regulator

MF Magic Formula

MIL Model In the Loop

MIMO Multi-Input-Multi-Output

MPC Model predictive control

NHTSA National Highway Traffi Safety Administration

NMPC Nonlinear Model predictive control

NMVCCS National Motor Vehicle Crash Causation Survey

PF Particle Filter

PID Proportional-Integral-Derivative

RADAR Radio Detection and Ranging

RTI Real-Time Iteration

SAE Society of Automotive Engineers

SMC Sliding Mode Control

SQP Sequential Quadratic Programming

SUMO Simulation of Urban MObility

TPMS Tyre Pressure Monitoring System

TRICK Tyre Road Interaction Characterization and Knowledge

TTC Time To Collision

TTS Time Temperature Superposition

UKF Unscented Kalman Filter

US United States

VSA Vehicle Side slip Angle

Chapter 1

State of art

1.1 Background and motivation

In the recent years the mobility industry is growing at a rapid pace in the autonomous direction, is an intrinsically multidisciplinary field that aims at designing advanced onboard control strategies by integrating principles from different disciplines including Mechanical, Control and Computer Science Engineering, Legal, Social and Economic fields.

This revolution in the automotive field has produced a reduction in the number of accidents and their severity even if, according to the World Health Organization, the number of deaths on the world's roads remains unacceptably high. Indeed, in 2018, 40 million people were injured and 1.35 million died due to road traffic related injuries. Otherwise, the Americas and Europe have the lowest regional rates of 15.6 and 9.3 deaths per 100,000 population respectively. In terms of progress made, in three of the six regions (Americas, Europe, Western Pacific), the rates of death have decreased since 2013 [20].

The high number of accidents is also a great economical issue: according to the Paris-based Organization for Economic Cooperation and Development, the great number of accidents accounts for 1-3% of the entire world's Gross Domestic Product (considering the cost of the hospital bills, properties' damage and so on): this means the Unites States alone have to pay about 200 billion dollar every year to handle road accidents [21].

To identify and quantify road safety problems throughout the European roads and to evaluate the different roads' efficiency, the European Commission created in 1993 a global database, named CARE - Community database on Accidents on the Roads in Europe. One widely adopted strategy to reduce such accidents is through partial or full automation of the driving task. Thanks to the introduction of assisted driving systems the number of road accidents reported by CARE and confirmed by NHTSA (National Highway Traffic Safety Administration) and British Columbia police report has decreased of more than 30% in 10 years [1].

In the Fig 1.1 the number of fatal accidents occurred every year on European roads has been reported, starting from year 2001.

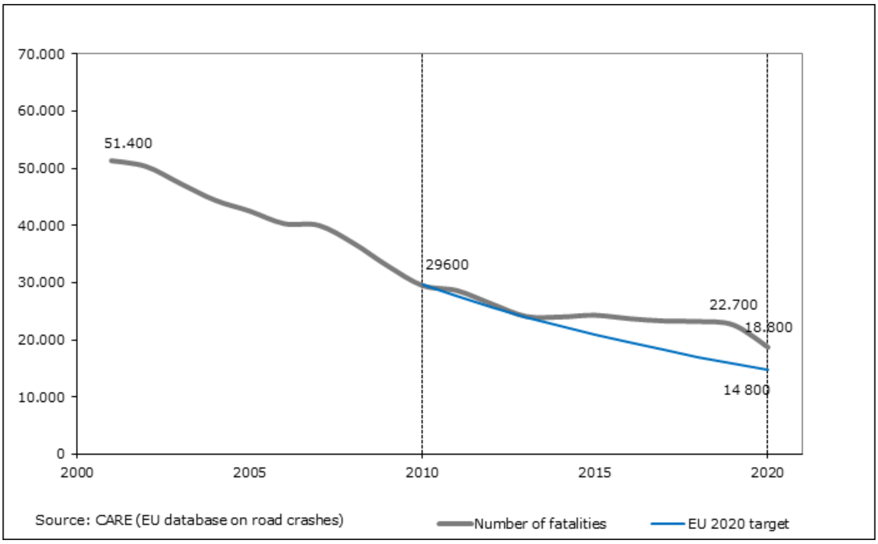

Fig. 1.1 Diagram showing the number of deaths deriving from road accidents in European Union over the years, starting from 2001. The blue curve represents the target death reduction the European Commission's 'Road Safety Program' aims to.

1.1.1 Contributing factors to road crashes

The contributing factors to road crashes (Fig 1.4) could be grouped on the basis of speed (exceeding speed limits), distracted driving/inattention, alcohol impairment, driver error, aggressive driving (following too closely; ignoring traffic control device, or officer/flagman/guard), environmental conditions (road with ice, snow, slush, water), and tyre condition (inflation pressure and trad depth). Studies conducted in the US indicate that the cause behind the vast majority (94%) of accidents is human error [22], and that 24% occur at poor operational conditions, e.g., fog, rain, sleet, snow, etc. [23].

Good condition requires regular monitoring and timely maintenance of all tyres on, or associated with, the vehicle. Nevertheless, it is not uncommon to find vehicles on the road, running on one or more underinflated/overinflated tyres or tyres with inadequate tread depth. Tyre pressure below the recommended pressure can cause high heat generation that in turn can cause rapid tyre wear and blowout. Similarly, inadequate tread depth can also cause blowouts of tyres. Tyre-related events such as tyre failure or blowout resulting from tyre deficiencies or other factors are risky and often add to the likelihood of crash occurrence. According to a 2003 NHTSA report, an estimated 414 fatalities, 10,275 non-fatal injuries, and 78,392 crashes occurred annually due to flat tyres or blowouts before tyre pressure monitoring systems were installed in vehicles.

The effect of tyre tread depth, an adequate tyre tread depth on all tyres of a vehicle is important to maintain proper grip on the road under different road conditions. The data show that of all the tyres observed with tread depth between 0 and 2/32”, 26.2% were mounted on tyre-related crash vehicles (Fig 1.2).

In addition, it is worth to underline that under extreme temperatures, tyres are vulnerable to tyre degradation, significant loss of tyre pressure, additional flexing, and stress on the sidewalls. These tyre conditions may lead to tyre failure or even blow out. In this analysis, three climatic conditions, cold

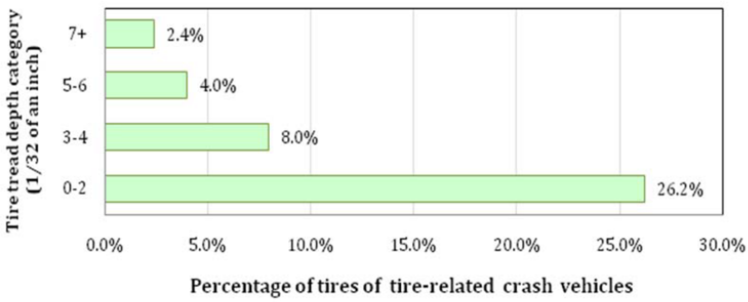

Fig. 1.2 Percentage of tyre-related crash vehicles in each category of tyre tread depth (Data Source: NMVCCS 2005-2007).

(November to February), hot (July to September), and mild (March to June, October) are considered based on the month of the year in which a crash occurred (Fig 1.3).

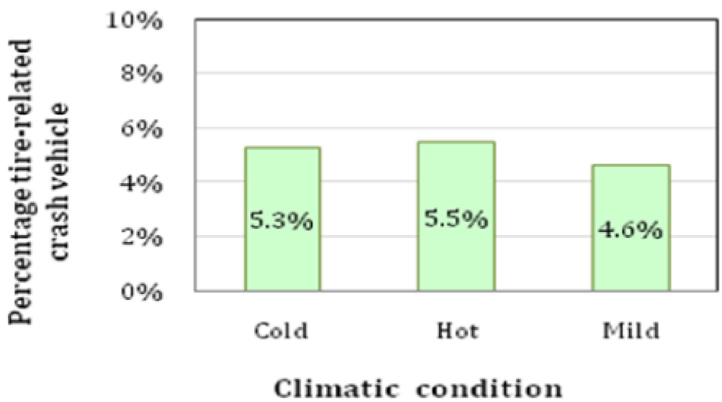

Fig. 1.3 Percentage of tyre-related crash vehicles by climatic condition (Data Source: NMVCCS 2005-2007).

Indeed, in vehicle operating conditions, referring to impervious environmental scenarios or to those linked to the tyre-road friction reduction, there could be a considerable performance decrease of the control onboard systems [24] [25] [26].

	Male drivers			Female drivers		
	Younger	Middle age	Older	Younger	Middle age	Older
Other driver (third party)	9.80	9.80	11.76	4.90	10.78	10.78
Unfamiliar with road (layout, route)	1.96	0.00	2.94	0.98	1.96	1.96
Drugs or alcohol	74.51	50.00	22.55	54.90	38.24	19.61
General driving ability (skills)	1.96	0.98	1.96	2.94	0.98	2.94
Excessive speed	69.61	54.90	23.53	52.94	46.08	23.53
Inexperience	38.24	0.00	0.98	49.02	5.88	2.94
Dangerous driving (peer pressure, showing off)	28.43	4.90	0.00	5.88	3.92	0.98
Distraction (phone, friends, kids, outside)	50.00	34.31	11.76	71.57	53.92	15.69
Driver error (poor judgement)	8.82	15.69	14.71	8.82	9.80	14.71
Road conditions (road layout, road hazard)	16.67	30.39	22.55	20.59	23.53	20.59
Inattention (concentration)	19.61	25.49	24.51	18.63	36.27	24.51
Careless, reckless or in a hurry	16.67	15.69	9.80	12.75	16.67	9.80
Vehicle defects (mechanical failure)	11.76	16.67	14.71	13.73	16.67	15.69
Weather	28.43	33.33	34.31	27.45	36.27	24.51
Overconfidence	3.92	2.94	1.96	2.94	0.00	0.00
Failed to look properly (poor observations)	0.98	0.98	0.98	0.00	0.98	1.96
Traffic	2.94	3.92	4.90	1.96	4.90	4.90
Fatigue	18.63	32.35	30.39	17.65	32.35	31.37
Driving too slow for conditions or slow vehicle	0.00	0.00	2.94	0.00	0.00	0.98
Slow driver reaction	0.00	0.00	19.61	0.00	0.98	18.63
Medical condition (physical impairment, medication)	2.94	19.61	43.14	1.96	14.71	41.18
Poor visibility	17.65	21.57	21.57	17.65	21.57	27.45
Eyesight (uncorrected or defective)	0.98	3.92	37.25	0.98	4.90	30.39
Dazzling light (headlights or sunlight)	2.94	1.96	3.92	1.96	2.94	5.88
Nervous or uncertain (hesitation, confusion, lack of confidence)	0.98	2.94	7.84	4.90	4.90	6.86

Fig. 1.4 Major factors contributing to fatalities.The percentage of each factor per age and gender of the driver in the hypothetical road accident scenarios is reported. The red color identifies the most frequent and the green one the least frequent factors.

1.1.2 The Road to Full Automation

The Fig. 1.5 introduces the levels of automation as defined in SAE J3016 Surface Vehicle Recommended Practice.

Systems at the lower automation levels (1 - Driver Assistance and 2 - Partial Automation) are already widespread in traffic systems throughout the world. Some provide convenience functions like Adaptive Cruise Control (ACC) and some are designed to avoid and/or reduce the severity of accidents. Such Advanced Driver Assistance Systems (ADAS) monitor the traffic scene and the driver during operation, and provides warning or intervenes to assist the driver if particular conditions indicate that there is increased risk of an accident. Forward Collision Warning, Automatic Emergency Braking, Lane

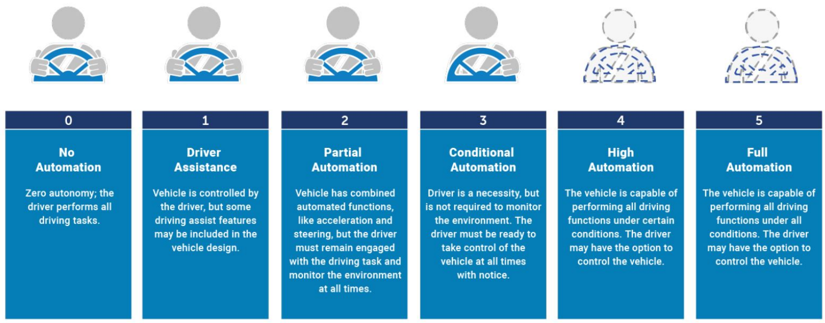

Fig. 1.5 SAE J3016 Levels of Automation [9].

Departure Warning, Lane Keeping Assistance, and Blind Spot Monitoring are a few of the functions that are currently available. Such features are gradually becoming included among standard features of road vehicles. For example, Automatic Emergency Brake is now required to get the highest safety rating from European New Car Assessment Programme (Euro NCAP), and requirements are likely to continue to increase towards more sophisticated accident Research and development for higher levels of automated driving (4 - High Automation and 5 Full Automation) have progressed immensely in the past two decades, to the point where several of the leading companies are offering level 4 autonomous taxi services to the general public, albeit in limited geographical areas. At levels 4 and 5, the vehicle is responsible for the complete driving operation. This has the potential of strong positive impact on traffic safety in terms of alleviating accidents caused by human error. At this level of sophistication, the vehicle can operate without human supervision. Level 4+ automated vehicles use a range of sensors to register their own state and the state of the surrounding traffic scene, for example radar, lidar, cameras, ultrasonic sensors, inertial measurement units, wheel and steering angle encoders and GPS/GNSS. In addition, prerecorded high definition 3d maps are often used to complement the vehicle's own sensors. Perception software processes all of this information and produces an internal digital representation of the traffic scene in terms of the vehicle's position relative to lanes and drivable area, road infrastructure like stop signs and traffic lights, as well as the predicted motions of all non-static traffic agents such as pedestrians, cyclists and other vehicles. This internal representation forms the basis for motion planning and control of the vehicle. Current sensor technologies are subject to fundamental limitations in terms of e.g., weather/light disturbances, occlusions, range and resolution which can only partially be overcome through sensor fusion and clever perception algorithms.

Within this technological paradigm, the ability of the vehicles to drive themselves in a safe manner highly depends on their prior capability to understand the external environment and to correctly estimate the vehicle state in all the possible operating and environment conditions [27–29]. It is worth to note that, as stated by SAE International, the difference between a Level 4 and Level 5 autonomous vehicle is the capability of driving itself in any situation, which implies adverse environmental scenarios like heavy rain, snow, or ice on the road surface [30].

Hence, in order to guarantee a greater safety-level with respect to environmental conditions [1–4], it is necessary to account for their effect since from the very beginning of the ADAS design phase, introducing advanced control strategies that could leverage both real-time measurements, coming from different in-vehicles sensors (camera, radar, lidar and combinations of those via sensor-based fusion techniques [5–8]), and on-board environmental estimation modules. Indeed, the use of only sensors' measurements could be not enough to perceive properly the external environment, since the vehicle control system has also to predict and discern how heavy rain, snow, ice condition or road singularities (e.g., oil stains, puddles, holes, or disconnected cobblestone) could impact on safety, so that the driving policy is to be tuned according to the actual environmental adversities.

Moreover, in extreme scenarios vehicle dynamics may be deeply affected by the non-linearity of tyres' dynamic behavior, therefore limiting the maneuverability in terms of both longitudinal and lateral accelerations and significantly reducing drive-ability and steer-ability. Furthermore, during emergency situations, which typically involve abrupt deceleration or steering, the tyres can be easily pushed to their unstable dynamic region, thus requiring a specific control policy depending from the current dynamics of the vehicle and its sub-components, that hence have to be estimated at each time instant [31].

1.1.3 Objective and research questions

This thesis aims to investigate on the potential of tyre-centered strategies into autonomous driving and safety mobility employing the physical model-based control to take into account the variations in terms of the dynamic behavior of the tyres and of the vehicle boundary conditions validating them in simulation environment. The information concerning the vehicle non-linear physical limits depending on the thermal and wear states of tyres, the pavement characteristics and the boundary conditions (wet or icy ground, under-inflated or worn tyre, etc) represents a fundamental additional value for the optimal behaviour of safety- and performance-oriented control strategy. Therefore, the advanced driving systems will become adaptive due a continuous physical evaluation of adherence, sensitive to environmental conditions, based on a scientifically reliable model-based fusion methodologies.

Being currently mainly based on mere empirical calibration, the physical model-based estimation can represent a crucial factor towards the improvement of the pedestrians' and passengers' active safety, enabling the management of the activation threshold ranges on the basis of the instantaneous operating and the environment boundary conditions. This can be already employed in the current ADAS to communicate to the driver the necessity to co-act in specific situations, but it also constitutes a fundamental root for the future driving automatization.

A proper understanding of the tyre dynamic behaviour and of its multiple intrinsic dependencies is a crucial topic for tyre manufacturers, to improve tyre performance and durability, for users, to set the optimal working conditions, and for researchers, to develop computationally efficient mathematical models able to represent the experimental behaviour with a high degree of accuracy. Friction phenomenon (Eq. 1.1), arising at the tyre-road interface, originates from three physical contributions: the adhesive term relative to molecular Van der Waals links arising between the two counter surfaces in mutual contact, the hysteretic term linked to the deformation losses within the elastomeric material, and the wear term. [32, 33].

$$F_{tot} = F_{ad} + F_{hys} + F_{w} \tag{1.1}$$

All of them are deeply interconnected and dependent on the specific tyre working conditions, in terms of sliding velocity, temperature and pressure distributions, arising at the tyre contact patch as a result of different excitation spatial frequency spectra, representative of diverse types of road pavement [34]. Furthermore, tyres may deeply modify their dynamic behaviour over time due to ageing effects, influencing the dynamic potential of the overall vehicle [35].

The enrichment of the vehicle state with the information concerning the tyre instantaneous and potential friction will allow, taking into account the tyre multiphysical variations, represents a key point in the development of control strategies, able to adapt to sudden variation in boundary conditions in order to guarantee the vehicles higher stability in critical scenarios.

Therefore, the research questions that fall as a subset of the project objective and the thesis flow are as follows:

- How it is possible taking into account the grip multi-physical dependence cited before into a tyre model? To this end in the Chapter 2 the analysis on the mentioned dependencies is described since the study on the viscoelastic propertied of the tyre compound. Moreover, an

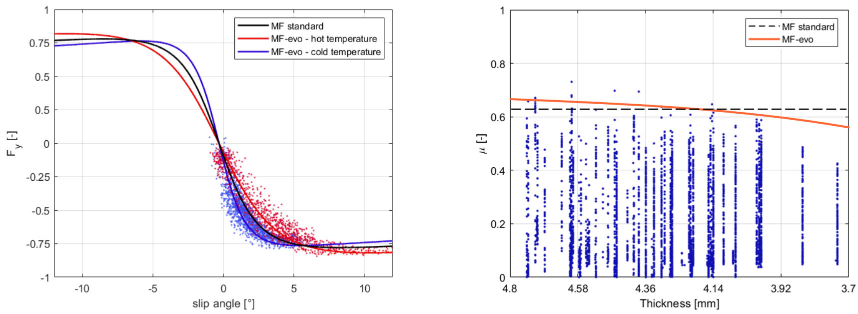

(a) (b)

Fig. 1.6 Tyre behaviour variations. (**a**) Compound temperature influence on the characteristic interaction shape. (**b**) Wear effect on available grip.

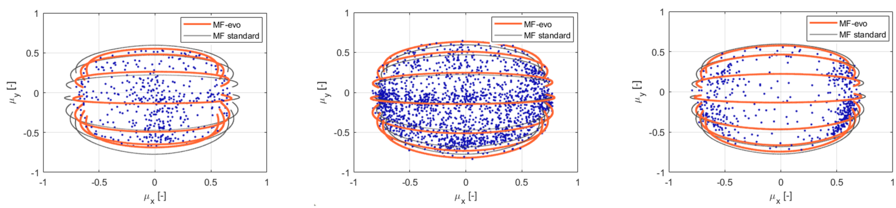

(a) (b) (c)

Fig. 1.7 MF-based tyre modelling in three thermal ranges (camber angle = $-2\,\mathrm{deg}$ | vertical load = $3000N$).

experimental analysis to the evaluation of the friction coefficient at different temperture and wear level has been carried out on real tyre tread specimens. Finally, starting from the experimental data obtained on track test, a multiphysical MF tyre model has been described.

- How the state estimation provide use full information regarding the vehicle parameters? To this purpose in the Chapter 3 a benchmark on the state estimator technique has been described.

- How the variation of tyre limits affect the performance of model-based control in critical scenario? Therefore, in the Chapter 4 an investigation on the control strategies which exploits the estimation of the parameters of the vehicle system has been done.

- It is possible to estimate in real-time the road friction and how a correct friction estimation improve the performance of a vehicle control strategy in a critical scenario? For this reason, in the Chapter 5 a friction estimator in co-simulation with a control strategy has been developed.
- It is a model-based optimal controller/s able to provide improved performance in terms of longitudinal behaviour by considering the tyre thermodynamics in the controller model? In the Chapter 6 has been studied the dynamics of the vehicle system that exploits at best the temperature magnitude that it evolves in the controller model.

1.2 Tyre mechanics

The tyre plays a fundamental role in vehicle dynamics field and many automotive companies spend a lot of time and resources on the development of tyre structure in order to improve its behaviour within the contact are with the road. Therefore, the tyres must fulfil several functions [36] [37], such as the providing sufficient traction for driving and braking manoeuvres or adequate steering control and direction stability. For these purposes, the analysis of the tyre mechanics is essential for comprehending the vehicle performances.

1.2.1 Tyre reference system

To describe the phenomena involved in tyre-road interaction and its forces and moments systems arising during the vehicle motion, an axis reference system need to be defined. One of the commonest used axis systems is recommended by ISO855 standard and it is shown in 1.8 [38].

In this reference system, the road is considered as flat and non-deformable. The x-axis is along the intersection line of the tyre-plane and the ground. The

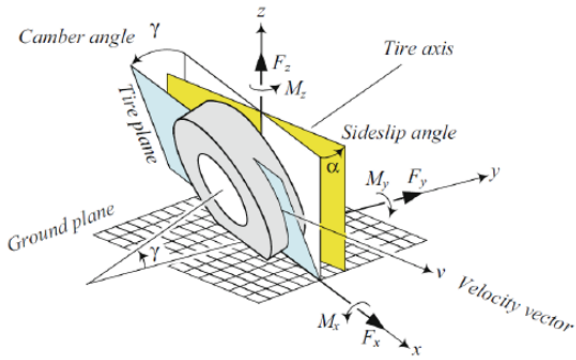

Fig. 1.8 Tyre ISO reference system

tyre plane is defined as the plane made by narrowing the tyre to a flat disk. The z-axis is perpendicular to the ground and upward, and the y-axis direction is chosen so that the axis system satisfies the right-hand rule.

The tyre orientation is defined by two angles. The camber angle γ is the angle between the tyre-plane and the equatorial plane passing through the x-axis; the sideslip angle α is the angle between the x-axis and the forward velocity vector v as shown in 1.8

The resultant force system occurring during the tyre-road interaction is assumed to be located at the centre of the tyre footprint and it can be decomposed along x, y and z axes. Therefore, the interaction of the tyre with the road generates a three-dimensional force system including three forces and moments shown in 1.8:

- *Longitudinal force* F_x is the tangential force acting along the x-axis and it is also called forward force. This force is positive during accelerations manoeuvres; otherwise is negative.
- *Normal force* F_z is the vertical force normal to the ground plane. It is also defined as wheel load. If the resultant force is upward, this magnitude is positive.

- *Lateral force F_y* is the force tangent to the ground and orthogonal to both F_x and F_z. This force is positive if its application direction matches with y-axis.
- *Roll moment M_x* is the longitudinal moment about the x-axis. It is also called overturning moment.
- *Pitch moment M_y* is the lateral moment about the y-axis and it is known as rolling resistance torque. This magnitude is positive if tends to turn the tyre about the y-axis and moves it forward.
- *Yaw moment M_z* is the upward moment about the z-axis and it is defined as aligning moment or self-aligning moment.

1.2.2 Tyre kinematics

Let Q be a point on the rim axis y_c (see Fig 1.9). The position of the rim with respect to the flat road depends only on the height h of the point Q and on the camber angle γ.

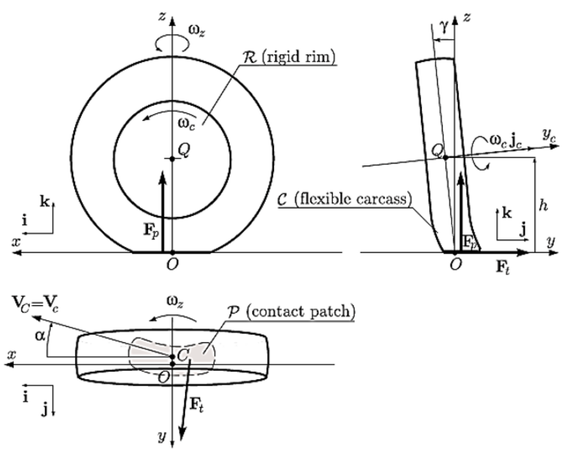

Fig. 1.9 Reference system planes

The latter is the angle between the rim axis and the road plane. The rim, being a rigid body, has a defined angular velocity Ω. Therefore, the velocity of any point P of the space moving together with the rim is given by the well – known equation:

$$V_P = V_Q + \Omega \times \overline{QP} \tag{1.2}$$

where V_Q is the velocity of the point Q and $\overline{QP}$ is the vector connecting Q to P. The three components of V_Q together with the Ω ones are the six parameters that completely determine the rim velocity field. The angle between the velocity $V_C P$ corresponding to the centre of contact patch, which is parallel to the flat road, and the x axis of the reference system is called slip angle α. The latter is fundamental in the lateral interaction between the tyre and road. In order to describe the wheel motion, it is used to evaluate the following vectorial magnitude, also called slip:

$$s = \frac{V - \Omega \times R}{V_x} \tag{1.3}$$

where V is the wheel centre velocity, which is parallel to the flat road, Ω is the angular velocity of the wheel, R is the effective rolling radius and V_x is the x axis component of the wheel centre velocity. The quantity $\Omega \times R$ is defined pure rolling velocity and matches with the wheel centre velocity as soon as the tyre works in free rolling conditions. Distinguishing the slip components along x and y axis, we can define the following magnitudes:

$$\begin{cases} s_x = \frac{V - \Omega \times R}{V_x} \\ s_y = \frac{V_y}{V_x} = \tan\alpha \approx \alpha \end{cases} \tag{1.4}$$

The first quantity is called longitudinal slip, whereas lateral slip is the second one. About the longitudinal slip, it is possible to differentiate the following cases:

- Wheel working in pure rolling condition: there are any differences between the wheel centre and each rim point velocity
- Wheel working in global slip condition (traction phase): the tyre rotates among the wheel axis, but the vehicle does not move forward
- Wheel working in global locking condition (braking phase): the tyre behaves as a rigid body during the vehicle-braking phase

However, taking into account what happens in the contact patch (Fig. 1.10), the tyre tread usually works in pseudo – slippage condition.

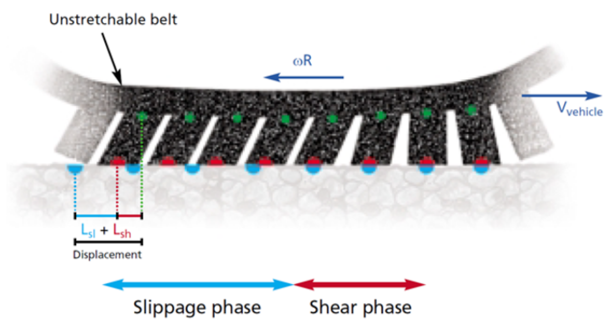

Fig. 1.10 Reference system planes

Actually, the tread of a tyre is deformable, whereas its belt is not stretchable. Consequently, for example, when a vehicle brakes, the road surface pulls the contact patch backwards, but only the tread is distorted. The tread blocks recline, and this outcomes in a relative movement between the bottom of the rubber block, in contact with the road surface, and the belt. This is the shear phase (or pseudo – slippage), which occurs at the leading edge of the contact patch [39]. As the rubber tread block gets closer to the trailing edge of the contact patch, the stress increases and the rubber block, whilst remaining sheared, goes into effective slippage condition with the road surface. This means that a mismatch in the velocity value occurs between the points of the tread in contact with the road (red points, Fig. 1.10) and the road surface ones (blue point).

1.2.3 Tyre dynamics

The tyre plays a fundamental role in the vehicle dynamics which in its turn is subjected to three different types of force fields: the gravitational forces field, the aerodynamic forces and the tyre – road interaction forces one. The interaction forces field refers to the phenomena occurring in the contact patch between the tyre and the road. This field is due to the application of a torque – driving or braking – around the wheel axis and a force applied on quantities are transmitted to the road thanks to the tyre contact patch. This force–torque system at a given point of the contact patch is statically equivalent to any set of forces or distributed load. Therefore, regardless of the degree of roughness of the road, the distributed normal and tangential loads in the contact patch yield a resultant force F and a resultant torque vector M:

$$\begin{aligned} F &= F_x i + F_y j + F_z k \\ M &= M_x i + M_y j + M_z k \end{aligned} \tag{1.5}$$

The resultant couple M is simply the moment about the point O, but any other point could be selected. The traditionally components of the magnitudes in equation set 1.5 are the following: F_x is the longitudinal force, F_y is the lateral force; F_z is the vertical load (or normal force); M_x is the over-tuning moment, My is the rolling resistance moment and M_z is the self–aligning torque [40][41]. Thanks to the experimental tests carried out on tyres and the physical–analytic models, it is possible to determine the tyre–road interaction forces law, nowadays. These expressions state that the vertical load depends on tyre crushing, whereas the longitudinal an lateral forces on the corresponding slip factor, longitudinal and lateral slips, respectively. In the following paragraph, the longitudinal and lateral load will be briefly described; for more details about the tyre–road interaction, see the suggested references [40] [41] [42].

Pure Longitudinal Interaction

The tyre testing aims at the full identification of the functions that are the relationships between the motion and the position of the rim and the force and moment exchanged with the road in the contact patch. It is meaningful to perform experimental tests for the so-called pure slip conditions. It means setting that the longitudinal and lateral forces depend only on the corresponding slip factors and on the vertical load, whereas the self – aligning moment on the vertical load and lateral slip factor [40] [41] [43].

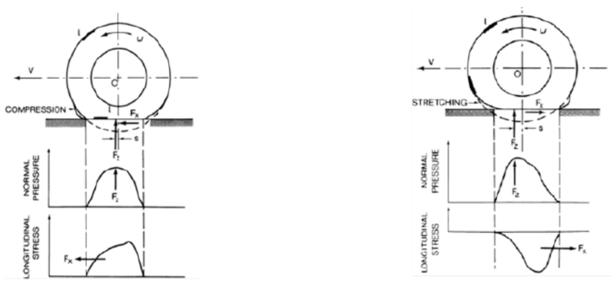

(a) Traction torque (b) Braking torque

Fig. 1.11 Longitudinal interaction physics.

To comprehend the phenomena involved in the contact patch during the longitudinal interaction, we should take into account a vehicle, which is going to brake. If no sliding takes place on the contact patch, the relationship between the longitudinal force F_x and the longitudinal slip s_x can be considered as linear:

$$F_x = C_x s_x \tag{1.6}$$

where s_x can be $s_{x,DT}$ in traction phase or $s_{x,BT}$ in braking phase. C_x is the tyre longitudinal stiffness, often called braking stiffness:

$$C_x = \left.\frac{\partial F_x}{\partial s_x}\right|_{s_x=0} \tag{1.7}$$

In Fig. 1.12, the typical behaviour of the longitudinal Force F_x as a function of the practical longitudinal slip under braking conditions, for several values of the vertical load F_z, is shown.

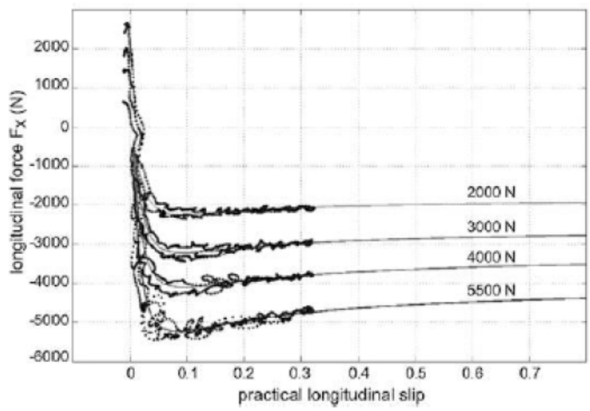

Fig. 1.12 Longitudinal interaction

It is important to point out that the longitudinal forces decrease as a linear function of the slippage ratio in a small range of longitudinal slip ratio s_x. In this case, the longitudinal tyre stiffness definition (eq. 1.7) is correct and the tyre blocks work in adherence. Moreover, the vertical load influence on the longitudinal force F_x: the latter grows less than proportionally with respect to the vertical one. Hence, the global longitudinal friction coefficient μ_x can be defined as the ratio between the peak value of the longitudinal force and the corresponding vertical load.

Pure lateral interaction

When a tyre is not subject to any force perpendicular to the wheel plane, it will move along this last; if a side force F_s is applied to a wheel, a lateral force will be developed at the contact patch, and the tyre will move along a path at an angle equal to the slip angle α with the wheel plane, mainly due to the lateral elasticity of the tyre, as shown in Fig. 1.13.

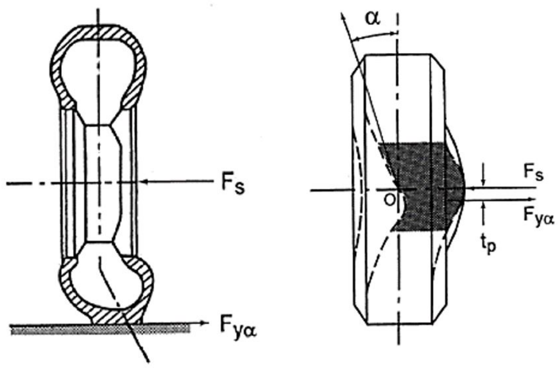

Fig. 1.13 Lateral interaction physics

The lateral force developed at the tyre/ground contact patch is usually called cornering force $F_{y\alpha}$ when the camber angle of the wheel is zero; the relationship between the cornering force and the slip angle is of fundamental importance to the directional control and stability of road vehicles. When the tyre is moving at a uniform speed, the side force F_s applied at the wheel centre and the cornering force $F_{y\alpha}$ developed in the ground plane are usually not collinear: at small slip angles, the cornering force in the ground plane is normally behind the applied side force, giving rise to a torque which tends to align the wheel plane with the direction of motion. This torque is called the "aligning" or "self-aligning torque", and it is one of the restoring moments which help the steered tyre return to the original position after performing a curving manoeuvre. The distance t_p between the side force and the cornering force is called the "pneumatic trail", and the product of the cornering force and the pneumatic trail determines the self-aligning torque. To properly approach a vehicle within a turn, the driver has to act on the steering wheel. Every vehicle taking a turn is subjected to a side force, which tends to force it out of its curve. To keep vehicle on the path, in each tyre-road contact area must arise a centripetal force, F_y, which globally stabilize the side force [40] [41]. The relationship between the cornering force and the slip angle is of fundamental importance to the vehicle handling and stability of road. Typical plots of the cornering force as function of the slip angle show that for angles below a certain range, the lateral force is approximately proportional to the slip values. Beyond them, the cornering force increases at a lower rate with an increment of the slip angle and reaches its maximum value as soon as the tyre begins sliding laterally. It is clear from the above diagram above, that for low slip angle values the lateral force increases linearly. Therefore, the relationship between the friction force and the corresponding kinematic parameter can be expressed as follows:

$$C_{y\alpha} = \left.\frac{\partial F_{y\alpha}}{\partial \alpha}\right|_{\alpha=0} \tag{1.8}$$

where $C_y\alpha$ is known as cornering stiffness. This quantity indicates the slope of the curve at the origin of the coordinate axis system. The cornering stiffness generally increases with the load, but the rate of increase declines as load increases (see Fig. 1.14). High performance vehicles on a dry road will exhibit their maximum cornering ability using large tyres operating at relatively light loads. Inflation pressure usually has a moderate effect on the cornering properties of a tyre, but in general, cornering stiffness increases with an increase of the inflation pressure.

However, the relationship between the cornering force and the normal load is non-linear (Fig.1.14); it means that the transfer of load from the inside to the outside tyre during a turning manoeuvre will reduce the total cornering force that a pair of tyres can perform, making so possible to act on

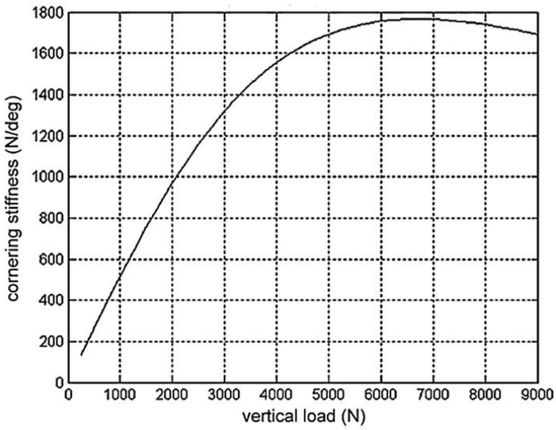

Fig. 1.14 Tyre cornering stiffness

the under/over steering behaviour of the whole vehicle modifying the value of the roll stiffness, able to manage the load transfers [37] [44].

It is further necessary to point out that the centrifugal force F_c applied at the wheel centre and the cornering force $F_{y\alpha}$ developed in the ground are usually not collinear, when a vehicle takes a bend path. At small slip angles, the cornering force is usually behind the applied centrifugal force, giving rise to a torque, which tends to align the wheel plane with the direction of motion. This torque is called self–aligning torque and depends on the slip angles values and vertical load ones.

Camber thrust

Camber causes a lateral force usually referred to as "camber thrust" $F_{y\gamma}$, and the development of this thrust may be explained in the following way: a free-rolling tyre with a camber angle would revolve about point O, as shown in Fig. 1.15; however, the cambered tyre in a vehicle is constrained to move in a straight line, developing therefore a lateral force in the direction of the camber in the ground plane. It has been shown that the camber thrust is approximately one fifth the value of the cornering force obtained from an equivalent slip angle for a bias-ply tyre and somewhat less for a radial-ply tyre.

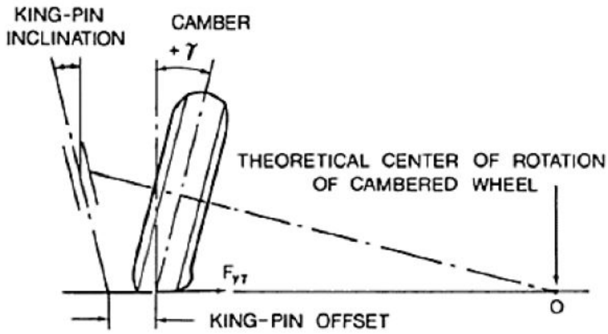

Fig. 1.15 Cambered tyre behaviour

To provide a measure for comparing the camber characteristics of different tyres, a parameter called "camber stiffness" is often used; it is defined as the derivative of the camber thrust with respect to the camber angle evaluated at zero camber angle:

$$C_{y\gamma} = \left.\frac{\partial F_{y\gamma}}{\partial \gamma}\right|_{\gamma=0} \tag{1.9}$$

Similarly to the cornering stiffness, normal load and inflation pressure have an influence on the camber stiffness. It has been calculated that for truck tyres, the value of the camber stiffness is approximately one tenth to one fifth of that of the cornering stiffness under similar operating conditions. The total lateral force of a cambered tyre operating at a certain slip angle is the sum of the cornering force $F_{y\alpha}$ and the camber thrust $F_{y\gamma}$:

$$F_y = F_{y\alpha} \pm F_{y\gamma} \tag{1.10}$$

If the cornering force and the camber thrust are in the same direction, the positive sign should be used in the above equation. For small slip and camber angles, the relationship between the cornering force and the slip angle and the one between the camber thrust and the camber angle are essentially linear; the total lateral force of a cambered tyre at a slip angle can, therefore, be determined by:

$$F_y = C_{y\alpha}\alpha \pm F_{y\gamma}\gamma \tag{1.11}$$

As discussed previously, the lateral forces due to slip angle and camber angle produce a torque, but the component due to slip angle, however, is usually much greater and mainly responsible of the aligning torque acting on tyres in ordinary driving conditions.

Interaction between tangential forces

In the discussion about the cornering behaviour of tyres, the effect of the longitudinal force has not been considered. However, quite often both the side force and the longitudinal force are present, such as braking in a turn. In general, tractive (or braking) effort will reduce the cornering force that can be generated for a given slip angle; the cornering force decreases gradually with an increase of the tractive or braking effort. At low values of tractive (or braking) effort, the decrease in the cornering force is mainly caused by the reduction of the cornering stiffness of the tyre. A further increase of the tractive (or braking) force results in a pronounced decrease of the cornering force for a given slip angle. This is due to the mobilization of the available local adhesion by the tractive (or braking) effort, which reduces the amount of adhesion available in the lateral direction. It is interesting to point out that if an envelope around each family of curves of figure 1.16 is drawn, a curve approximately semi-elliptical in shape may be obtained. This enveloping curve is often referred to as the friction ellipse.

The friction ellipse concept is based on the assumption that the tyre may slide on the ground in any direction if the resultant of the longitudinal force (either tractive or braking) and lateral (cornering) force reaches the maximum value defined by the coefficient of friction and by the normal load on the tyre. However, the longitudinal and lateral force components may not exceed

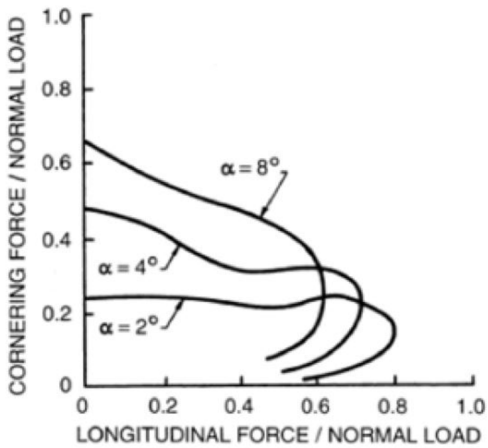

Fig. 1.16 Effect of longitudinal force on the cornering characteristics.

their respective maximum values $F_{x,max}$ and $F_{y,max}$, as shown in Fig. 1.17. $F_{x,max}$ and $F_{y,max}$ can be identified from measured tyre data and constitute respectively the major and minor axis of the friction ellipse.

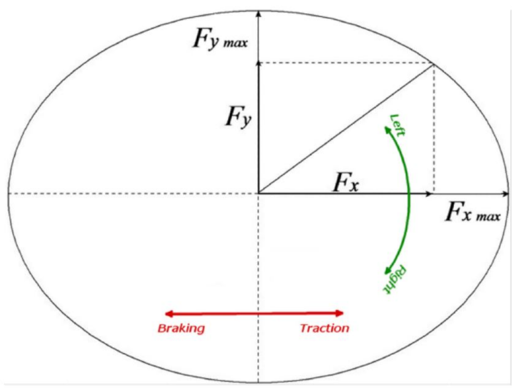

Fig. 1.17 Friction ellipse

1.2.4 Tyre multi-physical dependencies

The vehicle usually operates under a range of different external conditions, so the passenger or race tyres are subjected to varying load, pressure, speed and temperature. All these conditions influence not only the rolling resistance, but also the tyre tread response in transient phenomena during the interaction of the road [36] [11] [45].

Friction occurs between two surfaces that are in contact and being urged to slide over each other in the plane of contact. Strictly, there are two types, static and dynamic friction. Static friction describes the force necessary to get the relative motion started, whilst dynamic friction describes the force necessary to keep the relative motion going once started. In general, dynamic friction is less than static friction. Under a microscope, even very smoothest surfaces show irregular shapes in the form of local peaks and troughs. This means that only a very small part of the two objects is actually in contact as is shown in Fig 1.18.

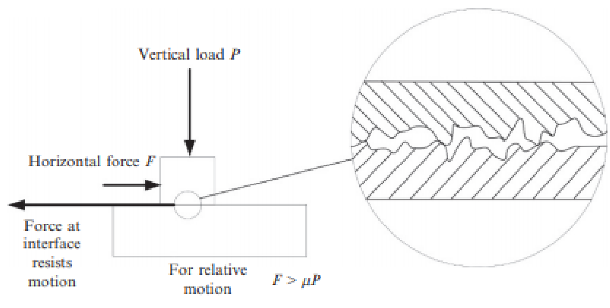

Fig. 1.18 Traditional model of friction.

The friction generated in the road-rubber interface is the result of a set of complex interactions between the tyre and the road, which can be summarised by two stress mechanisms: road roughness effect and molecular adhesion. Such effects arise from the viscoelastic properties of the tyre, which can be approximated by a spring K connected in parallel to a damper of damping coefficient η. The friction force between the tyre and the road is generated as a result of the relative slippage between the elastomer and the road surface. If there is no relative slippage then there is no tyre force.

- Molecular adhesion: The grip derived from the adhesion between the rubber and the road is the result of the Van der Waals bonding phenomena. The rubber's molecular chains form, stretch and break, following a cycle of stretching and breaking, and generating visco-elastic work. The bonding phenomena can be explained in a simplified manner by three steps. In the first step, the bond is created. After that, in the second step , the molecular chain is stretched, and a friction force which opposes the tyre skidding is generated. Finally, in the last step, the bond breaks and new bonds form again successively.

- Road roughness effect: As the aggregate indents the tyre, it engages with it in a way that is similar to a pinion engaging on a geared rack. This allows additional force to be generated at each indentation of the tyre. The road texture (with rough spots that vary from 1 centimetre to 1 micron) induce a high-frequency excitation on the rubber, which is distorted and undergoes several compression-relaxation cycles. As the rubber presents an inherent hysteresis, the rubber does not return immediately to its initial position. Such asymmetrical movement of the rubber block around the rough spot results in a force field, with a tangential component which opposes the slippage and is seen as the tyre force.

Tyre properties K, η are function of temperature. The tyre's modulus of elasticity, represented by the spring K, is maximum below the glass transition temperature Tg, and reduces for temperatures greater than that. The tyre's damping mechanism, also known as hysteresis or energy loss, represented by η is maximum at the glass transition temperature. For temperatures different to that, the energy loss is smaller. In fact, winter tyres are designed to have a lower glass transition temperature compared to summer tyres. When only the tyre force between the tyre and the road is considered, winter tyres generate larger forces at low temperatures compared to summer tyres and summer tyres generate larger forces at increased temperatures.

Tyre properties are also a function of stress frequency, the frequency at which the load is applied. At low excitation frequencies/velocity $\dot{y}$, the damper η does not contribute much, therefore the influence of the spring K is dominant. The opposite happens at higher frequencies, where the damper η becomes more important.

Hence, to understand how a tyre behaves, the tyre type needs to be considered and the temperature and stress frequency monitored. When temperature increases the material becomes softer (lower modulus of elasticity), while when stress frequency increases the material becomes more rigid (higher modulus of elasticity). Other parameters, such as the tyre inflation pressure, also influence the rigidity of the tyre, and therefore are expected to be monitored:

- Temperature : An increase in temperature will make the rubber softer and so allow it to form around the aggregate more easily, thus increasing mechanical grip. In addition, a warmer tyre will be more easily be penetrated by the aggregate, and the chemical reactions governing the bonding will happen more quickly making for increased chemical grip. Increasing the temperature will also reduce the shear modulus and yield stress in shear will drop, that means the tyre performance are reduced. At modest temperatures, for example, 50 or 60°C, the former effects dominate, and an increase in temperature results in better grip. Much beyond 100–120 degrees, the latter effects dominate, and an increase in temperature is accompanied by a reduction in grip. The typical performance of a tyre is shown in Fig. 1.19.

- Inflation Pressure: An overinflated or underinflated tyre will compromise performance, and in this case, the reason is very simple; unless the tyre is correctly inflated, the carcass will be out of shape, and the

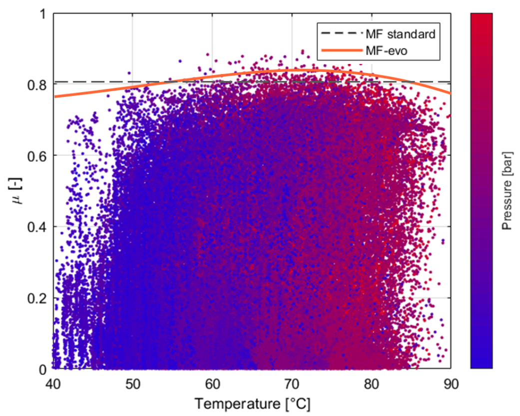

Fig. 1.19 Effect of temperature on grip.

contact patch area reduced. In Fig. 1.20, the normal inflation pressure is shown on the left. Racing tyres are in general rather larger than the road-going equivalents per unit weight, and so, inflation pressures are proportionately lower. Overinflation leads to the position shown in the centre of the figure with the tyre running only on the centre of the contact patch. In response, the central region gets overheated since a level of shear force sufficient for the whole tyre passes through a reduced region. This reduces the level of grip beyond that loss expected from the ratio of areas involved. The situation for underinflated tyres is shown on the right where the majority of the load is carried on the outer regions of the contact patch and similar problems are encountered.

- Ambient Conditions: The nature of the surface the car is used on can have a significant effect. If, for example, at the start of a racing session, the track is dusty and devoid of any rubber laid down from previous laps, then the first cars out will be at a considerable disadvantage and will clean the track up for the later cars who will no doubt be much faster. Rain and temperature change are also clearly important.

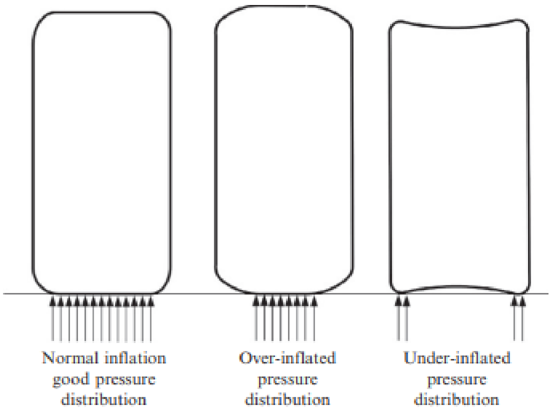

Fig. 1.20 Degree of inflation.

- Tyre Carcass Design: The main design aims for the tyre manufacturer are maintaining the static contact patch unchanged under tractive, braking or lateral force conditions. Controlling damping so that internal friction generates the desired working temperature. Using the tread pattern to reduce noise generation. Isolating the rim from vibrational input from, or contact with, the road. Arranging for the tread to expel water when in rain.

- Compound: The properties of rubber can be altered and controlled by heat treatment and chemical additions. The most obvious region where the material properties play a major role is the composition of the rubber tread in contact directly with the road. The choice of compound is simple. The softer it is, the better the grip will be, but the shorter the life and vice versa.

- Wear: Tyre wear is a topic of particular interest both for road safety enhancement and for vehicle performance optimization. In the first case, the reduction of the braking and directional capabilities due to the thinning of the tyre tread layer is one of the main responsible of the ineffective water drainage on wet soils and in general of the tyre-related accidents. As concerns handling performances, in particular in the racing field, wear reduces the maximum available friction coefficient value (Fig. 1.6) provided by tyres, that can implicate a considerable decrease in the driving forces at the ground, a way out of the optimal trajectory and a consequential increase in the lap-time.

1.3 Analytical tyre model approaches

The design of a pneumatic tyre is vital to vehicle performance. To achieve a proper tyre design that meets all the requirements, it is essential to understand the tyre dynamics characteristics experimentally and/or analytically. Experimental approach is ultimately considered to be necessary, direct and reliable, but expensive, time consuming and practically impossible to cover all operating conditions. Alternatively, analytical method via modelling and simulation becomes more and more popular for its significant advantages in many ways [46].

Like any other virtual models, the accuracy and predictability of a tyre model is most important. Ideally if one tyre model could be applied accurately for all operating conditions, it would be highly accepted by users. Unfortunately such an "ideal" tyre model may not be viable in engineering practice. Therefore in the past decades, various tyre models have been developed for different applications, such as handling and stability analysis, ride comfort analysis, and road load analysis, etc., and with different approach which can be both analitical and empirical [47]. Brush model is one of the earliest analytical tyre models, and it is an origin of many other analytical models, e.g. Fiala's theory [48], Gim's analytical model [49], Levin's tyre model [50] and CF-SAT system model [51]. As for the empirical tyre models, Pacejka's Magic Formula tyre model [52] is the most popular one and is still undergoing development. The latest version of MF tyre model is TNO MF-SWIFT [53, 52]. Other empirical tyre models include TMeasy tyre model [54] and

Svendentius's Semi-empirical tyre model [55]. Several authors refer to the tyre modelling using the Finite Element Method (FEM), adopted to evaluate static characteristics or to the multi-body tyre approaches, as [56–58], commonly adopted to study dynamic phenomena on uneven surfaces.

The main purposes for tyre models to be used for driving/braking and handling analysis are to predict the longitudinal force during braking/traction and/or the lateral force and self-align torque during cornering at on-road situation. For these types of analyses, the road is usually assumed to be flat and rigid and the tyre model is required to be valid up to around 8 Hz [59].

The second group of tyre models is the ride comfort tyre models [60], Takayama's tyre model [61]. More recent ride comfort tyre models include Belluzzo's road-noise model [62], Kim's 2D analytical tyre model [63] and Hegazy's quarter and half vehicle model [64]. The major concern is the human comfort and the tyre acts as a filter which is able to absorb the shock generated by the obstacle between the road and tyre. Human body sensitive frequency range is less than 20 Hz (ISO 2631-1, 1997).

Tyre models for load analysis are typically more complex. This type of models is required to be valid up to around 50 Hz [65] and is primarily applied for predicting the vehicle durability road loads.

Although, the above modelling techniques should be evaluated carefully to the purpose of their employment within the embedded on-board control electronics due to their particularly significant computational cost. It becomes, therefore, necessary the adoption of simpler modelling approaches, as semi-empirical and analytical models [47], whose computational cost is compliant with the capabilities of the modern on-board systems. In the next paragraph three different tyre model will be described in detail:

- Linear tyre model
- Dugoff tyre model
- Pacejka tyre model

1.3.1 Linear tyre model

It is the simplest one and assumes a linear relationship between the force and the corresponding slip. Remembering what said about the tyre working regions, it well fit only the initial linear region. The only input that this model requires is the corresponding slip, so no information about the effect of vertical load is taking into account. Additionally, the lateral and longitudinal forces are dis-joined, they do not affect one with each other. The tyre force formulation is:

$$\begin{aligned} F_{x_{ij}} &= C_{x_{ij}} k_{ij} \\ F_{y_{ij}} &= C_{\alpha_{ij}} \alpha_{ij} \end{aligned} \tag{1.12}$$

In order to take into account the effect of load transfer between wheels of the same axle in cornering maneuvers, a modified version can be found in literature, in which the stiffness is the sum between the value in static condition and a term that takes into account the amount of vertical force transferred. The absence of the saturation effect is the main flaw of this model.

1.3.2 Dugoff tyre model

It is a model reduced number of parameters but that could takes into account some basic phenomena such as the saturation, the behaviour with a peak in lateral and longitudinal forces, and the dependency on the vertical load. In other words it is a compromise between a little number of parameters and an adequate tyre forces description. The longitudinal and lateral forces are given by the following relationships:

$$\begin{aligned} F_{x_{ij}} &= C_{x_{ij}} \frac{\sigma_{x_{ij}}}{1+\sigma_{x_{ij}}} f(\lambda) \\ F_{y_{ij}} &= C_{\alpha_{ij}} \frac{\tan(\alpha)}{1+\sigma_{x_{ij}}} f(\lambda) \end{aligned} \tag{1.13}$$

where the term $\sigma_{x_{ij}}$ refers to a different formulation of the longitudinal slip, while all the other terms are the same as before. The term $\sigma_{x_{ij}}$ is:

$$\sigma_{x_{ij}} = \frac{\omega_{ij} R_{r_{ij}} - V_{x_{ij}}}{\omega_{ij} R_{r_{ij}}} = \frac{k_{ij}}{1 - k_{ij}} \tag{1.14}$$

the function $f(\lambda)$ is given by

$$\begin{aligned} \lambda_{ij} &= \frac{\mu_{max} F_{z_{ij}} (1 + \sigma_{x_{ij}})}{2\sqrt{(C_{x_{ij}} \sigma_{x_{ij}})^2 + (C_{\alpha_{ij}} \tan(\alpha_{ij}))}} \\ f(\lambda_{ij}) &= \begin{cases} (2 - \lambda_{ij})\lambda_{ij}, & \text{if } \lambda_{ij} < 1 \\ 1 & \text{if } \lambda_{ij} \geq 1 \end{cases} \end{aligned} \tag{1.15}$$

as can be seen, the Dugoff tyre model takes into account the combined interaction effect thanks to the function $f(\lambda)$. Even if this model overcomes the linear tyre model's flaws, it is not the best accurate tyre model. In [10] the differences between the Dugoff tyre model and the Pacejka Magic formula (shown in the next section) are highlighted. In the figure (1.21) can be seen that the difference between the two models increases with slip, in fact the Dugoff model continuously increasing with slip and no peak point is reached.

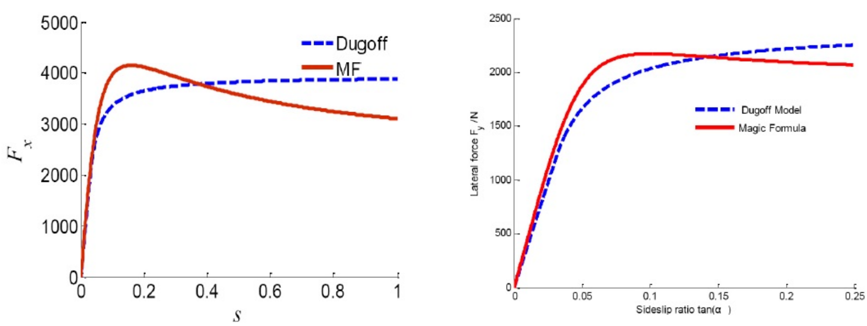

Fig. 1.21 Tyre forces computed using Dugoff model and Magic Formula [10]

in the same paper a modified version of the Dugoff model is presented, it exhibits good results if compared to the Magic formula, as shown in the following figure.

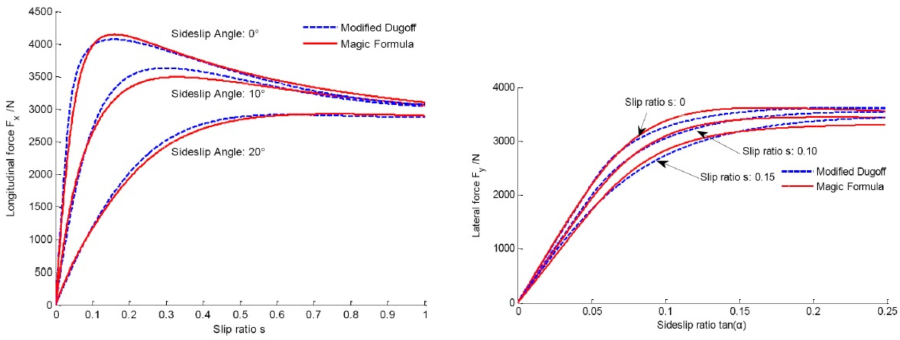

Fig. 1.22 Tyre forces computed using Dugoff model and Magic Formula [10]

1.3.3 Pacejka tyre model

It is one of the most diffused tyre-road interaction models and offers a full description of the tyre behaviour. It is a semi-empirical model that fit experimental tyre response curve, the formulation is also known as *Magic Formula*. However, this formulation has been improved over the years in order to achieve better performance, but all are based on the following anti-symmetric function:

$$F_0 = D\ \sin\{C\ \arctan[B\,x_s - E(B\,x_s - \arctan(B\,x_s))]\} + S_v \tag{1.16}$$

with

$$x_s = X_s + S_h \tag{1.17}$$

First of all the fact that this is a mathematical function that fit the experimental data has to be underlined, this means that all the parameters can be tuned in order to better fit the data. The formulation is the same for both planar forces, the independent variable X_s identify the longitudinal or the lateral condition, for example if one wants to fit the lateral force data, the independent variable is the tyre slip angle, on the other hand if the independent variable is the slip ratio, the relationship refers to the longitudinal force. Thus, this formulation refers to a *pure condition*, for this reason the computed force is indicated with the subscription "0". The tunable parameters may be fixed numbers or polynomial or exponential functions. In all the cases they are usually referred to as:

- B stiffness factor
- C shape factor
- D peak value
- E curvature factor

In addition, the parameters S_v and S_h are the shifts from the Cartesian axes centre.

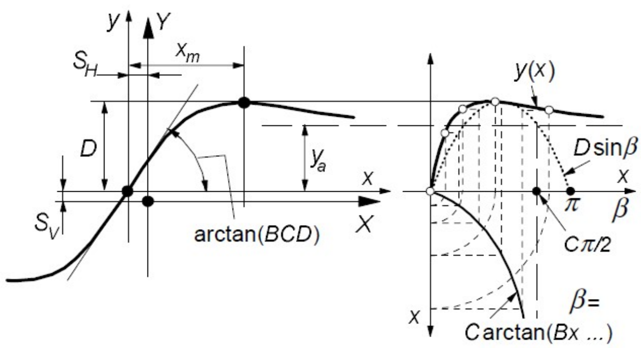

Fig. 1.23 Curve produced by the MF and the meaning of the curve parameters [11]

A vertical load dependence is adopted for the peak value, so it will be here considered as a nonlinear function of the vertical load:

$$D = D(F_z) = \mu F_z = (a_1\ F_z + a_2)F_z \qquad with \quad a_1 < 0 \tag{1.18}$$

in this case the terms a_1 and a_2 are fixed value parameters. As shown in figure (1.23), the parameters B, C and D define the slope in the linear region. In order to create a dependence between them a new parameter is introduced, it is named k and is the tangent of the slope. The dependence is given by the formulation:

$$B = \frac{k}{DC} \tag{1.19}$$

Note that now B depends on the vertical load as well, thanks to the presence of B in the denominator. It is possible to extend the use of the MF in the combined slip case as well, introducing the G-function (or Hill function):

$$G = \frac{\cos\{C_c\ \arctan[B_c\, x_c - E_c(B_c\, x_c - \arctan(B_c\, x_c))]\}}{\cos\{C_c\ \arctan[B_c\, S_{Hc} - E_c(B_c\, S_{Hc} - \arctan(B_c\, S_{Hc}))]\}} \tag{1.20}$$

with

$$x_c = X_c + S_{Hc} \tag{1.21}$$

Note the difference between (1.21) and (1.17), if X_s is the tyre slip angle so X_c is the slip ratio and vice versa. Also the G-function's parameters are different than the MF's ones in pure slip case. Finally the formulation of the MF force in combined slip case is given by:

$$F_c = F_0\, G \tag{1.22}$$

For the sake of completeness, it has to be said that other versions of the formulation exist, a more complex formulation involves the micro-parameters, that are much more than the parameters presented above, that are called macro-parameters. However, this more complex version gives the best results achievable using the MF-model. In this thesis work a simplified version of the MF is adopted, it is based on the macro-parameters version of the MF and the vertical dependence of D is considered, also the dependence in (1.19) is adopted. The other macro-parameters are fixed value.

At this point, the mathematical form of the three separate sets of equations said at the beginning of the section have been presented and commented, now the forces acting on the vehicle are presented and then the main two vehicle models are shown.

1.4 Vehicle modelling approaches

In this section the commonly used vehicle models are presented, first the double-track vehicle model is shown and then its equations are simplified in order to write the single-track vehicle model. A vehicle model is a collection of three groups of equations: kinematic (congruence) equations, equilibrium equations and constitutive tyre equations. Hereafter the equations of the model are recalled and deepened to have a complete overview of the models.

1.4.1 Double-track vehicle model

Double-track model means that the vehicle model is supposed to have all four wheels and therefore, two tracks. Using the congruence equations, the formulation of tyre slip angle and the slip ratio can be obtained. Considering

$\delta_{2j} = 0$ with $j = 1,2$:

$$
\begin{aligned}
Vx_{11} &= (u - \frac{rt_1}{2}) \cos(\delta_{11}) + (v + r\,a_1) \sin(\delta_{11}) \\
Vy_{11} &= (v + ra_1) \cos(\delta_{11}) - (u - \frac{rt_1}{2}) \sin(\delta_{11}) \\
Vx_{12} &= (u + \frac{rt_1}{2}) \cos(\delta_{12}) + (v + r\,a_1) \sin(\delta_{12}) \\
Vy_{12} &= (v + r\,a_1) \cos(\frac{rt_1}{2}) \sin(\delta_{12}) \\
Vx_{21} &= (u - \frac{rt_2}{2}) \\
Vy_{21} &= (v - r\,a_2) \\
Vx_{22} &= (u + \frac{rt_2}{2}) \\
Vy_{22} &= (v - r\,a_2)
\end{aligned}
\tag{1.23}
$$

Considering the general formulation of the slip ratio and of the tyre slip angle reported in (1.4) the slip ratio and tyre slip angle for the double-track model can be easily obtained substituting the equations above in the (1.4).
The equilibrium equations can be easily written starting from the projections of the vehicle acceleration vector onto the vehicle reference system gives:

$$
\begin{aligned}
m\,a_x &= m\,(\dot{u} - v\,r) = X \\
m\,a_y &= m\,(\dot{v} + u\,r) = Y \\
J_z\,\dot{r} &= N
\end{aligned}
\tag{1.24}
$$

as stated above, the terms on the right side are the sum of all the forces acting along/about the vehicle reference system. Considering the projection of the tyre forces onto the vehicle reference system, the terms are:

$$
\begin{aligned}
X &= (F_{x_{11}}\ \cos(\delta_{11}) + F_{x_{12}}\ \cos(\delta_{12})) - \\
&(F_{y_{11}}\ \sin(\delta_{11}) + F_{y_{12}}\ \sin(\delta_{12})) + F_{x_{21}}\ + F_{x_{22}} \\
Y &= (F_{y_{11}}\ \cos(\delta_{11}) + F_{y_{12}}\ \cos(\delta_{12})) + \\
&(F_{x_{11}}\ \sin(\delta_{11}) + F_{x_{12}}\ \sin(\delta_{12})) + F_{y_{21}}\ + F_{y_{22}} \\
N &= -F_{x_{11}}\ \cos(\delta_{11})\ \frac{t_1}{2} + F_{x_{11}}\ \sin(\delta_{11})\ a_1 + F_{x_{12}}\ \cos(\delta_{12})\ \frac{t_1}{2} + F_{x_{12}}\ \sin(\delta_{12})\ a_1 + \\
&+ F_{y_{11}}\ \cos(\delta_{11})\ a_1 + F_{y_{11}}\ \sin(\delta_{11})\frac{t_1}{2} + F_{y_{12}}\ \cos(\delta_{12})\ a_1 - F_{y_{12}}\ \sin(\delta_{12})\frac{t_1}{2} - \\
&+ F_{x_{21}}\frac{t_2}{2} + F_{x_{22}} t_2 2 - F_{y_{21}}\ a_2 - F_{y_{22}}\ a_2
\end{aligned}
\tag{1.25}
$$

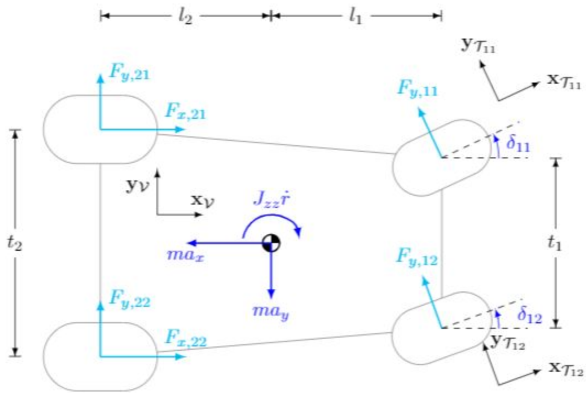

Fig. 1.24 Double-track vehicle model basic scheme

The tyre forces formulation descends from the tyre model adopted.
For what concerns the steering angles, they are computed starting from the steering wheel by nonlinear functions, the Taylor series expansions up to the second order of these two functions can be written as :

$$
\begin{aligned}
\delta_{11} &\simeq -\delta^0 + \tau\ \delta_{SW} + \varepsilon\frac{t_1}{2l}(\tau\ \delta_{SW})^2 \\
\delta_{12} &\simeq \delta^0 + \tau\ \delta_{SW} - \varepsilon\frac{t_1}{2l}(\tau\ \delta_{SW})^2
\end{aligned}
\tag{1.26}
$$

The first term δ^0 is the *static toe*, positive if toe-in. the second term $\tau\ \delta_{SW}$ is called *parallel steering* and it is the same for both wheels. τ is always positive and is the gear ratio of the steering system. The last term is the *dynamic toe* and ε is the *Ackermann coefficient*. If $\varepsilon = 0$ and $\delta^0 = 0$ the hypothesis of parallel steering is adopted.

1.4.2 Single-track vehicle model

There is only one wheel per axle in this model, this means that some additional hypothesis have to be stated. The Ackermann coefficient is set equal to zero, this means that if the static toe-in is considered null, the steering angle of the front wheels is the same (parallel steering). so δ_1 will be the front axle steering angle.

$$\begin{aligned} \delta_{11} = \delta_{12} = \delta_1 \\ \delta_{21} = \delta_{22} = \delta_2 = 0 \end{aligned} \tag{1.27}$$

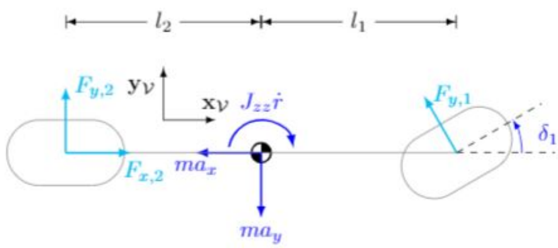

Fig. 1.25 Single-track vehicle model basic scheme

Considering the figure above, it is clear the transition from the double-track to the single-track. In term of equations, the kinematic equations in (1.23) simplify as follow:

$$
\begin{aligned}
Vx_1 &= u\cos(\delta_1) + (v + r\,a_1)\sin(\delta_1) \\
Vy_1 &= (v + r\,a_1)\cos(\delta_1) - u\sin(\delta_1)
\end{aligned}
$$

$$
\begin{aligned}
Vx_2 &= u \\
Vy_2 &= (v - r\,a_2)
\end{aligned}
\tag{1.28}
$$

substituting these equations in the general formulation of the tyre slip (1.4):

$$
\begin{aligned}
\alpha_1 &= \arctan\left(\frac{(v + r\,a_1)\cos(\delta_1) - u\sin(\delta_1)}{|u\cos(\delta_1) + (v + r\,a_1)\sin(\delta_1)|}\right) \\
k_1 &= \frac{\omega_1 R_{r_1} - u\cos(\delta_1) + (v + r\,a_1)\sin(\delta_1) -}{u\cos(\delta_1) + (v + r\,a_1)\sin(\delta_1)} \\
\alpha_2 &= \arctan\left(\frac{(v - r\,a_2)}{|u|}\right) \\
k_2 &= -\frac{\omega_2 R_{r_2} - u}{u}
\end{aligned}
\tag{1.29}
$$

Quite often the hypothesis of small steering angle is verified:

$$
\delta_1 \ll 1 \Rightarrow \begin{cases} \sin(\delta_1) \sim \delta_1 \\ \cos(\delta_1) \sim\ 1 \\ (v + r\,a_1)\sin(\delta_1) \sim\ 0 \end{cases}
\tag{1.30}
$$

and the equations simplify as follow:

$$
\begin{aligned}
\alpha_1 &= \arctan\left(\frac{v + r\, a_1 - u\delta_1}{u}\right) \simeq \frac{(v + r\, a_1) - u\delta_1}{u} \\
k_1 &= \frac{\omega_1 R_{r_1} - u}{u} \\
\alpha_2 &= \arctan\left(\frac{v - r\, a_2}{u}\right) \simeq \frac{(v - r\, a_2)}{u} \\
k_2 &= -\frac{\omega_2 R_{r_2} - u}{u}
\end{aligned} \tag{1.31}
$$

Finally the equilibrium equations are:

$$
\begin{aligned}
m\,(\dot{u} - v\, r) &= X \\
m\,(\dot{v} + u\, r) &= Y \\
J_z\, \dot{r} &= N
\end{aligned} \tag{1.32}
$$

where

$$
\begin{aligned}
X &= F_{x_1}\ \cos(\delta_1) - F_{y_1}\ \sin(\delta_1) + F_{x_2} \\
Y &= F_{y_1}\ \cos(\delta_1) + F_{x_1}\ \sin(\delta_1) + F_{y_2} \\
N &= F_{y_1}\ a_1 \cos(\delta_1) + F_{x_1}\ a_1 \sin(\delta_1) - F_{y_2}\ a_2
\end{aligned} \tag{1.33}
$$

1.5 System state estimation

The vehicle correct state estimation and the ability to mathematically describe such physical system in the widest possible range of operating conditions is crucial for vehicle control. The real-time knowledge of the correct vehicle state is needed not only to properly feed low-level control systems commonly used in commercial cars such as ABS, ESP and traction control, but also to allow the development of more accurate advanced driver assistance (ADAS) systems up to fully autonomous driving scenarios [66, 67]. In the automotive field, the research on state estimation through Kalman Filtering began in the late 90s [68], when the first Extended Kalman Filter (EKF) algorithms, based on single-track models, were proposed. The simplified single-track vehicle models have the advantage of requiring less computational effort and parametrization complexity, whereas Kalman filtering technique compensates for model approximations thanks to sensors' feedback. Usually, a trade-off has to be defined between the increased accuracy obtainable by a more detailed and well parametrized model and the computational capability of the system where the estimation algorithm has to be employed in real-time. Indeed, over time, the models have become more complex and several authors have begun to propose double-track vehicle models [69–72], which, at the cost of a higher computational effort, allow to obtain a better overall estimation accuracy, exploiting all the data and parameters, often available from OEMs (as tyre models parameters and the suspensions elasto-kinematic characterization obtained from laboratory tests). Another important scenario, where the double-track model outperforms a single-track model, regards the reproduction of vehicle dynamics in case of tyre combined interactions, especially in braking/accelerating phases during turning, where, due to the transfer of lateral load, the inner wheels can reach grip saturation, heavily affecting the cornering stiffness of the front axle [73, 74]. In some of the aforementioned works [69–71], but also in the more recent [75, 76], the modelling of the longitudinal dynamics has been tackled also exploiting the rotational angular velocity sensors as one of the model inputs. The main issue concerning the tyre-road longitudinal dynamics evaluation based on the measured wheels angular velocities, consists in the fact that even small errors linked to the wheel rolling radius estimation, or to the encoder measurement noise, can create high estimation errors within the forces estimated at the non-driving axle, which have to be compensated by the driving axle in order to ensure that the longitudinal acceleration of the model matches the measured one. Such potentially large misestimation of the longitudinal forces acts reducing lateral ones, affecting the estimation of the global grip at the tyre-road interface, which will result from 10% to 30% higher than the real one. Another critical point regards the fact that the tyre-road interaction characteristics could potentially considerably change during use, mainly due to the different road surface characteristics and weather conditions; on the other hand, the thermal and ageing effects occurring during the life cycle of the tyre have to be taken into account [35]. For this reason, almost all the papers cited propose an automatic adaptation of the tyre parameters; some include specific scaling quantities for the tyre physical parameters [68, 70, 72], others use more sophisticated methods [76]. It has to be highlighted that all the methods reported include the wheel model parameters, able to guarantee the maximum congruence between sensors signals and model estimations. However, none of these works have taken into account the road inclination effects within the model dynamics, which, if neglected, can represent an additional source of misestimation for the tyre parameters. The integration of all the cited aspects, the simultaneous estimation of side-slip angle, of maximum friction and banking angle, has been addressed in more recent times. In 2017, Hadum [77] proposed an estimation algorithm separated in different modules that included an EKF for the vehicle dynamics estimation, a friction estimation algorithm based on the steering rack force sensor and an algorithm for the banking estimation based on a kinematic relation.

In the Chapter 3 a benchmark on the state estimator algorithm, in particular on kalman and particle filter has been done. Finally, an application on the described technique in order to estimate the vehicle side slip angle on a go-kart has been carried out.

1.6 Introduction to the control theory

Optimal Control Theory (OCT) is a branch of mathematics that helps in calculating optimal control inputs to drive a dynamic system. This system could be a mathematical representation of any system.

To state, this theory tries to minimise a cost or maximise an objective function over a given time period subject to some constraints. These constraints are simply the mathematical representation of the system that we are trying to control. A linear programming problem can be considered as a very basic form of optimal control theory [78].

The optimal control problem is stated mathematically for a general non-linear time-invariant dynamical system below in a very general sense. This system is described in the state space format as follows:

$$\begin{gathered}\dot{\mathbf{x}}(t) = f(\mathbf{x}(t), \mathbf{u}(t), t), \quad \textit{where} \;\; \mathbf{x}(0) = x_o, \\ \text{and state } \mathbf{x} \in \mathbb{R}^n, \text{ control input } \mathbf{u} \in \mathbb{R}^m \text{ and } \mathbf{f} : \mathbb{R}^n \times \mathbb{R}^m \rightarrow \mathbb{R}^n\end{gathered} \tag{1.34}$$

The cost function is defined as follows in general:

$$J = \phi(\mathbf{x}(t_f)) + \int_{t_0}^{t_f} f_0(\mathbf{x}(t), \mathbf{u}(t), t)\, dt \tag{1.35}$$

then the optimal control problem is stated as follows:

$$\text{minimize } \phi(\mathbf{x}(t_f)) + \int_{t_0}^{t_f} f_0(\mathbf{x}(t), \mathbf{u}(t), t)\, dt \tag{1.36}$$

subject to

$$\dot{\mathbf{x}}(t) = \mathbf{f}(\mathbf{x}(t), \mathbf{u}(t), t) \tag{1.37}$$

where the cost function is minimised with a given time frame from t_0 to t_f such that the state has to optimally propagate from $\mathbf{x}(t_0)$ to $\mathbf{x}(t_f)$. The optimal control input $\mathbf{u}(t)$ obtained that results in minimum value of cost function is the optimal solution. Such a definition is very general for the reader to get a glimpse of OCT, avoiding the mathematical details that make the definition robust. The reader is recommended to go through [78, 79] to get a better understanding.

1.6.1 State dependent Riccati equation control

This method is a type of piecewise-linearised control method but not in the traditional sense of linearising the system. The method is actually derived from the well-known LQR method where the non-linear system is represented in a linear-like state-space format (State Dependent Coefficient SDC formulation), where the system matrices become state dependent.

The cost function in this technique is the same as used in the LQR method i.e. an infinite time quadratic performance index. As stated by Mracek and Cloutier [80], a non-linear input-affine system (1.38), holding an equilibrium at the origin $f(0) = 0$, can be driven to the origin (regulation) by minimising the infinite time quadratic performance index (1.39).

$$\dot{\mathbf{x}}(t) = \mathbf{f}(\mathbf{x}) + \mathbf{B}(\mathbf{x})\mathbf{u}(t) \tag{1.38}$$

where the state $\mathbf{x} \in \mathbb{R}^n$, the control input $\mathbf{u} \in \mathbb{R}^m$, and $t \in [0, \infty)$ with $C^1(\mathbb{R}^n)$ functions $\mathbf{f} : \mathbb{R}^n \to \mathbb{R}^n$ and $\mathbf{B} : \mathbb{R}^n \to \mathbb{R}^{n \times m}$, and $\mathbf{B}(\mathbf{x}) \neq 0 \, \forall \mathbf{x}$ as stated by Çimen [81].

$$J = \frac{1}{2} \int_{t_0}^{\infty} (\mathbf{x}^T \mathbf{Q}(\mathbf{x})\mathbf{x} + \mathbf{u}^T \mathbf{R}(\mathbf{x})\mathbf{u}) \, dt \tag{1.39}$$

here the matrices $\mathbf{Q}(\mathbf{x})$ and $\mathbf{R}(\mathbf{x})$ (state and input weighting, respectively) can also be state dependent and must be positive semi-definite and diagonal. After this, the system must first be represented in the state-dependent coefficient SDC formulation 1.40 which is non-unique for multi-variable systems as is shown by [81]. This non-uniqueness can also be exploited to tune the controller performance.

$$\dot{\mathbf{x}}(t) = \mathbf{A}(\mathbf{x})\mathbf{x} + \mathbf{B}(\mathbf{x})\mathbf{u}(t) \tag{1.40}$$

where

$$\mathbf{f}(\mathbf{x}) = \mathbf{A}(\mathbf{x})\mathbf{x} \tag{1.41}$$

As Çimen says, this formulation is linear-like and in general any linear control method could be applied to control this system. Cloutier, Stansbery and Sznaier [82] also show that the some of the classic methods to check the controllability and observability of the system can be used to check the existence of solution. The definition for the stabilisability [81] is stated as follows, as it's the most important property to make sure the system can be driven:

Definition: The SDC representation is a stabilisable parameterisation in a region $\Omega \in \mathbb{R}^n$ if the pair $(\mathbf{A}(\mathbf{x}), \mathbf{B}(\mathbf{x}))$ is pointwise stabilisable in the linear sense for all $\mathbf{x} \in \Omega$.

As shown in [83] and [84], similar to the LQR, using the maximum principle one can write the Hamiltonian H to combine the performance index and the system equations using the co-state ζ.

$$H = \frac{1}{2}(\mathbf{x}^T\mathbf{Q}(\mathbf{x})\mathbf{x} + \mathbf{u}^T\mathbf{R}(\mathbf{x})\mathbf{u}) + \zeta^T(\mathbf{A}(\mathbf{x})\mathbf{x} + \mathbf{B}(\mathbf{x})\mathbf{u}) \tag{1.42}$$

then,

$$\dot{\zeta} = -\frac{\partial H}{\partial \mathbf{x}} = -(\mathbf{Q}\mathbf{x} + \mathbf{A}(\mathbf{x})^T\zeta) \tag{1.43}$$

$$-\frac{\partial H}{\partial \mathbf{u}} = (\mathbf{R}\mathbf{u} + \mathbf{B}(\mathbf{x})^T\zeta) = 0 \tag{1.44}$$

then the control becomes

$$\mathbf{u} = -(\mathbf{R}^{-1}\mathbf{B}(\mathbf{x})^T\zeta) \tag{1.45}$$

Now, assuming $\zeta(t)$ to be as follows:

$$\zeta(t) = \mathbf{P}(t)\mathbf{x}(t) \tag{1.46}$$

and using equations 1.43, 1.45, and 1.46, we get the differential Riccati equation

$$\dot{\mathbf{P}} + \mathbf{P}\mathbf{A}(\mathbf{x}) + \mathbf{A}(\mathbf{x})^T\mathbf{P} - \mathbf{P}\mathbf{B}(\mathbf{x})\mathbf{R}^{-1}\mathbf{B}(\mathbf{x})^T\mathbf{P} + \mathbf{Q} = 0 \tag{1.47}$$

when the time horizon is ∞, the $\dot{\mathbf{P}} \to 0$ [84]. And the result by inserting this into equation 1.47 gives us the matrix algebraic Riccati equation (MARE).

$$\mathbf{P}\mathbf{A}(\mathbf{x}) + \mathbf{A}(\mathbf{x})^T\mathbf{P} - \mathbf{P}\mathbf{B}(\mathbf{x})\mathbf{R}^{-1}\mathbf{B}(\mathbf{x})^T\mathbf{P} + \mathbf{Q} = 0 \tag{1.48}$$

Solving such an equation numerically at each sampling instant is much easier than solving the differential equation, and can be done using various numerical techniques stated by [85].

Finally, using the solution P of the MARE, we can obtain the gain matrix as follows

$$\mathbf{u} = -(\mathbf{R}^{-1}\mathbf{B}^T\mathbf{P})\mathbf{x} = -\mathbf{K}\mathbf{x} \tag{1.49}$$

This way, at controller's each sampling time, the system matrices $\mathbf{A}(\mathbf{x})$ and $\mathbf{B}(\mathbf{x})$ are assumed constant for the gain K calculation (done by solving the MARE) and the state feedback helps update them (at each sampling time) to represent the system non-linearity.

The Figure 1.26 shows how the data flows in a general system with SDRE controller.

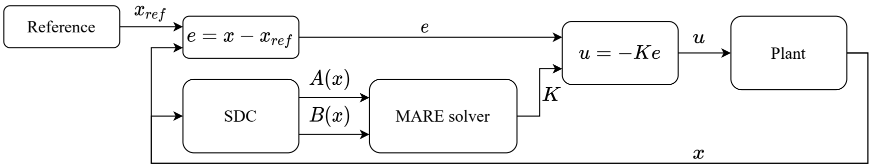

Fig. 1.26 SDRE tracking control - data flow

1.6.2 Non-linear model predictive control

Model predictive control MPC is formulated as the repeated solution of a finite horizon open-loop (open-loop because in each prediction computation, there is no feedback except the initial time instant feedback) optimal control problem subject to system dynamics, and input and state constraints [13]. When the incorporated system dynamics are represented in their non-linear formulation, the control is simply called non-linear model predictive control NMPC. It can simply be called as the practical approach of the optimal control theory with a finite horizon. The essence of this technique is to predict the performance of the system over a given *prediction horizon* while minimising a *cost function* that results in optimally calculated control inputs to drive the plant. When only the first control move is applied to the real plant, the technique is called receding horizon control and is the most common one used in applications. After the application of this control input, the whole computation is repeated at the next sampling instant of the controller. This technique helps involve the feedback aspect in the inevitable presence of plant-model mismatch in applications [86]. Figure 1.27 shows the above mentioned principle.

Below, we will see the mathematical form of the OCP description given above. The plant dynamics that act as a constraint in the OCP can be stated as follows:

$$\dot{\mathbf{x}}(t) = \mathbf{f}(\mathbf{x}(t), \mathbf{u}(t), t) \tag{1.50}$$

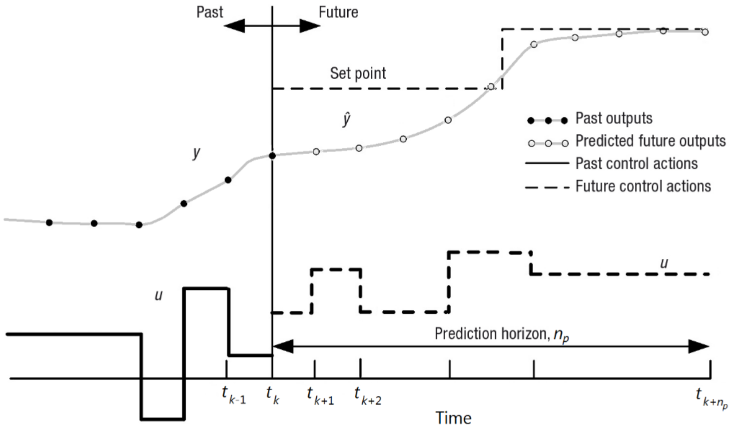

Fig. 1.27 Model predictive control illustration [12]

with an algebraic output equation

$$\mathbf{y}(t) = \mathbf{g}(\mathbf{x}(t), \mathbf{u}(t), t) \tag{1.51}$$

where the state $\mathbf{x} \in \mathbb{R}^n$, control input $\mathbf{u} \in \mathbb{R}^m$, the output $\mathbf{y} \in \mathbb{R}^p$ for time $t \in [0, \infty)$, and the functions $\mathbf{f} : \mathbb{R}^n \times \mathbb{R}^m \to \mathbb{R}^n$ and $\mathbf{g} : \mathbb{R}^n \times \mathbb{R}^m \to \mathbb{R}^p$ being $C^1(\mathbb{R}^n)$ and $C^1(\mathbb{R}^p)$ respectively.

Now, the OCP that must be solved at each controller's sampling instant is stated as follows, where the cost function is being minimised:

$$\begin{aligned} \underset{\mathbf{y}(\cdot),\mathbf{u}(\cdot)}{minimise} \int_{t_0}^{t_0+T_P} \left(\|\mathbf{y}(t) - \mathbf{y_{ref}}(t)\|_Q^2 + \|\mathbf{u}(t) - \mathbf{u_{ref}}(t)\|_R^2 \right) dt \\ + \|\mathbf{y}(t_0+T_P) - \mathbf{y_{ref}}(t_0+T_P)\|_P^2 \end{aligned} \tag{1.52}$$

subject to

$$\mathbf{x}(t_i) = \hat{\mathbf{x}}_\mathbf{0} \qquad \text{Initial conditions} \tag{1.53a}$$

$$\dot{\mathbf{x}}(t) = \mathbf{f}(\mathbf{x}(t), \mathbf{u}(t), t) \qquad \text{Plant dynamics} \tag{1.53b}$$

$$\mathbf{y}(t) = \mathbf{g}(\mathbf{x}(t), \mathbf{u}(t), t) \qquad \text{Output mapping} \tag{1.53c}$$

$$\underline{\mathbf{x}}(t) \leq \mathbf{x}(t) \leq \bar{\mathbf{x}}(t) \qquad \text{State constraints} \tag{1.53d}$$

$$\underline{\mathbf{u}}(t) \leq \mathbf{u}(t) \leq \bar{\mathbf{u}}(t) \qquad \text{Input constraints} \tag{1.53e}$$

where the weighting matrices are as follows: $\mathbf{Q} \in \mathbb{R}^p_{\geq 0}$, $\mathbf{R} \in \mathbb{R}^m_{\geq 0}$, and $\mathbf{P} \in \mathbb{R}^p_{\geq 0}$ and $\hat{\mathbf{x}}_\mathbf{0}$ is the measurement of the current state of the plant.

Although one would be interested in a closed-form solution of the OCP stated above, such that no on-line computation will be needed but the closed form solution cannot be found analytically [13]. Thus, the OCP is converted into a numerical optimisation problem using finite paramterisation of the input and state (piece-wise constant functions) which is solved using direct optimisation methods [13]. The most common and widely used method for which many open-source packages exist is the direct single or multiple shooting method. The direct multiple-shooting method is used in this work.

In these direct shooting methods, the *prediction horizon* is broken down into N_P *shooting intervals* like in any discrete system representation $[t_0, t_1, ..., t_{N_P}]$. The most common method is to define equidistant grids such that fixed steps are obtained. The input is parameterised using a piece-wise constant function defined as follows:

$$\mathbf{u}_i = \mathbf{q}_i \qquad \text{for} \qquad t \in [t_i, t_{i+j}) \tag{1.54}$$

where j could be anything from 1 to N_P, former corresponding to the case where the input is parameterised into the same size as the prediction horizon and the latter corresponding to a constant input across the whole prediction horizon. The choice depends on the move-blocking setting used which helps lower the number of variables to be optimised.

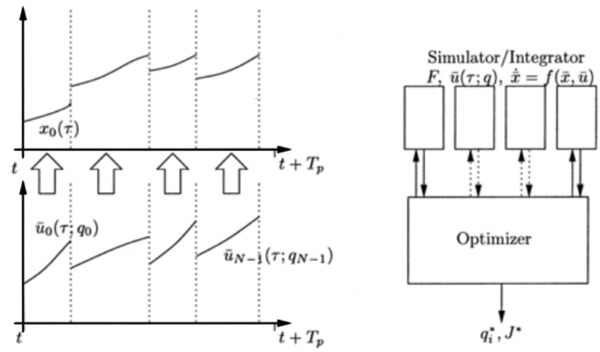

Fig. 1.28 Multiple shooting approach with simultaneous solutions illustration [13]

In the direct multiple shooting approach, the sampled prediction horizon receives local control paramterisations. The integration of the plant dynamics and the cost is done independently for each interval during each optimisation iteration as is seen in Figure 1.28. The initial value of states at the beginning of each interval are the additional optimisation problem parameters, and to ensure continuity of the final state trajectory there are the additional equality constraints [13].

This multiple shooting approach is better at handling strong non-linearities and stabilising the system than the single shooting approach [87]. After the setup as explained above, one obtains the non-linear programming NLP to be solved. This whole preparation of NLP from OCP is done using the MATMPC toolbox in this work [88]. The MATMPC toolbox has various options to solve the obtained NLP, whereas in this work qpOASES is employed [89], which is based on the active-set strategy.

Internally, the NLP is solved using sequential quadratic programming SQP. Here, the NLP is first converted into a QP and then condensed to obtain a dense QP problem which is solved by the above stated dense QP solver - qpOASES. To convert the NLP into a QP, the Gauss Newton method is used for the Hessian approximation. For more detail the reader can refer to [90, 13, 89, 91, 88].

Chapter 2

MFevo: Multi-physical MF-based tyre model

2.1 Introduction

Starting from the earliest phases of design of the vehicle and its control systems, the understanding of tyres is of fundamental importance to govern the overall vehicle dynamics and handling behaviour.

A properly characterized tyre-road interaction model is essential to achieve a reliable vehicle dynamics model on which more design variations can be studied directly in simulation environment optimizing both cost and time.

The described cost and time-oriented constrained optimization can be achieved only on the condition that the mathematical representation of the overall vehicle physical model (comprehending suspensions, powertrain, tyres, etc) is sufficiently accurate, at least within the domain of interest (i.e. operating and boundary conditions concerning kinematics, dynamics, temperature, pressure, road roughness, etc) [92, 93]. In such a scenario, tyre-road interaction models cover a fundamental role in the modelling of the vehicle system [94, 37], due to the tyre's composite structure and intrinsic non-linearity linked to inter-connected multiphysical phenomena [95–97], which must guarantee very strict computational constraints to allow the employment in even more severe real-time environments concerning onboard estimation and control logics [98, 99].

As mentioned in the Chapter 1, the Pacejka's Magic Formula (MF) [94, 14] is one of the most used ones in real-time automotive simulation environment because of its ability to fit quite easily a large amount of experimental data able to assure a high level of accuracy and reliability, for at least what concerns the dependencies upon the kinematics and vertical load [100].

Later, the original formulation did not take into account of the tyre states concerning its thermodynamics and wear condition, which affect tyre dynamics and are not negligible if full reliability requirement is needed, especially in the development of control algorithm and safety logics. As it will be possible in the next paragraph, the tyre exhibits its maximum performance in a narrow range of temperature and pressure.

The MF model has been further enhanced in [101], where the authors have proposed an advanced multiphysical MF-based (MF-evo) real-time tyre model with the aim to extend the Pacejka's Magic Formula tyre model in the whole range of the tyre operating conditions, taking into account its internal temperature distribution [102, 103], inflation pressure [52], tread wear [104, 35], compound viscoelastic characteristics and road roughness [32, 105].

In the next paragraphs, this chapter will address the concept at the basis of tyre's property variation starting from the study of viscoelastic material and the parametrization of the compound friction coefficient dependences in a controlled laboratory environment (a specifically designed experimental BP-evo rig has been employed) and experimental data acquired in outdoor testing session carried out with an industrial partner, on different types of road surface and in a wide range of operating conditions (sliding velocity, contact pressure, degradation due to abrasive wear). Therefore, a specific methodology has been developed to characterize and to identify with a high grade of accuracy and reliability the parameters of the MF-evo, directly from experimental data.

2.2 Theory of viscoelasticity

2.2.1 Definitions

The viscoelastic material is a deformable material with a behaviour which lays between that of viscous liquid and an elastic solid. This kind of solid does not show a linear relationship between stress and applied strain. Indeed, their behaviour deviates from Hooke's law and exhibits elastic and viscous characteristics at the same time. The most generic equation that describes this feature is the Newton's Law [42] [106] [32]:

$$\sigma(t) = \eta \frac{d\varepsilon(t)}{d(t)} \tag{2.1}$$

This relation defines the connection between the stress and the strain–rate through the viscosity coefficient η. All materials, which satisfied the Eq. 2.1, are called viscoelastic materials, with the stress–strain relationship function of time. Indeed, as concerns a viscoelastic material, the most important characteristics are the time–dependent behaviour and the load application speed at an established temperature value. It is necessary to point out that viscoelasticity is not plasticity [32]. A viscoelastic material will return to its original shape after any deforming force has been removed, even though it will take time to do so. The reason of this phenomenon is that the deformation energy is not totally stored, but partially dissipated through hysteretic mechanism. Contrariwise, when a perfectly elastic solid, like a spring, is subjected to a force, it distorts instantaneously in proportion to the applied load. Then, as soon as the force is no longer applied, the body returns to its initial shape. Moreover, it is important to highlight that the viscoelasticity of tyre rubber depends on the material molecular structure. Actually, the main constituent rubbers of a tyre are vulcanised elastomers. These elastomeric materials are made up of one or more polymers, long molecular chains, which spontaneously take on the shape of a wool ball and became entangled with each other. During the tyre manufacturing, these materials are vulcanised, which means they are treated with an incorporation of sulphur. This causes the creation of sulphur bridges between the polymer chains [32] [107] [108].

To better understand the mechanical behaviour in viscoelastic materials, two main types of experiment are usually carried out: transient and dynamic. While static characterization regard the quasi-static application of load or deformation, transient and dynamic testing procedures concern the analysis of material response to a time applied deformation or load function (elongation or shear). Two important categories, regarding the transient material testing, are commonly performed: creep experiment and stress relaxation experiment.

Creep experiment

In the creep experiment, the material is subjected to uniform load in order to analyse the strain time changes, as shown in Fig. 2.1. Creep phenomenon is one of the most important features, which points out the viscoelastic behaviour of materials. Creep consists in progressive increasing of deformation under uniform load applied on the specimen.

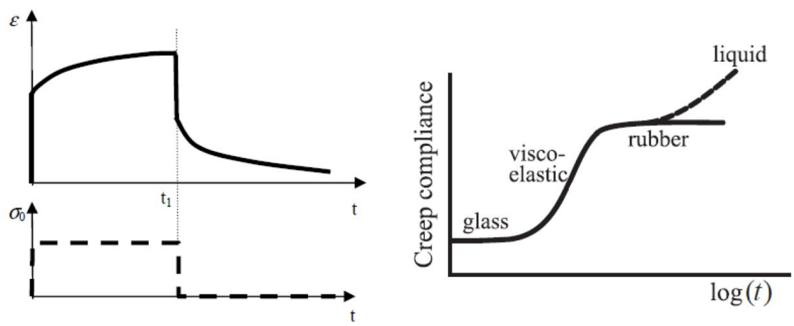

Fig. 2.1 Creep experiment and creep material compliance.

Creep phenomenon is one of the most important phenomena to characterize the viscoelastic behaviour of materials. Creep consists in progressive increasing of deformation under uniform load applied on the specimen. As described in Fig. 2.1 (on left), the strain quickly with time as the stress step function is applied, reaching the steady-state conditions at time t_1. Furthermore, if the load applied is instantly removed, the strain shows a transitional period to reach the unload initial conditions. The creep compliance module J (Fig. 2.1, on right) is defined as the ratio between the strain, obtained at define instant of time, and the load step applied:

$$J(t) = \frac{\varepsilon(t)}{\sigma_0} \tag{2.2}$$

From eq. 2.2, it is clear that creep compliance is time dependent. Particularly, the material behaves as a glassy solid if the load is applied with higher frequency values and it is similar to rubbery solid if the load is applied quasi statically. In the middle time range, the compliance shows a linear slope where the solid behaves as a viscoelastic material. In particular, in the middle time range which characterizes the linear viscoelastic slope trend, the creep compliance proportionally increases with time [108] [106].

Stress-Relaxation experiment

During the stress-relaxation experiment, material is subjected to a fixed deformation and the load required to maintain the deformation at a constant value is measured with time, as represented in Fig. 2.2.

Once the strain is applied to the specimen, the stress trend initially shows an instantaneous reaction, then it gradually decreases with time. As soon as the material comes back to undeformed shape, it tends to react with a stress opposite to the initially applied strain; then this stress tends to zero value. As well as for the Creep Compliance, we can define the Relaxation Modulus E is expressed as:

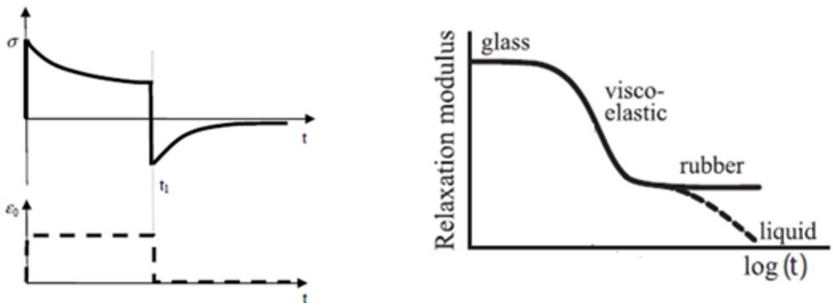

Fig. 2.2 Stress relaxation test and relaxation modulus.

$$E(t) = \frac{\sigma(t)}{\varepsilon_0} \tag{2.3}$$

In Fig. 2.2 (on right), the relaxation modulus E(t) variation with time is shown. Moreover, it is also possible to distinguish the rubbery and glassy plateaus, in which the material exhibits quite opposite behaviours [109]. These transient tests allow us to characterize the viscoelastic material reaction to a stress/strain load step. Another phenomena class, which describes the viscoelastic behaviour, is the dynamic experiments. These tests usually involve analysing the material reaction to a cyclic stress or strain applied:

$$\sigma(t) = \sigma_0 sin(\omega t) \tag{2.4}$$

where ω the angular frequency of is sinusoidal stress and depends on the time. In elastic materials, the strain generated by the stress also exhibits a sinusoidal trend with the same phase of the applied load. Contrarily, in viscoelastic materials the strain reaction shows a delay compared to stress, which is characterized by a phase angle δ. Therefore, the strain is given by [108] [110]:

$$\sigma(t) = \varepsilon_0 sin(\omega t - \delta) \tag{2.5}$$

The phase angle δ identifies the time displacement between applied stress and strain, as shown in Fig. 2.3:

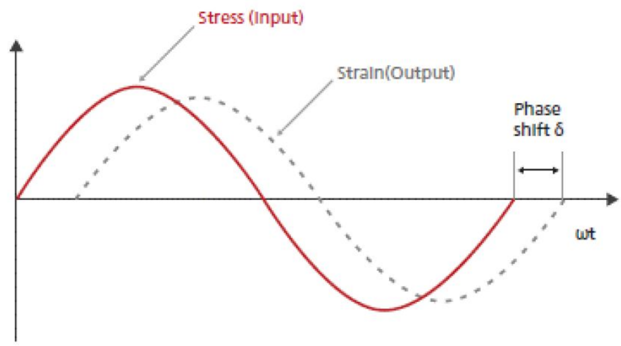

Fig. 2.3 Stress-strain time displacement.

Because of the phase displacement, the material dynamic stiffness can be considered as a complex variable E^*, according to Euler's formulation [108] [106]:

$$\frac{\sigma(\omega)}{\varepsilon(\omega)} = E^* = E' + iE\text{''} \tag{2.6}$$

Where E' is called Storage Modulus and E'' is called Loss Modulus. These quantities are deeply linked to the way the material dissipates a part of energy provided by means of a load/stress time function. Therefore, the both moduli are related to the phase angle δ, according to the vector diagram in Fig. 2.4.

Therefore, the phase angle value can be easily obtained by means of the ratio between imaginary and real part of the complex modulus E^*:

$$tan(\delta) = \frac{E\text{''}}{E'} \tag{2.7}$$

The phase angle tangent is called Loss Tangent and it denotes the entity of damping phenomenon in viscoelastic materials. It is important to see

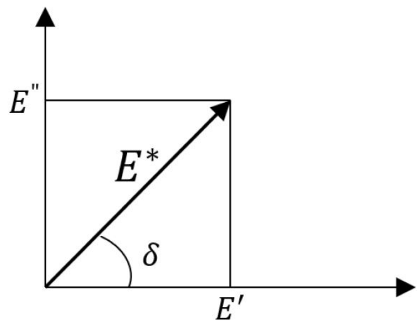

Fig. 2.4 E^* vector diagram.

that all these quantities, which characterized the viscoelastic behaviour, are function of the frequency at which the sinusoidal load is applied. To easily comprehend in which way these magnitudes are interconnected, a simple time load function can be applied to a polymer specimen. Analysing the material response, a part of the applied load is stored in the polymer to be release once the applied load is removed, meanwhile another part of the applied load is lost due to the internal mechanism of energy dissipation. On one hand, an increase of loss tangent indicates that the tested material dissipates a great amount of stored energy; on the other hand, a decrease of the loss tangent means that the polymer has more potential to store the elastic energy rather than to dissipate it.

2.2.2 Properties

The modulus, the energy loss and hysteresis of a viscoelastic material change in relation to two parameters: the frequency with which the force is applied and the material temperature the phenomena are evaluated on. It is important to point out that load frequency and material temperature produce opposite effects on the rubber behaviour, as represented in Fig. 2.5.

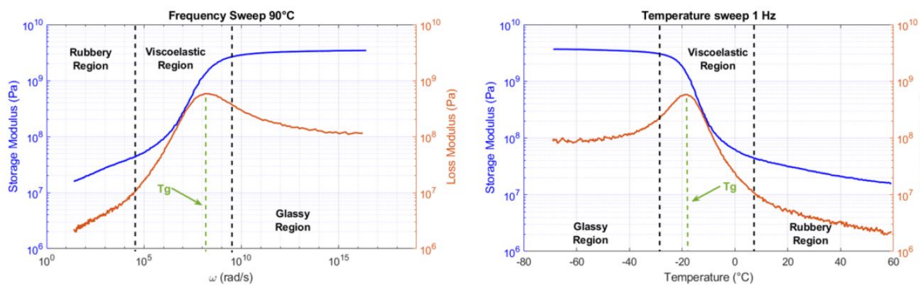

Fig. 2.5 Storage and loss moduli in temperature and frequency domains.

Frequency influence

Once the temperature was fixed, the Storage and Loss Modulus tendencies in frequency domain can be analysed. From a physical point of view, at low frequency the deformation occurs slowly. Keeping in mind the Voigt model, this means that the force required to move the dash pots is slight [111], offering a small resistance. In this case, the spring side is dominant, and the material appears to be fairly elastic (rubbery region). When this happens, the material is in a rubbery state and its hysteresis is low. Once the frequency increases, the force required to move the dashpot also increases due to its higher resistance. Hence, the material shows a viscoelastic behaviour (viscoelastic region). This is the most suitable behaviour range for tyre grip, because the hysteresis term is maximum in this frequency range. Indeed, the Loss Modulus *E*" reaches its highest value in this frequency-range. Clearly, if the frequency increases still further, the viscoelastic features fall again, and the material behaviour turns into glassy (glassy region). At this point, it is interesting to understand what happens inside the material. When the polymer molecular chains are subjected to stress, they start moving and being stretched in some directions and compressed in others. Each time the force is released, the chains relaxation occurs. The speed with which the chains return to undeformed shape depends on molecular mobility. So, there are three possible cases [112] [113]:

1. At low stress frequency, the polymer chains are relatively mobile and appear to be flexible and elastic;

2. If the frequency increases, the return to undeformed shape is delayed and the energy dissipation is marked (hysteresis phenomenon);

3. If the stress frequency still increases, the chains do not have the time to move and regress to initial conditions. Hence, the material becomes glassy and stops being viscoelastic.

All the above information linked to hysteretic behaviour are also valid, if we analyse the relationship between the Loss Factor (also called Loss Tangent) and the stress frequency. As soon as the Loss Tangent reaches its maximum, the material exhibits a hysteretic behaviour with energy loss. The presence of one loss peak is characteristic of most materials. Their loss factor peak is, in general, in the order of 0.6 or 0.8, such as for rubbers or rubber – like materials). Low loss peak (10^{-1} - 10^{-3}) is distinctive of hard plastic and other structural materials (steel, wood, etc.) [114].

Temperature influence

It has already been affirmed the frequency, with which the force is applied to polymer, and the temperature of the material affect the rubber in opposite ways. As shown in the temperature sweep diagram in Fig. 2.5, at very low temperatures, the storage modulus of the rubber is high. In this condition, at given frequency, the material is rigid and shows a glassy behaviour. At high temperature, the storage modulus is decreased, and the material more flexibly and elastically behaves.

In the intermediate temperature range, situated around the glass transition temperature, denoted as T_G, the material exhibits a viscoelastic behaviour. The T_G is known as the temperature below which the rubber tends closer to the glassy plateau and above which the polymer shows an increasingly rubbery state. At higher temperature, the polymer is sufficiently deformable in such a way that the chain segments between the sulphur bridges are able to move. During this motion, they scrub against adjacent chains, slowing down their movement and producing the energy dissipation (hysteresis) [115] [116]. The Glass Transition Temperature, as illustrated in Fig. 2.5, occurs near to the loss modulus maximum and is close to the middle point of the storage modulus into transition area. This feature usually takes place in rubbers with a very low fillers percentage. Anyway, if the examined rubber is a compound, just how usually happens in tyre structure, the maxima of loss factor and loss modulus do not match (see Fig. 2.6). This is due to the complexity of dynamic mechanical behaviour of these composites, which arises from the restricted movement of rubber molecules in presences of fillers [21, 23] [116].

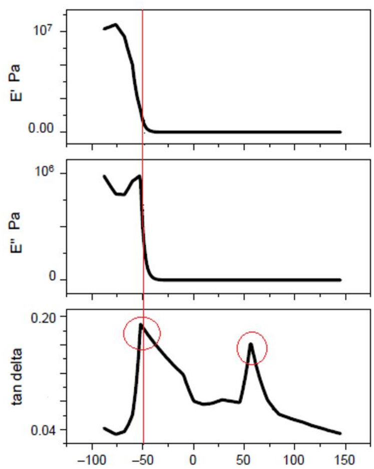

Fig. 2.6 Filler effect on the compound.

Moreover, the Loss Tangent diagram sometimes shows two peaks. Each peak is characteristic of the transition temperature for each filler in the rubber compound. The first peak usually occurs at low temperature, because it relates to the dynamic-mechanical behaviour of the rubber matrix, which exhibits the greatest damping (or hysteretic) effect. The second peak takes place at higher temperature and it arises from the mechanical behaviour of the additive fillers.

Time-temperature superposition

As already mentioned, the viscoelastic properties are related to the stress frequency and the material temperature. Actually, the frequency and temperature dependences are two phenomena closely interlinked to each other: there is an inversely proportional relation between an increase in the temperature and a reduction in the stress frequency. Whenever the stress frequency is increased at a given temperature, the polymer turns into glassy state; conversely, if the material heats up at a given stress frequency, it becomes softer [117] [106] [118]. These features arise from the balance between molecular velocity and the strain – rate. On one hand, if the strain-rate is greater than the speed at which the molecular chains can move in the polymer's structure, the material appears glassy; on the other, if the strain rate is lower than the molecular speed, the compound exhibits rubbery behaviour. Besides, the motion speed of chains inside the molecular structure is strictly dependent on the temperature at which the material is. This polymers' behaviour can be mathematically and physically explained introducing the Time-temperature superposition principle (or T.T.S.).

The T.T.S. states that, considering for example the Storage Modulus E', at two different temperature T_1 and T_0 such that $T_1 > T_0$, the value assumed by the modulus at the frequency ω_1 and the temperature T_1 will be the same at the frequency ω_0 and temperature T_0, which is also called reference temperature. Therefore, if T_1 is higher than T_0, the molecular processes are faster, and it is verified that $\omega_0 < \omega_1$. This phenomenon can be mathematically expressed as follows:

$$E'(\omega_{T_1}, T_1 = E'(\omega_{T_0}, T_0) \tag{2.8}$$

All the materials satisfying the equation (2.8) are called simple thermo-rheologic materials and their behaviour agrees with the time-temperature superposition theory. In this way, as the temperature changes, for example, (see Fig. 2.7, on left), the curve corresponding to $E' = f(\omega)$ relationship exhibits a horizontal shift according to the non-linear dependence on the temperature between the frequencies ω_1 and ω_0:

$$\omega_0 = \frac{\omega_1}{a_T(T_1)} \tag{2.9}$$

where the magnitude $a_T(T)$ is called shift factor and is defined by the following properties:

$$\begin{aligned} T_1 < T_0 &\rightarrow a_T(T_1) < 1 \\ T_1 = T_0 &\rightarrow a_T(T_1) = 1 \\ T_1 > T_0 &\rightarrow a_T(T_1) > 1 \end{aligned} \tag{2.10}$$

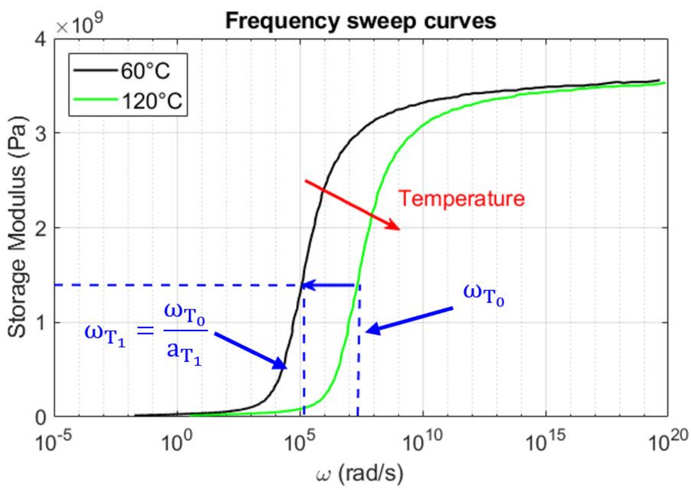

Fig. 2.7 Temperature shift in frequency domain.

Therefore, the superposition principle is used to determine the temperature dependency for mechanical properties of linear viscoelastic material from known properties at a reference temperature T_0. Moreover, the time – temperature superposition avoids the inefficiency of measuring a polymer's behaviour over long periods of time at a specified temperature by assuming that at higher temperatures and longer time the material will behave the same [108] [117] [118] [119]. In order to represent the E' curves at higher or lower temperatures, which superpose with the master curve at the reference temperature T_0, the shift factor has to be determined. This magnitude a_T is generally computed by means of an empirical relation first established by Malcolm L. Williams, Robert F. Landel and John D. Ferry. This relationship is known as W.L.F. equation and is expressed as:

$$log(a_T) = \frac{-C_1 * (T - T_0)}{C_2 + (T - T_0)} \tag{2.11}$$

where T is the temperature, T_0 is the reference temperature chosen to construct the generic master curve, C_1 and C_2 are empirical constants adjusted to fit the values of the superposition parameter $a_(T)$. The equation (2.11) can be used to fit discrete values of the shift factor a_T towards the temperature, as shown in Fig. 2.8.

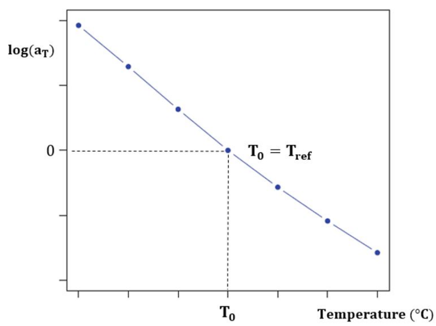

Fig. 2.8 Shift factor dependence on temperature.

The discrete values of the shift factor in Fig. 2.8 are determined thanks to experimental viscoelastic curves obtained at a series of temperatures over a specific time period. The values of the storage modulus frequency sweep tests estimated by means of a rheometer are shown in the left diagram in Fig. 2.9. After choosing a specific reference temperature, 120 degrees for example, the curves are then shifted one by one along the times scale until they superimpose and the master curve is identified, as shown in the right diagram in Fig. 2.9. Curves above the reference temperature are shifted to the right, and those below are shifted to the left [108] [117].

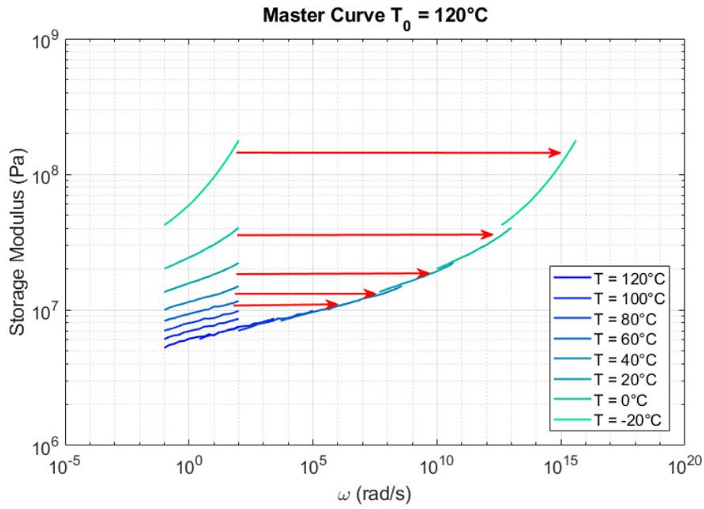

Fig. 2.9 Frequency shift and identified master curve.

Hence, the WLF equation allows to estimate the shift factors for different temperatures at which the material has been tested. However, when the WLF constants are found with data at temperatures above the glass transition temperature, the WLF can be used to temperatures at or above the glass transition ones.

Another common way to estimated shift factor at temperature below the glass transition ones is the method based on Arrhenius Law [7, 22 maio]:

$$log(a_T) = \frac{E_a}{2.303R}\left(\frac{1}{T} - \frac{1}{T_0}\right) \tag{2.12}$$

where E_a is the activation energy, R is the universal gas constant and T_0 is the reference temperature expressed in Kelvin. The activation energy in (2.12) can be evaluated through the modified Arrhenius equation:

$$\omega = \omega_0 e^{\left(\frac{E_a}{RT}\right)} \tag{2.13}$$

where ω is the measuring frequency and ω_0 is the frequency when the temperature approaches to infinity. The shift factor a_T, which is obtained thanks to equation (2.13), has the same value for all viscoelastic functions and it depends on the temperature chosen.

2.3 Experimental grip measurement in a controlled laboratory

With regard to the tyre grip testing, several methods have been already developed by many authors in literature, as shown in Fig. 1. Such tests can be carried out both indoor and outdoor, using proper tyre and tread specimens. The outdoor tests are usually executed with an instrumented vehicle/trailer on track to experiment different boundary conditions on the whole tyre. To evaluate the grip in the indoor tests on the whole tyre, specific test benches are used, as the rotating drum and flat track. Other indoor tests can be executed on a tread rubber specimen using pin on disk, in which the rubber specimen under investigation is approached to a rotating disc coated with different surfaces, and using a tribological test device called "British Pendulum", in which rubber specimen mounted at the end of a pendulum, slides on the testing asphalt when the pendulum is left free to oscillate from a given angular position. The analysed results in this section have been obtained by an acquisition campaign on an evolved version of the British Pendulum, described in detail in the following paragraphs.

2.3.1 BP-evo test rig

The proposed tribological bench available at the Tyre Lab of the Department of Industrial Engineering (DII) at Federico II University is based on an evolved version of the classic British Pendulum tester for skid resistance measurements. Contrariwise the old configuration of the BP-evo [120], which was developed during previous collaborations of the DII with Bridgestone Italia, this updated version has a new configuration of the load cell capable of reading the three forces channels (the tangential and the normal ones) according to the sensor reference system. The BP-evo and its conceptual scheme are shown in Fig. 2.10

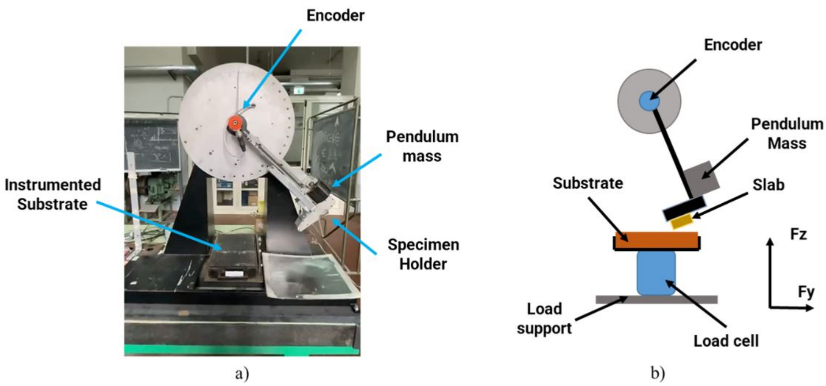

Fig. 2.10 a) British Pendulum evolved; b) test bench scheme

As represented in these figures, the tri-axial load cell is fixed on a rigid support and the rough substrate is fixed above the sensor. The cell is positioned in order to acquire positive normal load F_z and negative tangential force F_y along the sliding direction; moreover, the positioning is centred with respect to the plane of the pendulum motion allowing to acquire of neglectable values of F_x. The previous layout of the BP-evo included the load cell mounted on the pendulum arm, making the acquired signals processing more complicated due to inertial forces calculation and detraction from the global values. An encoder is installed in the revolute join to measure the angular speed of the pendulum arm, on which is fixed a mass so that the sliding body exhibits enough potential energy to win the frictional resistance forces. On the opposite side of the arm, a 100 N pre-loaded spring is mounted and a levers system exploits the spring reaction on the tread specimen holder. The pre-load spring is changeable and particular attention is dedicated to the levers system with spring, whose stiffness is responsible for the contact pressure reached at the specimen/road interface, as shown in Fig. 2.11. The 20x20 mm specimens are usually obtained from tyre tread or compound slabs and then fixed on the holder, which can be regulated so that the material correctly slides. The distance between the revolute join and the substrate is adjustable thanks to a regulation mechanism beyond the pendulum. This regulation is fundamental in order to set the proper sliding distance. The forces and encoder signals are acquired by an A/D board and processed in Matlab environment to convert the respectively from Volt to N/m and rad/s.

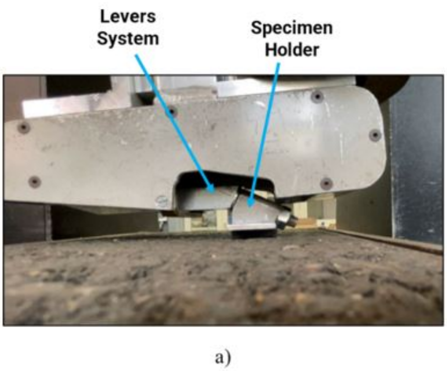

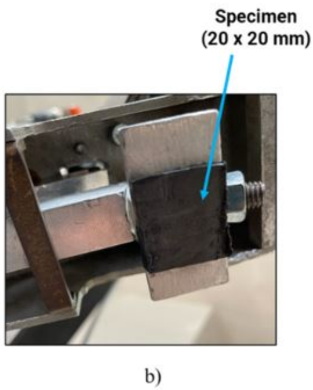

Fig. 2.11 a) Levers-spring system acting on specimen; b) specimen fixed on suitable holder

A regulable release mechanism of the pendulum arm is available in order to change the starting position and perform a set of measurements with high repeatability, as shown in Fig. 2.12. It is important to change the drop position because different sliding velocity ranges can be reached during the motion and therefore, the friction coefficient values with respect to v_s can be analysed in the post-processing phase.

a)

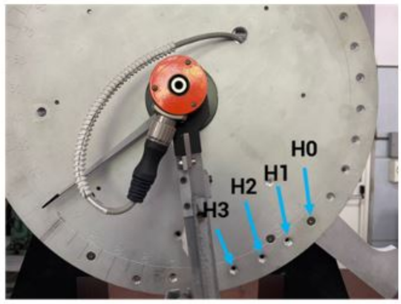

b)

Fig. 2.12 a) Pendulum drop button; b) Different starting position of the mass

Testing procedure

The testing procedure consists of performing 10 measurements for the DOE outlined in Table 2.1 on different compound specimens. For each substrate-temperature-starting position combination, 100 N pre-load spring is taken into account, because higher pre-load values do not affect the friction coefficient due to the levers system acting on the specimen holder and lowers give rise to nominal contact pressure far from the working range of the tested compounds, which belongs to truck/passenger automotive fields. The four different starting positions are chosen in order to analyse the friction coefficient in the sliding velocity range [1, 2] m/s.

Table 2.1 DOE for BP-evo testing - temperature and sliding velocity dependence

Temperature	20°C	45°C	70°C
Starting Position	H0	H1	H2
Pre-load Spring	100N	100N	100N
Wear level	0 %	0%	0%

Moreover, in order to taking into account the wear dependencies on the friction coefficient, the same procedure has been carried out in a fixed temperature of 45°C (corresponding to the nominal working temperature for a passenger tyre) for the DOE in Table 2.2

Table 2.2 DOE for BP-evo testing - wear and sliding velocity dependence

Temperature	45°C	45°C	45°C
Starting Position	H1	H1	H1
Pre-load Spring	100N	100N	100N
Wear level	0 %	30%	50%

Lower values of sliding velocity cannot be reached through the BP-evo testing because it would require very small contact lengths to avoid the pendulum stop during the specimen/road interaction: actually, if the motion starts from an almost vertical position of the mass with respect to the asphalt, the pendulum does not have enough potential energy to overcome the frictional resistance and the test is not useful. The friction coefficient of each specimen can be easily analysed with respect to the compound temperature: before starting the single test, a thermal gun is used to warm the specimen up to the temperature of interest, which is measured and checked by means of an IR pyrometer. It is important to highlight that a sort of “scrubbing” of the new specimen is always carried out on the selected asphalt because the requires a sort of “stabilization” before exploiting the effective friction coefficient. The scrubbing procedure consists of N test at ambient temperature, in which the pendulum slides starting from the same initial position, H0 for example. The amount of repetition N depends on the compound behaviour unless the corresponding friction coefficient reaches a stable average value as shown in Fig.2.13. Regarding the analysis on abrasive wear, the wear level on the specimens has been accelerated employing a sandpaper in order to accelerate the process.

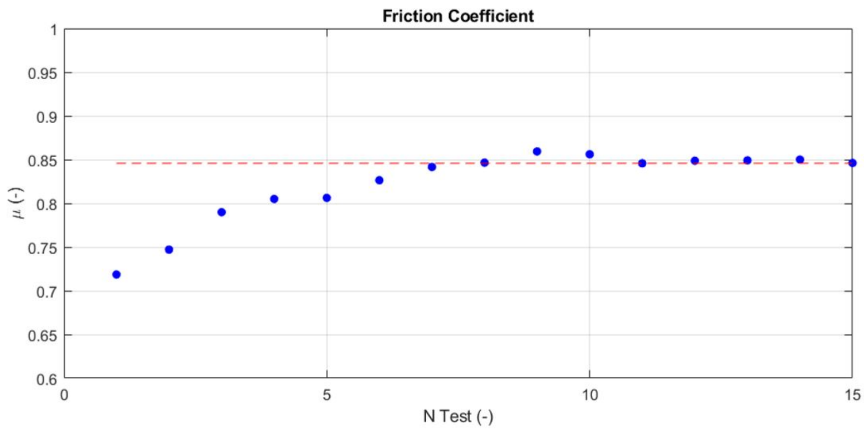

Fig. 2.13 Scrubbing procedure on a new tread compound specimen

Post-processing procedure

The friction coefficient can be estimated by processing the raw data acquired through BP-evo testing. For this purpose, the forces and sliding velocity have to be analysed in the time range corresponding to the contact phase between the compound specimen and the instrumented substrate. In the approach proposed in this paragraph, it is assumed that the contact starts when the maximum pendulum velocity is reached and it finishes when the F_z is close to 10 N. This threshold has been chosen because a significant part of the specimen area would no longer be in contact with the asphalt in correspondence with this normal load value. The signals extrapolated are displayed in red in Fig. 2.14

Once extrapolated the signals in the contact phase, the ratio of the absolute value of F_y respect to the normal force, F_z, is analysed towards the measured velocity. In Fig. 2.15 a, the ratio values towards the velocity for each test at ambient temperature and starting position H10 are shown. In this diagram, the friction coefficient exhibits a stable trend in the middle-velocity range (or time range), where a full contact with the rubber area and the substrate usually occurs; in the lower and higher velocity ranges, this ratio exhibits a little noise

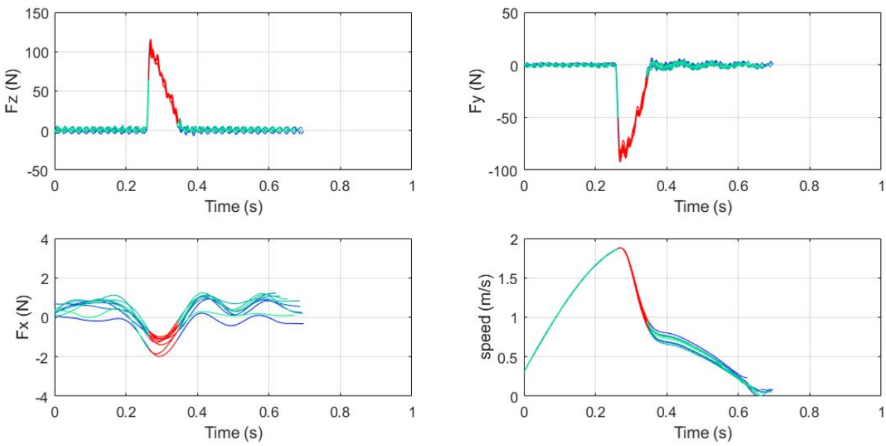

Fig. 2.14 Signals extrapolated in the contact phase (red lines)

since the contact at the leading edges is not complete and therefore, these areas are excluded in the analysis. In Fig. 2.15 b, the average value of the F_y/F_z in the highlighted area are displayed for every single test. The standard deviation of the $\mu_a vg$ over 10 measurements is very low (0.03) as proof of the trustworthiness of the test procedure repeatability, except for the first test, whose mean value is a bit out of the range. This processing approach can be carried out on experimental data acquired also for other starting positions test.

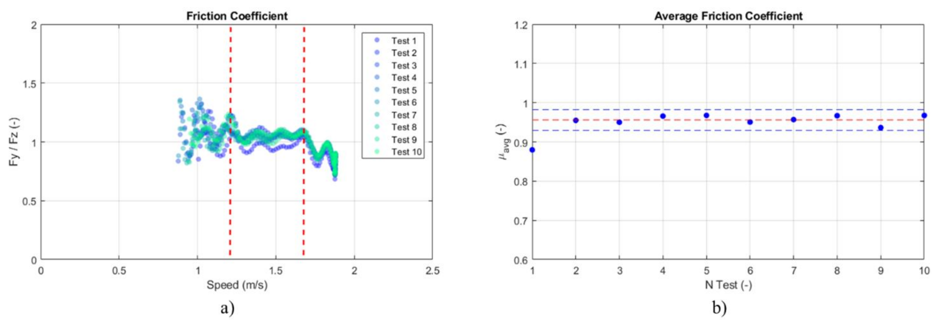

Fig. 2.15 a) Forces ratio towards the measured speed; b) average friction coefficient over 10 tests

2.3.2 Experimental campaign results

The experimental analysis of friction coefficient is performed on different slabs specimens belonging to different tyre tread compound application. Each compound has been characterised employing the data given by the industrial partner obtained through dynamic mechanical analysis (DMA). In Fig. 2.16 the master curves normalised to the maximum value is reported for 6 compounds used for experimental analysis through BP-evo. Due to confidential agreement the compound have been called A-B-C-D-E-F.

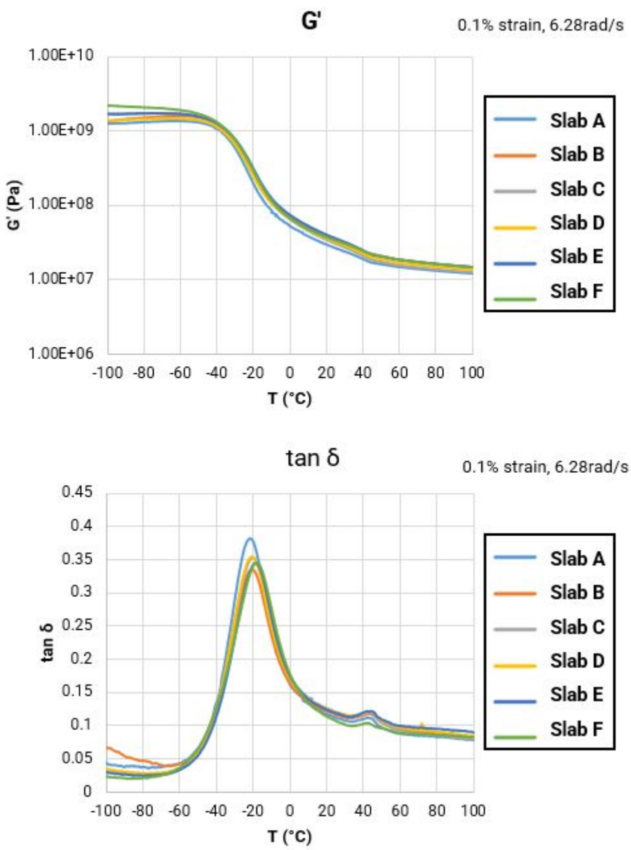

Fig. 2.16 DMA 1Hz normalised master curves for compounds of interest

Temperature effect

The experimental friction measurements are performed following the DOE outlined in Table 2.1. The results are displayed in terms of subplot for each tyre tread specimen with the aim to identify the friction coefficient variations due to temperature – sliding conditions effects. The author highlights that the experimental results at low speed could be affected by inaccuracies due to the low sliding distance for the completion of the pendulum motion. In the Fig. 2.17, it is possible to observe with different color the the trend friction coefficient with the temperature, in particular at 20°C, 45°C and 70°C highlited respectively in blue, red and black.

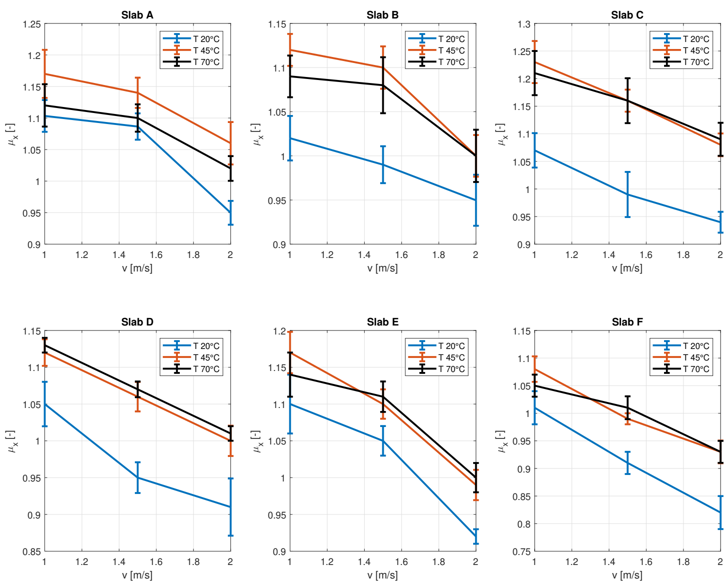

Fig. 2.17 Friction results on 6 different compound at three different temperature

The graphs show a small difference on the maximum value of the friction coefficient, an expected result because the viscoelastic properties of the six compounds are too similar (Fig. 2.16. In addition, the results are in line with the literature, because a downward slope path with the sliding velocity can be observed for all the analyzed compounds, and a parabolic trend with temperature that emphasizes a thermal dependence for the friction coefficient and an optimal working temperature.

Wear effect

The experimental friction measurements are performed following the DOE outlined in Table 2.2. The test campaign aimed at establishing how the friction coefficient varies was therefore carried out under nominal conditions of fixed temperature and sliding (45°C, 1.5 m/s and 100N preload).

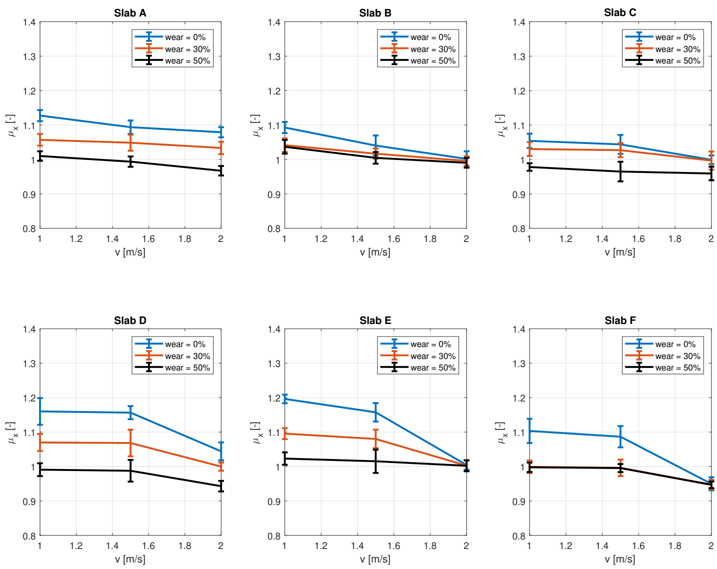

Fig. 2.18 Friction results on 6 different compound at three different wear level

The abrasive wear process was accelerated using sandpaper for three levels of wear in terms of percentage by abraded weight: 0%, 30% and 50% corresponding to New, Middle age and Worn tyre conditions. It was not possible to investigate beyond 50% wear due to constructional limitations of the pendulum. From the above graphs a decreasing trend of the friction coefficient with wear can be seen.

2.4 MF-evo tyre model

The general expression of the MF can be analytically described as follows:

$$y(x) = D \cdot \sin\left[C \cdot \arctan\left\{B \cdot x - E \cdot (B \cdot x - \arctan(B \cdot x)\right\}\right] \tag{2.14}$$

with

$$Y(x) = y(x) + S_v$$
$$x = X + S_h$$

where $Y(x)$ is a dynamic output (F_x, F_y or M_z), X is the kinematic input (slip ratio or slip angle), B is the rigidity factor, C is the shape factor, D is the peak value, E is the bending factor, S_v and S_h are the vertical and horizontal shifts, respectively.

The above six quantities are known as MF macro-coefficients, defining Pacejka's curve shape. Each macro-coefficient is itself a polynomial (linear, quadratic, trigonometric, exponential) function of tyre's kinematic and dynamic variables, combining several micro-parameters without a clear physical meaning (Figure 2.19a)). The equation (2.14) describes only the pure conditions, which can be extended to the combined ones, introducing the "hill function" G (Figure 2.19b)):

$$G = \frac{\cos(C \cdot \arctan(B \cdot x - E \cdot (B \cdot x - \arctan(B \cdot x))))}{\cos(C \cdot \arctan(B \cdot S_{h,x} - E \cdot (B \cdot S_{h,x} - \arctan(B \cdot S_{h,x}))))} \tag{2.15}$$

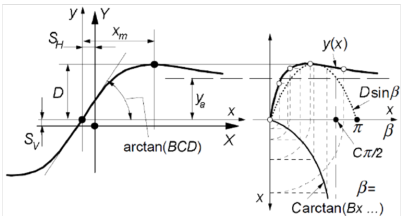

(a) *Pacejka's pure interaction curves*

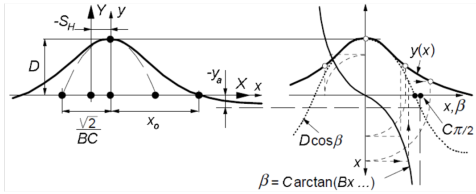

(b) *Pacejka's hill function G for combined interactions*

Fig. 2.19 Pacejka's Magic Formula [14]

Despite the fact that the MF model offers several advantages, embodying a good robustness and a relatively low computational cost, its original analytical form does not take into account of tyre's thermodynamic and wear conditions, which could considerably affect the tyre dynamics, especially in motorsport applications. It is possible to observe that the use of the standard MF (in dashed) formulation does not allow to take into account of the influence of compound temperature and internal pressure on the friction coefficient (Fig. 2.21a)), of tyre temperature on the tyre stiffness (Fig. 2.21b)), and of the grip variation due to tread thickness variation and chemical degradation (Fig. 2.21c)).

The temperature of the different internal tyre layers are acquirable by invasive thermocouples inserted at different levels levels of the tread thickness to evaluate the temperature gradient with reference to the deep layers usually not reachable by IR measurement instrumentation. On the other hand, the wear level could be in theory acquirable by optical vehicle onboard or test bench systems.

Reference temperature used to underline the stiffness-temperature correlation is Tread Core temperature. Tread Core (in red, Figure 2.20) is situated between Tread Surface (in blue) and Tread Base (in black), whereas Tread Base represents the part of the compound in direct contact with the tyre belt layer.

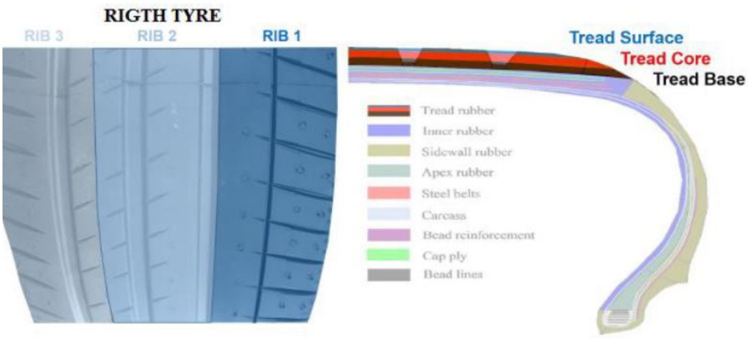

Fig. 2.20 Tyre thermal layers

By means of a tyre thermal model, it is possible to predict the temperature gradient with a high level of accuracy within the entire tyre structure. Starting from the model outputs in terms of temperatures and local thermal exchanges, the physical considerations particularly suitable to distinguish the optimal thermal range of each compound and the variation of tyre dynamic behaviour due to the thermal effect, can be further performed.

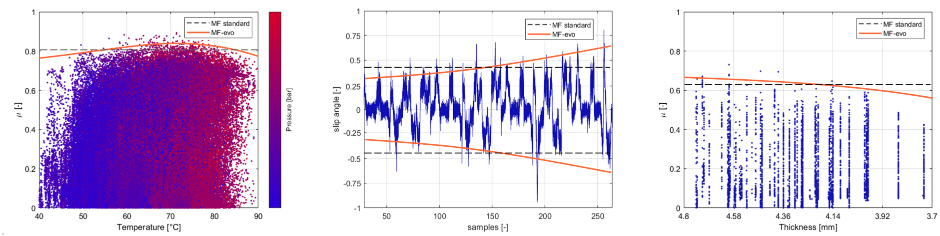

(a) *Compound temperature effect* (b) *Slip angle variation* (c) *Wear influence*

Fig. 2.21 MF-std and MF-evo in a multiphysical data domain.

To overcome the above modelling limits, the authors have proposed in [101] an advanced methodology making use of the additional polynomial formulations for the analytical description of the macro- and micro-parameters:

$$y_{evo} = f(x_{std}, x_{evo}, T_{compound}, T_{carcass}, p_{internalAir}, w) \tag{2.16}$$

where x_{std} is the original set of MF parameters, x_{evo} represents an array of additional polynomial coefficients, accounting for the thermodynamic $T_{compound}$ (tyre compound temperature), $T_{carcass}$ (tyre carcass temperature), $p_{internalAir}$ (tyre internal pressure), and the wear w (compound wear level) dependencies. With MF-evo, the original MF macro- and micro- coefficients are modified on the basis of the compound and carcass temperatures, inner air pressure and wear level, allowing to extend the analytical formulation validity within the whole tyre working range.

The above MF-evo outputs have been calculated employing the friction coefficient μ (Fig. 2.22d)) and the stiffness quantity C (Fig. 2.22e)), evaluated starting from the polynomial representation of the micro-parameters of Magic Formula towards the temperature (Fig. 2.22a)), the pressure (Fig. 2.22b)) and the wear level (Fig. 2.22c)) effects. The visual representation clearly evidences the optimal window towards the tyre temperature and the inflation pressure quantities, where the maximum amount of friction performance can be achieved. Friction coefficient μ and stiffness C can be evaluated for each combination of tyre compound temperature and internal inflation pressure, and of tyre carcass temperature and inflation pressure, respectively. However, the above quantities remain valid only for a specific wear level condition, since usually the amount of grip available decreases due to wear phenomenon, as well as tyre can become stiffer with abrasive phenomena and chemical degradation, linked to the thermal fatigue within the tyre compound. This means that the mentioned surfaces will differ for different wear levels, adding a further necessary variable dimension to the multiphysical operating domain of the tyre integrated system.

It follows that such a complex and multiphysical model, based on the MF empirical formulation and data-driven parametrization, has to be properly

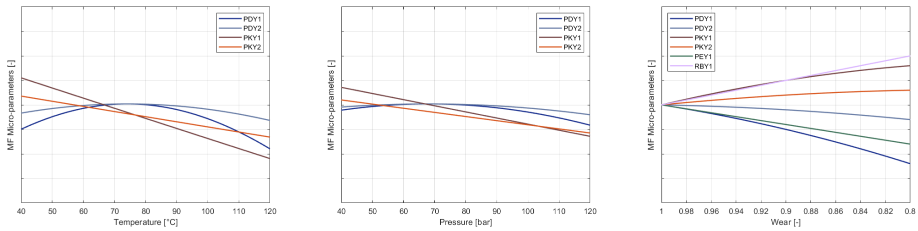

(a) *Temperature effect* (b) *Pressure effect* (c) *Wear effect*

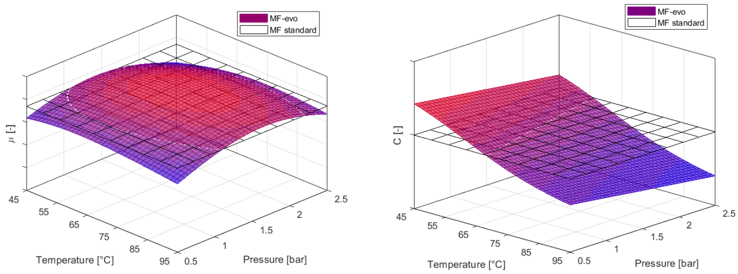

(d) *Friction multiphysical dependencies* (e) *Stiffness multiphysical dependencies*

Fig. 2.22 MF-evo micro-parameters and tyre characteristics.

calibrated, acting on a set of micro- and macro-parameters able to reproduce the overall behaviour shown by the experimental evidences. This work focuses on the calibration of the MF-evo model addressing the specific procedure developed to pre-select the nominal range towards temperature, internal pressure and wear level conditions, where the standard set of Pacejka's Magic Formula parameters can be identified, describing the additional necessary steps allowing to extend the analytical formulation validity within the entire operating domain of the tyre. The procedure has been developed and validated with an industrial motorsport partner; therefore, figures are reported in non-dimensional scale due confidentiality agreements.

It appears clear that the standard MF model can be calibrated only to reproduce the response of the tyre towards kinematic and dynamic inputs without taking into account the variations of the tyre characteristics towards further physical effects, as evidenced with black lines in the above figures.

2.4.1 Data analysis

Grip analysis

The analysis shows that grip depends on both tread-surface and tread-core temperatures. The tyre external surface temperature varies with faster dynamics, which is not well correlated with the grip variation which does not show fast dynamics. This means that the surface temperature is not able to modify in so short time the whole tread mechanical characteristic. The grip shows an excellent correlation with a temperature weighted averages between tread surface and tread core, the tread-core layer shows a slower dynamic, so the mean average temperature dynamics have the same trend of the grip. The tyre frictional behaviour can be practically linked to the tread core-surface weighted averages temperature which can be used to optimize the compound mechanical characteristics starting from its thermal behaviour. The above temperature can clearly be evaluated only by means of a specific tyre thermal model. After a sensitive analysis, the most suitable temperature to identify the grip variation is a weighted average between tread-surface and the tread-core, in particular:

$$T_{GRIP} = 0.25 \cdot T_{treadsurface} + 0.75 \cdot T_{treadcore} \tag{2.17}$$

The trend of the grip shows the presence of a temperature range in which grip reaches its maximum values. Moreover, the trend of grip with the wear show a not linear trend. With the aim of modelling the noted trend, grip law as function of temperature and grip has been assumed as a Gaussian function. Moreover, Gaussian function for each pressure and wear level shows its maximum value at increasing temperature values as pressure increases and initial tread thickness.

In this way, it is possible to scale the Pacejka curves, identified at about maximum performance-temperature, pressure and wear levels, and to get the interaction forces at any temperature or pressure value, multiplying the scale factor LMUY for lateral interaction and LMUX for longitudinal interaction by the gain-function output corresponding to that temperature or pressure and wear value.

Stiffness analysis

It is possible to say that cornering stiffness and braking stiffness depend on both tread-base and tread-core temperatures and therefore wear level. Thus, reference temperature for stiffness functions identification has been evaluated as a weighted average of tread-base and tread-core temperature, provided by a tyre thermal model:

$$T_{STIFFNESS} = 0.7 \cdot T_{treadsurface} + 0.3 \cdot T_{treadcore} \tag{2.18}$$

The functions displayed assume a unitary value in correspondence with maximum performance-temperature and pressure and allows to scale Pacejka curves depending on the temperature and pressure level by multiplying the scaling factor LKY for lateral interaction and LKX for longitudinal interaction.

2.4.2 Calibration approaches

In order to obtain a correct Pacejka's MF microparameters identification, starting from the experimental data, it is necessary to prepare and accurately select the data to be identified. Indoor testing (See par. 2.3.1) is commonly performed on specific test benches [120], aiming to reproduce the tyre operating conditions in completely controlled environment. Diverse methodologies, making use of Inertial Measurement Unit (IMU), Global Position System (GPS), vehicle side slip sensors (See Chapter 3, wheel force transducers, encoders and sophisticated moving benches, have been developed for outdoor testing.

The operation of data pre-processing is of fundamental importance considering that the optimizer is blind to the correctness and, above all, to the physicality of the data itself.

The concept of intelligent tool lies in guiding the user in a series of fundamental steps for data cleaning. In fact, when collecting data from several streams and with manual input from users, information can carry mistakes, be incorrectly inputted, or have gaps. Incorrect or inconsistent data can lead the optimization algorithm to misidentification and false conclusions. Data cleaning is the process of preparing data for analysis by detecting data that is incorrect, incomplete, irrelevant, duplicated and then replacing, modifying, or deleting them. These data are usually not necessary or helpful when it comes to analyse data because it may hinder the identification process or provide inaccurate results. Data cleaning is not simply whereas the purpose is to find a way to maximize a data set's accuracy without deleting information. The first step within data pre-processing is outliers' detection. The second step consist in the identification of the starting MF parameters set valid in a specific range of thermodynamic and wear conditions which will be extended to reproduce the entire operative range by means of the specific multiphysical dependencies of the MF parameters towards temperature, pressure and wear effects.

Data pre-processing

The techniques regarding the outliers' detection can be generally classified in statistical and data-mining methods. Statistical models were the earliest adopted for outlier detections. They are mostly based on the comparison of some statistical properties to test whether outliers exist. Anscombe and Guttman proposed a general principle for statistical models for outlier detection - An outlier is an observation which is suspected of being partially or

wholly irrelevant because it is not generated by the stochastic model assumed
.

In the case under study, since a distribution function isn't known and it cannot be identified a priori on the data, non-statistical or data-mining methodologies should be preferable. Furthermore, one of the main advances of the proposed technique compared to [121] regards the fact that any a priori assumptions are assumed about the underlying data distribution. Data-mining methods do not require any prior assumptions about the data distribution and they are comparatively simple to implement, but the associated computational effort is not always negligible [122].

- **Data clustering** is a classification method where observations are classified into groups (clusters) so that observations within a cluster are more similar to each other than they are to observations belonging to another cluster. While clustering methods' main objective is the classification, they can also be utilized in outlier detection by for example considering clusters of small sizes or clusters of one as outliers [122].

  A partitioning method creates k partitions, called clusters, from given set of n data objects. Initially, each data objects are assigned to some of the partitions. An iterative relocation technique is used to improve the partitioning by moving objects from one group to another. Each partition is represented by either a centroid or a medoid. A centroid is an average of all data objects in a partition, while the medoid is the most representative point of a cluster. The fundamental requirements of the partitioning based methods are each cluster must contain at least one data object, and each data objects must belong to exactly one cluster.

  One of simplest and widely used clustering algorithm is k-means, which is firstly proposed by MacQueen (1967) [123]. k-Means can be used to automatically recognize groups of similar instances/items/objects/points in data training. The algorithm classifies instances to a pre-defined number of clusters specified by the use (e.g. assume k clusters). The first important step is to choose a set of k instances as centroids (centers of the clusters) randomly, usually choose one for each cluster as far as possible from each other. Next, the algorithm continues to read each instance from the dataset and assigns it to the nearest cluster. There are some methods to measure the distance between instance and the centroid but the most popular one is Euclidian distance. The cluster centroids are always recalculated after every instance insertion. This process is iterated until no more changes are made.

- **Distance - based models** outlier detection methods determine the label of an instance based on the distance to its neighbors, and they are also known as Nearest Neighbor (NN)-based algorithms [123]. As non-parametric approaches, they make no assumptions about the underlying distribution from which the datasets are generated. Instead, the most important motivation is the local similarity. It suggests that when the distance between instances in feature space are small under a specific distance metric, they share similar mode of behavior. In other words, the proximity of an outlier object to its neighbors is very different from that of a normal object. The region of the neighbors is determined by the top k instances of the ascending sequence of distances to the reference point. A distance-based outlier is defined by Ng and Knorr as follows: A point p in a dataset is an outlier with respect to parameters k and δ if at least k points in the data set lies greater than distance δ from p. This definition generalizes the definition of outlier in statistics and it is suitable when the dataset does not fit any standard distribution.

- **Ramaswamy outliers' detection method**.Among the data-mining related methods [124, 125, 111, 126], the Ramaswamy distance-based technique described in [124], has been chosen. In the context of the tyre-road interaction data, where the forces are function of a considerable number of inputs and the parameters, a distance-based measure $D_k(P)$

is adopted to objectively quantify the similarity between objects in feature spaces (i.e. longitudinal and lateral interaction characteristics), where the forces and the torques instances not respecting the above threshold for the same input conditions u are disregarded as outliers. Ramaswamy algorithm detects the outliers on the basis of the distance $D_k(P)$ between each point P and a set of k data points nearest to it. To detect outliers, a partition-based algorithm is presented that first partitions the input points using a clustering algorithm and computes lower and upper bounds on D^f or points in each partition. It then uses this information to identify the partitions that cannot possibly contain the top n outliers and prunes them. Outliers are then computed from the remaining points (belonging to unpruned partitions) in a final phase. The key idea underlying the partition-based algorithm is to first partition the data space, and then prune partitions as soon as it can be determined that they cannot contain outliers. Since n is typically small, our algorithm prunes a significant number of points, and thus results in substantial savings in the amount of computation. Consequently, k^{th} nearest neighbor computations need to be performed for very few points, thus speeding up the computation of outliers. The steps performed by the partition-based algorithm are described below:

where k is user-specified parameter controlling the smoothing effect, to be defined on the basis of the data quality and the expected accuracy of measurement and estimation methodologies. The following figures show the influence of the parameter K on the outliers' detection for an experimental dataset provided by a top-ranking motorsport team. Data have been adimensionalized due to confidentiality agreements. Experimental points have been colored from blue to red for increasing $log(D^k)$ values.

The data pre-processing phase should also include a specific binning process, in order to remove redundancies and to prepare the dataset for the

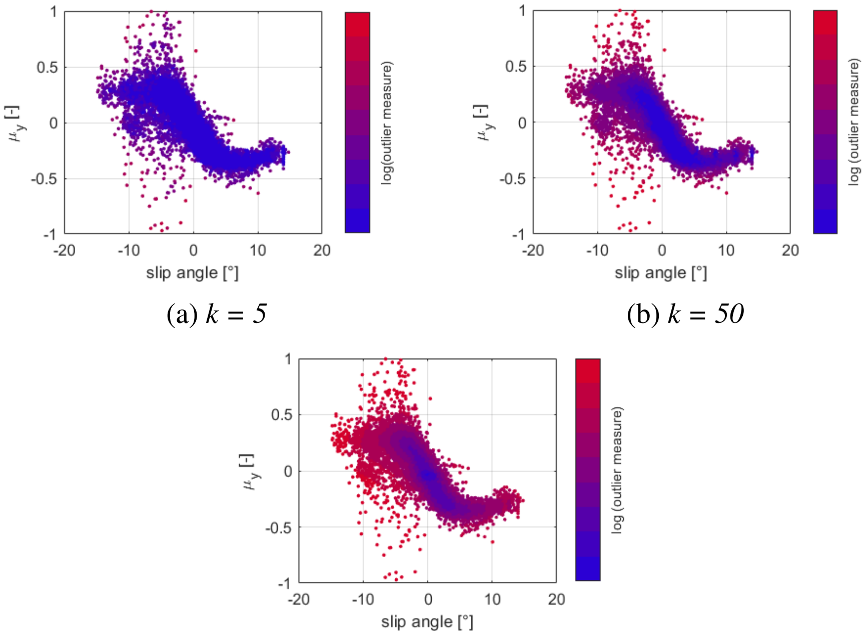

(a) k = *5*

(b) k = *50*

(c) k = *500*

Fig. 2.23 Ramaswamy method for outliers detection - k sensitivity.

ultimate model parameterization phase. Among the binning methods available in the literature, the equal-frequency methods, which divide the data into bins of equal number of samples, and the equal-width methods, which cluster the data into bins of equal width, could be highlighted. An equal-width method is be more suitable for a highly non homogeneous dataset, avoiding penalization in the low-frequency observation areas (i.e. possible transient unstable operating conditions) which could be essential to ensure the correct modelling extrapolation [127]. The choice of the number of bins is certainly decisive for the model calibration, since a too high number would not give consistent results, while a too small number could lead to an excessive loss of information.

Identification of MF-evo parameters

Once the data have been properly pre-processed and clustered, the determination of the above reference range can be achieved employing multidimensional heat maps, coloured respect to quantity of samples belonging to each cluster for every dimension of interest (temperature, pressure and wear).

Once the reference multidimensional range for the parametrization of the MF-std model has been determined, the MF identification procedure consists of three consecutive steps: pure MF identification, combined model MF identification, and MF refinement.

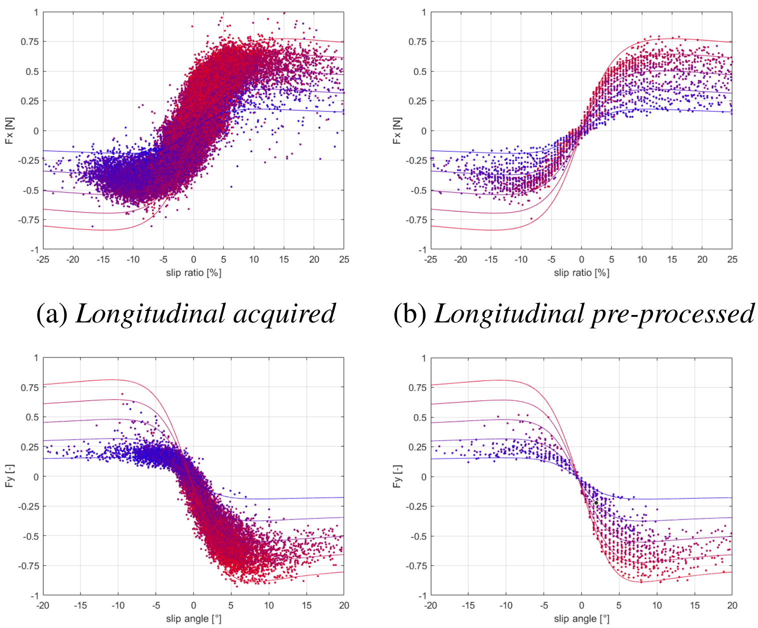

(a) *Longitudinal acquired* (b) *Longitudinal pre-processed*

(c) *Lateral acquired* (d) *Lateral pre-processed*

Fig. 2.24 Pacejka's standard MF in a reference multidimensional cluster.

In particular, the pure MF parameters are identified considering the working conditions characterized by slip ratio values lower than 0.1% to parametrize the pure lateral interaction, and slip angle values lower than $0.1deg$ to identify the pure longitudinal interaction; the combined MF identification is carried out keeping pure interactions parameters constant. The final phase concerns the refinement of the micro-coefficients' set by means of an iterative procedure in an increasingly narrow range per each step k until the convergence criteria are reached. The results of the implemented methodology are reported in the figures 2.24a) and b), corresponding to longitudinal and lateral interactions, respectively.

It is worth noting that the minimization procedure using the pre-processed dataset, represented in the figures 2.24b) and 2.24d), allows not only to guide better the identification towards the optimum solution, but also to minimize the computational time and the identification-linked resources involved.

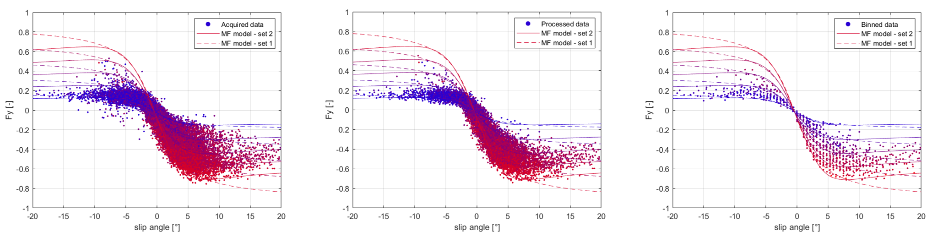

(a) *Acquired data* (b) *Processed data* (c) *Binned data*

Fig. 2.25 Comparison of the MF model towards data for two different micro-parameters sets

Table 2.3 MF model error towards the experimental data.

MF set	#	Mean percentage error (%)			R-squared error (-)		
		acquired	processed	binned	acquired	processed	binned
identified	1	13.07	8.64	6.41	0.85	0.88	0.89
expected	2	14.28	8.78	4.44	0.84	0.87	0.95

More specifically, the necessity and the importance of a proper preliminary data processing and the consequent improvement in the micro-coefficients' identification can be clearly appreciated in the figure 2.25 and in the table 2.3.

Two diverse data-driven identifications have been computed starting from raw experimental data (MF set 1 - dashed lines) and from pre-processed data (MF set 2 - lines) and compared towards differently processed data samples: the raw experimental data (Fig. 2.25a)), the processed data with the removal of outliers (Fig. 2.25b)), and fully pre-processed data (Fig. 2.25c)). The relative percentage spread and the R-squared error have been also reported in the table 2.3. It is easy to note that in all the cases the data pre-processing allows to achieve an obvious reduction of the model error. However, with respect to the raw data, the MF set 1 provides a higher R-squared value than the MF set 2, even if the MF set 1 presents a non-physical trend (without any decay after the peak), due to the majority of samples concentrated in the linear working range.

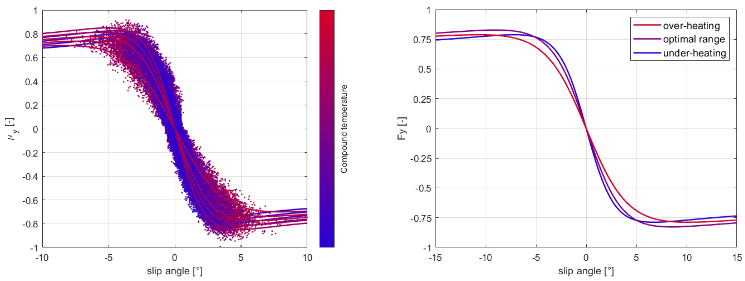

(a) *MF-evo curves with data* (b) *MF-evo identified trend towards temperature*

Fig. 2.26 MF-evo - lateral interaction towards tyre temperature.

Once the MF micro-coefficients have been properly pre-identified in a reference operating range, the variations of the MF-evo coefficients, taking into account of the thermal and wear state, can be introduced. In particular, as shown in figure 2.26, the stiffness of the MF-evo lateral interaction decreases with increasing temperature, while the friction peak is maximum in correspondence of an optimal thermal range and decreasing in both under-heating and over-heating conditions.

2.4.3 Results

A motorsport case study, making use of the presented methodology for the correct calibration of a MF-based multiphysical tyre model, is presented in the results section. The experimental data employed to calibrate the MF-evo multiphysical model and to validate the calibration methodology have been collected with a motorsport research partner: for this reason, due to confidentiality agreements, the scales in all the following figures are non-dimensional.

The data employed for the tyre parametrization have been acquired during the common handling tests on track, where the purpose is usually not to explore as many different operating conditions possible, but rather to maximize the vehicle overall performance (i.e. with tyres employed in a linear range and in a narrow thermodynamic working window). To exclude the impact that different asphalts could have on the maximum achievable performance, only runs belonging to a single track have been employed within the case study. The experimental session has consisted of:

1. long run tests, allowing to investigate the warm-up, stabilized and over-heating phases, both in terms of the tyre thermal dynamics and wear;

2. qualifying tests, aiming to achieve the tyre maximum performance for diverse initial conditions of the tyre (i.e. temperature and internal pressure) and of the vehicle setup;

3. specific maneuvers (i.e. wheel locking in braking or wheel-spin), allowing to explore unstable operating zone with higher slip values.

Several tests have been also performed with tyres with different initial wear levels to investigate the effect of wear phenomenon on the tyre dynamic behaviour.

The vehicle has been equipped with a significant amount of instrumentation to evaluate the kinematics and the dynamics at each corner, as well as the thermodynamics of each tyre:

1. encoders mounted on the wheel spindles, measuring the wheel angular velocity [128];
2. an inertial measurement unit to acquire angular velocities and linear accelerations [129];
3. an optical speed sensor, measuring the vehicle's linear velocities [130];
4. infrared temperature sensors pointing on the tread external and internal surfaces [131, 132];
5. TPMS sensors, monitoring inner air pressure and temperature [132];
6. a steering-angle sensor [128].

The kinematic and the dynamic quantities concerning a single corner can be reliably acquired and estimated [44] [35] [103]. Compound and carcass temperatures, inner air pressure and wear level are among the additional inputs of the MF-evo model, and they can be provided by means of both additional sensors and physical predictive models. The temperatures of the different internal tyre layers are acquirable by invasive thermocouples inserted at different levels of tread thickness to evaluate the temperature gradient with reference to the deep layers usually not reachable by IR measurement instrumentation, but in this way their presence could arise singularities within the stress-strain distribution and therefore the thermal state of the tyre. On the other hand, the wear level could be in theory acquirable by optical vehicle onboard or test bench systems. In the light of the above, the availability of the tyre physical thermodynamic and wear real-time models, able to evaluate in run-time all the necessary additional physical quantities concerning the tyre integrated system, becomes absolutely crucial. Indeed, once properly calibrated and validated towards experimental data, the MF-evo-based real-time co-simulation tyre system can be employed within offline vehicle setup optimization routines, advanced data analysis algorithms, hard real-time simulation environments for driver-in-the-loop, software-in-the-loop and hardware-in-the-loop, and, finally, embedded onboard model-based control logics. In [102] [103] the authors describe the real-time tyre thermal model, able to calculate the temperatures governing the grip and stiffness properties, whereas the procedure to take into account of tread wear and compound degradation thanks to physical grip model is presented in [35].

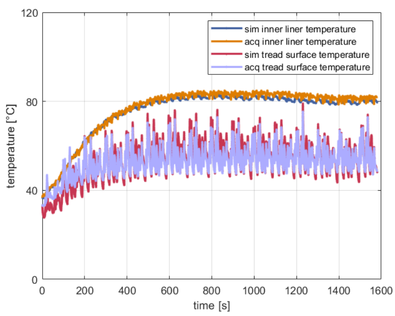

(a) *Thermal model outputs*

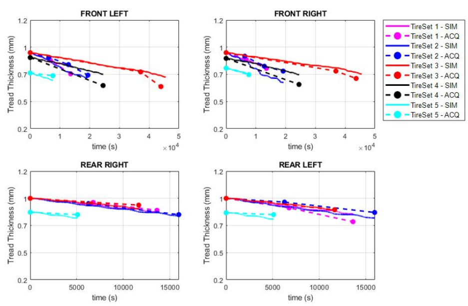

(b) *Wear model outputs*

Fig. 2.27 Validation of the physical models on experimental data

As an example, the impossibility to represent the tyre behaviour at different thermal ranges has been quantified for a given long run of a representative track testing session in the table 2.4, where the model percentage spread for grip μ and stiffness C has been evaluated through the equation (2.19) for both MF-std and MF-evo formulations with respect to the data collected in cold initial and hot tyre working conditions.

$$e_{\%}(x) = \frac{\sum_{i=1}^{n} \left| \frac{y_i(u_i) - f(x,u_i)}{y_i(u_i)} \right|}{n} \cdot 100 \tag{2.19}$$

As demonstrated by the experimental evidences, it appears clear that the standard MF model can be calibrated only to reproduce the response of the tyre towards kinematic and dynamic inputs without taking into account the variations of the tyre characteristics towards further physical effects, as evidenced with black lines in the above figures and synthesized in the table 2.4.

Table 2.4 MF-std and MF-evo model error comparison towards track experimental data.

	μ_{cold}	C_{cold}	μ_{hot}	C_{hot}
MF-std	6.62%	18.91%	4.47%	11.49%
MF-evo	2.45%	5.48%	2.12%	4.27%

A properly calibrated MF-evo model can be employed in co-simulation with thermodynamic and wear models in software-in-the-loop, hardware-in-the-loop or driver-in-the-loop scenarios. An example of a possible MF-evo employment advantage is illustrated in figure 2.28, where the steering angles, resulting from the simulation and the acquired ones, are compared. It is evident that the MF-evo model allows to simulate the effect of stiffness reduction as observed experimentally with increasing temperature, highlighted by the fact that the demand in steering increases through time as the thermal tyre state evolves.

Thanks to the availability of a multiphysical tyre model, the reliability of the whole vehicle model radically increases, providing an important instrument to better study the possible safety and performance strategies, allowing to optimize the vehicle setup directly in the simulation environment.

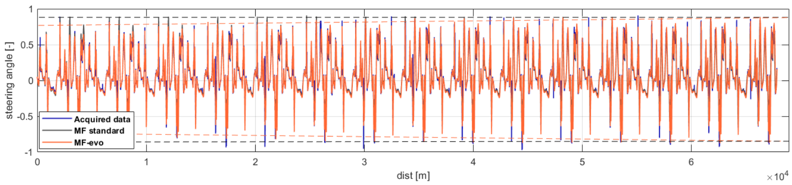

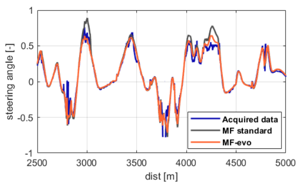

(a) *Warm-up*

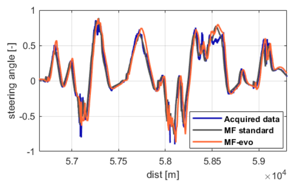

(b) *Thermal steady-state*

Fig. 2.28 Comparison within the steering angle employed in reality and in simulations using the MF standard and MF-evo models

Chapter 3

System state estimation approaches

3.1 Introduction

State estimators adopted are based on the filtering technique and only their discrete-time form is considered in this thesis work, in order to be easily implemented in a recursive algorithm.
The term "filtering" assumes a new meaning in state estimation, it is well beyond the idea of separation of the components of a mixture. According to [133] it can be seen as the solution of an inversion problem, in which one knows how to represent the *measurable variables* as functions of the variables of principal interest, called *state variables*. In essence, it inverts this functional relationship and estimates the independent variables as inverted functions of the dependent measurable variables. These variables of interest are also allowed to be dynamic, with dynamics that are only partially predictable. However one needs to define what the term "state" means before presenting the state estimators. The states of a system are those variables of principal interest that provide a complete representation of the status of the system at a given instant of time. If the values of the measurable variables are known

at the present time, it is possible to estimate the values of the output of the system using *state-space models*. State-space models can be generally divided into linear models and nonlinear.

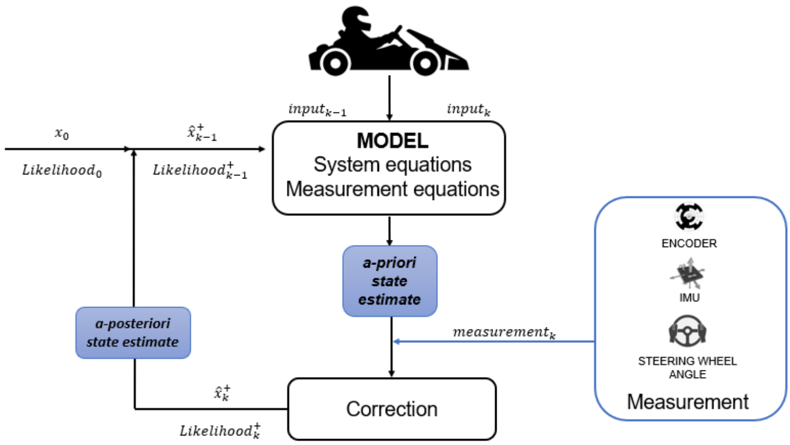

Fig. 3.1 Discrete Kalman filter cycle

All state estimators presented in this chapter can be summarized using the flow chart in figure 3.1. Considering a discrete representation of the time, the figure is representative of what happen in a generic time step, from the previous time step $k-1$ to the current one k. Starting with the statistical knowledge of the state (mean value and covariance) at $k-1$, it is possible to propagate them with time using the system model equations.
In the *Process box* there are two sets of equations, the first one propagates the state with time using the system equations, giving the *a-priori state estimate* as output, the second one computes the *measurement estimate* based on the knowledge of the *a-priori state estimate*. The *measurement estimate* is compared to the *actual measurement* in order to correct the *a-priori state estimate* and then to obtain the *a-posteriori state estimate*, that is the state estimate referring to the time step k. This is what happen in the *Correction box*, whose output is the *current time state estimate*. The acquired (actual)

measurements are available at each time step using the filtering technique, unlike smoothing technique. An initial state estimate must be defined at the beginning and this is the first *previous time state estimate* of the iterative algorithm.

The *system equations* and the *measurement equations* constitute the plant model, represented in figure 3.1 as the process box. Both sets of equations are obtained from the single track vehicle model presented in the previous chapter. The forward Euler method is adopted to write them in a discrete-time form. It is important to highlight that the equations listed below are the same for all the implemented state estimators, they represent the physical core of the state estimator. There is the need for state estimator because only the physical model of the vehicle is not able to replicate the actual vehicle behaviour in different maneuvers. The state estimator is a mathematical tool that is able to correct the state estimate given by the physical model. It is possible to take into account the inaccuracy of the physical model introducing the *process noise*. In the same way one introduces the *measurement noise* in order to take into account the noisy acquired measurements. There are several noise models in probability theory literature, only the *white noise model* is considered in this thesis work. Also the noise is *Gaussian*, *zero-mean*, *uncorrelated* and considered as *additive*.
For what said above a general form of the equations is:

$$
\begin{aligned}
\hat{x}_k^- &= f(\hat{x}_{k-1}^+, u_{k-1}) + w_{k-1} \\
z_k &= h(\hat{x}_k^-, u_k) + v_k
\end{aligned}
\tag{3.1}
$$

where x_{k-1}^+ is the *a-posteriori state estimate* at the previous time step and x_k^- is the *a-priori state estimate* at the current time step, also $f(\cdot)$ and $h(\cdot)$ are respectively representative of the system equations and of the measurements equations. The other measurable variables in $f(\cdot)$ and $h(\cdot)$ are indicated as u_k and u_{k-1}. Finally w_{k-1} and v_k are respectively the *process noise* and the *measurement noise*, considered additive. In addition they are Gaussian, zero-mean and uncorrelated with Q and R as their covariance matrix.

$$\begin{aligned} w &\sim (0, Q) \\ v &\sim (0, R) \end{aligned} \tag{3.2}$$

3.2 Kalman filter

3.2.1 Linear Kalman filter

The linear Kalman filter manages how the mean of the state and the covariance of the state propagate with time. From now on it is referred to as KF.
It only deals with linear dynamic systems, estimating the state $\hat{x} \in \Re^n$, where n is the number of states.

At the generic time step k an estimation of x_k is computed before processing the measurements acquired at the time step k, this is called *a-priori state estimate* and indicated as $\hat{x}_k^-$, also its covariance is computed and indicated as P_k^-. Then the estimate of x_k is refined processing the measurement, the resulting estimate is the *a-posteriori state estimate* and indicated as $\hat{x}_k^+$, and its covariance as P_k^+. What said can be summarized in a mathematical form:

$$\begin{aligned} \hat{x}_k^- &= E[x_k | y_1, y_2, .., y_{k-1}] \\ P_k^- &= E[(x_k - \hat{x}_k^-)(x_k - \hat{x}_k^-)]^T \\ \hat{x}_k^+ &= E[x_k | y_1, y_2, .., y_k] \\ P_k^+ &= E[(x_k - \hat{x}_k^+)(x_k - \hat{x}_k^+)]^T \end{aligned} \tag{3.3}$$

Let now introduce a generic linear system written in the matrix formulation and also adopting the discrete-time form, in order to be implemented in the KF recursive algorithm.

$$x_k = F_{k-1} x_{k-1} + G_{k-1} u_{k-1} + w_{k-1} \tag{3.4}$$

the matrix F_{k-1} relates the state at the previous time step to the state at the current one, while the latter is related to the other measurable variables by the matrix G_{k-1}. Both matrices can be constant or time-dependent, in (3.4) time-dependent matrices are considered and each matrix element is referred to the previous time step $k-1$. Moreover in (3.4) an additive noise is considered. The measurement equation can be defined under the same hypothesis:

$$z_k = H_k x_k + v_k \tag{3.5}$$

this equation uses the current time state computed by (3.4) in order to update the measurements z to the current time. The matrix H_k can be constant or time-dependent as well, also note that in (3.5) its elements refer to the current time step. An additional noise is present in (3.5) as in (3.4), they fulfil the hypothesis stated in (3.2).
Both the equations constitute the process model, that is the physical core of the KF.
The KF algorithm can be divided into two step:

- Time update, it projects the last computed state estimate ahead in time. It is also called *prediction step*.

- Measurement update, it adjusts the projected estimate by an actual measurement at that time. It is also called *correction step* [134].

The KF equations can be written using the nomenclature adopted in (3.3) and the hypothesis in (3.2). The time update equations are:

$$\begin{aligned} \hat{x}_k^- &= F_{k-1}\hat{x}_{k-1}^+ + G_{k-1}u_{k-1} \\ P_k^- &= F_{k-1}P_{k-1}^+F_{k-1}^T + Q_{k-1} \\ z_k &= H_k\hat{x}_k^- \end{aligned} \tag{3.6}$$

while the measurement update equations are:

$$
\begin{aligned}
K_k &= \frac{P_k^- H_k^T}{H_k P_k^- H_k^T + R_k} \\
\hat{x}_k^+ &= \hat{x}_k^- + K_k(y_k - z_k) \\
P_k^+ &= (I - K_k H_k) P_k^-
\end{aligned}
\tag{3.7}
$$

Equations (3.6) and (3.7) can be easily implemented in a recursive algorithm, but the first *previous time state estimate* and its covariance must be defined. They are indicated as:

$$
\begin{aligned}
\hat{x}_0^+ &= E[x_0] \\
P_0^+ &= E[(x_0 - \hat{x}_0^+)(x_0 - \hat{x}_0^+)]^T
\end{aligned}
\tag{3.8}
$$

where x_0 is an initial value of the state. Note that in (3.7) the amount of the correction is proportional to the *residual error* between the actual measurements, y_k, and the predicted value of the measurements, z_k. Also, the *Kalman gain* takes into account the process noise and the measurement noise through their covariance matrices.

This section is necessary in order to point out the basis of the next KFs, in fact the equations (3.6) and (3.7) are common to every KFs but each one is characterized by the strategy adopted to deal with the nonlinearity of the process.

3.2.2 Extended Kalman Filter

The EKF is based on the linearization of the nonlinear system around the state estimate.

It is necessary to rewrite the process equations with the aim to translate into a mathematical form what that means. The actual state and measurement vectors can be written using the general form of the process equations with nonadditive noise[1]:

$$\begin{aligned} x_k &= f(x_{k-1}, u_{k-1}, w_k) \\ y_k &= h(x_k, u_k, v_k) \end{aligned} \tag{3.9}$$

Performing now a first-order Taylor expansion of the equations around the previous time state estimate, $\hat{x}_{k-1}^{+}$

$$\begin{aligned} x_k &\approx f(\hat{x}_{k-1}^{+}, u_{k-1}) + \left.\frac{\partial f}{\partial x}\right|_{\hat{x}_{k-1}^{+}} (x_{k-1} - \hat{x}_{k-1}^{+}) + \left.\frac{\partial f}{\partial w}\right|_{\hat{x}_{k-1}^{+}} w_{k-1} \\ y_k &\approx h(\hat{x}_k^{-}, u_k) + \left.\frac{\partial h}{\partial x}\right|_{\hat{x}_k^{-}} (x_k - \hat{x}_k^{-}) + \left.\frac{\partial h}{\partial v}\right|_{\hat{x}_k^{-}} v_k \end{aligned} \tag{3.10}$$

where the Jacobian matrices are

$$\begin{aligned} \left.\frac{\partial f}{\partial x}\right|_{\hat{x}_{k-1}^{+}} &= \frac{\partial f(\hat{x}_{k-1}^{+}, u_{k-1}, 0)}{\partial x} = F_{k-1} \\ \left.\frac{\partial f}{\partial w}\right|_{\hat{x}_{k-1}^{+}} &= \frac{\partial f(\hat{x}_{k-1}^{+}, u_{k-1}, 0)}{\partial w} = W_{k-1} \\ \left.\frac{\partial h}{\partial x}\right|_{\hat{x}_k^{-}} &= \frac{\partial h(\hat{x}_k^{-}, u_k, 0)}{\partial x} = H_k \\ \left.\frac{\partial h}{\partial v}\right|_{\hat{x}_k^{-}} &= \frac{\partial h(\hat{x}_k^{-}, u_k, 0)}{\partial v} = V_k \end{aligned} \tag{3.11}$$

considering now additive noise, the equations (3.10) are

$$\begin{aligned} x_k &\approx \hat{x}_k^{-} + F_{k-1}(x_{k-1} - \hat{x}_{k-1}^{+}) \\ y_k &\approx z_k + H_k(x_k - \hat{x}_k^{-}) \end{aligned} \tag{3.12}$$

[1] nonadditive noise is only considered in this case and for reasons of generality, as shown in [134].

Defining the *prediction error* as the difference between the actual vector and the approximated (predicted) vector:

$$\begin{aligned} \tilde{e}_{x_k} &\equiv x_k - \hat{x}_k^- \\ \tilde{e}_{z_k} &\equiv y_k - z_k \end{aligned} \tag{3.13}$$

substituting the (3.13) in (3.10)

$$\begin{aligned} \tilde{e}_{x_k} &\approx F_{k-1}(x_{k-1} - \hat{x}_{k-1}^+) + \varepsilon_k \\ \tilde{e}_{z_k} &\approx H_k(x_k - \hat{x}_k^-) + \nu_k \end{aligned} \tag{3.14}$$

where ε_k and ν_k represent new indipendent random variable having zero mean and covariance matrices $W_{k-1}QW_{k-1}^T$ and $V_kRV_k^T$ respectively. those equations are linear and their form is quite similar to the KF's time-update equations (3.6). Thus applying the KF logic:

$$\hat{x}_k^+ = \hat{x}_k^- + \hat{e}_k \tag{3.15}$$

where $\hat{e}_k$ is the estimated error using a hypothetical KF, according to [134], where the KF's equation is :

$$\hat{e}_k = K_k\tilde{e}_{z_k} \tag{3.16}$$

substituting the latter in the (3.15)

$$\hat{x}_k^+ = \hat{x}_k^- + K_k\tilde{e}_{z_k} = \hat{x}_k^- + K_k(y_k - z_k) \tag{3.17}$$

this equation can be used in the measurement-update of the EKF.
This type of filter is referred to as *FO-EKF* from now on, this is because of the first-order Taylor expansion (3.10).

It is now possible to write the time update equations and measurement update equations of the *FO-EKF*. A generic nonlinear process is considered for this purpose, the noise model is now considered additive, Gaussian, zero-mean and uncorrelated, differently than in (3.9):

$$\begin{aligned} x_k &= f(x_{k-1}, u_{k-1}) + w_k \\ y_k &= h(x_k, u_k) + v_k \\ w_k &\sim (0, Q) \\ v_k &\sim (0, R) \end{aligned} \tag{3.18}$$

The following algorithm is based on the hypothesis stated above, so the partial derivative of the process equations with respect to noise terms is null because of that.

Algorithm 1 First-Order Extended Kalman Filter algorithm

$\hat{x}_0^+ = E[x_0]$ ▷ *Initial state*
$P_0^+ = E[(x_0 - \hat{x}_0^+)(x_0 - \hat{x}_0^+)^T]$ ▷ *Initial state Covariance*
procedure FO-EKF(T, $\{u\}_{k=1}^T$)
  for $k = 1 \rightarrow T$ **do**
    $\hat{x}_k^- = f(\hat{x}_{k-1}^+, u_{k-1}, 0)$ ▷ *a-priori state estimate*
    $P_k^- = F_{k-1} P_{k-1}^+ F_{k-1}^T + Q$ ▷ *a-priori state estimate covariance*
    $z_k = h(\hat{x}_k^-, u_k, 0)$ ▷ *a-priori measurement estimate*
    $K_k = P_k^- H_k^T (H_k P_k^- H_k^T + R)^{-1}$ ▷ *Kalman gain*
    $\hat{x}_k^+ = \hat{x}_k^- + K_k(y_k - z_k)$ ▷ *a-posteriori state estimate*
    $P_k^+ = (I - K_k H_k) P_k^-$ ▷ *a-posteriori state estimate covariance*
  end for
end procedure

Iterated Extended Kalman Filter

The Iterated Extended Kalman Filter (I-EKF) reduces the linearization error in the EKF for highly nonlinear systems, as well as the Second Order Extended Kalman Filter in the next section.

The FO-EKF approximates *measurement equations* by expanding it in a Taylor series around $\hat{x}_k^-$, the reason is because it is the best estimate of x_k before the measurement at time k is taken into account. But when the *a-posteriori*

state estimate is obtained, the best estimate of x_k is $\hat{x}_k^+$. The basic idea of the I-EKF is to reduce the linearization error by reformulating the Taylor series expansion around $\hat{x}_k^+$. This process can be repeated as many times as desired, although for most problems the majority of the possible improvement is obtained by only relinearizing one time [16].
The main difference between SO-EKF and I-EKF is the iteration cycle that refines the measurement update equations at time k, so the more the measurement equations are nonlinear the more effective the refinement is.
All the equations used in this type of EKF have the same mathematical form as seen in the FO-EKF, the algorithm is almost the same, in addition there is the recursive update of the state estimate using the best state estimate available.

Algorithm 2 Iterated Extended Kalman Filter algorithm

```
$\hat{x}_0^+ = E[x_0]$                                        ▷ Initial state
$P_0^+ = E[(x_0 - \hat{x}_0^+)(x_0 - \hat{x}_0^+)^T]$          ▷ Initial state Covariance
procedure I-EKF($T$, $\{u\}_{k=1}^T$, N)
    for $k = 1 \to T$ do
        $\hat{x}_k^- = f(\hat{x}_{k-1}^+, u_{k-1}, 0)$          ▷ a-priori state estimate
        $P_k^- = F_{k-1} P_{k-1}^+ F_{k-1}^T + Q$               ▷ a-priori state estimate covariance
        $\hat{x}_{k,1}^+ = \hat{x}_k^-$
        for $i = 1 \to N$ do
            $z_{k,i} = h(\hat{x}_{k,i}^+, u_k, 0) - H_{k,i}(\hat{x}_k^- - \hat{x}_{k,i}^+)$   ▷ a-priori measurement estimate
            $K_{k,i} = P_k^- H_{k,i}^T (H_{k,i} P_k^- H_{k,i}^T + R)^{-1}$                  ▷ Kalman gain
            $\hat{x}_{k,i+1}^+ = \hat{x}_k^- + K_{k,i}(y_k - z_{k,i})$                        ▷ a-posteriori state estimate
            $P_{k,i+1}^+ = (I - K_k H_k) P_k^-$                    ▷ a-posteriori state estimate covariance
        end for
    end for
end procedure
```

Second Order Extended Kalman Filter

The Second Order Extended Kalman Filter (SO-EKF) perform a second order Taylor expansion of the process equations, $f(\cdot)$ and $h(\cdot)$.
The SO-EKF presented in this section is based on [135], that provides a small correction in the original derivations of the SO-EKF. In addition, it

is a simplified version as reported by [16], that means ignoring the Taylor expansion around the noise terms.
Starting from the equations in (3.9), performing the second-order Taylor expansion around the last best state estimate $\hat{x}$ [2]:

$$\begin{aligned} x_k \approx f(\hat{x}_{k-1}^{+}, u_{k-1}) + \left.\frac{\partial f}{\partial x}\right|_{\hat{x}_{k-1}^{+}} (x_{k-1} - \hat{x}_{k-1}^{+}) + \\ + \frac{1}{2}\sum_{i=1}^{n} \phi_i (x_{k-1} - \hat{x}_{k-1}^{+})^T \left.\frac{\partial^2 f_i}{\partial x^2}\right|_{\hat{x}_{k-1}^{+}} (x_{k-1} - \hat{x}_{k-1}^{+}) \end{aligned} \tag{3.19}$$

$$\begin{aligned} y_k \approx h(\hat{x}_k^{-}, u_k) + \left.\frac{\partial h}{\partial x}\right|_{\hat{x}_k^{-}} (x_k - \hat{x}_k^{-}) + \\ + \frac{1}{2}\sum_{i=1}^{m} \phi_i (x_k - \hat{x}_k^{-})^T \left.\frac{\partial^2 h_i}{\partial x^2}\right|_{\hat{x}_k^{-}} (x_k - \hat{x}_k^{-}) \end{aligned} \tag{3.20}$$

before evaluating their mathematical form at the last best estimate, lets focus on the second order term in the Taylor expansion of the system equations. It is computed by the summation of the product between a $nx1$ column vector ϕ_i, with all zeros except for a one in the ith element, and the nxn matrix $(x_{k-1} - \hat{x}_{k-1}^{+})^T \left.\frac{\partial^2 f_i}{\partial x^2}\right|_{\hat{x}_{k-1}^{+}} (x_{k-1} - \hat{x}_{k-1}^{+})$, where $\frac{\partial^2 f_i}{\partial x^2}$ is the Hessian of the system equations.
The quadratic term of the summation can be written as:

$$(x_{k-1} - \hat{x}_{k-1}^{+})^T \left.\frac{\partial^2 f_i}{\partial x^2}\right|_{\hat{x}_{k-1}^{+}} (x_{k-1} - \hat{x}_{k-1}^{+}) = Tr\left[\left.\frac{\partial^2 f_i}{\partial x^2}\right|_{\hat{x}_{k-1}^{+}} \right. \tag{3.21}$$

[2] the last best state estimate $\hat{x}$ is always the last computed, so it is the previous time state estimate $\hat{x}_{k-1}^{+}$ for the system equations and it is the a-priori state estimate $\hat{x}_k^{-}$ for the measurement equations.

and because of the value of $(x_{k-1} - \hat{x}^+_{k-1})$ is not known, it can be replaced with its expected value, which is the covariance of the Kalman filter:

$$(x_{k-1} - \hat{x}^+_{k-1})^T \left.\frac{\partial^2 f_i}{\partial x^2}\right|_{\hat{x}^+_{k-1}} (x_{k-1} - \hat{x}^+_{k-1}) \approx Tr\left[\left.\frac{\partial^2 f_i}{\partial x^2}\right|_{\hat{x}^+_{k-1}} P^+_{k-1}\right] \tag{3.22}$$

hence repeating the same for the one in the Taylor expansion of the measurements equations

$$(x_k - \hat{x}^-_k)^T \left.\frac{\partial^2 h_i}{\partial x^2}\right|_{\hat{x}^-_k} (x_k - \hat{x}^-_k) = Tr\left[\left.\frac{\partial^2 h_i}{\partial x^2}\right|_{\hat{x}^-_k} (x_k - \hat{x}^-_k)(x_k - \hat{x}^-_k)^T\right] \tag{3.23}$$

$$(x_k - \hat{x}^-_k)^T \left.\frac{\partial^2 h_i}{\partial x^2}\right|_{\hat{x}^-_k} (x_k - \hat{x}^-_k) \approx Tr\left[\left.\frac{\partial^2 h_i}{\partial x^2}\right|_{\hat{x}^-_k} P^-_k\right] \tag{3.24}$$

It is now possible to evaluate the modified (3.19) and the (3.20) at $x = \hat{x}$

$$x_k = f(\hat{x}^+_{k-1}, u_{k-1}) + \frac{1}{2}\sum_{i=1}^{n} \phi_i Tr\left[\left.\frac{\partial^2 f_i}{\partial x^2}\right|_{\hat{x}^+_{k-1}} P^+_{k-1}\right] \tag{3.25}$$

$$y_k = h(\hat{x}^-_k, u_k) + \frac{1}{2}\sum_{i=1}^{m} \phi_i Tr\left[\left.\frac{\partial^2 h_i}{\partial x^2}\right|_{\hat{x}^-_k} P^-_k\right] \tag{3.26}$$

Finally, the SO-EKF algorithm is reported.

Pros and Cons of the Extended Kalman Filters

The EKFs presented are the most used and popular form, there are other different forms. The EKFs provide a simple state representation, because they only exploits the first two moments of the estimate random variable: the mean is the first moment and its variance is the second moment. The EKFs rely on the computation of the Jacobian matrices and also Hessian

Algorithm 3 Second Order Extended Kalman Filter algorithm

1: $\hat{x}_0^+ = E[x_0]$ ▷ *Initial state*
2: $P_0^+ = E[(x_0 - \hat{x}_0^+)(x_0 - \hat{x}_0^+)^T]$ ▷ *Initial state Covariance*
3: **procedure** SO-EKF(T, $\{u\}_{k=1}^T$)
4: **for** $k = 1 \to T$ **do**
5: $\hat{x}_k^- = f(\hat{x}_{k-1}^+, u_{k-1}, 0) + \frac{1}{2}\sum_{i=1}^{n} \phi_i Tr\left[\frac{\partial^2 f_i}{\partial x^2}\bigg|_{\hat{x}_{k-1}^+} P_{k-1}^+\right]$ ▷ *a-priori state estimate*
6: $P_k^- = F_{k-1}P_{k-1}^+F_{k-1}^T + Q$ ▷ *a-priori state estimate covariance*
7: $z_k = h(\hat{x}_k^-, u_k, 0) + \frac{1}{2}\sum_{i=1}^{m} \phi_i \mathrm{Tr}\left[\frac{\partial^2 h_i}{\partial x^2}\bigg|_{\hat{x}_k^-} P_k^-\right]$ ▷ *a-priori measurement estimate*
8: $K_k = P_k^- H_k^T (H_k P_k^- H_k^T + R)^{-1}$ ▷ *Kalman gain*
9: $\hat{x}_k^+ = \hat{x}_k^- + K_k(y_k - z_k)$ ▷ *a-posteriori state estimate*
10: $P_k^+ = (I - K_k H_k)P_k^-$ ▷ *a-posteriori state estimate covariance*
11: **end for**
12: **end procedure**

matrices in SO-EKF, their computation may be quite difficult expecially for high nonlinear systems. They can be evaluated analytically or numerically, in the first case the computational burden required is smaller than in the second case, but at the same time the first approach could lead to mathematical and algebraic errors during the execution of partial derivatives or the conversion in code. Another flaw of the EKFs concerns the impossibility of linearization of the process, in fact some processes could be discontinuous, have singularities and the Jacobian matrix can't be computed. Considering a general process, whose linearization is possible, the main EKFs flaw is the linearization of a nonlinear process, in fact the linearized transformation is a good estimation method only when error propagation can be well approximated by a linear model. At best it affects the performance and the quality of the estimation, at worst it brings to a divergence of the estimated state. This could force the use of very small sampling times, in which the linearization is not a so high approximation of the nonlinear process.

3.2.3 Unscented Kalman Filter

Unscented Kalman Filter (UKF) aims to overcome the main EKFs' flaw, it provides a simpler and more immediate way to propagate mean and covariance of random variables through a non-linear transformation. Suppose that x is a random variable with mean $\bar{x}$ and covariance P_{xx}, a second random variable y is related to x through the nonlinear function $y = f(x)$, the goal is to calculate the mean $\bar{y}$ and the covariance P_{yy} of y. The statistics of y are calculated by determining the density function of the transformed distribution and by evaluating the statistics from that distribution. In some special cases (for example when $f(\cdot)$ is linear) exact closed form solutions exist, this is the KF case. However, such solutions do not exist in general and approximate methods must be used. The method should yield consistent statistics. Ideally, these should be efficient and unbiased. The transformed statistics are consistent if the inequality holds

$$P_{yy} - E[(y-\bar{y})(y-\bar{y})^T] \geq 0 \tag{3.27}$$

This condition is extremely important for the validity of the transformation method. If the statistics are not consistent, the value of Pyy is under-estimated. If a Kalman filter uses the inconsistent set of statistics, it will place too much weight on the information and under estimate the covariance, raising the possibility that the filter will diverge. By ensuring that the transformation is consistent, the filter is guaranteed to be consistent as well. However, consistency does not necessary imply usefulness because the calculated value of Pyy might be greatly in excess of the actual mean squared error. It is desirable that the value of the left hand side should be minimised (efficient transformation). Finally, it is desirable that the estimate is unbiased or $\bar{y} \approx E[y]$. As remarked by [15], the problem of developing a consistent, efficient and unbiased transformation procedure can be examined by considering the Taylor series expansion of the nonlinear equation about $\bar{x}$. This series can be expressed as:

$$f(x) = f(\bar{x}+\Delta x) = f(\bar{x}) + \nabla f \Delta x + \frac{1}{2}\nabla^2 f \Delta x^2 + \frac{1}{3!}\nabla^3 f \Delta x^3 + \frac{1}{4!}\nabla^4 f \Delta x^4 + \dots \tag{3.28}$$

where Δx is a zero mean Gaussian variable with covariance Pxx, and $\nabla^n f \Delta x^n$ is the appropriate nth order term in the multidimensional Taylor Series. According to [15], it can be shown that the transformed mean and covariance are

$$\begin{gathered}\bar{y} = f(\bar{x}) + \frac{1}{2}\nabla^2 f P_{xx} + \frac{1}{2}\nabla^4 f E[\Delta x^4] + \dots \\ P_{yy} = \nabla f P_{xx}(\nabla f)^T + \frac{1}{2x4!}\nabla^2 f(E[\Delta x^4] - E[\Delta x^2 P_{yy}] - E[P_{yy}\Delta x^2] + P_{yy}^2)(\nabla^2 f)^T + \\ + \frac{1}{3!}\nabla^3 f E[\Delta x^4](\nabla f)^T + \dots\end{gathered} \tag{3.29}$$

In other words, the nth order term in the series for $\bar{x}$ is a function of the nth order moments of x multiplied by the nth order derivatives of $f(\cdot)$ evaluated at $x = \bar{x}$. If the moments and derivatives can be evaluated correctly up to the nth order, the mean is correct up to the nth order as well. Similar comments hold for the covariance equation as well, although the structure of each term is more complicated. Since each term in the series is scaled by a progressively smaller and smaller term, the lowest order terms in the series are likely to have the greatest impact. Therefore, the prediction procedure should be concentrated on evaluating the lower order terms. Linearization assumes that the second and higher order terms of Δx can be neglected. Under this assumption

$$\begin{aligned}\bar{y} &= f(\bar{x}) \\ P_{yy} &= \nabla f P_{xx}(\nabla f)^T\end{aligned} \tag{3.30}$$

it is clear that these approximations are accurate only if the second and higher order terms in the mean and fourth and higher order terms in the covariance are negligible. However, in many practical situations linearization introduces significant biases or errors. In practice the inconsistency can be resolved by introducing additional stabilising noise which increases the size of the transformed covariance. This is one possible of why EKFs are so difficult to tune, in other words sufficient noise must be introduced to offset the defects of linearization. However, introducing stabilising noise is an undesirable solution since the estimate remains biased and there is no general guarantee that the transformed estimate remains consistent or efficient. In the figure below are shown the mean and standard deviation ellipses for the actual and linearized form of the transformation, for a highly nonlinear process as shown in [15]. The true mean is at *x* and the uncertainty ellipse is solid. Linearization calculates the mean at *o* and the uncertainty ellipse is dashed.

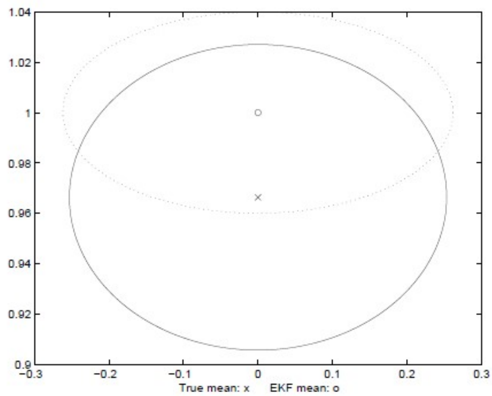

Fig. 3.2 True and linearized mean and standard deviation ellipse [15]

After describing the problem statement for applying a Kalman filter to nonlinear systems, in which the main EKFs flaw is highlight, it is time to introduce the UKFs' basic idea. The *unscented transformation* is used to calculate the statistics of a random variable which undergoes a nonlinear transformation. It is based on two fundamental principles. First, it is easy to perform a nonlinear transformation on a single point (rather than an entire pdf). Second, it is not too hard to find a set of individual points in state space whose sample pdf approximates the true pdf of a state vector. Those points are called *sigma points*. This means that the nonlinear function is applied to each *sigma points* in turn to yield a cloud of transformed points. This approach has something in common with the Monte Carlo method, that will be the basic idea of the Particle Filter, but there is an extremely important and fundamental difference. In this case, the samples are not drawn at random but rather according to a specific, deterministic algorithm. Since the problems of statistical convergence are not an issue, high order information about the distribution can be captured using only a very small number of points. Keeping the notation using above, if x is an $nx1$ vector that is transformed by the nonlinear function $y = f(x)$, the $2n$ *sigma points* are

$$\begin{aligned} x^{(i)} &= \bar{x} + \tilde{x}^{(i)} \qquad i = 1, \ldots, 2n \\ \tilde{x}^{(i)} &= (\sqrt{nP_{xx}})_i^T \qquad i = 1, \ldots, n \\ \tilde{x}^{(n+i)} &= -(\sqrt{nP_{xx}})_i^T \qquad i = 1, \ldots, n \end{aligned} \tag{3.31}$$

where $\sqrt{nP_{xx}}$ is the matrix square root of nP_{xx} such that $(\sqrt{nP_{xx}})^T\sqrt{nP_{xx}} = nP_{xx}$, and $(\sqrt{nP_{xx}})_i$ is the ith row of $\sqrt{nP_{xx}}$. The Cholesky factorization can be used to find a matrix square root, but other methods may be found in literature. Applying the nonlinear function to each individual *sigma points*, the transformed *sigma points* are computed as follows:

$$y^{(i)} = f(x^{(i)}) \qquad i = 1, \ldots, 2n \tag{3.32}$$

the approximated mean of y is given by

$$\bar{y} = \frac{1}{2n}\sum_{i=1}^{2n} y^{(i)} \tag{3.33}$$

therefore it is the mean value of the the transformed *sigma points*. It may be shown that the computed mean matches the true mean of y correctly up to the third order, whereas linearization only matches the true mean of y up to the first order as seen before. The same may be shown concerning the estimate covariance.

$$P_{yy} = \frac{1}{2n}\sum_{i=1}^{2n} [f(x^{(i)}) - \bar{y}][f(x^{(i)}) - \bar{y}]^T \tag{3.34}$$

The equations in (3.31), (3.33) and (3.34) represent the *unscented transformation* for a generic nonlinear function $y = f(x)$.

The UKFs rely on the *unscented transformation*, so their algorithm is slightly different than the EKFs'. In general, the UKFs propagate the mean and covariance of the *sigma points* using system nonlinear equations and the *a-priori state estimate* is the weighted mean of them. As well, predicted measurements for each propagated *sigma point* can be computed the using the measurement equations and the predicted measurements vector is the weighted mean of them. Unlike the EKFs, in UKFs there is the *cross-covariance matrix*. The following algorithm is the simpliest UKF because it uses $2n$ *sigma points* and also they have the same weight. For this reason it is here called Simply Unscented Kalman Filter (S-UKF). Considering as for the previous algorithm a generic nonlinear system as in (3.18).

The *unscented transformation* as presented in (3.31), (3.33) and (3.34) is not the only one that exists. In the next sections several other possible transformations are presented.

Algorithm 4 Simply Unscented Kalman Filter algorithm

$\hat{x}_0^+ = E[x_0]$ ▷ *Initial state*

$P_0^+ = E[(x_0 - \hat{x}_0^+)(x_0 - \hat{x}_0^+)^T]$ ▷ *Initial state Covariance*

procedure S-UKF(T, $\{u\}_{k=1}^T$)

  for $k = 1 \to T$ **do**

    $\hat{x}_{k-1}^{(i)} = \hat{x}_{k-1}^+ + \left(\sqrt{nP_{k-1}^+}\right)_i^T \qquad i = 1, \ldots, n$ ▷ *first n sigma points*

    $\hat{x}_{k-1}^{(n+i)} = \hat{x}_{k-1}^+ - \left(\sqrt{nP_{k-1}^+}\right)_i^T \qquad i = 1, \ldots, n$ ▷ *second n sigma points*

    $\hat{x}_k^{(i)} = f(\hat{x}_{k-1}^{(i)}, u_{k-1}, 0)$ ▷ *time update of sigma points*

    $\hat{x}_k^- = \frac{1}{2n}\sum_{i=1}^{2n} \hat{x}_k^{(i)}$ ▷ *a-priori state estimate*

    $P_k^- = \frac{1}{2n}\sum_{i=1}^{2n} (\hat{x}_k^{(i)} - \hat{x}_k^{(-)})(\hat{x}_k^{(i)} - \hat{x}_k^{(-)})^T + Q$ ▷ *a-priori state estimate covariance*

    $z_k^{(i)} = h(\hat{x}_k^i, u_k, 0)$ ▷ *predicted measurements for each propagated sigma point*

    $z_k = \frac{1}{2n}\sum_{i=1}^{2n} z_k^{(i)}$ ▷ *predicted measurements*

    $P_k^y = \frac{1}{2n}\sum_{i=1}^{2n} (z_k^{(i)} - z_k)(z_k^{(i)} - z_k)^T + R$ ▷ *predicted measurements covariance*

    $P_k^{xy} = \frac{1}{2n}\sum_{i=1}^{2n} (\hat{x}_k^{(i)} - \hat{x}_k^{(-)})(z_k^{(i)} - z_k)^T$ ▷ *cross covariance*

    $K_k = P_k^{xy}(P_k^y)^{-1}$ ▷ *Kalman gain*

    $\hat{x}_k^+ = \hat{x}_k^- + K_k(y_k - z_k)$ ▷ *a-posteriori state estimate*

    $P_k^+ = P_k^- - K_k P_k^- K_k^T$ ▷ *a-posteriori state estimate covariance*

  end for

end procedure

General Unscented Kalman Filter

Based on [136] and [137], it can be shown the same order of mean and covariance estimation accuracy can be obtained by choosing $(2n+1)$ *sigma points* instead of $(2n)$ as before. This type of UKF il called General Unscented Kalman Filter (G-UKF). The new *sigma points* are:

$$\begin{aligned} x^{(0)} &= \bar{x} \\ x^{(i)} &= \bar{x} + \tilde{x}^{(i)} \qquad i = 1, \dots, 2n \\ \tilde{x}^{(i)} &= (\sqrt{(n+k)P_{xx}})_i^T \qquad i = 1, \dots, n \\ \tilde{x}^{(n+i)} &= -(\sqrt{(n+k)P_{xx}})_i^T \qquad i = 1, \dots, n \end{aligned} \tag{3.35}$$

unlike before, now the *sigma points* have a different weight factors:

$$\begin{aligned} W^{(0)} &= \frac{k}{n+k} \\ W^{(i)} &= \frac{1}{2(n+k)} \qquad i = 1, \dots, 2n \end{aligned} \tag{3.36}$$

this means that the $2n$ *sigma points* are symmetrically distributed around the mean value $\bar{x}$. The term k can be used to reduce the higher-order errors of the mean and covariance approximation. As reported in [136] and [137] if x is Gaussian then $k = 3 - n$ minimizes some of the errors in the fourth-order terms in the mean and covariance approximation. Therefore applying the nonlinear function (3.32) to each individual *sigma points* the unscented mean and coraviance are:

$$\begin{aligned} \bar{y} &= \sum_{i=0}^{2n} W^{(i)} y^{(i)} \\ P_{yy} &= \sum_{i=0}^{2n} W^{(i)} [f(x^{(i)}) - \bar{y}][f(x^{(i)}) - \bar{y}]^T \end{aligned} \tag{3.37}$$

Note that if $k = 0$, the *sigma points* are $2n$ and they have the same weight factor, as reported in (3.33) and (3.34).
The G-UKF's algorithm and the S-UKF's algorithm are quite the same, the main difference is the number of *sigma points* computed at each time step and their weight factors. For this reason the algorithm is not reported here.
Sometimes a different version of this type of UKF can be found in literature and applied in case study. It is based on [138]. In this version the spread of the sigma points around the mean state value is controlled by two parameters α and k. A third parameter, β, impacts the weights of the transformed points during state and measurement covariance calculations. α determines the spread of the sigma points around the mean state value. It is a scalar value between 0 and 1, and usually it is a small value. Smaller values correspond to sigma points closer to the mean state. k is a second scaling parameter that is typically set to 0. Smaller values correspond to sigma points closer to the mean state. The spread is proportional to the square-root of k. β incorporates prior knowledge of the distribution of the state. For Gaussian distributions, $\beta = 2$ is optimal. These three parameters can be used to tune the filter. Using

these adjustable parameters, the *sigma points* and weight factor are:

$$\begin{aligned}
x^{(0)} &= \bar{x} \\
x^{(i)} &= \bar{x} + \tilde{x}^{(i)} \qquad i = 1, \dots, 2n \\
\tilde{x}^{(i)} &= (\sqrt{\alpha^2(n+k)P_{xx}})_i^T \qquad i = 1, \dots, n \\
\tilde{x}^{(n+i)} &= -(\sqrt{\alpha^2(n+k)P_{xx}})_i^T \qquad i = 1, \dots, n \\
W_m^{(0)} &= \frac{\alpha^2(n+k)-n}{\alpha^2(n+k)} \\
W_m^{(i)} &= \frac{1}{2\alpha^2(n+k)} \qquad i = 1, \dots, 2n \\
W_c^{(0)} &= (2-\alpha^2+\beta) - \frac{n}{\alpha^2(n+k)} \\
W_c^{(i)} &= \frac{1}{2\alpha^2(n+k)} \qquad i = 1, \dots, 2n
\end{aligned} \tag{3.38}$$

in this case the weight factors of the mean and the weight factors of the covariance are different. This means:

$$\begin{aligned}
\bar{y} &= \sum_{i=0}^{2n} W_m^{(i)} y^{(i)} \\
P_{yy} &= \sum_{i=0}^{2n} W_c^{(i)} [f(x^{(i)}) - \bar{y}][f(x^{(i)}) - \bar{y}]^T
\end{aligned} \tag{3.39}$$

Simplex Unscented Kalman Filter

Considering again [137], a new set of *sigma points* and weight factors can be introduced. It can be shown that if x has n elements then the minimum number of sigma points that gives the order of estimation accuracy of the previous section is equal to $(n+1)$. These *sigma points* are called simplex sigma points. It is here reported the case in which $(n+2)$ *sigma points* are used, but the number can be reduced to $(n+1)$ by choosing one of the weights

to be zero. This type of filter aims to reduce the computational effort reducing the number of *sigma points* without losing in estimation accuracy.
The *sigma points* are computed as reported in the following algorithm.

Algorithm 5 Simplex Unscented Transformation

1: $W^{(0)} \in [0,1)$ ▷ *Initial choice*

2: $W^{(i)} = \begin{cases} 2^{-n}(1-W^{(0)}) & i = 1,2 \\ 2^{i-2}W^{(1)} & i = 3,\dots,n+1 \end{cases}$ ▷ *Weights initialization*

3: $\sigma_0^{(1)} = 0 \qquad \sigma_1^{(1)} = \frac{-1}{\sqrt{2W^{(1)}}} \qquad \sigma_2^{(1)} = \frac{1}{\sqrt{2W^{(1)}}}$ ▷ *Sigma vector initialization*

4: **for** $j = 2 \to n$ **do**

5: $\sigma_i^{(j)} = \begin{cases} \begin{bmatrix} \sigma_0^{(j-1)} \\ 0 \end{bmatrix} & i = 0 \\ \begin{bmatrix} \sigma_i^{(j-1)} \\ \frac{-1}{\sqrt{2W^{(j+1)}}} \end{bmatrix} & i = 1,\dots,j \\ \begin{bmatrix} 0_{(j-1)} \\ \frac{j}{\sqrt{2W^{(j+1)}}} \end{bmatrix} & i = j+1 \end{cases}$ ▷ *Sigma vector building*

6: **end for**

7: $x^{(i)} = \bar{x} + \sigma_i^{(n)}\sqrt{P_{xx}} \qquad i = 0,\dots,n+1$ ▷ *Sigma points*

Note that 0_{j-1} is the column vector containing j zeros and $\sigma_i^{(n)}$ is an n-element row vector because $(i = 0,\dots,n+1)$.
Choosing $W^{(0)} = 0$ in the algorithm, the number of *sigma points* will be $(n+1)$ instead of $(n+2)$, the algorithm is then modified in the obvious way.
The problem with the SIMP-UKF is that the ratio of $W^{(n)}$ to $W^{(1)}$ is equal to 2^{n-2}, where n is the dimension of the state vector x. It can be shown that the ratio of the largest element of $\sigma_i^{(n)}$ to the smallest element is 2^{n-2} as well. As the dimension of the state increases, this ratio increases and can quickly cause numerical problems. The only reason for using the SIMP-UKF is the computational savings as said, and computational savings is an issue only for problems of high dimension (in general). This makes the SIMP-UKF of limited utility and leads to the Spherical Unscented Transformation in the following section.

Spherical Unscented Kalman Filter

The Spherical Unscented Transformation aims to rearrange the *sigma points* of the simplex algorithm in order to obtain better numerical stability, as reported in [139] and [137]. The filter based on this transformation is called Spherical Unscented Kalman Filter (SPHE-UKF). The *spherical sigma points* are computed as reported in the following algorithm.

Algorithm 6 Spherical Unscented Transformation

1: $W^{(0)} \in [0,1)$ ▷ *Initial choice*
2: $W^{(i)} = \frac{1-W^{(0)}}{n+1} \qquad i = 1,\ldots,n+1$ ▷ *Weights initialization*
3: $\sigma_0^{(1)} = 0 \qquad \sigma_1^{(1)} = \frac{-1}{\sqrt{2W^{(1)}}} \qquad \sigma_2^{(1)} = \frac{1}{\sqrt{2W^{(1)}}}$ ▷ *Sigma vector initialization*
4: **for** $j = 2 \rightarrow n$ **do**
5: $$\sigma_i^{(j)} = \begin{cases} \begin{bmatrix} \sigma_0^{(j-1)} \\ 0 \end{bmatrix} & i = 0 \\ \begin{bmatrix} \sigma_i^{(j-1)} \\ \frac{-1}{\sqrt{j(j+1)W^{(1)}}} \end{bmatrix} & i = 1,\ldots,j \\ \begin{bmatrix} 0_{(j-1)} \\ \frac{j}{\sqrt{j(j+1)W^{(1)}}} \end{bmatrix} & i = j+1 \end{cases}$$ ▷ *Sigma vector building*
6: **end for**
7: $x^{(i)} = \bar{x} + \sigma_i^{(n)} \sqrt{P_{xx}} \qquad i = 0,\ldots,n+1$ ▷ *Sigma points*

in this case, all the weight factors are identical, in contrast to the Simplex Unscented Transformation. The ratio of the largest element of $\sigma_i^{(n)}$ to the smallest element is

$$\frac{n}{\sqrt{n(n+1)W^{(1)}}} / \frac{1}{\sqrt{n(n+1)W^{(1)}}} = n \tag{3.40}$$

therefore the Spherical Unscented Transformation is less affect by numerical problem than the Simplex Unscented Transformation when the number of element of the state vector increases.

Pros and Cons of the Unscented Kalman Filters

The UKFs don't require the computation of Jacobian o Hessian, unlike the EKFs, this is a great advantage that make them easily usable for all the nonlinear system. The main obstacle is that the state covariance matrices must be positive semidefinite in order to have real matrices after applying the Cholesky decomposition. This goal can be achieved tuning the noise covariance matrices or considering the use of the Square-root Unscented Kalman Filter, in fact the Square-Root form have the added benefit of numerical stability and guaranteed positive semi-definiteness of the state covariances [138]. As seen, numerical stability problems could occur when the number of state vector increases, but adopting the SIMP-UKF or SPHE-UKF this problems can be overcome, saving computational cost as well. If the number of state vector increases, the computational cost could be a drawback because of the evaluation of the *sigma points* is required ad each time step. This aspect doesn't affect the EKFs, especially if the Jacobian and Hessian matrices are computed analytically rather than numerically.

3.3 Particle Filter

Particle Filter (PF) aims to estimate the state of a nonlinear process investigating the properties of sets of particles rather than the properties of individual particles. It is a completely nonlinear state estimator, unlike the UKFs and the EKFs presented before, that are based on the approximation of the nonlinear system.

The PF is a numerical implementation of the Bayesian estimator, so a brief introduction to the Bayesian approach to state estimation is required.

3.3.1 Bayesian State Estimation

Considering a generic nonlinear process, with uncorrelated and white noise, of which pdf is known, as in (3.9)[3]. The goal of a Bayesian estimator is to approximate the conditional pdf of x_k based on measurements $y_1, y_2, \dots, y_k$. This conditional pdf is denoted as $p(x_k|Y_k)$, where Y_k is the vector containing the measurements acquired till the k-th time step. The first measurements is obtained at $k = 1$, so the initial condition of the estimator is the pdf of x_0, $p(x_0) = p(x_0|Y_0)$, where Y_0 is defined as the set of no measurements. The conditional pdf may be multimodal, in which case the mean x_k of the estimate may be not useful. In [16] there is an example, reported here in figure, in which the mean of x is 0, but there is zero probability that x is equal to 0.

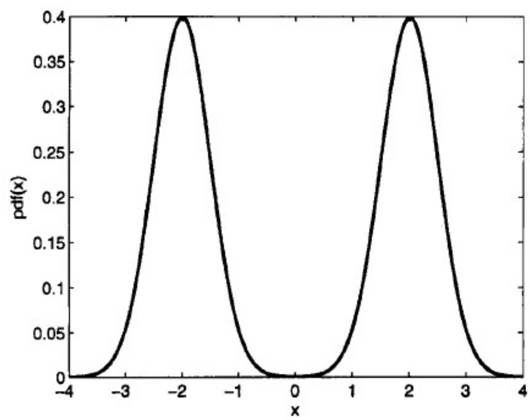

Fig. 3.3 An example of a multimodal probability density function. [16]

However, before finding the conditional pdf $p(x_k|Y_k)$, it is necessary to find the conditional pdf of x_k given all the measurements prior to the time k, $p(x_k|Y_{k-1})$, or in other words the conditional pdf of the a-priori state estimate.

[3] nonadditive noise is only considered in this case and for reasons of generality, as shown in [16]

It may be shown that

$$\begin{aligned} p(x_k|Y_{k-1}) &= \int p[(x_k, x_{k-1})|Y_{k-1}]dx_{k-1} \\ &= \int p[x_k|(x_{k-1}, Y_{k-1})]p[x_{k-1}|Y_{k-1}]dx_{k-1} \end{aligned} \tag{3.41}$$

The two pdf on the right side of the equation can now be analyzed. As seen in (3.9) x_K is entirely determined by x_{K-1}, u_{K-1} and w_K, so $p[x_k|(x_{k-1}, Y_{k-1})] = p[x_k|x_{k-1}]$, it is the pdf of the state at time k given a specific state at time $(k-1)$. Therefore the first term is known thanks to the knowledge of the system equation $f(\cdot)$ and of the pdf of the noise w_k. The second term is not available yet, but it is available at the initial time.
As shown in[16], the conditional pdf of the a-posteriori state estimate is given by:

$$p(x_k|Y_k) = \frac{p(y_k|x_k)}{p(y_k|Y_{k-1})}p(x_k|Y_{k-1}) \tag{3.42}$$

all the pdf's on the right side are available. Analyzing all the term: the pdf $p(y_k|x_k)$ is available from the knowledge of the measurement equation $h(\cdot)$ and of the pdf of the noise v_k, the pdf $p(x_k|Y_{k-1})$ is the a-priori conditional pdf, finally the pdf $p(y_k|Y_{k-1})$ is given by

$$p(y_k|Y_{k-1}) = \int p[(y_k, x_k)|Y_{k-1}]dx_k = \int p[y_k|(x_k, Y_{k-1})]p(x_k|Y_{k-1})dx_k \tag{3.43}$$

but z_k is completely determined by x_k,u_k and v_k, so $p[y_k|(x_k, Y_{k-1})] = p(y_k|x_k)$. As shown both terms of the above equation are available, thus all the terms on the right side of the a-posteriori conditional pdf are available. Analytical solutions to these equations are available only if $f(\cdot)$ and $h(\cdot)$ are linear, and x_0,W_k, and v_k are additive, independent, and Gaussian, then the solution is the Kalman filter discussed in section (3.2.1). This way of obtaining the Kalman filter is more complicated than the least squares approach usually used. It is important to highlight that when the Kalman filter is derived using the least squares approach, then no conclusions can be drawn about the optimality of the filter when the noise is not Gaussian. In fact, other optimal (nonKalman) filters have been derived for other noise distributions. Nevertheless, the Bayesian derivation proves that when the noise is Gaussian, the Kalman filter is the optimal filter. However, the least squares derivation shows that the Kalman filter is the optimal linear filter, regardless of the pdf of the noise.

After the presentation of the Bayesian approach to state estimation, that is a recursive approach, its numerical implementation is shown in the next section, this is the Particle filtering.

3.3.2 Particle Filtering

The Particle filters (PFs), is a sequential Monte Carlo (MC) based filter. It is a technique for implementing a recursive Bayesian filter by MC simulations. The key idea is to represent the required posterior density function by a set of random samples with associated weights and to compute estimates based on these samples and weights. As the number of samples becomes very large, this MC characterization becomes an equivalent representation to the usual functional description of the posterior pdf [140]. Therefore the basic idea is to randomly generate a given number N state vectors based on the initial pdf $p(x_0)$, that is known. These state vectoris are called *particles* and are denoted as $x^+_{0,i}$, with $i = 1,\dots,N$. At each time step, the *particles* are propagated to the next time step using the system equation $f(\cdot)$:

$$\hat{x}^-_{k,i} = f(\hat{x}^+_{k-1,i}, u_{k-1}) + w^{(i)}_{k-1} \qquad i = 1,\dots,N \tag{3.44}$$

In the above equation a nonlinear system is considered and an additive noise is supposed, this is in order to use the same system equation and the same type of noise in all the filter implemented. The additive noise term $w^{(i)}_{k-1}$ is the noise vector, randomly generated on the basis of the known pdf of w_{k-1}.

After that the measurements at time k is received, the conditional relative likelihood of each *particle* $\hat{x}^{-}_{k,i}$ can be computed using the conditional pdf $p(z_k|\hat{x}^{-}_{k,i})$. In fact, thanks to the knowledge of the measurement equation and of the pdf of the measurement noise, the relative likelihood q_i that the estimate measurement z_k is equal to a specific measurement y_k, given the premise that x_k is equal to the particle $\hat{x}^{-}_{k,i}$, can be computed as follow:

$$\begin{aligned} q_i &= P[(z_k = y_K)|(x_k = \hat{x}^{-}_{k,i})] = P[v_k = y_K - h(\hat{x}^{-}_{k,i})] \\ &\sim \frac{1}{(2\pi)^{m/2}|R|^{1/2}} exp\left(\frac{-[y_k - h(\hat{x}^{-}_{k,i})]^T R^{-1}}{2}[y_k - h(\hat{x}^{-}_{k,i})]\right) \end{aligned} \tag{3.45}$$

In the expression above on the right side there is the definition of the multivariate Gaussian probability distribution of an m-element random variable, and R is the noise covariance matrix. The $\sim$ symbol means that the probability in not really given by the expression on the right side. So if this equation is used for all the particles $\hat{x}^{-}_{k,i}$, then the relative likelihoods that the state is equal to each particle will be correct. The relative likelihoods obtained is normalized, in order to ensure that the sum of all the likelihoods is equal to one.

$$q_i = \frac{q_i}{\sum_{j=1}^{N} q_j} \tag{3.46}$$

At this point of the filter a *resampling strategy* is applied, in other words a brand new set of particles is computed, these are randomly generated on the basis of the relative likelihoods q_i. A lot of *resampling strategy* can be found in literature, in the next section only three strategies will be presented and then implemented. The basic idea of resampling is to eliminate particles that have small relative likelihood and to concentrate on particles with large one. The last step of a generic *resampling strategy* is

$$\hat{x}^{+}_{k,i} = \hat{x}^{-}_{k,j} \qquad \textit{with probability} \quad q_j \qquad (i, j = 1, \ldots, N) \tag{3.47}$$

so it is a resample (with replacement) that takes into account the relative likelihood of each particle. The output of the *resampling strategy* is the set of particles $\hat{x}^{+}_{k,i}$, that are distributed according to the pdf $p(x_k|y_k)$. Finally, for each step time the a-posteriori state estimate is computed as a weighted sum of the resampled particles:

$$\hat{x}^{+}_{k} = \sum_{j=1}^{N} q_j \hat{x}^{-}_{k,j} \tag{3.48}$$

The following algorithm refers to a generic particle filter as described in [140], the resampling strategies are here only mentioned and listed below in detail. Ns is the number of particle.

Algorithm 7 General Particle Filter algorithm

$\hat{x}^{+}_{0} = E[x_0]$ ▷ *Initial state*
$\hat{x}^{+}_{0,i} = \mathcal{N}(x_0, P_0) \qquad i = 1, \dots, Ns$ ▷ *random particles from initial state*
$q_{0,i} = 1/Ns$ ▷ *initial particles weights*
procedure G-PF(T, $\{u\}_{k=1}^{T}$)
  for $k = 1 \to T$ **do**
    $\hat{x}^{-}_{k,i} = f(\hat{x}^{+}_{k-1,i}, u_{k-1}) + w_{k-1,i}$ ▷ *time update of particles*
    $z_{k,i} = h(\hat{x}^{-}_{k,i}, u_k)$ ▷ *measurements estimate based on particles*
    $p_i(y_k|\hat{x}^{-}_{k,i}) = \mathcal{N}((y_k - z_{k,i}), R)$ ▷ *observation likelihood pdf*
    $p_i(\hat{x}^{-}_{k,i}|\hat{x}^{+}_{k-1,i}) = \mathcal{N}((\hat{x}^{-}_{k,i} - f(\hat{x}^{+}_{k-1,i}, u_{k-1})), Q)$ ▷ *a-priori estimate likelihood pdf*
    $q_{k,i} = q_{k-1,i} p_i(y_k|\hat{x}^{-}_{k,i}) p_i(\hat{x}^{-}_{k,i}|\hat{x}^{+}_{k-1,i})$ ▷ *a-posteriori particles weight*
    $q_{k,i} = \frac{q_{k,i}}{\sum_{i=1}^{Ns} q_{k,i}}$ ▷ *normalization*
    $[\hat{x}^{+}_{k,j}, q_{k,j}] = RESAMPLE(\hat{x}^{-}_{k,i}, q_{k,i})$ ▷ *resampling strategy*
    $\hat{x}^{+}_{k} = \sum_{j=1}^{Ns} q_{k,j} \hat{x}^{+}_{k,j}$ ▷ *a-posteriori state estimate*
  end for
end procedure

3.3.3 Resampling Strategies

The resampling strategies implemented are listed in this section, and also their algorithm are shown in detail. In literature there are a lot of strategies an exhaustive collection is done in [141].

Multinomial Resampling

The core idea of multinomial resampling is to generate independently Ns random numbers, u_k^i with $i = 1, \ldots, n$, from the uniform distribution on $(0, 1]$ and use them to select particles from $\hat{x}_{k,i}^-$. In the n-th selection, the particle $\hat{x}_{k,m}^-$ is chosen when the following condition is satisfied

$$Q_k^{(m-1)} < u_k^{(n)} \leq Q_k^{(m)} \qquad where \qquad Q_k^{(m)} = \sum_{i=1}^{m} q_{k,i} \tag{3.49}$$

Thus, the probability of selecting $\hat{x}_{k,m}^-$ is the same as that of $u_k^{(n)}$ being in the interval bounded by the cumulative sum of the normalized weights as shown. This sampling scheme satisfies the unbiasedness condition. Multinomial resampling is also referred to as simple random resampling. Since the sampling of each particle is random, the upper and lower limits of the number of times a given particle is resampled are zero (not sampled) and N_t (sampled N_t times), respectively. This yields the maximum variance of the resampled particles.

Algorithm 8 Multinomial Resampling

procedure MULTI-RES($\hat{x}_{k,i}^-$, $q_{k,i}$, Ns)
 for $m = 1 \rightarrow Ns$ **do**
  $Q_k^{(m)} = \sum_{i=1}^{m} q_{k,i}$ ▷ *cumulative sum vector*
 end for
 $n = 0$ ▷ *counter*
 while $n < Ns$ **do**
  $u \in (0, 1]$ ▷ *random number*
  $m = 1$
  while $Q_k^{(m)} < u$ **do**
   $m = m + 1$ ▷ *resampled index*
  end while
  $n = n + 1$
  $idx(n) = m$
 end while
 $\hat{x}_{k,i}^+ = \hat{x}_{k,idx}^-$ ▷ *resampling*
 $q_{k,j} = 1/Ns$ ▷ *equal weights for resampled particles*
end procedure

As reported in [141], multinomial resampling is not efficient, and this has motivated a search for faster methods. The variance of the number of times a particle is resampled can be reduced by stratification sampling.

Stratified Resampling

Stratified resampling divides the whole population of particles into subpopulations called strata. It prepartitions the $(0,1]$ interval into N disjoint subintervals $(0,1/Ns] \cup \cdots \cup (1-1/Ns,1]$. The random numbers $u_k^{(n)}$ are drawn independently in each of these subintervals and then the bounding method based on the cumulative sum of normalized weights as shown in (3.49).

Algorithm 9 STRATIFIED RESAMPLING

procedure STRA-RES($\hat{x}_{k,i}^{-}$, $q_{k,i}$, Ns)
  for $m = 1 \rightarrow Ns$ **do**
    $Q_k^{(m)} = \sum_{i=1}^{m} q_{k,i}$ ▷ *cumulative sum vector*
  end for
  $T = linspace(0, 1-1/Ns, Ns) + rand(1, Ns)/Ns$ ▷ *subintervals*
  $n = 1 \quad m = 1$ ▷ *counter*
  while $n \leq Ns \quad and \quad j \leq Ns$ **do**
    while $Q_k^{(m)} < T(n)$ **do**
      $m = m + 1$ ▷ *resampled index*
    end while
    $idx(n) = m$
    $n = n + 1$
  end while
  $\hat{x}_{k,j}^{+} = \hat{x}_{k,idx}^{-}$ ▷ *resampling*
  $q_{k,j} = 1/Ns$ ▷ *equal weights for resampled particles*
end procedure

Systematic Resampling

Systematic resampling also exploits the idea of strata but in a different way. Now,$u_k^{(1)}$ is drawn from the uniform distribution on $(0,1/Ns]$, and the rest of the numbers are obtained deterministically, $u_k^{(n)} = u_k^{(1)} + \frac{n-1}{Ns}$ with $n = 2,3,\ldots,Ns$. As seen the algorithms of SYST-res and STRA-res are quite

Algorithm 10 SYSTEMATIC RESAMPLING

procedure SYST-RES($\hat{x}^-_{k,i}$, $q_{k,i}$, Ns)
  for $m = 1 \to Ns$ **do**
    $Q_k^{(m)} = \sum_{i=1}^{m} q_{k,i}$ ▷ *cumulative sum vector*
  end for
  $T = linspace(0, 1-1/Ns, Ns) + rand/Ns$ ▷ *subintervals*
  $n = 1 \quad m = 1$ ▷ *counter*
  while $n \leq Ns$ *and* $m \leq Ns$ **do**
    while $Q_k^{(m)} < T(n)$ **do**
      $m = m + 1$ ▷ *resampled index*
    end while
    $idx(n) = m$
    $n = n + 1$
  end while
  $\hat{x}^+_{k,j} = \hat{x}^-_{k,idx}$ ▷ *resampling*
  $q_{k,j} = 1/Ns$ ▷ *equal weights for resampled particles*
end procedure

the same.the systematic method is computationally more efficient than the stratified method because of the smaller number of random numbers that are generated.

3.3.4 Pros and Cons of the Particle Filters

The price that must be paid for the high performance of the particle filter is an increased level of computational effort. There may be problems for which the improved performance of the particle filter is worth the increased computational effort. There may be other applications for which the improved performance is not worth the extra computational effort. These trade-offs are problem dependent and must be investigated on an individual basis. The main implementation issue is the sample impoverishment, the region of state space in which the pdf $p(y_k|x_k)$ has significant values does not overlap with the pdf $p(x_k|Y_{k-1})$. This means that if all of the a-priori particles are distributed according to $p(x_k|Y_{k-1})$, and then the computed pdf $p(y_k|x_k)$ is used to resample the particles, only a few particles will be resampled to become a-posteriori particles. This is because only a few of the a-priori particles will be in a region of state space where the computed pdf $p(y_k|x_k)$ has a significant value. Eventually, all of the particles could collapse to the same value. This can be overcome by a brute-force method of simply increasing the number of particles Ns, but this can quickly lead to unreasonable computational demands, and often simply delays the inevitable sample impoverishment. Several ways of dealing with this problem can be used, as regularized particle filtering, Markov chain Monte Carlo resampling, and auxiliary particle filtering. In addition, one approach that has been proposed for improving particle filtering is to combine it with another filter such as the EKFs or the UKFs. In this approach, each particle is updated at the measurement time using the EKFs or the UKFs, and then resampling is performed using the measurement. This is like running a bank of N Kalman filters (one for each particle) and then adding a resampling step after each measurement.

3.4 Calibration of filters

All the filters presented are characterized by the noise terms presence, they capture what the deterministic model fails to. As reported in [142], the noise is usually the result of a number of different effects:

1. Mis-modeled system and measurement dynamics.

2. The existence of hidden state in the environment not modeled by the filter.

3. The discretization of time, which introduces additional error.

4. The algorithmic approximations of the filter itself, such as the Taylor approximation commonly used for linearization.

In order to reduce the perturbations in state estimation, several optimization algorithms are proposed in the paper, in this thesis work only two of them are considered and implemented. Despite the algorithms are based on Kalman Filter training, and applied in the paper using EKF, they work quite well for the UKFs and PFs as well. The basic idea is to "train" the filter using an optimizator, in order to find the process noise covariance matrix and the measurements noise covariance matrix that minimize the error between the "real state" and the state estimate. The techniques presented below use additional measurements provided by high-end sensors, called $y_1, y_2, \ldots, y_m$ and the measure of the full or partial state $x_1, x_2, \ldots, x_n$ acquired by high-end sensors as well. [4]. A generic function $g(\cdot)$ is a projection which extracts the subset of the variables in x_t that correspond to the y_t, where t is the generic time step.

$$y_t = g(x_t) + \gamma_t \tag{3.50}$$

In other words, the equation above uses the high-end sensors measures of the state vector in order to obtain the value of the additional measures $y_1, y_2, \ldots, y_m$, taking into account the process. The more the process model is an approximation of the real one, the more the difference between $y_1, y_2, \ldots, y_n$ and $g(x_k) + \gamma_k$ is. The term γ_k is the noise term with covariance P. The difference between high-end measurements and the measurements commonly used to feed the filter is very important, this because the first ones are used only during the training phase, the second ones are used during the filter execution. To better highlight this difference, the second ones are called low-end measurements because they are acquired using cheaper sensors. The two algorithm chosen are different, the main difference is that the first one presented doesn't run the filter, while the second needs to run the filter.

[4] note that these measurements are different than the ones used in the filter, despite the same nomenclature. In this case they are acquired by high-end sensors, that are not used during the filter execution.

Generative Approach: Maximizing The Joint Likelihood

This approach requires access to the full state vector, although it is not always possible. Assuming that this is possible, the function $h(\cdot)$ is the identity function and the noise γ is so small that it can safely be neglected. Let $x_{0:T}$ denote the entire state sequence $(x_0, x_1, \ldots, x_T)$, also let $u_{1:T}$, $y_{0:T}$ and $z_{0:T}$ denote the known input, the first two are high-end measurements and the last is low-end measurement. Assuming the initial probability distribution $p(x_0)$, the joint probability distribution till the time step T is:

$$p(x_{0:T}, y_{0:T}, z_{0:T}|u_{1:T}) = p(x_0)\prod_{t=1}^{T} p(x_t|x_{t-1}, u_t)\prod_{t=0}^{T} p(y_t|x_{t-1})p(z_t|x_{t-1}) \tag{3.51}$$

where

$$\begin{aligned} p(x_t|x_{t-1}, u_t) &= \mathcal{N}(x_t; f(x_{t-1}, u_t), Q) \\ p(y_t|x_{t-1}) &= \mathcal{N}(y_t; g(x_t), P) \\ p(z_t|x_{t-1}) &= \mathcal{N}(z_t; h(x_t), R) \end{aligned} \tag{3.52}$$

The method proceeds by maximizing the likelihood of all the data. Since the full state vector is observed ($y_k = x_k$), the covariance matrices R_{joint} and Q_{joint} are estimated as follows:

$$[R_{joint}, Q_{joint}] = arg\ max_{Q,R}\ [log\big(p(x_{0:T}, z_{0:T}|u_{1:T})\big)] \tag{3.53}$$

it can be shown that subtistuting the (3.51) and the (3.52) in the above equation, it decomposes into the two equations listed below

$$\begin{aligned} Q_{joint} &= arg\ max_Q\ [-T log(2\pi Q) - \sum_{t=1}^{T}(x_t - f(x_{t-1}, u_t))^T Q^{-1}(x_t - f(x_{t-1}, u_t))] \\ R_{joint} &= arg\ max_R\ [-(T+1) log(2\pi R) - \sum_{t=0}^{T}(z_t - g(x_t))^T R^{-1}(z_t - g(x_t))] \end{aligned} \tag{3.54}$$

However the optimal R_{joint} and Q_{joint} can actually be computed in closed form and are given by:

$$\begin{aligned} Q_{joint} &= \frac{1}{T}\sum_{t=1}^{T}(x_t - f(x_{t-1},u_t))(x_t - f(x_{t-1},u_t))^T \\ R_{joint} &= \frac{1}{1+T}\sum_{t=0}^{T}(z_t - g(x_t))(z_t - g(x_t))^T \end{aligned} \tag{3.55}$$

As said, this approach never actually run the filter, it trains the elements of the filter. It therefore implicitly assumes that training the elements individually is as good as training the filter as a whole.

Minimizing The Residual Prediction Error

The above technique requires the full state knowledge and doesn't execute the filter. It is here presented a technique that overcome these potential limits. This technique minimizes the prediction error for the values of y_t given by

$$E[y_t|u_{1:t}, z_{0:t}] = g(\hat{x}_t) \tag{3.56}$$

$\hat{x}_t$ is the state estimate provided by the filter algorithm adopted. This is the a-posteriori state estimate, so it takes into account the observations $z_{0:t}$ and the additional input (as known as control input) $u_{1:t}$, considered acquired by high-end sensors. Therefore $\hat{x}_t$ depends implicitly on R and Q. This technique seeks the parameters R and Q that minimize the quadratic deviation of y_t, and so the expectation above, weighted by the inverse covariance P.

$$\langle Q_{res}, R_{res}\rangle = arg\ min_{Q,R} \sum_{t=0}^{T}(y_t - g(\hat{x}_t))^T P^{-1}(y_t - g(\hat{x}_t)) \tag{3.57}$$

but if P is any multiple of the identity matrix, this simplifies to

$$\langle Q_{res}, R_{res} \rangle = arg\ min_{Q,R} \sum_{t=0}^{T} \|y_t - g(\hat{x}_t)\|_2^2 \tag{3.58}$$

in other words this technique choose the parameters R and Q that cause the filter to output the state estimates that minimize the squared differences to the measured values y_t. Unlike the previous technique, this one evaluates the actual performance of the filter. In order to implement this technique a genetic algorithm or a surrogate optimization algorithm may be used, fixing the lower and the upper boundaries to guide the optimizator.

3.5 Case study: Vehicle model-based estimation of go-kart side-slip angle

The typical active safety systems that control the dynamics of passenger cars rely on real-time monitoring of vehicle side-slip angle (VSA), but the VSA is not measured directly because it requires the use of high-end instruments, which usually cannot be equipped in the passenger cars due to the significant related costs and bulky instrumentation [143]. However, this is not the only application field, indeed an accurate knowledge of the VSA may improve the ADAS system or may be used to improve the trajectory in autonomous vehicle [144]. In the motorsport field, the application of the VSA is used to enhance the overall vehicle performance during the race. In all these application fields the VSA estimation is increasingly diffused, and it is evaluated employing different measurements available onboard, such as wheel velocities, linear and angular accelerations [145] [146].

The technical literature is plenty of articles about VSA estimation. There are different approaches to estimate the VSA starting from the observer-based methods [147], [148], [149] up to neural network data-based techniques

[150], [151]. The observer-based methods are characterized by the type of state estimator adopted, e.g. Extended Kalman filters [152], in which the Jacobian matrix computation is required and the nonlinear problem is linearized through a Taylor expansion. In [27] and [153], Unscented Kalman filters are adopted. The application of such filters is widely used due to an easier implementation because they do not require the computation (analytical or numerical) of the Jacobian matrix. In this work, another type of state estimator is considered in addition to the ones mentioned above, consisting in the Particle filter. The main applications of this latter involve the tracking problems, as reported in [140].

All the filters are based on the mathematical modeling of the process to estimate, a mathematical representation of the vehicle is required in this application. Different assumption have to be stated in order to model the vehicle dynamics. Two kinds of vehicle models can be found in the literature, which are denoted respectively as kinematic and dynamic [37]. The kinematic model is concerned with the vehicle motion with no reference to forces; thus, it does not need complex parameters such as those regarding tyres, which often are the cause of the non-linearity of the vehicle model. However, the main issue of VSA estimation using a kinematic vehicle model lays in the fact that it does not work when the vehicle yaw rate is relatively small or zero, this leads to the system unobservability, as reported in [154]. The dynamic model, on the other hand, provides a more detailed description of the vehicle dynamics, as it is based on the equilibrium equations. It can have different levels of detail/complexity and hypotheses used, each of them affects the estimation accuracy. Several authors introduce simplifying hypotheses, such as a single-track vehicle model as in [155] and [156]. Additional assumptions may be adopted, as the availability of the vehicle longitudinal speed or the hypothesis of small steering angles. Quite often the equilibrium equations are coupled with a tyre model but it is not strictly necessary as proposed in [157], there are several approaches, the most used are: linear models, Pacejka

Fig. 3.4 GoKart employed in order to estimate the vehicle sideslip angle

models, rational tyre model [158] and Dugoff model [10]. The use of a dynamic model can lead to a good VSA estimation, however, the accuracy of the results strongly depends on the tyre model parameters. Unmodeled effects, such as road conditions and tyre wear, can dramatically worsen the reliability of the estimation, meanwhile other secondary effects as the type of suspension adopted [159] and the thermodynamics of the tyre inner chamber [160] can be neglected easier in certain hypothesis. Several authors attempt to deal with this issue employing algorithms which provide an online update of tyre parameters as in [161] and [162]. In this chapter, a single-track vehicle model and a simplified Pacejka tyre model are adopted in order to compare the performance of different types of state estimators using the same plant model. The benchmark is not only based on the estimate accuracy but also on the run-time capability of each proposed algorithm.

The data-set employed to this aim has been provided by an electric go-kart of the Eidgenössische Technische Hochschule (ETH) Zürich (Fig. 3.4). It is equipped with sensors, described in the following section, in order to acquire the necessary input signals to feed the process model of the filters. In addition, an S-motion is used to acquire the true VSA and to validate the estimate one.

3.5.1 Kalman filtering

All the filters implemented attempt to estimate the vehicle side slip angle (VSA) but not directly evaluating it, in fact it is given by:

$$\beta = \arctan\left(\frac{v}{u}\right) \tag{3.59}$$

Being the process equations are separated into two sets of equations: the first one is the set of the *system equations* which propagates the state from the time step $k-1$ to k and provides the a-priori state estimate, the second one is the set of *measurement equations* which use the a-priori state estimate in order to compute the estimate values of some measurements. First of all the state to be estimated and the measurements must be defined. The state vector elements are:

$$x_k = [u_k, v_k, r_k]^T \tag{3.60}$$

longitudinal and lateral vehicle velocity $[m/s]$ and yaw rate $[rad/s]$ respectively. [5] The measurement vector elements are:

$$z_k = [\omega_{1,1_k}, \omega_{1,2_k}, r_k, a_{y_k}, a_{x_k}]^T \tag{3.61}$$

respectively rotational velocity of the front-left and front-right wheels $[rad/s]$, yaw rate $[rad/s]$ and longitudinal and lateral vehicle linear acceleration $[m/s^2]$.

The implemented vehicle model refers to an electric go-kart. It is equipped with two electric motors at the rear axle, one per wheel, and also the braking system operates only on the rear axle. Therefore the front axle has not braking or tractive powered. The two electric motors work in order to simulate an

[5] Note that in (3.1) and (3.60) the same letter refers to different things, for example in (3.60) u_k is the vehicle longitudinal velocity while in (3.1) it represents the measurable variables in system equations and also it is a vector. This is because it preserves the nomenclature adopted in the respective literature despite the ambiguity that this might create in this application.

open differential, so no torque vectoring effects are present. In addition, the same can be said about the braking system. The go-kart has no suspension system and the chassis deflection and tyre vertical deformations are assumed to be null. There are no aerodynamic devices and the drag force effect on the vehicle dynamics is neglected. These vehicle characteristics fulfill in a certain way the assumptions stated about the vehicle model. However the hypothesis of small steering angle can not be considered, in fact the steering angle reached by the vehicle during the tests are not so small to be neglected. This is because the tests are made with the aim to reach high value of VSA as will be shown. It is important to highlight that the front axle wheels have no braking or tractive power, so the longitudinal slip are very small and can be easily neglected in the vehicle model. This leads to the fact that the rotational velocity of the front wheels can be evaluated using the kinematic equations as shown in the section about the measurement equations.

3.5.2 System equations

As shown in the equation (3.1), the set of system equations uses the state estimate and additional input at the previous time step to compute the time propagation of the state. The process noise terms are considered additive and Gaussian, zero-mean and uncorrelated with Q as covariance matrix. It is here reported the general form of the system equation:

$$\hat{x}_k^- = f(\hat{x}_{k-1}^+, u_{k-1}) + w_{k-1} \tag{3.62}$$

The vehicle model implemented is nonlinear, or in other words the functions $f(\cdot)$ are nonlinear functions. The functions $f(\cdot)$ are linearized using a first-order Taylor expansion, only in the SO-EKF a second-order Taylor expansion is considered.

The discrete-time form of the equations is reached using the forward Euler method. Considering the state at time $k-1$, the time propagation of the state is given by:

$$x_k = x_{k-1} + \Delta t \; \dot{x}_{k-1} \tag{3.63}$$

The mathematical form of the vector $\dot{x}_{k-1}$ is obtained using the equations (1.32) and (1.33). In fact the vector is $\dot{x}_{k-1} = [\dot{u}_{k-1}, \dot{v}_{k-1}, \dot{r}_{k-1}]^T$ which can be obtained by the equations below:

$$\begin{aligned} m\;(\dot{u} - v\;r) &= F_{x_1}\;\cos(\delta_1) - F_{y_1}\;\sin(\delta_1) + F_{x_2} \\ m\;(\dot{v} + u\;r) &= F_{y_1}\;\cos(\delta_1) + F_{x_1}\;\sin(\delta_1) + F_{y_2} \\ J_z\;\dot{r} &= F_{y_1}\;a_1\cos(\delta_1) + F_{x_1}\;a_1\sin(\delta_1) - F_{y_2}\;a_2 \end{aligned} \tag{3.64}$$

Handling them in order to obtain the formulation for the elements of $\dot{x}_{k-1}$:

$$\begin{aligned} \dot{u}_{k-1} &= v_{k-1}\;r_{k-1} + \frac{1}{m}\left(F_{x_{1,k-1}}\;\cos(\delta_{1,k-1}) - F_{y_{1,k-1}}\;\sin(\delta_{1,k-1}) + F_{x_{2,k-1}}\right) \\ \dot{v}_{k-1} &= -u_{k-1}\;r_{k-1} + \frac{1}{m}\left(F_{y_{1,k-1}}\;\cos(\delta_{1,k-1}) + F_{x_{1,k-1}}\;\sin(\delta_{1,k-1}) + F_{y_{2,k-1}}\right) \\ \dot{r}_{k-1} &= \frac{1}{J_z}\left(F_{y_{1,k-1}}\;a_1\cos(\delta_{1,k-1}) + F_{x_{1,k-1}}\;a_1\sin(\delta_{1,k-1}) - F_{y_{2,k-1}}\;a_2\right) \end{aligned} \tag{3.65}$$

Finally the $f(\cdot)$ equations are given by:

$$u_k = u_{k-1} + \Delta t \Bigg(v_{k-1} r_{k-1} + \frac{1}{m} \big(F_{x_{1,k-1}} \cos(\delta_{1,k-1}) - F_{y_{1,k-1}} \big) \sin(\delta_{1,k-1}) + F_{x_{2,k-1}} \big) \Bigg) \tag{3.66}$$

$$v_k = v_{k-1} + \Delta t \Bigg(-u_{k-1} r_{k-1} + \frac{1}{m} \big(F_{y_{1,k-1}} \cos(\delta_{1,k-1}) + F_{x_{1,k-1}} \sin(\delta_{1,k-1}) + F_{y_{2,k-1}} \big) \Bigg) \tag{3.67}$$

$$r_k = r_{k-1} + \Delta t \Bigg(\frac{1}{J_z} \big(F_{y_{1,k-1}} a_1 \cos(\delta_{1,k-1}) + F_{x_{1,k-1}} a_1 \sin(\delta_{1,k-1}) - F_{y_{2,k-1}} a_2 \big) \Bigg) \tag{3.68}$$

Unlike in (3.63), in the other equations presented above the a-priori and a-posteriori nomenclature is not reported for sake of simplicity, but note that all the terms on the left side are the a-priori state estimate at time k and all the term on the right side are the a-posteriori state estimate at time step $(k-1)$.

The tyre forces are given by:

$$\begin{aligned} F_{x_i} &= F_{0,x_i}\ G_{x_i} \\ F_{0,x_i} &= D_{x_i}\ \sin\{C_{x_i}\ \arctan[B_{x_i} K_i - E_{x_i}(Bx_i k_i - \arctan(B_{x_i} k_i))]\} \\ G_{x_i} &= \cos\{C_{c,x_i}\ \arctan[B_{c,x_i}\ \alpha_i - E_{c,x_i}(B_{c,x_i}\ \alpha_i - \arctan(B_{c,x_i}\ \alpha_i))]\} \end{aligned} \tag{3.69}$$

$$\begin{aligned} F_{y_i} &= F_{0,y_i}\ G_{y_i} \\ F_{0,y_i} &= D_{y_i}\ \sin\left\{C_{y_i}\ \arctan[B_{y_i} \alpha_i - E_{y_i}(By_i \alpha_i - \arctan(B_{y_i} \alpha_i))]\right\} \\ G_{y_i} &= \cos\left\{C_{c,y_i}\ \arctan[B_{c,y_i}\ k_i - E_{c,y_i}(B_{c,y_i}\ k_i - \arctan(B_{c,y_i}\ \alpha_i))]\right\} \end{aligned}$$

where α_i and k_i are given by (1.29) and the subscript i refers to the axle ($i = 1$ if front axle and $i = 2$ if rear axle). As seen before the macro-parameter D is given by (1.18), it is a quadratic function of the tyre vertical load. In this case the vertical load is referred to the axle, and sum the forces referring to the same axle:

$$\begin{aligned} F_{z_1} &= F_{z_1}^0 - \frac{\Delta Z_x}{2} = \frac{m\,g\,a_2}{l} - \frac{m\,a_x\,h}{l} \\ F_{z_2} &= F_{z_2}^0 + \frac{\Delta Z_x}{2} = \frac{m\,g\,a_1}{l} + \frac{m\,a_x\,h}{l} \end{aligned} \tag{3.70}$$

Note that the term ΔZ_{y_i} is not present.

Only in the SO-EKF, the system equations include the second-order Taylor expansion of $f(\cdot)$. Here is reported the general formulation[6]:

$$\hat{x}_k^- = f(\hat{x}_{k-1}^+, u_{k-1}, 0) + \frac{1}{2}\sum_{i=1}^{n} \phi_i Tr\left[\left.\frac{\partial^2 f_i}{\partial x^2}\right|_{\hat{x}_{k-1}^+} P_{k-1}^+\right] + w_{k-1} \tag{3.71}$$

where $f(\hat{x}_{k-1}^+, u_{k-1}, 0)$ is given by the equations (3.68) and P_{k-1}^+ is the covariance matrix of the a-posteriori state estimate at the time step $(k-1)$. The second term at the right side is a three elements column vector.

3.5.3 Measurements equations

The measurements equations evaluate the measurements estimation z_k at time step k, knowing the a-priori state estimate $\hat{x}_k^-$ and the additional input values u_k at the same time step. In a mathematical form this means:

$$z_k = h(\hat{x}_k^-, u_k) + v_k \tag{3.72}$$

The estimated measurement vector is

$$z_k = [\omega_{1,1_k}, \omega_{1,2_k}, r_k, a_{y_k}, a_{x_k}]^T \tag{3.73}$$

[6]Note that the argument u_{k-1} in the $f(\cdot)$ notation refers to all the additional input required by the vehicle model, that are acquired by sensors. Do not confuse them with the longitudinal velocity u_k which is an element of the state vector, despite the same notation is used

while the acquired signal vector is

$$y_k = [\omega_{1,1_k}^{ENCODER}, \omega_{1,2_k}^{ENCODER}, r_k^{IMU}, a_{y_k}^{IMU}, a_{x_k}^{IMU}]^T \tag{3.74}$$

The functions $h(\cdot)$ attempt to estimate the y_k using the vehicle dynamics equations presented in Chapter 1. These latter are an approximation of the real vehicle behaviour, so the estimated measurements are named z_k.
As said before the first two equations descend from the kinematic longitudinal tyre velocity, because the front wheel longitudinal slip can be considered null. Considering the equation (1.23) :

$$\begin{aligned} Vx_{11,k} &= (u_K - r_K t_1/2)\cos(\delta_{11,k}) + (v_K + r_K\, a_1)\sin(\delta_{11,k}) = \omega_{11_k} R_{r_1} \\ Vx_{12,k} &= (u_K + r_K t_1/2)\cos(\delta_{12,k}) + (v_K + r_K\, a_1)\sin(\delta_{12,k}) = \omega_{12_k} R_{r_2} \end{aligned} \tag{3.75}$$

where the tyre radius is considered constant and equal to the tyre geometric radius. Thus handling the equations above:

$$\begin{aligned} \omega_{11_k} &= \frac{\cos(\delta_{11,k})}{R_{r_1}} u_k + \frac{\sin(\delta_{11,k})}{R_{r_1}} v_k + \frac{a_1 \sin(\delta_{11,k}) - t_1/2\cos(\delta_{11,k})}{R_{r_1}} r_k \\ \omega_{12_k} &= \frac{\cos(\delta_{12,k})}{R_{r_2}} u_k + \frac{\sin(\delta_{12,k})}{R_{r_2}} v_k + \frac{a_1 \sin(\delta_{12,k}) - t_1/2\cos(\delta_{12,k})}{R_{r_2}} r_k \end{aligned} \tag{3.76}$$

unlike the system equations, in this case the two front wheels are considered individually. Each steering angle is computed by the nonlinear equations $\delta_{11,k} = \delta_{11,k}(\delta_{SW})$ and $\delta_{12,k} = \delta_{12,k}(\delta_{SW})$, where δ_{SW} is the steering wheel angle.
The yaw rate is a state variable and an element of the estimated measurement vector as well. It is acquired by the IMU, so the third equations of $h(\cdot)$ is an identity:

$$r_k = r_k \tag{3.77}$$

The other two equations of $h(\cdot)$ descend from the single-track equilibrium equations in (3.64):

$$
\begin{aligned}
a_{y_k} &= \frac{1}{m}\left(F_{y_1,k}\ \cos(\delta_{1,k}) + F_{x_1,k}\ \sin(\delta_{1,k}) + F_{y_2,k}\right) \\
a_{x_k} &= \frac{1}{m}\left(F_{x_1,k}\ \cos(\delta_{1,k}) - F_{y_1,k}\ \sin(\delta_{1,k}) + F_{x_2,k}\right)
\end{aligned}
\tag{3.78}
$$

Finally the functions of $h(\cdot)$ are given by (3.76), (3.77) and (3.78). Note that it is not reported the nomenclature indicating the estimated value, for sake of simplicity, but the terms u_k, v_k and r_k are the a-priori state estimate value. The tyre forces in (3.78) are the estimated value, which are based on the a-priori state estimate (used for computing the slips).

3.5.4 Additional inputs

In the previous sections additional inputs are mentioned, they are measurements acquired by sensor. These measurements require sensors which are commonly used for the basic data acquisition, sometimes they equip common vehicle and are used to prevent critical events. The additional inputs in this application are:

- Steering wheel angle δ_{SW}
- Wheels rotational velocity ω_{ij}
- Longitudinal acceleration a_x

The first one is used to compute the steering angle of the front wheels in (3.76), using a nonlinear steering law. In the other process equations the mean value of the two steering angles is considered. The rotational velocity of the wheels is used to evaluate the slip ratio in $f(\cdot)$ and $h(\cdot)$, again the mean value of the angular velocities referring to the same axle is considered. Note that the front wheels rotational velocity is used in y_k. The Longitudinal acceleration is used in the computation of the tyre forces, because the macro-parameter D is a quadratic function of the vertical load, as shown in (1.18). The tyre vertical forces are given by (3.70).

3.5.5 Vehicle sensor description

The sensors employed are:

- Steering wheel encoder
- Front wheels encoder
- Electric motor encoder
- IMU
- S-motion
- Lidar

The first four sensors are necessary for filters working, the S-motion is used to compare the results and the Lidar acquired data are not used in this thesis work.

The front wheel encoder uses the Hall effect in order to provide the angular wheel velocity. One of the two poles rotates integrally with the wheel hub. The sampling frequency is proportional to the angular velocity, so there is not a fixed value.

The IMU used is produced by Izze-Racing and provides the two linear accelerations and the yaw rate. The sampling frequency is 240 Hz and the acceleration accuracy is minus than 1% of full scale (FS) and the angular rate accuracy is minus than 1.5% FS. The default measurement range is ± 8 g for acceleration and ± 245 °/s for angular rate.

The S-motion is produced by Kistler and enable direct, slip-free measurement of longitudinal and transverse speed as well as Side-slip angle in

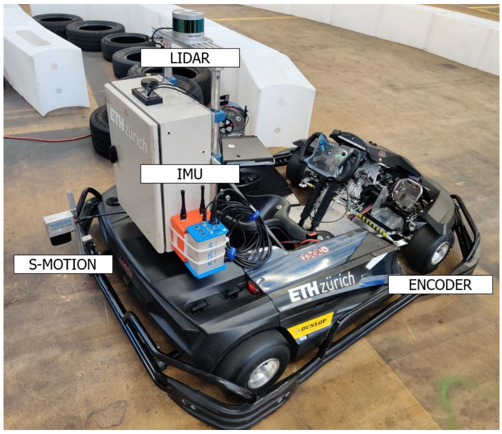

Fig. 3.5 Strumented vehicle and sensors position

vehicle driving dynamics tests. It is used to compare the filter results, in fact it acquires the longitudinal and lateral velocities (the vehicle side slip angle is obtained using (3.59). The sampling frequency is 500 Hz and the speed accuracy is minus than $\pm 0.2\%$ FS and the guaranteed angle measurement accuracy is minus than $\pm 0.2°$. The default measurement range is ± 200 km/h for speed and ± 30 ° for angles.
The lidar is produced by Velodine and provides high definition 3-dimensional information about the surrounding environment. The sampling frequency is 20 Hz, but the acquired data are interpolated in order to reach 50 Hz.
The entire data-set is down-scaled to 50 Hz in order to be processed at the same frequency, which will be the filter frequency.

3.6 Results and validation

In this section the obtained results are presented, comparing each estimate VSA to the experimental one acquired by the S-Motion in four different test. In fact the root mean square error (RMSE) of the estimated VSA is used as term of comparison. The RMSE is computed each time step, at the generic time step k it is:

$$RMSE_k^{VSA} = \sqrt{\sum_{i=1}^{k} \frac{\hat{\beta}_i - \beta_i}{k}} \tag{3.79}$$

Where $\hat{\beta}_i$ is computed using (3.59) in which $\hat{v}_i$ and $\hat{u}_i$ are the estimated value at time step i, and β_i is acquired by the S-motion. The map of the track is here reported using the data acquired by the lidar.

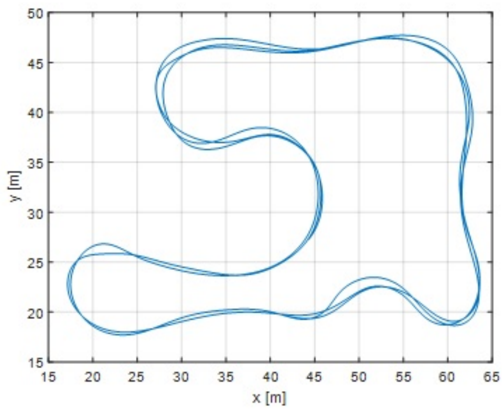

Fig. 3.6 Track map

Moreover, the axle longitudinal and lateral forces against the corresponding slip are reported for each test, the target values are obtained using a technique based on the T.R.I.C.K. [44].The longitudinal forces at the front axle, due to the rear wheel drive, are caused by the rolling resistance.

3.6.1 EKFs

This type of filters rely on the approximation of the nonlinear process. The Jacobian and Hessian matrices are analytically computed and numerically validated, this means that the filter does not execute the derivatives at each time step, saving computational burden. The results in term of VSA estimation and RMSE are shown in the next figures.

The I-EKF is characterized by a low RMSE value at the beginning of each run, this is because of the iteration cycles executed at each time step, which refines the estimation. The number of iterations that the implemented I-EKF execute each time step is 5, it is obtained by a sensitivity analysis, higher value does not introduce any improvement in this case study. Comparing the FO-EKF and the SO-EKF estimations, they are almost equal despite the greater accuracy expected by the SO-EKF, due to the Hessian use. The overall performance of the implemented EKFs are quite similar, but the implementation of each filter does not. In fact, the FO-EKF is the most easy to implement, it only needs the Jacobians computation, whereas the SO-EKF requires the Hessians computation as well, that is quite tough considering the implemented tyre model. The I-EKF is the most time consuming among the EKFs, this is due to the iteration cycle.

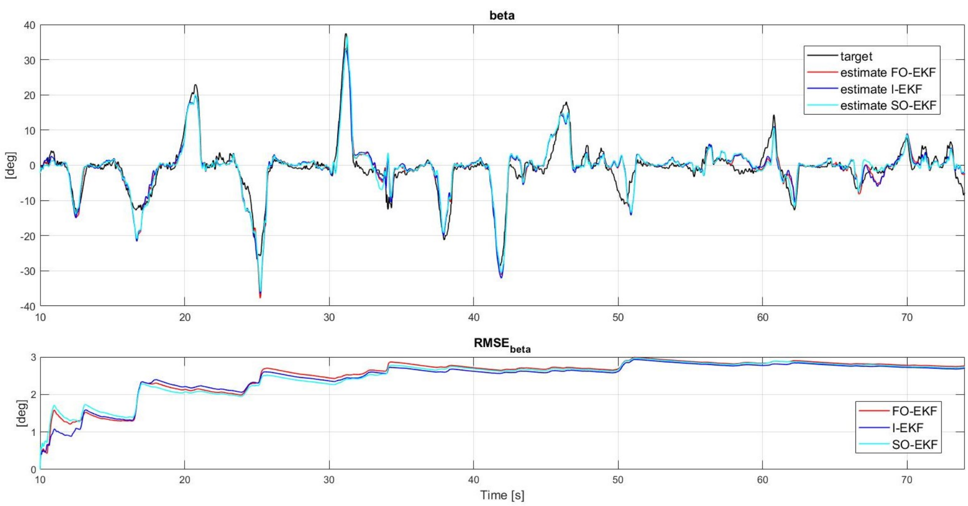

Fig. 3.7 VSA estimated by EKFs and acquired by S-motion during test #1

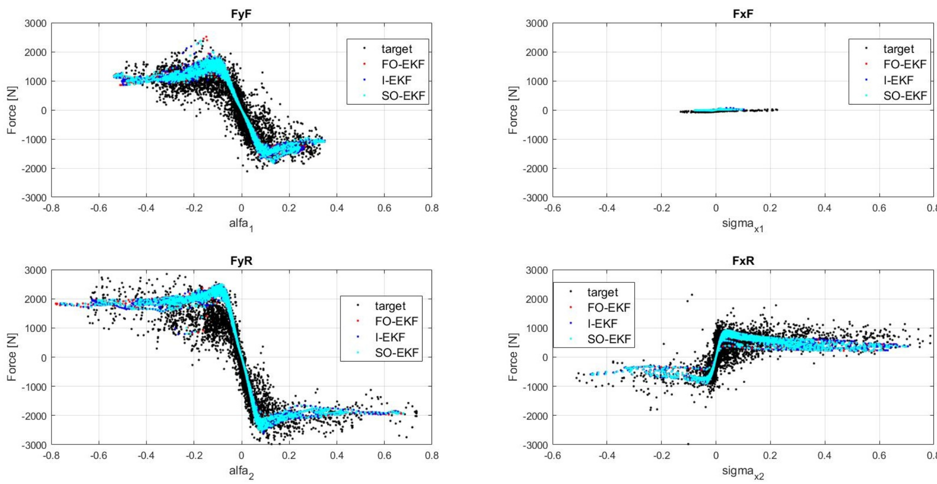

Fig. 3.8 Lateral and Longitudinal axle forces estimated by EKFs - test #1

Another filter's index of performance taken into account in this work is the run-time. The mean run-time required by each algorithm is reported in the table 3.2. This may be useful in the real-time application, for this reason the time taken by each implemented filter to estimate 1 s of real time acquired data is considered.

Table 3.1 EKF RMSE mean values for each test.

[deg]	TEST 1	TEST 2	TEST 3	TEST 4	MEAN
FO-EKF	2.52	1.18	2.23	2.02	2.03
I-EKF	2.46	1.26	2.09	2.26	2.02
SO-EKF	2.48	1.20	2.36	2.22	2.06

3.6.2 UKFs

This type of filters rely on the unscented transformation. The main difference concerns the weights associated to the sigma points, the S-UKF does not consider the central sigma point, all the others does. In the following figure

Table 3.2 Time taken by each EKF implemented filter to estimate 1 s of real time acquired data.

[ms/s]	TEST 1	TEST 2	TEST 3	TEST 4	MEAN
FO-EKF	8.20	8.86	8.64	7.49	8.30
I-EKF	22.91	24.35	25.19	22.37	23.71
SO-EKF	18.26	20.63	19.31	17.84	19.01

the results of the filters in term of VSA estimation with RMSE and planar forces is shown.

The G-UKF implemented is the version in (3.38), the parameters value are:

$$\begin{aligned} \alpha &= 0.6 \\ \beta &= 2 \\ k &= 0 \end{aligned} \tag{3.80}$$

These values are the result of a sensitivity analysis. Note that α is higher than the commonly used value (about 0.001), this means that the sigma points are not so close to the mean state. In other words the central sigma point affect the state estimation in a negative way in this application, in fact lower values of α give higher RMSE values. In addition, considering the weights as defined in (3.36) and also considering that for random variable with Gaussian distribution $k = 3 - n$ with $n = 3$ in this application, therefore the G-UKF becomes an S-UKF.

The SIMP-UKF and SPHE-UKF tunable parameters are the result of a sensitivity analysis as well, in this case the tunable parameter is the central sigma point weight, but this value affects all the other weight values as shown in sections (3.2.3) and (3.2.3). They are both equal to 0.6.

The UKFs implemented exhibit different overall performance, there is no one of them that is the best for each test. An optimization analysis of the tunable parameters, integrated in the Q and R optimization method adopted, could lead to better results in term of VSA estimation. However unphysical results may be obtained, this is because the optimizator attempts to minimize the residual prediction error acting on the tunable parameters but it does not take into account the physical effect of these values on the axle forces for example. In other words, different local minimum of the prediction error could be reached but this does not mean that all the others physical quantity have reached their optimal values consistent with the expected or acquired ones. This happens because the filter and the optimizator attempt to minimize only the error between the state estimate and the true state measurement, during training phase no information about the other quantities are provided. In order to reach better results and above all consistent with the expected ones, the optimization phase could take into account additional quantities. Considering the implemented filters, better results have been reached in term of RMSE but the axle forces does not exhibit the saturation effect that are expected to be in according to the "target" value.

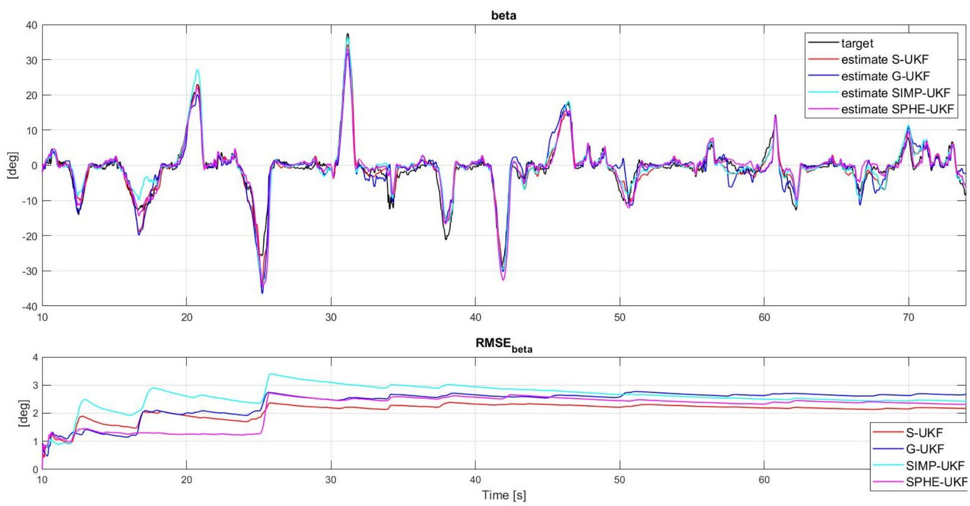

Fig. 3.9 VSA estimated by UKFs and acquired by S-motion during test #1

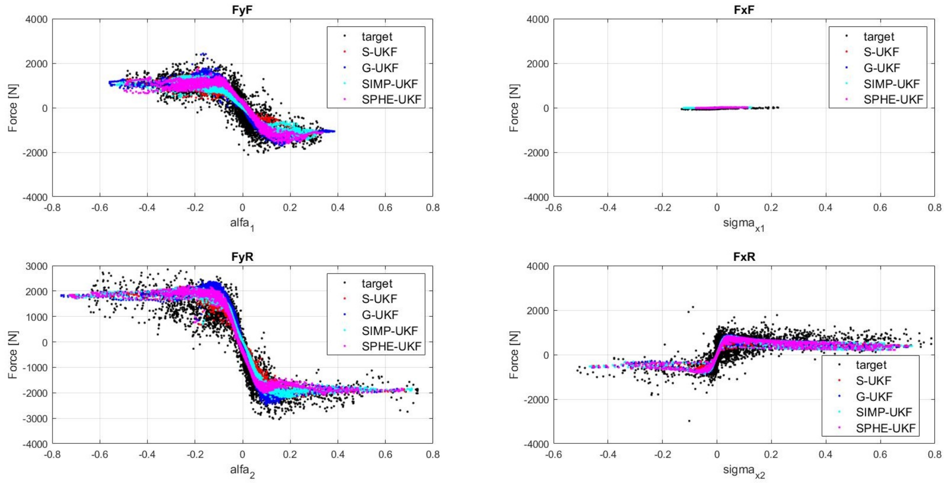

Fig. 3.10 Lateral and Longitudinal axle forces estimated by UKFs - test #1

Table 3.3 UKF RMSE mean values for each test.

[deg]	TEST 1	TEST 2	TEST 3	TEST 4	MEAN
S-UKF	2.10	1.32	2.38	1.59	1.85
G-UKF	2.40	1.06	2.72	2.87	2.26
SIMP-UKF	2.60	1.39	2.95	1.86	2.20
SPHE-UKF	2.17	1.43	2.82	2.70	2.28

3.6.3 PFs

This type of filter is based on the idea of represent the probability density function using a set of random samples with associated weights, these samples are randomly computed starting from the previous time step state estimate. In order to compare the filters, based on different resampling strategies, the random number generator is fixed.The number of particles is fundamental, an higher number may lead to better accuracy in state estimation but the sample impoverishment is always lurking. The simplest resampling strategies are implemented, although the literature is plenty of other type of strategies.

Table 3.4 Time taken by each UKF implemented filter to estimate 1 s of real time acquired data.

[ms/s]	TEST 1	TEST 2	TEST 3	TEST 4	MEAN
S-UKF	27.78	27.36	27.79	25.952	27.22
G-UKF	39.08	37.20	35.98	34.08	36.59
SIMP-UKF	25.73	25.13	23.28	22.24	24.10
SPHE-UKF	25.08	25.42	23.52	22.45	24.12

The aim of this choice is to explore the use of the PFs in vehicle dynamics estimation, in particular in the VSA estimation, in fact no works about that have been found in common literature. The main works available in common literature use the PFs for tracking problem.

In the following figure the results of the filters in term of VSA estimation with RMSE and planar forces is shown. The number of particles adopted is 30, it is a trade of between computational burden and estimation accuracy. The resampling strategy is applied each time step, it is possible to not execute it at each time step but several tests shown that better results in term of RMSE are always achieved in the first case.

The estimated VSA, but all the other estimated quantities as well, are characterized by a noisy trend. This is due to the fact that the sample are very close one each other but the same sample has different weight factors at each time stem, this means that at consecutive time step the estimated value is not so close to the previous as in the previous filters. This effect is more visible in the SYSres-PF and STRAres-PF, in which the random number of the resampling strategy is always different (see algorithm (9) and (10)), however in the MULTIres-PF could happen that the random number are very close or even the same. Having different random number lead to a more effective resampling e thus better filter accuracy.

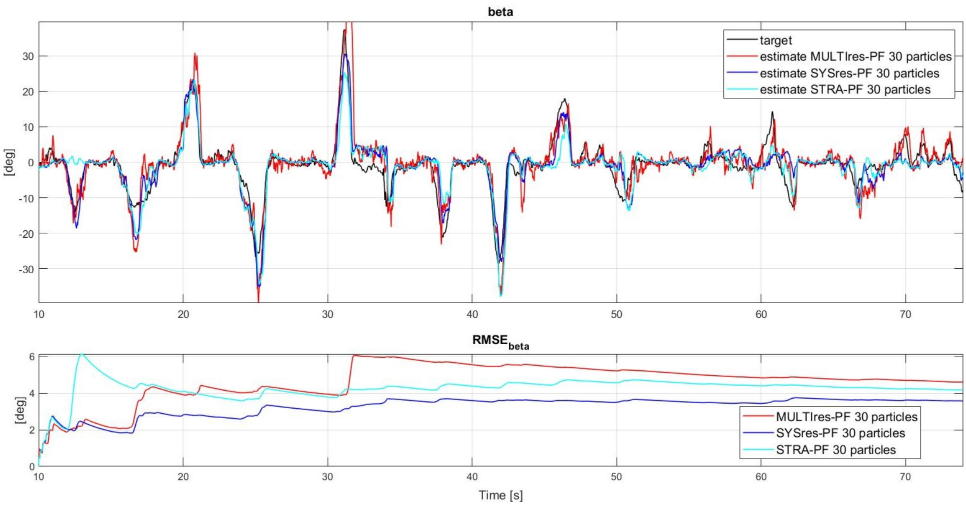

Fig. 3.11 VSA estimated by PFs and acquired by S-motion during test #1

Table 3.5 PF RMSE mean values for each test.

[deg]	TEST 1	TEST 2	TEST 3	TEST 4	MEAN
MULTIres-PF	4.62	1.32	3.53	3.80	3.32
SYSTres-PF	3.26	1.38	3.24	3.65	2.88
STRAres-PF	4.28	1.44	3.88	3.99	3.40

3.6.4 Overall performance analysis

Concerning the obtained results, the EKFs and the UKFs show a better state estimation using the vehicle model presented and the Pacejka macroparameters computed. Considering the mean value of the RMSE computed per each tests, the S-UKF exhibits the lowest value whereas the other UKFs exhibit a value which is about the 20% higher; the EKFs show the same mean value if compared one each other but this is about the 10% higher than the one reached by the S-UKF; Finally, the SYSTres-PF shows the lowest RMSE mean value if compared with the other implemented PFs, but if compared to

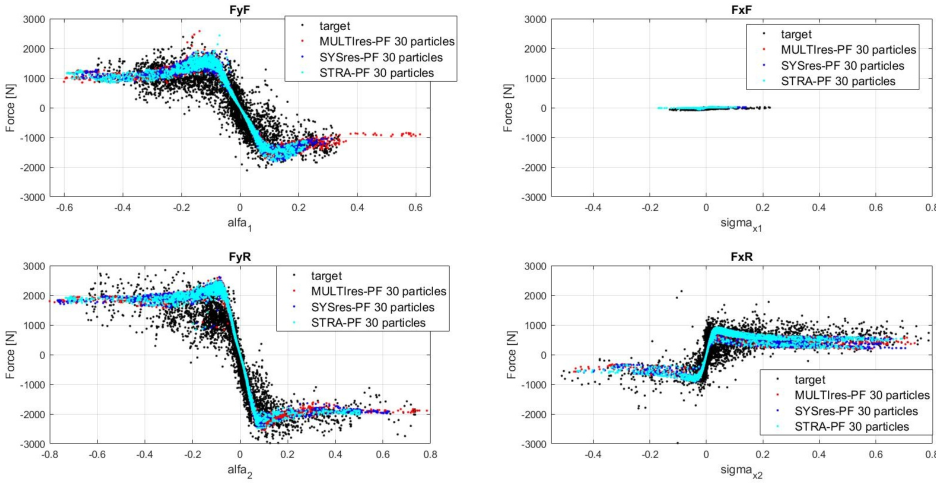

Fig. 3.12 Lateral and Longitudinal axle forces estimated by PFs - test #1

Table 3.6 Time taken by each implemented PF filter to estimate 1 s of real time acquired data.

[ms/s]	TEST 1	TEST 2	TEST 3	TEST 4	MEAN
MULTIres-PF	311.0	310.9	306.0	305.8	308.5
SYSTres-PF	309.4	303.2	306.1	304.0	305.7
STRAres-PF	308.2	302.9	308.1	306.8	306.5

the others the PFs exhibit the higher values, in particular the STRAres-PF shows the highest one. Concerning the computational burden required by each state estimator which can be considered as proportional to the time taken by the filter to estimate 1 second of real time, the FO-EKF is characterized by the lowest amount of time required, thanks to its simple algorithm. The other EKFs present a value which is about the 150% higher. Considering the UKFs, the SIMP-UKF and the SPHE-UKF require lower run-time than the S-UKF and the G-UKF, this latter is characterized by the highest one if considering only the Kalman-based filters, it is about the 340% higher than the lowest one. Considering the PFs, the time required is one order of magnitude higher than the Kalman-based one, they take about one-third of second to estimate 1 second of real time. However, the overall state estimate is not always accurate, in same cases the estimate VSA is quite different than the actual one, this may be mitigated adopting a complete Magic Formula, with micro-parameters instead of macro-parameters. Moreover, it may be interesting to consider a tricycle vehicle model instead of a bicycle one in order to take into account the lateral load transfer effect.

In order to improve the VSA estimation the tyre model may be a key factor, in this work the macro-parameters are fixed, but considering their update during filter execution, due to thermodynamics and wear effect, could lead to better results, and more important it could be possible, as mentioned in the introduction of this chapter, estimate the multi-physical dynamics of the tyre employing the described methodology.

Table 3.7 Overall RMSE mean values for each test.

[deg]	TEST 1	TEST 2	TEST 3	TEST 4	MEAN
FO-EKF	2.52	1.18	2.23	2.02	2.03
I-EKF	2.46	1.26	2.09	2.26	2.02
SO-EKF	2.48	1.20	2.36	2.22	2.06
S-UKF	2.10	1.32	2.38	1.59	1.85
G-UKF	2.40	1.06	2.72	2.87	2.26
SIMP-UKF	2.60	1.39	2.95	1.86	2.20
SPHE-UKF	2.17	1.43	2.82	2.70	2.28
MULTIres-PF	4.62	1.32	3.53	3.80	3.32
SYSTres-PF	3.26	1.38	3.24	3.65	2.88
STRAres-PF	4.28	1.44	3.88	3.99	3.40

Table 3.8 Time taken by each implemented filter to estimate 1 s of real time acquired data.

[ms/s]	TEST 1	TEST 2	TEST 3	TEST 4	MEAN
FO-EKF	8.20	8.86	8.64	7.49	8.30
I-EKF	22.91	24.35	25.19	22.37	23.71
SO-EKF	18.26	20.63	19.31	17.84	19.01
S-UKF	27.78	27.36	27.79	25.952	27.22
G-UKF	39.08	37.20	35.98	34.08	36.59
SIMP-UKF	25.73	25.13	23.28	22.24	24.10
SPHE-UKF	25.08	25.42	23.52	22.45	24.12
MULTIres-PF	311.0	310.9	306.0	305.8	308.5
SYSTres-PF	309.4	303.2	306.1	304.0	305.7
STRAres-PF	308.2	302.9	308.1	306.8	306.5

Chapter 4

Advantages of tyre state knowledge in motion planning

4.1 Introduction

The information concerning the vehicle's non-linear physical limits depending on the thermal and wear states of tyres, the pavement characteristics, and the boundary conditions (wet or icy ground, under-inflated or worn tyre, etc.), as shown in the previous chapters, represents a fundamental additional value for the optimal behavior of safety- and performance-oriented control logics [18, 163, 164].

The objective of this chapter consists in the integration of the information concerning the tyre dynamic limits within the definition of a virtual driver (VD), implemented as a vehicle controller aiming at testing the vehicle behavior at limit of handling condition, and demonstrating the advantages in terms of both enhanced active safety and optimized performance.

An interesting VD definition that addresses the problem of real-time obstacle avoidance on low-friction road surfaces has been proposed in [165], where the code generation tool ACADO [166] has been used to define and solve the NMPC problem.

The main advantages of the NMPC approach are the capability of the controller of handling all significant features of the process dynamics directly: in this way, the constraints on variables involved in the task (track limits, actuator constraints) can be easily integrated into the optimal control problem, hence guaranteeing the maximal exploitation of vehicle capabilities. Moreover, it is a predictive technique that allows optimizing the vehicle behavior over a future horizon in time, and therein system states and controls. In this way, the controller is allowed to retrieve information about future vehicle behavior and about possible dangerous situations, aiming at anticipating actions and providing suitable controls for challenging vehicle handling.

The information concerning the vehicle non-linear physical limits depending on the thermal and wear states of tyres, the pavement characteristics and the boundary conditions (wet or icy ground, under-inflated or worn tyre, etc.) represents a fundamental additional value for the optimal behavior of safety- and performance-oriented control logics [167–169], as it allows to maximize the potential to avoid obstacles and to reduce the severity of collisions [25].

This study aim to lay the foundation of the future advanced driving systems, sensitive to environmental conditions and adaptive to continuously varying characteristics of the underlying non-linear system. Being currently mainly based on mere empirical calibration, the physical model-based estimation can represent a crucial factor towards the improvement of the pedestrians' and passengers' active safety, enabling the management of the activation threshold ranges on the basis of the instantaneous operating and the environmental boundary conditions [170, 171]. This can be already employed in the current ADAS to communicate to the driver the necessity to co-act in specific situations, but it also constitutes a fundamental root for the future driving automatization [172, 173].

4.2 Plant model

The plant model has to reproduce with high fidelity the real vehicle in order to test the control logic with a good level of accuracy. For this reason, to parametrize the vehicle and the tyre model, have been collected data with a chosen GT vehicle in a specific test session on track. Due to a non-disclosure agreement with the industrial research partner, the vehicle and the track will not be specified. The described vehicle model will be considered also for the application reported in the Chapter 5 and 6.

The track session has consisted of handling tests in the widest possible range of tyre operating conditions in terms of temperature, pressure, and wear level. Following the vehicle model parametrization and the tyre parameters' estimation procedures described in [44, 121], the vehicle non-linear system has been completely characterized in all the conditions of interest, being able to faithfully reproduce the experimental data in the virtual environment.

The vehicle plant has been modelled in 14 degrees of freedom (DoF), based on the mathematical representation described in [174], has been modeled in a MATLAB/Simulink environment as follows:

- 6 DoF to reproduce longitudinal, lateral, vertical, pitch, roll, and yaw motion of the vehicle body;
- 4 DoF concerning the wheel rotation and 4 DoF for the wheel normal displacement, with the hypothesis that the degrees of freedom to the relative motion between the wheel and the vehicle body can be neglected along the longitudinal and lateral directions, allowing only the independent rotational and vertical displacements.

Furthermore, the parameterized vehicle is rear-wheel drive with front steering and internal combustion engine. The tyre model is described by Pacejka's magic formula model, whose parameters have been characterized for different conditions of temperature, pressure, and wear as described in the Chapter 2. Per each road surface under study (dry, wet, snowy, and icy), the tyre-road friction coefficient has been supposed constant and is applied as an additional scaling factor of the λ_{μ_x} and λ_{μ_y} parameters [94], linearly combining the tyre characteristics identified on a reference road with the ones potentially achievable on diverse pavement surfaces.

The vehicle dynamic behavior in the reference tyre conditions has been validated in a slow-ramp-steer maneuver, whose parameters are summarised in the Table 4.1 and outputs are illustrated in the Figure 4.1, feeding the model with the steering input presented in the Figure 4.2a):

Table 4.1 Slow-ramp-steer inputs

Description	**Value**	**Unit**
start time	13.26	s
end time	20.3	s
initial velocity	27.9	m/s
initial gear	3	-
ramp duration	7.04	s
initial steer	0	deg
slope steer	-22.29	deg/s

4.2.1 Validation

For the validation purpose, lateral acceleration a_y, steering angle δ, side slip angle β have been compared for the same inputs. Figure 4.1 shows the comparisons between experimental data and model outputs shown on the classic $a_y - \delta$ and $a_y - \beta$ diagrams. An aspect that is worth pointing out is the difference between the black dashed and continuous lines: the first one is obtained using the starting parameters provided by the research partner, the second one is obtained employing the calibration procedure described in

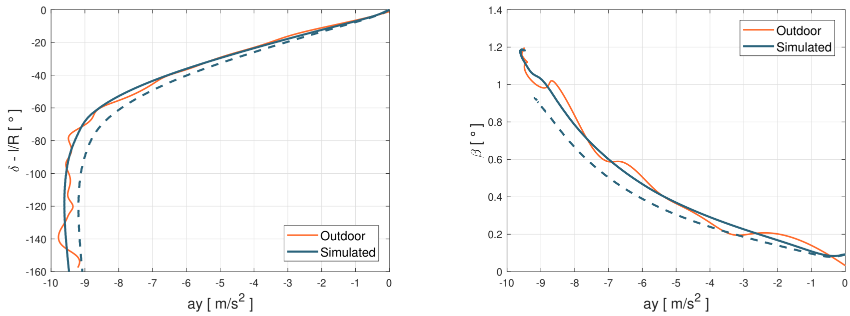

(a) (b)

Fig. 4.1 Comparison between outdoor acquisitions and simulation output. (**a**) Steering angle vs. lateral acceleration diagram. (**b**) Sideslip angle vs lateral acceleration diagram.

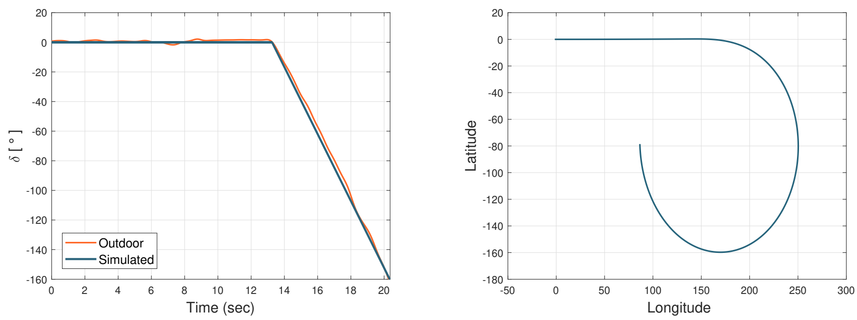

(a) (b)

Fig. 4.2 Example of lateral maneuver's input reproduction. (**a**) Experimental and simulation steering angle comparison. (**b**) Slow-ramp-steer trajectory in virtual environment.

[121]. In particular, the starting under-steering characteristics (dashed lines) have been revised better identifying the parameters linked to the anti-roll bars stiffness and the steering maps, leading to a less under-steering behavior within the handling diagram, in agreement with the experimental data.

The enhanced parametrization has led to a higher slope in the linear section (Figure 4.1a), but also higher lateral grip and side-slip angle values, related to the rear axle behavior (Figure 4.1b). Once the vehicle and the tyres' subsystems have been properly characterized in the specific range of temperature, pressure, and wear, the validity range of the MF tyre model has been extended adopting the MF-Evo one, described in [101]. In particular, the tyre model calibration process can be summarized in three fundamental steps: the first one is related to the pre-processing of the experimental data (which allows to discern useful information contained in the acquired data and to eliminate the non-physical outliers); the second one concerns the identification of the standard MF micro-coefficients in a specific range of temperature, pressure, and wear; the third step aims at the calibration of the additional multi-physical analytical formulations, taking into account of the entire dataset and, thus, extending the tyre model towards thermal and degradation phenomena.

The calibration results are visible in terms of adherence ellipse in the Figure 1.6, where the experimental data have been compared towards the MF and MF-evo outputs within different temperature working ranges of the tyre. Finally, the parameters of the MF-evo model have been further modified to extend the applicability of the tyre model on different road surfaces, modifying the identified friction factors towards the pavement characteristics, as reported in the Table 4.2. The resulting interaction characteristics for different tyres, in diverse thermodynamic conditions and in contact with different road surfaces have been summarized in Figures 4.3 and 4.4.

In steady-state conditions, the global force exerted by the tyres is in a dynamic equilibrium with the centrifugal force, as a function of the longitudinal velocity of the vehicle v and the instantaneous cornering radius R, relating the lateral acceleration a_y and the longitudinal velocity v of the vehicle's center of mass (CM) by the equation:

$$a_y = \frac{v^2}{R}; \tag{4.1}$$

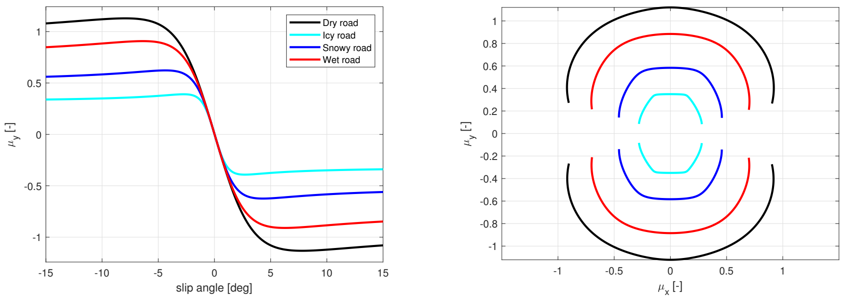

(a) (b)

Fig. 4.3 New tyre in optimal thermal condition in contact with different road surfaces. (**a**) Lateral interaction characteristics. (**b**) Adherence ellipse.

Table 4.2 Summary of the velocity maximum values assumed for each road scenario.

Friction Coefficient $[-]$	**Lateral Acceleration** $[m/s^2]$	**Longitudinal Velocity** $[m/s]$
0.35	0.35	5.92
0.55	0.70	8.37
0.80	1.50	12.2
1.00	2.52	15.9

To demonstrate the potential influence of the road surface characteristics on the overall vehicle behavior, a set of simulations has been conducted with different tyre parameters described in Figure 4.3 in a steady-state lateral slow-ramp-steer (SRS) maneuver. The maximum achievable value of the forward velocity v for a given curvature and $a_y - \delta$ characteristics are reported for dry, wet, snowy, and icy pavement conditions in the Figure 4.5a,b, respectively.

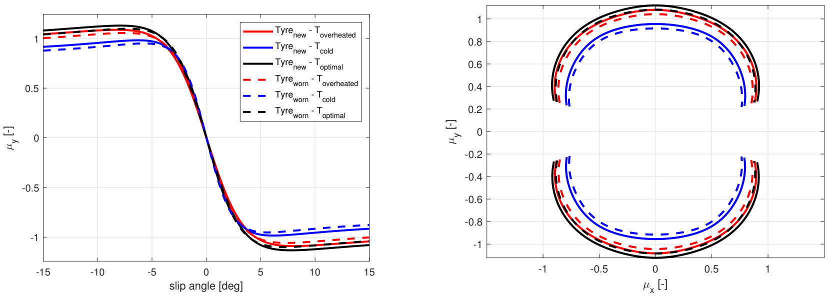

(a) (b)

Fig. 4.4 New and worn tyres in diverse thermal conditions in contact with the dry road. (**a**) Lateral interaction characteristics. (**b**) Adherence ellipse.

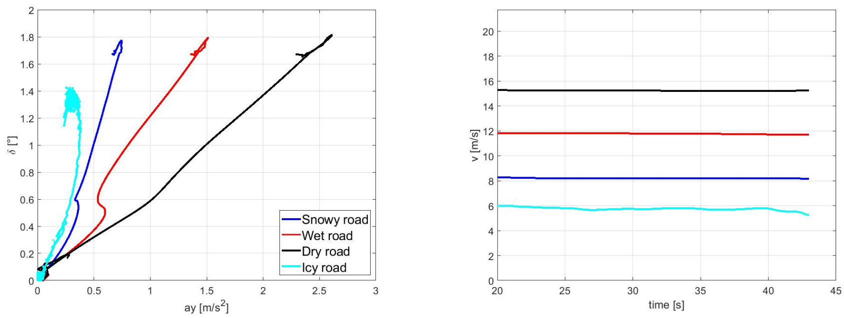

(a) (b)

Fig. 4.5 SRS maneuver on different road surfaces. (**a**) Vehicle understeer characteristics. (**b**) Maximum velocity achieved.

4.3 Motion planning

4.3.1 Model predictive control

Model Predictive Control (MPC) is a control technique that utilizes an analytical model of the system, along with possible constraints, in order to predict its future evolution. The main concern of MPC is to obtain a control input that minimizes a certain objective function which represents the future behavior of

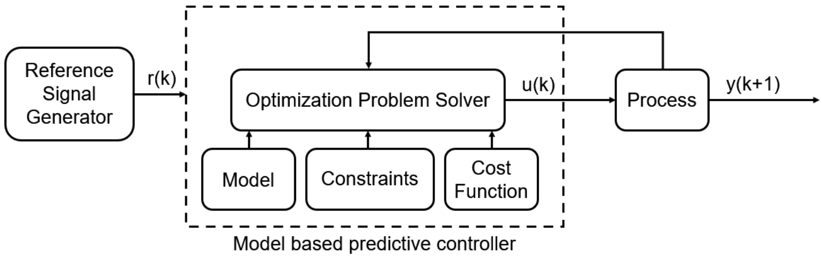

Fig. 4.6 MPC block scheme.

the system in a specific, finite prediction time horizon $[t_0, t_f]$. However, only the first step of the optimal input is actually applied to the system. Indeed the prediction horizon is shifted forward by one step and the minimization problem is solved again using the new systems states as initial conditions. This procedure is repeated at each sampling instant, so the overall control technique solves a sequence of optimization problems in an on-line fashion, based on the last measurement of the system state.

An MPC-based control strategy has several positive aspects, namely the ability to handle multiple-input multiple-output (MIMO) systems, the possibility to include the constraints of the system in the minimization problem and the achievement of an optimal behavior operating in closedloop. However, the computational cost of solving the minimization problem is often quite high, which can prevent a real-time implementation of the control scheme. Fig. 4.6 shows the block diagram of a typical MPC workflow.

4.3.2 NMPC

If the considered system follows a non-linear evolution model, MPC is termed Nonlinear Model Predictive Control (NMPC). The non-linearities of the model give a more detailed representation of the system, leading to a more precise control response, while increasing the complexity of the optimization problems involved with respect to a linear system. For this reason, the minimization problem could be too complex for a real-time solution, and other strategies are in order like the choice of a sub-optimal solution that still satisfies the constraints. The MPC schemes with a sub-optimal solution can be classified according to the solution method. Numerical methods for solving optimization problems are divided into direct and indirect methods. The first are based on a suitable parametrization of the problem in continuous time, in order to obtain a finite-dimensional non-linear programming problem. The second exploit calculus of variations or the Pontryagin's Maximum Principle.

Optimal control problem

Consider a non-linear system with system state vector $x \in \mathbb{R}^{n_x}$, control input vector $z \in \mathbb{R}^{n_z}$ and denote by $p \in \mathbb{R}^{n_p}$ the vector containing the system parameters. The system model can be written as

$$\dot{x}(t) = f(t, x(t), u(t); p) \tag{4.2}$$

Eq. 4.2 refers to a system of ordinary differential equations (ODE) and represents the dynamics of the process to be controlled. Given an initial condition $x(t0) = x_0$ and a control trajectory $u(t)$, the existence of a unique solution $x(t)$ on a certain interval, i.e. $t \in [t0, tf]$, is ensure by Picard's existence theorem, under the hypothesis that f is uniformly Lipschitz in x and u and continuous in t [175]. The MPC formulation is based on the solution at each time instant of a minimization problem of the form

$$
\begin{aligned}
\min_{x(\cdot),u(\cdot)} \quad & \tilde{J} = \int_{t_0}^{t_f} \phi(t,x(t),u(t);p),dt + \Phi(x(t_f)) \\
s.t. \quad & x(t_0) = x_0 \\
& \dot{x}(t) = f(t,x(t),u(t);p) \qquad \forall t \in [t_0,t_f] \\
& r(x(t),u(t);p) \leq 0 \qquad \forall t \in [t_0,t_f] \\
& l(t_f) \leq 0
\end{aligned}
\tag{4.3}
$$

where ϕ and Φ are the objective functions, r the constraints on the trajectories, l the limit conditions. Given the current state x0, an optimal solution $(x(\cdot),u(\cdot))$ in the prediction horizon $[t_0,t_f]$ can be computed using Eq. 4.3.

Direct multiple Shooting

Direct methods for solving optimal control problems are very popular, due to their flexibility and the fast implementations of numerical solvers. The basic idea is to parametrize the minimization problem in such a way that it can be solved by available advanced numerical solvers. There are several ways to parametrize the state and the control variables in Eq. 4.3, in particular we mention multiple shooting as an effective approach in NMPC applications [176]. In direct multiple shooting the prediction horizon is divided into N temporal intervals (also called shooting intervals) defined as $[t_k,t_{k+1}]$ with $k = 0,1,\ldots,N-1$, and is therefore decomposed in $N+1$ points on a temporal grid: $t_0 < t_1 < \ldots < t_N = t_f$. The control trajectory is then parametrized on these intervals, utilizing a piecewise linear representation defined as:

$$u(t) = u_k \qquad \forall y \in [t_k,t_{k+1}] \tag{4.4}$$

The state $x(t)$ is also parametrized on N intervals, and $N+1$ shooting points $(s_0,s_1,...,s_N)$ are introduced as additional optimization variables. Each point s_k is defined exactly on the points t_k of the temporal grid and represents the initial condition of the subsequent initial value problem on the shooting interval $[t_k, t_{k+1}]$:

$$\dot{x}(t) = f(t, x_k(t), u_k(t); p) \quad \forall t \in [t_k, t_{k+1}], \quad x_k(t_k) = s_k \tag{4.5}$$

The dynamic constraints defined in Eq. 4.3 become then continuity constraints:

$$s_{k+1} = \Xi(t_k, s_k, u_k; p) \qquad k = 0, 1, ..., N-1 \tag{4.6}$$

where $\Xi(\cdot)$ is an integration operator that solves the initial value problem in Eq. 4.5 and returns the solution evaluated in the final point t_{k+1}. Similarly, the constraints on the trajectories in Eq. 4.3 are parametrized on the points defined in discrete time:

$$r(s_k, u_k; p) \leq 0 \qquad k = 0, 1, ..., N-1 \tag{4.7}$$

Finally, the objective function $\tilde{J}$ is rewritten as follows

$$\sum_{k=0}^{N-1} \bar{J}_k = \sum_{k=0}^{N-1} \int_{t_0}^{t_f} \phi(t_k, s_k, u_k; p), dt + \Phi(s_N) \tag{4.8}$$

and can be approximated using a discrete sum

$$\sum_{k=0}^{N-1} \bar{J}_k = \sum_{k=0}^{N-1} \phi(t_k, s_k, u_k; p) dt + \Phi(s_N) \tag{4.9}$$

Therefore, given the parametrizations in Eq. 4.5, 4.7 and 4.9, the optimization problem in Eq. 4.3 can be rewritten as follows

$$
\begin{aligned}
\min_{x(\cdot),u(\cdot)} \quad & \sum_{k=0}^{N-1} \phi(t_k, s_k, u_k; p)dt + \Phi(x(t_f)) \\
s.t. \quad & s_0 = x_0 \\
& s_{k+1} = \Xi(t_k, s_k, u_k; p) \qquad k = 0, 1, \ldots, N-1 \\
& r(s_k, u_k; p) \leq 0 \qquad k = 0, 1, \ldots, N-1 \\
& l(s_N) \leq 0
\end{aligned}
\tag{4.10}
$$

where $s = [s_0^T, s_1^T, \ldots, s_N^T]^T$, and $u = [u_0^T, u_1^T, \ldots, u_N^T]^T$ are the state and input variables, respectively. An explanatory plot for the direct multiple shooting is depicted in Fig. 4.7 and Fig.4.8. In the first step, a guess of the total state and of the control trajectory is necessary to solve the problem, however this guess may not satisfy all the constraints. In practice, all the constraints in Eq. 4.10, in particular the continuity constraints of Eq. 4.5 are usually violated in the beginning and during the solution of the non-linear programming problem, while they are completely satisfied only when reaching the optimal solution.

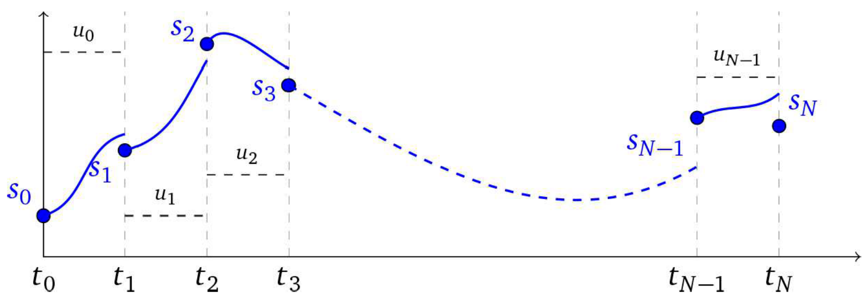

Fig. 4.7 Multiple shooting initial discontinuous trajectory.

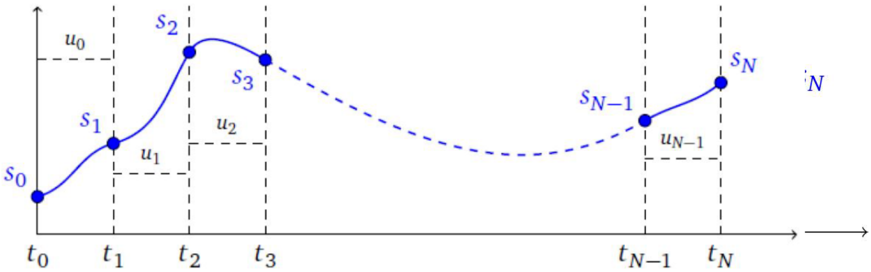

Fig. 4.8 Multiple shooting final continuous trajectory.

NLP algorithm

Consider now the problem in Eq. 4.10 which can be rewritten in standard form as

$$
\begin{aligned}
\min_{z} \quad & a(z) \\
s.t. \quad & b(z) = 0 \\
& c(z) \leq 0
\end{aligned}
\tag{4.11}
$$

where

$$
\begin{aligned}
z &= [z_0^T, z_1^T, \ldots, z_{N-1}^T, s_N] \in \mathbb{R}^{n_z} \\
z_k &= [s_k^T, u_k^T] \quad \in \mathbb{R}^{n_x+n_z} \qquad k = 0, 1, \ldots, N-1
\end{aligned}
\tag{4.12}
$$

is a vector that contains all the optimization variables, while the functions $b : \mathbb{R}^{n_b} \to \mathbb{R}^{n_z}$, $c : \mathbb{R}^{n_c} \to \mathbb{R}^{n_z}$ contain all the constraints given as

$$b(z) = \begin{bmatrix} x_0 - s_0 \\ \Xi(s_0, u_0) - s_1 \\ \vdots \\ \Xi(s_{N-1}, u_{N-1}) - s_N \end{bmatrix} \qquad c(z) = \begin{bmatrix} r(s_0, u_0) \\ \vdots \\ r(s_{N-1}, u_{N-1}) \\ l(s_N) \end{bmatrix} \tag{4.13}$$

A possible way of solving such non-linear programming problem involves using the Sequential Quadratic Programming (SQP) technique [177]. In SQP the solution is reached iteratively, using a local quadratic approximation of the objective function and linearizing the constraints. The optimal solution z^* is reached when the Karush-Kuhn-Tucker (KKT) firstorder optimality condition relatively to problem 4.12 is satisfied with a user-defined level of approximation. A possible improvement on the above algorithm can be derived by noticing that the non-linear program does not vary substantially between two consecutive sampling instants (if a sufficiently high sampling frequency is used) . Moreover, a lower precision of the optimal solution could be enough given that it is often the case where it is not required with perfect accuracy. The Real-Time Iteration (RTI) [175] scheme exploits the above considerations and allows obtaining a fast implementation stopping the SQP method at the first iteration and returning a suboptimal solution of the problem.

MATMPC

Recently, many open-source softwares have been developed for the solution of MPC problems, but not many are at the same time easy to use, efficient and suited to NMPC problems. Indeed, the difficulty of an efficient linearization and the complexity of non-convex optimization make the adaptation of MPC solvers for NMPC problems difficult. In this thesis, the MATMPC packet was used. This software is MATLAB-based and tailored for solving NMPC problems; it was developed at the University of Padova by Yutao Chen [175].

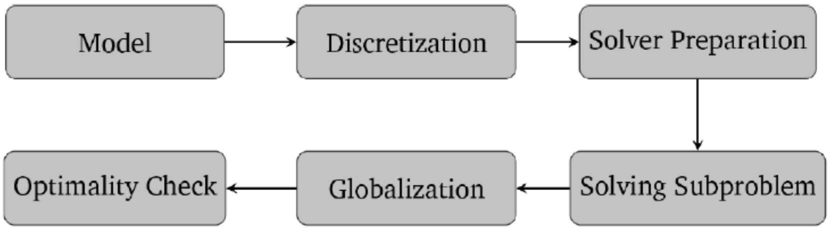

Fig. 4.9 MPC block scheme.

Among the advantages of using MATLAB as a base software it can be count the simplicity of utilization, the availability of many linear algebra routines, and the computational efficiency granted by MATLAB Executable (MEX) functions which allow the seamless integration of C or Fortran code into the process. The MATMPC workflow is presented in Fig. 4.9 . MATMPC requires a continuous-time model, implemented with the CasADi programming language [20], which is discretized with the multiple shooting described in Section 4.3.2 exploiting the Runge-Kutta numerical integrator. At this point the problem is prepared for a specific solver. In particular in this thesis the hpipm sparse solver is employed, which uses interior point method (IPM) for solving sparse QP problems. Next, an iterative procedure is executed to reach an optimal solution where the local minima is found using a line-search algorithm. Then, the KKT first-order optimality conditions are evaluated at this point: the lower the KKT value, the more the solution is close to the real one.

4.4 Controller model

A four-wheel vehicle model based on the description in [178] has been used as the internal model for the NMPC controller. Specific characterization of load transfers, gear shift predictions, longitudinal force saturation, and an ellipsoidal tyre friction constraint have been also introduced in the model definition to improve the overall prediction capabilities of the controller. Finally, the model dynamics have been reformulated in spatial coordinates with respect to the curvilinear abscissa s along the track. In this way, track constraints can be defined with respect to space and the time can be considered as a minimization variable, as already highlighted in previous works [179, 180, 178].

The continuous-time dynamics model is described as

$$\dot{\xi} = \phi(\xi(t), u(t); p(t)) \tag{4.14}$$

where the state is represented by $\xi(t) \in \mathbb{R}^{n_x}$, $u(t) \in \mathbb{R}^{n_u}$ is the input, whereas the time-varying parameter vector is $p(t) \in \mathbb{R}^{n_p}$.

$$\begin{aligned} \ddot{x} &= \dot{y}\dot{\psi} + \frac{1}{m}\left(\sum_{i,j} F_{x_{i,j}} - F_x^d\right), \ \ddot{y} = -\dot{x}\dot{\psi} + \frac{1}{m}\left(\sum_{i,j} F_{y_{i,j}}\right) \\ \ddot{\psi} &= \frac{1}{I_z}\left[a\left(\sum_j F_{y_{f,j}}\right) - b\left(\sum_j F_{y_{r,j}}\right) + c\left(\sum_i F_{x_{i,r}} - \sum_i F_{x_{i,l}}\right)\right] \end{aligned} \tag{4.15}$$

where longitudinal and lateral positions are x, y, while ψ is the yaw angle. m and I_z are the mass and the inertia around the vertical axis of the vehicle, respectively. a, b, c are the vehicle dimensional parameters, front wheels to CM longitudinal distance, rear wheels to CM longitudinal distance, and wheels to CM lateral distance, respectively. $F_{\{x,y\}_{\{i,j\}}}$ are the lateral and longitudinal forces on the wheels and F_x^d is the longitudinal drag force in the vehicle's reference frame. Subscripts $i \in \{f, r\}$ refer to front or rear wheels, $j \in \{l, r\}$ left or right wheels. Figure 4.10 illustrates the physical quantities involved and the reference systems chosen. δ_f is the steering angle of the front wheels, assumed the same for the both front tyres, and $\beta_{f,j}$ is the side slip angle of the f, j-th tyre. The projection of cornering and longitudinal forces in the vehicle frame, the position and the dynamics of the vehicle's CM in the inertial frame X, Y, and the vehicle side slip angle β are described in [178], whereas the longitudinal drag force and the down-force are modeled as [181].

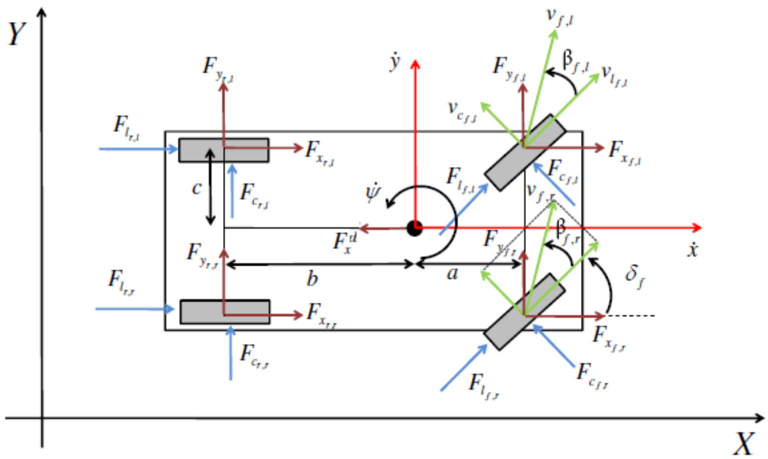

Fig. 4.10 Internal vehicle model for control.

Differently from [178], the longitudinal tyre forces in each wheel reference frame are computed as

$$F_{l_{i,j}} = f_{\text{eng}_{i,j}} - f_{\text{brk}_{i,j}} \tag{4.16}$$

where the engine and braking forces are

$$f_{\text{eng}_{i,j}} = \text{sat}\left(\frac{\tau_{\text{eng}_i}}{r_w}\,\mu F_{z_{i,j}}\right), \quad f_{\text{brk}_{i,j}} = \text{sat}\left(\frac{\tau_{\text{brk}_i}}{r_w}\mu F_{z_{i,j}}\right) \tag{4.17}$$

where μ is the tyre friction coefficient, r_w is the wheel radius and the saturation function is defined in (4.20). Then, the engine and braking torques at the wheels are:

$$\tau_{\text{eng}_i} = \gamma_t\,(\tau^{\max}_{\text{eng},i} - \tau^{\min}_{\text{eng}i}) + \tau^{\min}_{\text{eng},i}, \quad \tau_{\text{brk}_i} = \gamma_b\,\tau^{\max}_{\text{brk},i} \tag{4.18}$$

where $\gamma_{t,b}$ are the normalized throttle and braking efforts, $\tau^{\max}_{\text{brk},i}$ is the maximum torque given by the braking system to front/rear wheels, $\tau^{\max}_{\text{eng},i}$ and $\tau^{\min}_{\text{eng},i}$

are the maximum and minimum torque values expressed by the engine at front/rear wheels at a given gear and are changed as a time-varying parameter to the actual model gearshift. To compute the torques in the prediction horizon, an iterative strategy predicting the engine rpm, and, hence, gearshift, based on the predicted velocity is used [178]. Specifically, the engine rpm quantity is computed as

$$\mathrm{rpm}^{\mathrm{pred}} = \frac{v_x^{\mathrm{pred}}}{r_w} \frac{\mathrm{diff}_{\mathrm{ratio}}}{\mathrm{gear}_{\mathrm{ratio}}} \frac{60}{2\pi} \tag{4.19}$$

where $\mathrm{diff}_{\mathrm{ratio}}$ and $\mathrm{gear}_{\mathrm{ratio}}$ are the input/output torque ratios at the differential and at the gearbox (in a specific gear), respectively. The dependence of $\tau_{\mathrm{eng},i}^{\mathrm{max,min}}$ w.r.t. the engine rotational velocity has been neglected. Finally, the saturation function is defined as:

$$\mathrm{sat}(f_a, f_b) = \frac{f_b}{1 + \exp(-5(\frac{f_a}{f_b} - \frac{1}{2}))} \tag{4.20}$$

The normal forces $F_{z_{i,j}}$ are modeled considering the load transfer in steady-state condition as described in [37]. The algebraic loop in the model has been avoided by considering F_x^{sat0} (total longitudinal force expressed in the vehicle frame saturated at nominal F_z) and F_y^{static} (the sum of the lateral forces computed at nominal F_z on each wheel) as the forces used for the load transfer dynamics.

Finally, the lateral forces model is based on the simplified MF model described in [11], expressed by means of the macro-parameters B, C, D, E.

4.4.1 NMPC Algorithm

The goal of the NMPC controller for the virtual driver is to compute a reliable sequence of steering, throttle, brake commands in a prediction horizon, given a tailored cost function. The NMPC algorithm is based on MATMPC [182, 183], described in the previous paragraphs.

In MATMPC, a non-linear programming problem (NLP) is formulated at sampling instant i by applying direct multiple shooting [184] to an optimal control problem (OCP) over the prediction horizon $S = [s_0, s_f]$, which is divided into N *shooting intervals* $[s_0, s_1, \ldots, s_N]$, as follows

$$\min_{\xi_{\cdot|i}, u_{\cdot|i}} \sum_{k=0}^{N-1} \frac{1}{2} \| h_k(\xi_{k|i}, u_{k|i}) \|_W^2 + \frac{1}{2} \| h_N(\xi_{N|i}) \|_{W_N}^2 \tag{4.21}$$

$$s.t. 0 = \xi_{0|i} - \hat{\xi}_0 \tag{4.22}$$

$$0 = \xi_{k+1|i} - \phi_k(\xi_{k|i}, u_{k|i}; p_{k|i}), k \in [0, N-1] \tag{4.23}$$

$$\underline{r}_{k|i} \leq r_k(\xi_{k|i}, u_{k|i}) \leq \overline{r}_{k|i}, k \in [0, N-1] \tag{4.24}$$

$$\underline{r}_{N|i} \leq r_N(\xi_{N|i}) \leq \overline{r}_{N|i} \tag{4.25}$$

where $\xi_{\cdot|i} = (\xi_{0|i}^\top, \xi_{1|i}^\top, \ldots, \xi_{N|i}^\top)^\top$, and $u_{\cdot|i} = (u_{0|i}^\top, u_{1|i}^\top, \ldots, u_{N-1|i}^\top)^\top$, while $\hat{\xi}_0$ represents the measurement of the current state. System states $\xi_{k|i} \in \mathbb{R}^{n_\xi}$ are defined at the discrete arc-length point s_k for $k = 0, \ldots, N$ and the control inputs $u_{k|i} \in \mathbb{R}^{n_u}$ for $k = 0, \ldots, N-1$ are piece-wise constant. Their definitions are given in (4.26) and (4.27). Here, (4.24) is defined by $r(\xi_{k|i}, u_{k|i}) : \mathbb{R}^{n_\xi} \times \mathbb{R}^{n_u} \to \mathbb{R}^{n_r}$ and $r(\xi_{N|i}) : \mathbb{R}^{n_\xi} \to \mathbb{R}^{n_l}$ with lower and upper bound $\underline{r}_{k|i}, \overline{r}_{k|i}$. Equation (4.23) refers to the *continuity constraint* where $\phi_k(\xi_{k|i}, u_{k|i}; p_{k|i})$ is a numerical integration operator that solves (4.28) with initial condition $\xi(0) = \xi_{0|i}$ and returns the solution at s_{k+1}. The time has been included as a state variable with the following ODE $\dot{t} = \frac{1}{\dot{s}}$ to fulfil the minimization of the travel time over the prediction horizon. The full state vector is then given by:

$$\xi = [\dot{x}, \dot{y}, \dot{\psi}, e_\psi, e_y, \delta_f, \gamma_t, \gamma_b, t]^T \tag{4.26}$$

where e_ψ, e_y are orientation and lateral error of the vehicle with respect to the center-line of the path, respectively. The input computed by the algorithm is then:

$$u = [\dot{\delta}_f,\, \dot{\gamma}_t,\, \dot{\gamma}_b,\, \varepsilon_{\text{slip}}\, \varepsilon_{\text{err}},\, \varepsilon_{\text{gg}}]^T \tag{4.27}$$

where $\dot{\delta}_f$, $\dot{\gamma}_t$, $\dot{\gamma}_b$ are the derivatives of the actual input to the vehicle and ε are slack variables. This formulation allows a smooth action of the controller and avoids too aggressive, unrealistic behaviors.

The dynamics equation of the model used in the NMPC algorithm can be compactly written as

$$\xi' = \phi(\xi(s), u(s); p(s)), \tag{4.28}$$

where $p(s) = \left[\zeta(s), \tau_{\text{eng},i}^{\text{MAX,min}}(s)\right]^T$.

The real-time iteration scheme (RTI) [185] is employed to reduce the time required to solve the (4.21) problem. Moreover, a non-uniform grid strategy [186] has been used for lowering the computational burden and let the controller predict a sufficiently long horizon (chosen 400 meters in advance for the specific vehicle).

The cost function for the NMPC is defined as:

$$\begin{aligned} h_k(\xi_k, u_k) &= [\beta, \gamma_t \cdot \gamma_b, \zeta \cdot \gamma_t, t, \dot{\delta}_f, \dot{\gamma}_t, \dot{\gamma}_b, \varepsilon_{\text{slip}}, \varepsilon_{\text{err}}, \varepsilon_{\text{gg}}]^\top, \\ h_N(\xi_N) &= [\beta, \gamma_t \cdot \gamma_b, \zeta \cdot \gamma_t, t, e_y - e_y^{\text{ref}}, \dot{e}_y, e_\psi - e_\psi^{\text{ref}} + \\ &\quad + \beta, \dot{e}_\psi]^\top. \end{aligned} \tag{4.29}$$

The penalty on the vehicle side slip β is used to limit the sliding behavior of the vehicle; simultaneous throttling and braking are penalized by the cost $\gamma_t \cdot \gamma_b$. The $\zeta \cdot \gamma_t$ cost is included to make the controller accelerate smoothly during the final phase of the track corner exit. The objective variable time t is added to minimize the time on the prediction horizon. Smooth control actions are ensured by the objective terms on the inputs. The three slack variables are also adopted to define the *soft constraints* [187], which increase the robustness of the overall procedure. Finally, the terms related to errors e_y and e_ψ, used only as terminal objective variables, are introduced to integrate information about the trajectory over the prediction horizon.

The constraints are defined as

$$
\begin{aligned}
r_k &= [\delta_f, \gamma_t, \gamma_b, \dot{\delta}_f, \dot{\gamma}_t, \dot{\gamma}_b, \varepsilon_{\text{slip}}, \varepsilon_{\text{err}}, \varepsilon_{\text{gg}}, \beta + \varepsilon_{\text{slip}}, \\
&\qquad e_y + \varepsilon_{\text{err}}, (\mu_x \frac{\ddot{x}_{\text{ext}}}{g})^2 + (\mu_y \frac{\ddot{y}_{\text{ext}}}{g})^2 + \varepsilon_{\text{gg}}]^\top, \\
r_N &= [\delta_f, \gamma_t, \gamma_b]^\top
\end{aligned}
\tag{4.30}
$$

where the constraints on δ_f, γ_t, and γ_b are intrinsic bounds of the actual vehicle controls, while those on $\dot{\delta}_f$, $\dot{\gamma}_t$, and $\dot{\gamma}_b$ are added in order to improve the smoothness of the computed inputs and can be used to easily tune the aggressivity of the NMPC driving commands. Additionally, the slack variables have been constrained in order to help the optimization procedure restricting the *search space* of the inputs. The slack variables are used for defining the soft constraints: the first one is introduced on the side-slip of the vehicle and helps the controller to regain control of the vehicle in case of high skidding; the second one is used to correct the trajectory when the vehicle is out of track; the third one instead is designed to make the controller respect the required *gg diagram*, which represent the maximum combined longitudinal-lateral acceleration that can be induced by the combined longitudinal-lateral behavior of the specific tyre spec [188]. μ_x and μ_y are the longitudinal and lateral friction coefficient of the tyres, respectively, whereas the considered accelerations on the vehicle are

$$
\begin{aligned}
\ddot{x}_{\text{ext}} &= \frac{\sum_{i,j} F_{x_{i,j}-F_d^x}}{m} \\
\ddot{y}_{\text{ext}} &= \frac{\sum_{i,j} F_{y_{i,j}}}{m}
\end{aligned}
\tag{4.31}
$$

At the i-th sampling instant, considering that the QP solution is Δu^{i^*}, the control input is updated by

$$
u^{i^*} = u^{i-1^*} + \Delta u^{i^*} \tag{4.32}
$$

The first sample of u^{i^*} is applied to the vehicle, the prediction horizon is shifted forward and the optimization procedure is repeated with updated state measurement.

4.5 Co-simulation platform

The co-simulation platform, represented in the Figure 4.11, is composed of the following subsystems:

- Plant model: a 14 DoF vehicle model reproducing the overall vehicle dynamics behavior;
- Road pavement: a boundary condition module concerning the asphalt condition and computing the tyre-road friction coefficient to reproduce dry, wet, snowy, and icy contact;
- Tyre: MF-Evo tyre model reproducing the tyre dynamic behavior in different thermal and wear conditions;
- Path reference: the track geometrical representation defined by the specific maneuver and employed to compute the cost function.

The maneuver chosen for the current study is the emergency double-lane-change maneuver, generally performed on the highway to overtake another vehicle [189]. The test is commonly adopted because it correlates the ability of controlling the vehicle at the limits of handling with an enhanced safety for the vehicle occupants in scenarios concerning the presence of obstacles on the path [190]. Given the criteria for ideal lane-change path, prescribing a minimal length path with a smooth and continuous curvature at a given vehicle forward velocity, the trajectory of the DLC maneuver is computed without violating the track boundaries and assuring that all the tyres remain always in contact with the road surface (possible lift motions are avoided

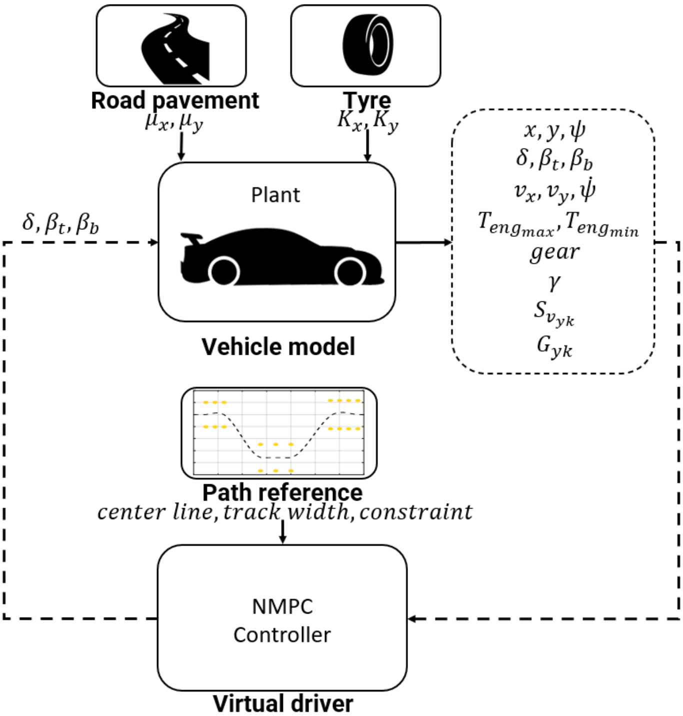

Fig. 4.11 Co-simulaton platform.

with constraints modelled within the maximum load transfers, as described in [191]).

The co-simulation is conducted in MATLAB/Simulink environment, coupling the plant model with NMPC controller and performing the dynamic simulation of the plant model at f_{sim} = 1000 Hz, while the control action is updated by NMPC at f_{ctrl} = 100 Hz. The simulations have been computed on a Windows 10 machine with Intel(R) Core(TM) i7-7700HQ @ 2.80GHz CPU.

4.6 Scenario and results

The knowledge of the instantaneous and potential grip directly on board and in real-time potentially allows the vehicle control logic to maximize the probability of avoiding obstacles and reducing the severity of collisions. To investigate the possible outcomes of a model-based control within a vehicle safety-linked scenario, the authors have performed within the DLC maneuver a complete design of experiment comprehending:

- *Case A:* the adoption of two different sets of NMPC weights (best and global) in the definition of the cost function.
  The best NMPC set of weights addresses the maximum achievable performance of the underlying vehicle plant model, specifically calibrated for a new tyre working in the optimal thermal range in contact with the dry road, whereas the global NMPC set of weights represents the trade-off solution to guarantee ability of the vehicle to complete the DLC maneuver in the worst proposed dynamic scenario, i.e., a worn cold tyre in contact the icy road surface. In this case, the parameters of the plant and the controller models are the same for each simulation;

- *Case B:* the analysis of the vehicle dynamic response in case of different tyre thermal and ageing conditions on the same road and in case of the tyre with a specific thermal and wear state on different pavements. In this case, the parameters of the plant and the controller models are the same for each simulation;

- *Case C:* the possibility to employ the non-linear model predictive controller calibrated with the average set of weights in conditions where the parameters of the controller model can be updated in real-time on the basis of the actual state of the plant model or can be constant and with an estimation on the friction value affected by a percentage error respect the real value.

> This particular scenario has been conducted to highlight the importance of the correct estimation of the parameters of the controller model, potentially aware of the actual knowledge of tyre-road friction. The simulation outputs with average tyre parameters within the controller model have been compared towards the ones obtained with the instantaneous parameters of the co-simulated vehicle plant to put in evidence the importance of the correct information concerning the tyre friction and stiffness for the vehicle dynamics control.

The simulation outputs have been compared in terms of the vehicle trajectory, the forward velocity, the vehicle side slip angle, and yaw angle.

4.6.1 *Case A*

In this section, the impact of two possible sets of weights, defined within the NMPC cost function, is investigated. Both the plant and controller models share the same model parameters of a new tyre in the optimal thermal window in contact with the dry road.

The *best* set of NMPC weights represents the most suitable solution to perform the DLC maneuver with both the plant model and the controller model in the maximum performance conditions of the tyre, corresponding the the maximum dynamic limits of the vehicle. The *global* set of NMPC weights stands for the conservative trade-off solution, calibrated to guarantee the accomplishment of the maneuver in all the possible tyre-linked and boundary conditions, in which the plant and controller models share the same physical parameters (i.e., the performance of the vehicle controller is limited by the worst possible dynamic scenario of a cold and worn tyre in contact with the icy road).

In the Figure 4.12a the trajectories of the vehicle with the *best* (red) and *global* (black) sets of NMPC weights are compared. It is easy to observe that the optimized set of weights allows the vehicle performing at a larger trajectory and achieving significantly higher velocities both in the first part of the curves and at the end of the DLC maneuver (Figure 4.12 b). It is worth highlighting that the *best* set also demonstrates higher side slip and yaw angles (Figure 4.13 a,b), because it is specifically optimized to perform in the scenario of a new optimal tyre in contact with the dry road, therefore allowing the vehicle to reach the actual friction limits. Furthermore, the *best* set allows the vehicle to approach to the DLC manuever and to end the scenario 6.62 and 8.34 seconds before, respectively (Figure 4.13 c).

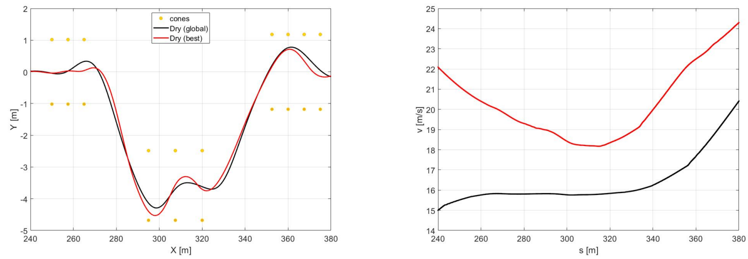

(a) (b)

Fig. 4.12 (**a**) Vehicle trajectory performed in the DLC maneuvers in a different road surface (dry in black, wet in red, snow in blue, and icy in light blue), but with the same tyre (new tyre in optimal range temperature) for a NMPC tuned to better perform the maneuver in all road surface, tyre, and temperature condition. (**b**) Vehicle velocity.

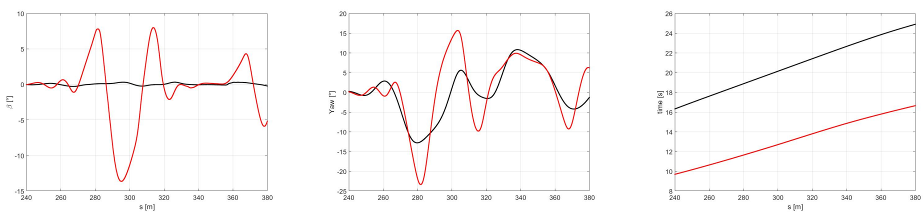

(a) (b) (c)

Fig. 4.13 (**a**) β angle. (**b**) Yaw angle. (**c**) Time.

4.6.2 *Case B*

In this section, only the *global* set of NMPC weights has been employed to compare the dynamic response of the vehicle in two scenarios: (1) different road characteristics (dry, wet, snowy, and icy) with the new tyre within the optimal thermal range, and (2) different tyre thermal and ageing conditions in contact with the dry road. The plant and the controller models share the same physical parameters for each iteration.

- *Scenario B1*
  In the Figure 4.14a it is possible to observe how the vehicle maneuver characterized by the highest friction coefficient (dry pavement) performs the DLC with a largest trajectory and the highest velocity Figure 4.14b in minimum amount of time Figure 4.15c and Table 4.3.

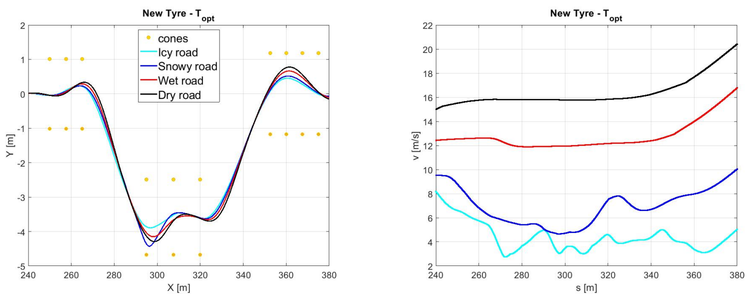

(a) (b)

Fig. 4.14 (**a**) Vehicle trajectory. (**b**) Vehicle velocity.

Since the *global* NMPC set is limited by the most critical dynamic condition (worn cold tyre in contact with the icy road), the Figure4.15a shows higher values in terms of side slip angle for snowy and icy road surfaces, foreseeing the possibility to perform the maneuver in more aggressive way for dry and wet road conditions.

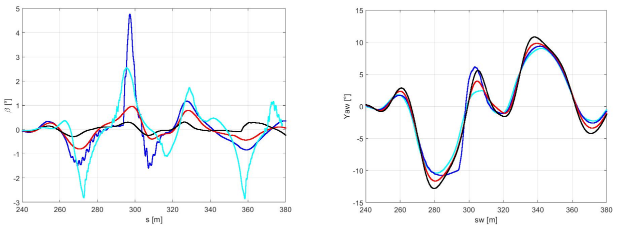

(a) (b) (c)

Fig. 4.15 (**a**) Side slip angle. (**b**) Yaw angle. (**c**) Time.

Table 4.3 Summary of time's maneuver for each scenario.

Road Surface	Time $[s]$
Dry	24.8
Wet	26.2
Snowy	40.8
Icy	51.7

Such a conservative behavior can be motivated by the fact that the *global* set of weights is a result of a trade-off between completely different dynamic scenarios in the respect of vehicle maneuverability and safety.

- *Scenario B2*
  The comparison between a same road condition (dry) performing with different tyre condition (new or worn, in the optimal temperature range, cold or overheated) are shown in the following figure. Regarding the analysis of trajectories, shown in the Figure 4.16a it is possible to observe how they are too similar each other due to the same road pavement, however in the new tyre condition a little largest trajectory has been carried out to achieve an highest velocity Figure 4.16.

The analysis side slip angle show a dependence of β angle with the tyre stiffness, indeed the highest value of β has been performed to highest

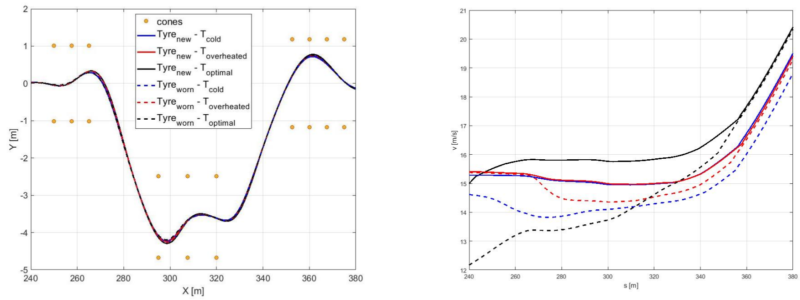

(a) (b)

Fig. 4.16 (**a**) Vehicle trajectory performed in the DLC maneuvers in a dry road, with different tyre condition (New tyre (continuous lines) and worn tyre (dashed lines) in optimal (black), cold (blue), and overheated (red) temperature range. (**b**) Vehicle velocity.

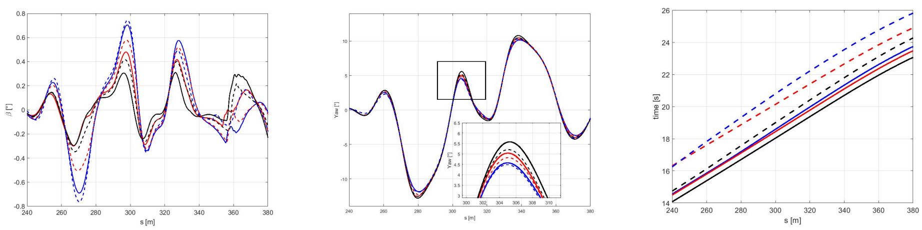

(a) (b) (c)

Fig. 4.17 (**a**) Side slip angle. (**b**) Yaw angle. (**c**) Time.

cornering stiffness Figure 4.17a. Finally, in the Table 4.4 are shown the performing time for each condition.

4.6.3 *Case C*

- *Scenario C1*

  In this paragraph the aim of the authors is to argue the following query: *If the plant and the controller do not share the same model parameters, i.e., the parameters of the controller model are not updated by a specific*

Table 4.4 Summary of time's maneuver for each scenario.

Tyre Condition	Time $[s]$
$New - T_{opt}$	23.0
$New - T_{cold}$	23.7
$New - T_{overheated}$	23.44
$Worn - T_{opt}$	24.24
$Worn - T_{cold}$	25.8
$Worn - T_{overheated}$	24.8

co-simulated estimator of the vehicle parameters and state, and of the tyres' and the road conditions are not known a priori, how a controller model with an average "parameters'" configuration could perform with different plant model employment scenarios within the DLC maneuver? With this purpose, the controller model has been fed with the parameters of friction and stiffness corresponding the mean value of the all possible tyre-road conditions explored.

It is worth highlighting that, as expected, it is not possible to perform the DLC maneuver with the icy road with the above configuration. Indeed, as appears clear in the Figure 4.18, the rear axle achieves the maximum slip ratio, not allowing to complete the simulation in safety.

For this reason, in the following figures, only dry, wet, and snowy road conditions are reported. In the Figure 4.19a,b it is possible to observe how the difference between the three pavement surfaces are less pronounced towards the results discussed in Scenario B. Moreover, the vehicle in contact with the wet road achieves a maximum velocity, even higher than with the dry surface, completing the maneuver in less time Figure 4.20c).

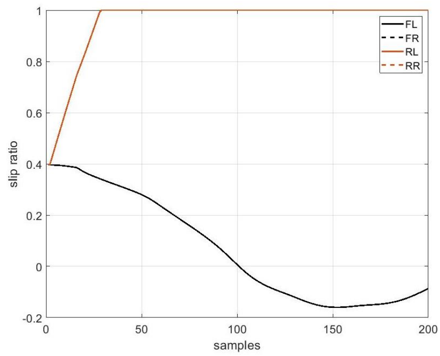

Fig. 4.18 Slip ratio achieved for the four tyres.

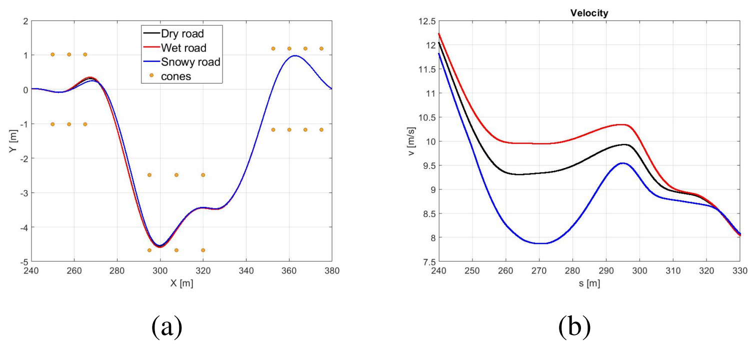

Fig. 4.19 (**a**) Vehicle trajectory performed in the DLC maneuvers in a dry, wet, and snow road, with new tyre in optimal range temperature. (**b**) Vehicle velocity

The reason for such behavior can be conducted to the conservative control action, particularly visible in dry boundary condition, since the absolute difference in terms of the friction limit is particularly high between the plant and the controller models in this scenario. Indeed, in the Figure 4.20a the the side slip angle is similar for three conditions explored. Furthermore, even the maneuver in snow conditions is achieved in a comparable time period, since the friction limit of the average controller model is similar to the one of the plant model working in snowy boundary conditions Figure 4.20b.

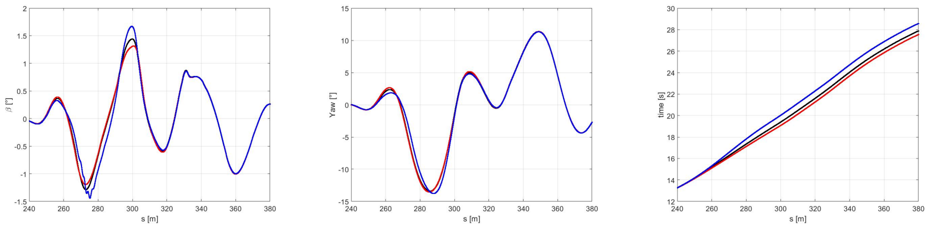

(a) (b) (c)

Fig. 4.20 (**a**) Side slip angle. (**b**) Yaw angle. (**c**) Time.

- *Scenario C1*

  Remarking that an accurate online friction coefficient estimation becomes absolutely necessary to allow exploiting the vehicle dynamics in maximum performance conditions within a combined DLC maneuver, in this paragraph the aim of the authors is to argue another possible query: *In a real scenario, where an onboard tyre-road friction estimator able to estimate (among others) the grip parameter with a certain degree of accuracy and to update the control model parameters in run-time, is available, how a controller model with a percentage error concerning the vehicle instantaneous conditions could perform within the same maneuver?*

  With this purpose, the parameter concerning the tyres' friction of the controller model has been considered with an intrinsic error with a supposed standard deviation of $\pm 15\%$ respect to the actual grip value of the vehicle plant model.

It is worth noting that in a scenario where the grip factor is overestimated, the controller with the global configuration of the cost function computes more aggressive control actions leading to out-of cones trajectories and undesirable sliding effect. To avoid this issue, a robust global configuration has been introduced in order to let the controller being effective in managing the vehicle behavior in overestimated grip-linked scenarios. The above new configuration leads to more conservative actions and, consequently, to a considerable loss of performance in terms of velocity. In particular, the loss in performance in terms of the average speed (in percentage) in the four cases analyzed has been objectively quantified in Table 4.5.

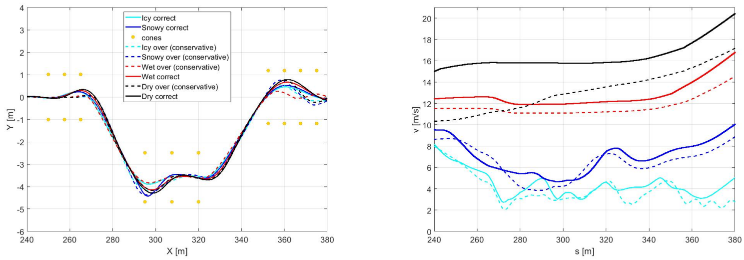

(a) (b)

Fig. 4.21 (**a**) Vehicle trajectory performed in the DLC maneuvers in conservative vs global configuration. (**b**) Vehicle velocities

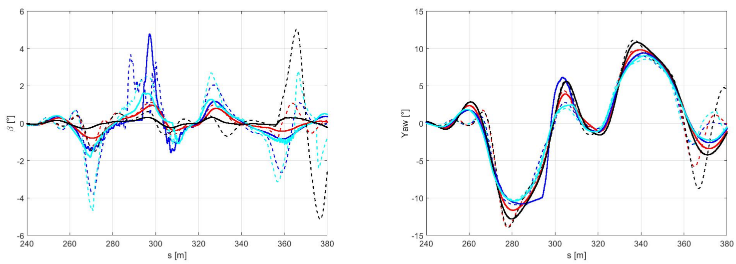

(a) (b)

Fig. 4.22 (**a**) Side slip angles. (**b**) Yaw angles.

In Figures 4.21 and 4.22, the performance obtained by the two configurations in terms of trajectories, speed, side-slips, and yaw angles are also compared. Notably, the side-slip in Figure 4.22 reaches peaks of 5 degrees, confirming that the configurations obtained controls the vehicle at the limit of handling.

Table 4.5 Summary of the difference in velocity mean values (%) and lateral error assumed for each road scenario.

Road Surface [−]	Friction Estimation [−]	Longitudinal Velocity [%]
Icy	correct	–
Icy	overestimation	−16.02
Snowy	correct	–
Snowy	overestimation	−8.36
Wet	correct	–
Wet	overestimation	−8.30
Dry	correct	–
Dry	overestimation	−21.00

Chapter 5

Application of friction estimation algorithm in vehicle following control strategy

5.1 Introduction

In the previous chapters, the role of the tyre in vehicle dynamics and especially the concept of potential friction and instantaneous friction has been extensively discussed. In particular, the friction coefficient has been characterized and it has been seen how this changes during the life cycle of the tyre in relation to the aging and wear of the tyre itself and in relation to the boundary conditions and environmental conditions. Specifically, in Chapter 2 the coefficient of friction and the maximum explicable forces of the tyre were characterized as a function of sliding speed, temperature, wear, road texture and in dry and wet conditions. In Chapter 4 we introduced the concept of state estimator and its importance in control systems, since the higher and more accurate the knowledge of the state of the system we want to control, the more effective will be the control strategy. In Chapter 4, instead, we investigated how the variation of the tyre properties affect the vehicle dynamics and the controller decisions. For these reasons, this chapter will describe a first control architecture responsible for the longitudinal dynamics of the vehicle chassis, composed of two ADAS functionalities—namely Adaptive Cruice Control (ACC) and Autonomous Emergency Braking (AEB)—in addition to the Antilock Braking System (ABS), which is road-grip aware in the sense that it is able to properly regulate the vehicle motion on the base of the on-line estimation of the road friction coefficient per single tyre.

ADAS for the safe automatic driving mostly tackles the stabilization of the chassis longitudinal motion and the actuation of the emerging braking via a wide variety of control techniques. Among others, Model Predictive Control (MPC) has been effectively used in [192–195] in order to synthesize an ACC system. Regarding the AEB, typically event-based controllers have been realized through a continuous evaluation of the braking distance [196, 197] or the collision time [198]. Alternative formulations can be found in [199], where the authors classify the collision risk upon the definition of potential fields, or in [200] where an impedance controller is synthesized, thus resulting in a time based controller. Some ADAS combine ACC and AEB strategies for multiple driving situations: in [201] a Linear Quadratic Regulator (LQR) works jointly with a Time-To-Collision (TTC)-based logic and in [202] a Proportional-Integral-Derivative (PID)-based velocity control embeds a continuous time collision avoidance mechanism with the aim of reducing excessive jerk. More complex architectures can be found in [203, 204], where nonlinear MPC and reinforcement learning formulations have been designed for safely steering the longitudinal vehicle's dynamics.

Consider a front-wheel driven vehicle where the propulsion is obtained through an electric engine. Moreover assume the vehicle is equipped with proprioceptive sensors for the measurement of its state variables (e.g., chassis velocity, acceleration, yaw rate, and tyres' angular velocities), as well as with exteroceptive sensors (e.g., radar, camera, lidar, or a combination of these) for the sensing of the external environment and for the mapping of external obstacles (details on sensing technologies can be found in [205] and the corresponding references).

The aim of this Chapter is to describe a methodology capable to perform the autonomous vehicle-following process in a safe, controlled and comfortable manner even in poor weather conditions, like ice, snow and heavy rain, starting from the information available thanks to a computationally cost effective model-based tyre-road friction coefficient technique. The data from proprioceptive sensors are collected in run-time, processed with the physical model-based estimator and, then, employed in loop with a vehicle control strategy. From the point of view of the control, the objective is to develop grip-aware functionalities in order to improve driving performance and safety, starting from the strategies for ACC, AEB and ABS longitudinal maneuvers, leveraging the on-board estimation of the road conditions.

In other words, a new model-based technique is proposed for real-time road friction estimation under different environmental conditions. The proposed technique is based on both bicycle model to evaluate the state of the vehicle and a tyre Magic Formula model based on a slip-slope approach to evaluate the potential friction. The results, in terms of the maximum achievable grip value, have been involved in autonomous driving vehicle-following maneuvers, as well as the operating condition of the vehicle at which such grip value can be reached. The effectiveness of the proposed approach is disclosed via an extensive numerical analysis covering a wide range of environmental, traffic, and vehicle kinematic conditions. Results confirm the ability of the approach to properly automatically adapting the inter-vehicle space gap and to avoiding collisions also in adverse road conditions (e.g., ice, heavy rain).

5.2 Friction estimation

In the Chapter 2 has been described that the tyre friction forces change during its life cycle due to temperature, wear, road surface etc. It is common knowledge that the tribological characteristics of an asphalt can vary significantly depending on the distributed uniform dry, wet, snow or icy conditions (linked to meteorological aspects), or on the presence of the eventual local singularities as oil spots, puddles, kerbs or potholes (linked to local maintenance conditions of the road surface). In order to guarantee the optimum employment of the advanced functionalities of the autonomous driving logic, besides the information concerning the actual friction condition of the road surface, it is even more important providing the potential friction coefficient and the kinematic conditions, in terms of the tyre-road interaction slip ratio quantity. Attempts to account for the road conditions into specific ADAS driving features have only recently been developed; research of the tyre-road friction estimation is a topic that has been extensively addressed and the study is continuing to this day. According to [206], it is possible to divide the different approaches on friction estimation into two main groups: experiment-based and model-based approaches.

The experimental based methods use additional sensor measurement as optical or acoustic sensors and cameras to evaluate the friction based on the fact that wet asphalt is dark grey with a higher clarity of texture than dry asphalt [207]. Moreover, such methods employ acoustic sensors to classify the road surface condition exploiting the noise, as well as, tyre tread sensors to estimate the tyre-road friction as a function of the tread deformation, caused by the total force acting on the tyre. The disadvantages associated with this category lie in the high frequency of these sensors get dirty, and therefore distort the results. In addition, the vehicles are generally not equipped with the sensors mentioned above and are difficult to maintain.

With regard to the model-based group, the friction information is evaluated thanks to the mathematical models describing the vehicle system and its subsystems, starting from the information, measured by the sensors installed on the vehicle. Such methodology has demonstrated to be able to evaluate the actual grip in the most environmental condition, but not the potential grip. In

[167], the authors experimentally evaluate a set of parameters, as peak friction, interaction shape and curvature factors, for different road environmental condition (dry, snow, ice) to estimate the tyre stiffness. Then a run-time switch selects the set of parameters in memory corresponding to the current stiffness of the tyre, leading to evaluate the potential grip.

The limit of this approach is dictated by the number of parameters to be stored in the memory, able to describe the different asphalt conditions [208]. Differently from the [167], the friction peak value has been researched imposing relatively large magnitudes of braking/accelerating or steer inputs to achieve sufficient variations in tyres' dynamic responses. To this purpose, a different speed control strategies have been developed for the front and rear wheels in order to identify the stiffness and the tyre road friction coefficient without severely influencing vehicle forward speed. However, these maneuvers may not be practical in every vehicle operating condition, as in [209], in which the tyre-road friction estimator has been activated when the vehicle reached constant speeds. The latest methodology belonging to model-based approaches is the slip-slope [210], based on the assumption that in small slip ranges the correlation between slip and μ could be represented by a linear function, and at higher values of slip ratio the normalized longitudinal interaction force is assumed to saturate. The potential friction coefficient can be then evaluated starting from knowledge of the slope of the tyre-road interaction curve even from low slip values, obtainable during not particularly aggressive driving conditions, employing linear regression models.

5.3 In-Vehicle road-grip estimation

5.3.1 From Vehicle Sensors to Tyres' State

In recent years the number of sensors installed on vehicles has increased exponentially, facilitating the modelization of the entire system towards the target to consider the standard-instrumented vehicle as a mobile laboratory.

Indeed, starting from the acquisition of the physical signals coming from all the sensors installed, employing currently widely-available and affordable mobile calculators, it is possible to properly process the time-evolving dynamic quantities with the aim to feed the real-time state estimators directly on-board. Furthermore, starting from the global quantities referring to the vehicle total behavior, it is currently possible to evaluate even the kinematic and dynamic states of its sub-components, as tyres. The developed algorithm, based on the T.R.I.C.K. methodology described in [44], allows us to evaluate in a specifically dedicated on-board module the fundamental kinematic and dynamic quantities for the tyre characterization in real time, starting from the experimental signals available within the vehicle CAN bus (Controller Area Network) and s-motion measurement or, as the case in exam, employing a specific set of sensors pre-configured on the vehicle. Such methodology also allows us to evaluate the potential of an estimation process in terms of tyre interaction curves, such as in [211].

The originally designed model, described in [44], referred to a quadricycle vehicle fully described from the dynamic point of view. Since the study under analysis aims at simulating the emergency braking manoeuvres et similia, involving only the vehicle longitudinal dynamics, the model can be simplified considering its plane of symmetry **xz** (ISO reference system). Taking into account the above hypothesis, the vehicle can be represented as a bicycle model, whose constitutive equations are described by 3 degrees of freedom within the reference plane **xy**. The above assumption allows us to reduce also the analytical computational cost linked to the model state evaluation per step, as well as the number of parameters to be identified in order to physically reproduce the model dynamics concerning the longitudinal maneuvers, object of investigation. The simplified vehicle model, able to evaluate the kinematics and the dynamics at each axle, feeds the specifically designed logic of the control system providing both actual and potential friction coefficient in run-time.

To perform the analyses, the following modelling and environment assumptions have been considered:

- The road is modelled completely flat with eventual banking and local geometrical effects (i.e., potholes, kerbs, micro- and macro- roughness) absent.

- The tyre is modelled only in terms of its kinematic-dynamic transfer function without taking into account its eventual transient dynamics. Furthermore, the multi-physical effects, as thermal or wear abrasive and degradation influences, have not been taken into account at the current stage.

- Since the vehicle is involved in analyses concerning only the longitudinal dynamic maneuvers and considering the vehicle body symmetry hypotheses, the steering angle signal is assumed to be always zero and, therefore, it is not employed within the modelling and the estimation of the vehicle state.

- The vehicle is described only in terms of its intrinsic global geometric and mass-inertia parameters. The longitudinal load transfer is considered taking into account the position of the vehicle body centre of gravity.

- The vertical load distribution on each axle is evaluated starting from the static load data, load transfers due to the geometric position of the vehicle body centre of gravity within the **xz** plane and the aerodynamic force. The estimation of the tangential interaction forces, due an intrinsic non-linearity of each tyre system, need an additional convergence algorithm for a correct partition of the global longitudinal force, located at the centre of gravity, into its two contributes based on the front and on the rear axles. Indeed, starting from the vertical loads calculated at each axle the convergence algorithm evaluates the above longitudinal forces, consistent with the vertical loads applied, the kinematics evaluated and the intrinsic dynamic characteristics of a pre-calibrated tyre (neglecting the tyres' transient behavior at the current stage).

- The suspensions and steering system kinematics and compliances have been taking into account by acquiring the invariable KC curves by means of physical bench testor as an output of simulations performed by means of a multibody model.

The inputs of the T.R.I.C.K.-based methodology, optimized for the longitudinal vehicle dynamics estimation, comprise the following signals acquired thanks to the sensors acquired and processed directly on-board:

- Wheels' angular velocity (rad/s).
- Longitudinal velocity evaluated at the vehicle's centre of gravity (m/s).
- Longitudinal acceleration evaluated at the vehicle's centre of gravity (m/s^2).
- Throttle position (%).
- Braking position (%).

The model outputs, referring to the axle kinematic and dynamic quantities as well as to the additional, are reported below:

- Axles' slip ratio (-).
- Axles' vertical interaction force (N).
- Axles' longitudinal interaction force (N).
- Axles' actual friction coefficient (-).

Since the double track model, i.e. since the dynamics of the vehicle axle, and analyzing a longitudinal maneuvers, the assumption in [37] related to consider the left and right gear ratio of the steering system almost equal, small steering angles and negligible of lateral load transfer and the body roll effect are accepted. Due to the vehicle body symmetry hypotheses made to develop a single track model, the forces acting on the tyre have been considered equal. Therefore, the forces acting on the single tyres of a single track model are equal to the forces of the entire axle. The vehicle model and the reference system considered are shown in Figure 5.1.

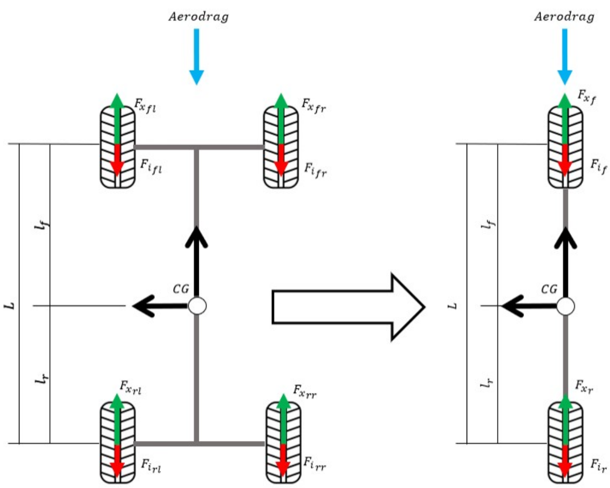

Fig. 5.1 Friction Estimator: Vehicle model and reference system in which the **z** axis is perpendicular to the road equivalent plane **xy**.

In order to evaluate the vertical forces, the loads acting on axles in a stationary condition ($v = 0$ and $a = 0$), called ”static loads", W_f and W_r, have to be evaluated. Such values depend on the position of the vehicle body centre of gravity:

$$W_f = \frac{mgl_r}{L}, \tag{5.1}$$

$$W_r = \frac{mgl_f}{L}. \tag{5.2}$$

For the longitudinal load equation [37], the load transfer are:

$$\Delta F_z = \frac{mha_x}{l}. \tag{5.3}$$

The aerodynamic downforces are expressed by following equation:

$$Fz_{aero_i} = \frac{1}{2}\rho A_v v^2 C_{z_i}, \tag{5.4}$$

with $i = [1,2]$ are defined the axles (respectively front and rear).

Therefore, the axles vertical loads result equal to:

$$F_{z_i} = -(W_i - \Delta F_z + Fz_{aero_i}). \tag{5.5}$$

The effect due to the inertia resistance of the axles is equal to:

$$F_{inertia_i} = \frac{I_w \dot{\Omega}_i}{R_{r_i}}. \tag{5.6}$$

The longitudinal interaction forces can be estimated starting from the information regarding the velocity estimated at the vehicle centre of gravity, acquirable by means of specific sensors or employing a model-based technique, taking into account the vehicle kinematics and the vertical load estimated at each wheel hub [212]. Therefore, in order to obtain the axle forces, the kinematic and load vehicle state estimator provides the accurate vehicle speed v_x, the longitudinal acceleration a_x, the wheel speed Ω, the inclination angle (IA) and the normal load F_z.

To this purpose, the global longitudinal dynamic equilibrium of the vehicle has been implemented considering axles' longitudinal forces as given by sums of singular tyres' forces, distributed equally between the left and the right side:

$$F_x = F_{x_l} + F_{x_r}, \tag{5.7}$$

in which the contribution of the single tyre, for symmetry hypothesis, is assumed to be equal to:

$$F_{x_i} = \frac{F_x}{2}. \tag{5.8}$$

The longitudinal interaction forces is a non-linear function of longitudinal acceleration, normal loads, inclination angle, longitudinal speed evaluated at the contact point, wheel speed and longitudinal spindle velocity:

$$F_{x_{i,j}} = f(a_x, F_{z_i}, v_{x_{CP_{i,j}}}, IA_{i,j}, \Omega_{i,j}, v_{x_{spindle_{i,j}}}). \tag{5.9}$$

The $v_{x_{CP}}$ has been evaluated as:

$$v_{x_{CP_{i,j}}} = R_{i,j}\Omega_{i,j}, \tag{5.10}$$

with $R_{i,j}$ has been assumed the rolling radius as:

$$R_{i,j} = f(F_{z_{i,j}}, IA_{i,j}, \Omega_{i,j}). \tag{5.11}$$

Finally, the slip ratio (λ) is:

$$\lambda_{i,j} = \frac{v_{x_{CP_{i,j}}} - v_{x_{spindle_{i,j}}}}{v_{x_{spindle_{i,j}}}}. \tag{5.12}$$

5.3.2 On-Board Estimation of Actual and Potential Friction

The tyre model parameters, employed within the estimation of the potential friction coefficient, depend on the parameters characterized and identified on the road characteristics where the experimental activities took part. Starting from the pre-calibrated set parameters of the tyre model, depending, in its turn, on the peculiar dynamic set of equation chosen to describe the tyre dynamics, and on the actual grip quantity obtainable from the vehicle state information, the potential friction coefficient achievable by each tyre is evaluated. The potential friction quantity is assumed reachable varying only the slip ratio quantity (i.e., relative velocity within the tyre-road interface) with all other operating conditions remaining the same (wheel alignment, vertical load and wheel spindle longitudinal speed). There are different approaches to tyre modelling in the literature, which can be both physical and empirical. Several authors refer to the tyre modelling using the Finite Element Method (FEM), adopted to evaluate static characteristics or to the multi-body tyre approaches, as [56–58], commonly adopted to study dynamic phenomena on uneven surfaces. Although, the above modelling techniques should be evaluated carefully to the purpose of their employment within the embedded on-board control electronics due to their particularly significant computational cost. It becomes, therefore, necessary the adoption of simpler modelling approaches, as semi-empirical and analytical models [47], whose computational cost is compliant with the capabilities of the modern on-board systems.

The typical tyre characteristics curve is described in Figure 5.2, where three different regions of tyre working range are represented.

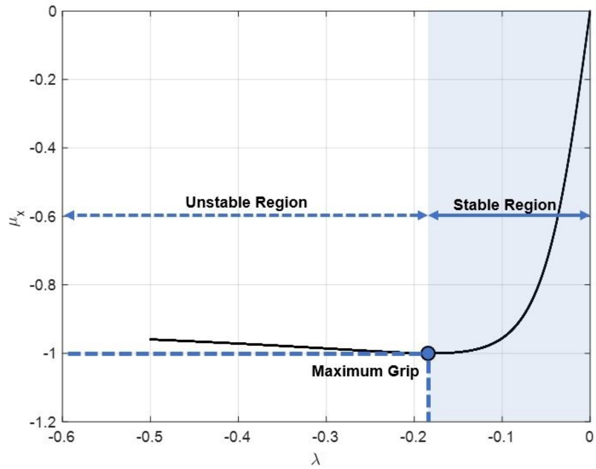

Fig. 5.2 Tyre characteristics curve and potential friction coefficient.

The ratio between longitudinal and vertical forces gives the instantaneous friction coefficient, i.e., the actual run-time coefficient between road surface and tyre, expressed as follows:

$$\mu_{x_{i,actual}} = \frac{F_{x_i}}{F_{z_i}}. \tag{5.13}$$

The actual friction coefficient μ_x depends both on the condition of the asphalt and on the peculiar operating conditions the tyre is stressed with (i.e., vertical load, wheel alignment, slip ratio, longitudinal speed). Therefore, each tyre operating point, describable by the actual friction coefficient μ_x and the corresponding slip ratio λ, can be represented in Figure 5.3, the point 1.

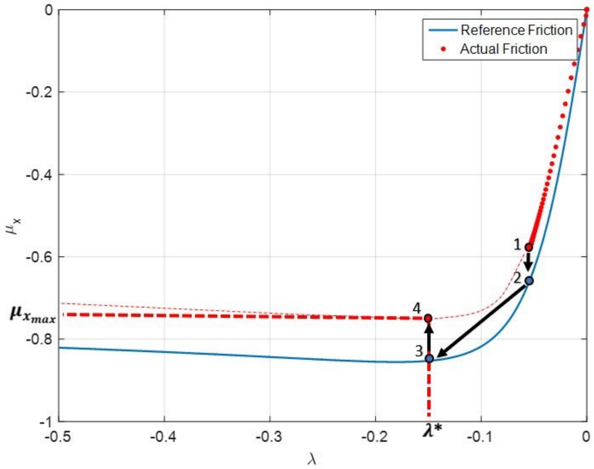

Fig. 5.3 Procedure to evaluate potential friction coefficient.

The eventual changes in terms of friction coefficient within the tyre-road interface are assumed to be referred only to the road surface, since the tyre has been especially pre-calibrated on a reference asphalt surface. Assuming a linear behaviour of the tyre in the typical working conditions of the vehicle, a linear proportion between the reference tyre-road and the actual tyre-road friction coefficients can be assumed. Starting from the actual friction coefficient quantity, obtained in particular working conditions of the vehicle and therefore of the tyre, and from the model parameters already able to properly represent the tyre dynamics in run-time, the potential friction is evaluated in the following steps, represented in Figure 5.3:

- Once the actual friction coefficient (point 1) has been calculated (5.13), the equivalent grip for the reference tyre-road (point 2) can be evaluated:

$$\mu_{x_{i,refRoad}} = \frac{F_{x_{i,refRoad}}}{F_{z_i}}, \tag{5.14}$$

- Furthermore, starting from the tyre model parameters calibrated on a reference road surface, the model is able to provide a valuable output in terms of the maximum longitudinal force, achievable for the same conditions of vertical load, wheel alignment and vehicle longitudinal speed, at the optimal value λ^* of the slip ratio (point 3 in Figure 5.3):

$$\mu_{x_{i,refRoad}}^{max} = \frac{F_{x_{i,refRoad}}^{max}}{F_{z_i}}, \tag{5.15}$$

- The potential friction coefficient (point 4) is obtainable, using the proportionality criterion already adopted for the point 2, assuming the linearity of the tyre behavior within the working conditions of the vehicle, as follows:

$$\widehat{\mu}_{x_i} = \frac{\frac{F_{x_i}}{F_{z_i}}}{\frac{F_{x_{i,refRoad}}}{F_{z_i}}} \mu_{x_{i,refRoad}}^{max}. \tag{5.16}$$

In Figure 5.4, the overall architecture of the developed model is shown. In particular, starting from the sensor-acquired input channels (on the left), the kinematic and load estimator calculate the vehicle state up to the kinematics on the wheel hubs. Then the tyre model evaluates the state at the tyre-road interface, and, using the above information, the actual and potential friction estimator module.

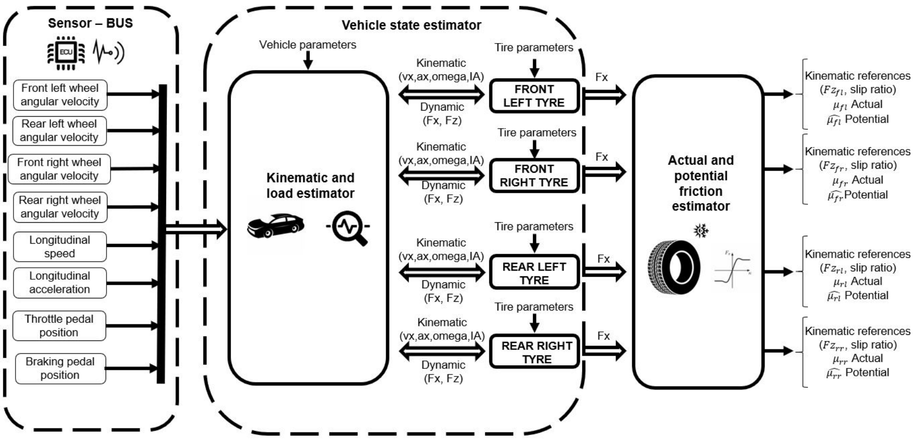

Fig. 5.4 Architecture of the vehicle state estimation system.

5.4 Control module

The road-grip aware driving functionalities for the four-wheel electric vehicle, leveraging the in-vehicle road grip estimate as in Equation (5.16) is described in this section. Specifically $\widehat{\mu}$ has been chosen as $\widehat{\mu}_{x_i}$ with $i = 1$ if only the front wheel drive is used, and as a weighted sum of $\widehat{\mu}_{x_i}$ with with $i = 1, 2$, if both axles are used for actuation. The control module is compose by a predictive ACC and by an AEB.

To achieve the above mentioned tracking capability, the ACC system has not only to safely adjust the ego-vehicle speed to approach the velocity of the leading vehicle, but it has also to keep the vehicle spacing to an expected value d_{des} that must be adaptable on the base of the estimated road grip, as:

$$d(t) \to d_{des}(t, \mu), \tag{5.17}$$

$$\Delta v(t) \to 0, \tag{5.18}$$

where $v(t)$ is the ego vehicle velocity measured on-board by proprioceptive sensors, while $d(t)$ is the distance between the ego vehicle and the leading one and $\Delta v(t)$ is the relative velocity w.r.t. the leading v_{lead}, computed leveraging the on-board exteroceptive sensors. Here, the grip-aware desired space gap d_{des} can be set according to the following the headway time rule [213]:

$$d_{des}(t,\mu) = d_0 + \tau_H(\mu)v(t), \tag{5.19}$$

where d_0 is the constant spacing at standstill and $\tau_H(\mu)$ is the headway time to be properly adapted on the base of the road friction coefficient to be on-line estimated.

In order to further reduce the risks of crashes, the ACC works jointly with the AEB that, sharing the same on-board sensors, continuously monitors the area in front of the car, automatically detects a risk and hence activates the vehicle braking system (via the ABS, Anti Brake-locking System) decelerating the vehicle with the purpose of avoiding or mitigating a possible collision. It follows that, unlike the ACC, the AEB is activated only when a collision index highlights the possibility of a crash. Here, we exploit the well-known TTC index [214] and the AEB is hence activated if its value is under some threshold depending on the estimate road conditions, as:

$$TTC = -\frac{d(t)}{\Delta v(t)} < TTC_{th}(\mu), \quad \text{being } \Delta v(t) < 0. \tag{5.20}$$

When the emergency braking is requested by the AEB, the maximum torque is applied to the wheels via the ABS control chain. The wheel actuation systems decreases the longitudinal slip value, thus generating a braking force on the chassis. However, if the slip ratio is below the optimal value, depending on the actual road condition, the dynamics could become unstable with a consequent lock of the wheels. It follows that an efficient control strategy for automatic safe braking during emergency has to adapt the optimal slip value on the base of the estimation of the grip in order to enhance the performance of the ABS, and thus of the overall vehicle.

The above grip-aware ACC, AEB and ABS functionalities have been embedded into the on-board control architecture depicted in Figure 5.5. The on-line road-grip estimate module implemented on-board firstly calculates the actual friction conditions, estimating the tyre-road interaction kinematics and dynamics, and then it provides the actual and the potential friction coefficients per each tyre. This estimate, indicated in what follows as $\widehat{\mu}$, is hence exploited to control the longitudinal dynamics of the ego vehicles via grip-aware ACC, AEB and ABS controllers. Note that a supervisor (the so called decision-making unit in Figure 5.5) is responsible of classifying the specific driving conditions and of choosing the required driving functionality accordingly [215].

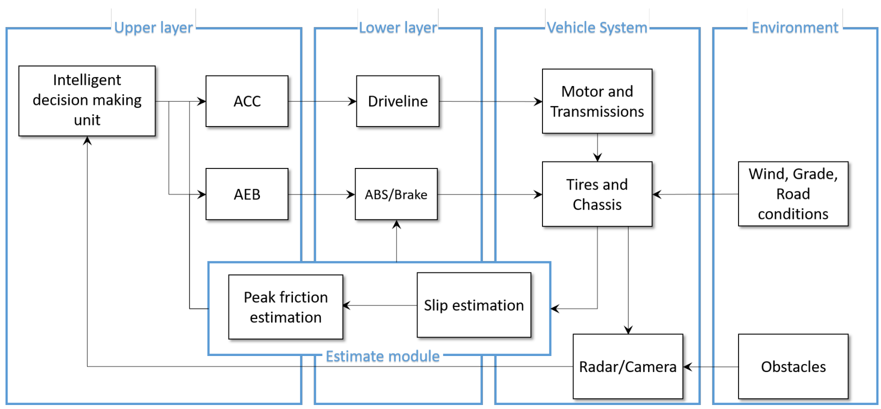

Fig. 5.5 On-board Control Architecture.

5.4.1 ACC Design

The ACC is responsible for longitudinal tracking in the autonomous vehicle-following process, so that the vehicle velocity is regulated to a desired speed, while maintaining a safety distance from the preceding vehicle, often named as leading vehicle in the technical literature. The controller is hierarchical and it is composed of a double feedback layer. Namely, the upper-control layer, acts as a reference governor generating the appropriate acceleration profile to be tracked, while also complying additional constraints related to driving comfort and energy consumption. The lower level is responsible for commanding the actuators and, hence, its robust design depends on the specific vehicle configuration.

Here, we focus on the design of the upper layer controller generating reference trajectories able to also improve driving safety leveraging the on-line prediction of road conditions. The predicted ACC is designed following the Model Predictive Control (MPC) - described in the Chapter 4 - approach allowing the continuous constrained optimization of the vehicle longitudinal dynamics. In contrast to the LQR, the MPC solves the problem over a finite time window, or prediction horizon, to make it tractable online. The optimization generates a sequence of control inputs to be imposed over the control horizon, but, according to the receding horizon principle, only the first element of the sequence is effectively applied to the plant. New inputs are received at the following time intervals and the procedure is iteratively repeated.

In order to design the controller, let us define a control oriented mode according the vehicle-following paradigm: [216]:

$$\dot{d}(t) = \Delta v(t), \tag{5.21}$$

$$\dot{\Delta} v(t) = a_{lead}(t) - a(t), \tag{5.22}$$

where $d(t)$ is the distance between the leading vehicle and the ego vehicle, while $\Delta v(t) = v - v_{lead}$ is their relative velocity (while a_{lead} is the leading acceleration) and the velocity of the chassis of the ego vehicle $v(t)$ undergoes the following longitudinal dynamics: [216]:

$$\dot{v}(t) = a(t), \tag{5.23}$$

$$\dot{a}(t) = \frac{1}{\tau}(-a(t) + u(t)), \tag{5.24}$$

where $a(t)$ is the actual vehicle acceleration and τ the driveline time constant and $u(t)$ the acceleration input.

Define now the distance error with respect to the desired space gap as $e(t) = d(t) - d_{des}(t)$, where the spacing policy $d_{des}(t)$ is computed as in Equation (5.19) with the head-way time being the following piece-wise function of the road grip:

$$\tau_H = \begin{cases} \widetilde{\tau}_H/0.2 & \widehat{\mu} \leq 0.2 \\ \widetilde{\tau}_H/\widehat{\mu} & 0.2 < \widehat{\mu} \leq 1 \\ \widetilde{\tau}_H & \widehat{\mu} > 1 \end{cases} \tag{5.25}$$

where $\widehat{\mu}$ is the estimated maximum available grip and $\widetilde{\tau}_H$ is the constant headway for an ideal dry road [195]. Note that Equation (5.25) ensures that the safety distance increases as the peak road friction decreases.

Let the state vector $x(t)$ and the output vector $y(t)$ as:

$$x(t) = [d(t)\ \Delta v(t)\ v(t)\ a(t)]^T \in \mathbb{R}^4 \tag{5.26}$$

$$y(t) = [e(t)\ \Delta v(t)\ v(t)\ a(t)]^T \in \mathbb{R}^4 \tag{5.27}$$

and $w(t) \in \mathbb{R}$ as the leader acceleration, i.e. $w(t) = a_{lead}(t)$. The system in Equations (5.21) and (5.23) can be easily recast in the following state space representation:

$$\dot{x}(t) = Ax(t) + Bu(t) + Ww(t), \tag{5.28}$$

$$y(t) = Cx(t) - Z, \tag{5.29}$$

being

$$A = \begin{bmatrix} 0 & 1 & 0 & 0 \\ 0 & 0 & 0 & -1 \\ 0 & 0 & 0 & 1 \\ 0 & 0 & 0 & -\frac{1}{\tau} \end{bmatrix}, B = \begin{bmatrix} 0 \\ 0 \\ 0 \\ \frac{1}{\tau} \end{bmatrix}, W = \begin{bmatrix} 0 \\ 1 \\ 0 \\ 0 \end{bmatrix}, C = \begin{bmatrix} 1 & -\tau_H & 0 & 0 \\ 0 & 1 & 0 & 0 \\ 0 & 0 & 1 & 0 \\ 0 & 0 & 0 & 1 \end{bmatrix}, Z = \begin{bmatrix} d_0 \\ 0 \\ 0 \\ 0 \end{bmatrix}. \tag{5.30}$$

However, in order to synthesize the MPC controller, Equation (5.28) are discretized with a fixed sample time T_s leveraging the zero-order-hold method, thus yielding:

$$x(k+1) = Ax(k) + Bu(k) + Ww(k), \tag{5.31}$$

$$y(k) = Cx(k) - Z, \tag{5.32}$$

where, with an abuse of notation, the discrete-time system matrices have been labelled as the ones of the continuous-time model. Moreover, by augmenting the state vector as $[x(k)\ u(k)]^T$, we can resort to the following off-set free formulation as:

$$x(k+1) = \begin{bmatrix} A & B \\ 0 & 1 \end{bmatrix} x(k) + \begin{bmatrix} B \\ 1 \end{bmatrix} \Delta u(k) + \begin{bmatrix} W \\ 0 \end{bmatrix} w(k), \tag{5.33}$$

$$y(k) = \begin{bmatrix} C & 0_{4\times 1} \end{bmatrix} x(k) - Z. \tag{5.34}$$

Note that the above formulation is really beneficial since the increment $(\Delta u(k)/T_s)$ is the chassis jerk in discrete time, which is the crucial index for the driving comfort.

The ACC problem in Equation (5.17) is solved when system in Equation (5.33) is regulated to the origin while fulfilling at the same time additional tracking, comfort, consumption and safety constraints for all times k.

With respect to safety, road-grip constraints are introduced for the desired and actual acceleration, as:

$$u_{min}(\widehat{\mu}) \leq u(k) \leq u_{max}(\widehat{\mu}), \tag{5.35}$$

$$a_{min}(\widehat{\mu}) \leq a(k) \leq a_{max}(\widehat{\mu}), \tag{5.36}$$

with $a_{max}(\widehat{\mu}) = u_{max}(\widehat{\mu}) = \min(2, \widehat{\mu}g)$, $a_{min}(\widehat{\mu}) = u_{min}(\widehat{\mu}) = \max(-4, -\widehat{\mu}g)$, where $\widehat{\mu}$ is the estimated maximum available grip and g the acceleration of gravity. The saturation values (i.e., 2 and -4) are chosen as upper and lower limit, related to the ideal value for the grip set as 1 [195].

The constraints on the spacing and the maximum velocity are given as:

$$d_{min} \leq d(k) \leq d_{max}, \tag{5.37}$$

$$v(k) \leq v_{max}, \tag{5.38}$$

where d_{min} is set to the standstill value d_0 (see Equation (5.19)) and v_{max} is the maximum admissible speed depending on the legal requirements on the specific traveled road (urban, extra-urban, etc.). Note that this information can be acquired from a map-based on board service leveraging the GPS (Global Positioning System).

5.4.2 Autonomous Emergency Brake

Road accidents and fatalities statistics are reported annually, showing the relation between accidents and drivers behaviour [2, 1]. Moreover, the authors in [217] showed that the collision risk increases with the degradation of road conditions. The Autonomous Emergency Brake is one of the most effective driving functionalities for collision prevention and social cost lowering linked to accidents. Nonetheless, EuroNCAP tests are being carried on roads with friction peaks of at least 0.9, even if in real situations a lower value reduces the safeness and the robustness of the whole system.

In this perspective, the aim of the grip-aware AEB system proposed by the authors is to identify the collision risk depending on the actual road conditions and, hence, to take control of the brakes to avoid possible accidents or at least to reduce their severity. Here, we base the decision-making of AEB according to the Time-To-Collision (TTC) in Equation (5.20), where the detection threshold depends on the estimated road-grip as:

$$TTC_{th}(t, \widehat{\mu}) = \frac{v(t)}{\widehat{\mu} a_{brk}}, \tag{5.39}$$

where a_{brk} is the deceleration value commanded to the ABS in case of emergency, i.e., $9.8 m/s^2$.

5.4.3 Anti-Lock Braking System

Once an emergency braking is commanded from the AEB, the ABS has to drive the brake system preventing wheels from locking during the hard braking maneuver. Here we propose a Sliding Mode (SMC) ABS controller that leverages the on-line estimation of the road-grip in order to provide a safe braking automatic maneuver for a vehicle-following process also in the presence of hard rainy or icy pavement. This choice is due to SMC's enhanced stability performances with respect to classical control architectures [218] (e.g., proportional action). In particular it can be shown that matched disturbances (uncertainties entering the system through the same channel as the control) are rejected, at least below the actuation limits, moreover due to the controller nonlinear nature, larger stability margins can be achieved.

First, let us define a control-oriented model, i.e., the quarter car model, in which we neglect the lateral and yaw motion of the wheel, thus obtaining a model dealing with the wheel rotational dynamics and longitudinal vehicle dynamics. The rotational dynamics of the wheel is described by

$$I_w\dot{\Omega} = -T_b - R_r F_x, \tag{5.40}$$

where I_w is the moment of inertia about the wheel axis of rotation, Ω is the angular velocity, T_b is the braking torque, R_r is the wheel rolling radius and F_l is the force produced by the friction reaction. The longitudinal vehicle dynamics are simply modeled as

$$m\dot{v} = -F_x. \tag{5.41}$$

where m is the vehicle mass.

The control goal is to yield λ to a reference value λ^* during braking [219]. To this aim we define the following sliding surface

$$\sigma(t) = \lambda(t) - \lambda^\star, \tag{5.42}$$

where $\lambda^\star$ is the optimal slip obtained from the friction estimator and λ is the longitudinal slip with dynamics as:

$$\dot{\lambda} = -\frac{1}{v}(\frac{1-\lambda}{m} + \frac{R_r^2}{I_w})F_x + \frac{R_r}{vI_w}T_b. \tag{5.43}$$

Due to the inertia differences between wheel and vehicle, we can consider the velocity v as slowly varying, thus reducing Equation (5.43) to a single-input single-output system, where the control law can be defined as:

$$u(t) = T_b = u_c(t) + u_{sw}(t), \tag{5.44}$$

where u_c is the continuous term, or *equivalent control* [218], and u_{sw} the discontinuous term. The equivalent control input is is responsible for keeping the trajectories on σ, i.e.,

$$\dot{\sigma} = 0 \Rightarrow u_c = (\frac{(1-\lambda)I_w}{mR_r} + R_r)F_z\mu_{x_{i,actual}}, \tag{5.45}$$

where the force $F_x = F_z\mu_{x_{i,actual}}$, where F_z is the tyre vertical load, and $\mu_{x_{i,actual}}$ the instantaneous friction value provided by the estimation module; note that the subscript $i = [1,2]$ identifies front and rear tyre depending from the axle involved (see Equation (5.13)).

Closed-loop stability can be easily proven by considering the following Lyapunov function $V(\lambda) = \frac{1}{2}\sigma^2$ and its derivative $\dot{V}(\lambda) = \sigma\dot{\sigma}$. Substituting Equations (5.44) and (5.45) into the expression of $\dot{V}$, we obtain

$$\dot{V}(\lambda) = \sigma\dot{\sigma} = \sigma(\frac{R_r}{vI_w}u_{sw}). \tag{5.46}$$

Hence, selecting $u_{sw} = -\frac{vI_w}{R_r}\eta sgn(\sigma)$ it follows that

$$\dot{V}(\lambda) = -\eta\sigma sgn(\sigma) = -\eta|\sigma| < 0, \tag{5.47}$$

where $\eta > 0$. In so doing, the surface σ is attractive and the closed-loop is asymptotically stable.

Note that, in order to avoid the well-known chattering problem of sliding mode controllers, for its practical implementation the sign function in Equation (5.47) has been substituted by the hyperbolic tangent function. Furthermore, since controllability is lost when the vehicle speed is approaching zero (see Equation (5.43)), following a common practice for implementing the ABS, the controller is disabled at the very low velocities.

5.5 Co-simulation platform

The design for improved solutions of safety related features has been significantly eased thank to the usage of appropriate simulation platforms, enabling engineers to design, test and validate the control architectures through models in a singular platform, and therefore reducing the development cost and the time to market.

Here, we propose a co-simulation platform for Model-In-the-Loop (MIL), where autonomous vehicle has been tested in a realistic traffic scenario. This co-simulation environment, represented in Figure 5.6, has been built leveraging the following four main components :

- MATLAB/Simulink platform, a widely used framework to model dynamical systems and to design control architectures. Indeed, through an easy to use of its graphical interface, it is possible to develop controllers according to the well-known Model-based Control Design approach. The vehicle dynamics model, implemented in the MATLAB/Simulink environment and employed for the evaluation of the control strategy performance in vehicle-following maneuvers, is the same vehicle plant model described in the Chapter 4.

- SUMO (Simulation of Urban MObility), an open-source road traffic simulation package, enabling the user to model entities such as vehicles, traffic lights, road networks, vehicle routing. Each entity is simulated microscopically, meaning that it is possible to control each of them singularly, while the whole scenario is emulated by its internal engine built upon realistic driving models.

- Friction estimator module, allowing the on-board estimation of the current tyre-road interaction state and the potential friction value.

In particular, the Simulink environment has been adopted to describe a highly detailed dynamical behavior of the autonomous vehicle under control, while SUMO emulates the traffic scenario and the road network, where the actual road grip in different scenario can change to mimic the effect of different environmental conditions to be studied.

The interaction between the different modules for the co-simulation is allowed by *Traci*, an integration tool provided by SUMO. The library *TraCI4Matlab* has been employed to couple the vehicle, the road and the SUMO environment model in Simulink.

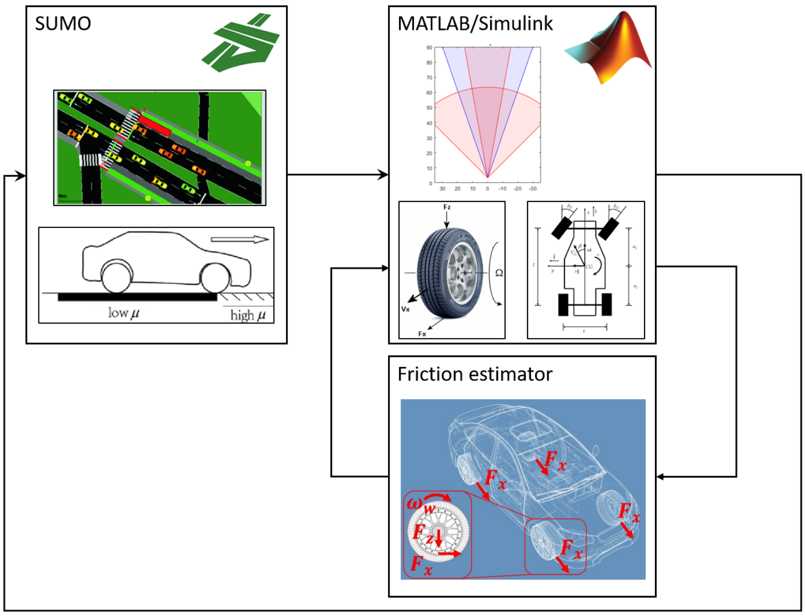

Fig. 5.6 Co-simulation Platform.

5.6 Results

The co-simulation platform has been exploited to assess the effectiveness of the proposed grip-aware functionalities.

The illustrative results, reported in the following, refer to a vehicle-following process along a typical motorway where the ego vehicle moves with an initial velocity of $v(0) = 30$ m/s, having an initial space gap $d(0) = 90$ m from its predecessor (leader) that moves with an initial speed of $v_{lead}(0) = 20$ m/s. The leader is a human-driven vehicle emulated through SUMO, whose realistic velocity profile accounts for both speed limits and driver imperfection parameters (details on how to model the human-drivers via SUMO can be found in [220] and references therein).

The first exemplar driving scenario refers to vehicles moving in the presence of heavy rain, with actual road grip $\mu = 0.5$. Due to the presence of an obstacle, at the time instant $t = 150$ s the leading vehicle performs a sudden hard-brake inducing the maximum deceleration allowed by the road grip, i.e., μg . Results in Figure 5.7 show how leveraging the on line estimation of the actual road condition (reported in Figure 5.7c), the ego vehicle is able to safely perform the velocity tracking while always preserving the desired safe space gap about $d_{des}(t, \widehat{\mu})$, depending on the grip estimate.

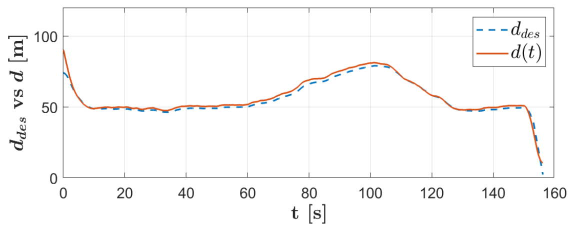

(a)

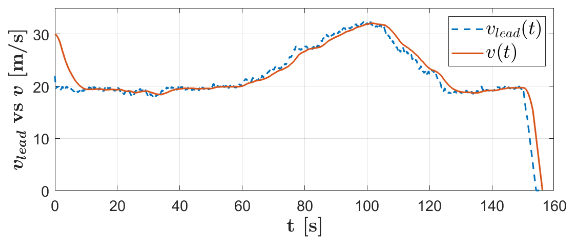

(b)

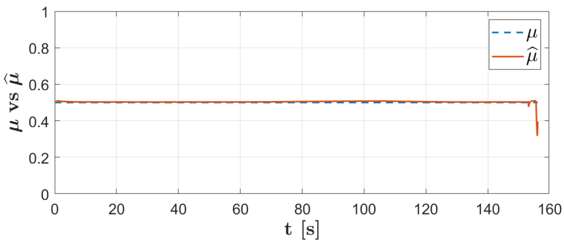

(c)

Fig. 5.7 Road-Grip aware Driving Functionalities: vehicle-following and hard emergency braking. (**a**) Time-history of the current distance gap, d, and of the desired one, d_{des}. (**b**) Time-history of the ego velocity v and leader velocity v_{lead} . (**c**) On-board road-grip estimate, $\mu(t)$ vs. $\widehat{\mu}$.

In addition, it is worth to note that the emergency brake is safely performed and vehicles correctly reach the required standstill distance when they finally stops without colliding. According to the theoretical derivation, the Predictive ACC also guarantees both acceleration and jerk of the ego vehicle fulfill the comfort constraints until the leading vehicle performs the hard brake at time instant $t = 150$ s (see Figure 5.8). Indeed, from this time instant the ACC tries to handle this hazardous braking maneuver, but the necessity of hard deceleration leads to the activation of the AEB, which hence commands the maximum braking torque to be imposed, obviously ignoring the comfort constraints which have less priority w.r.t. the safety.

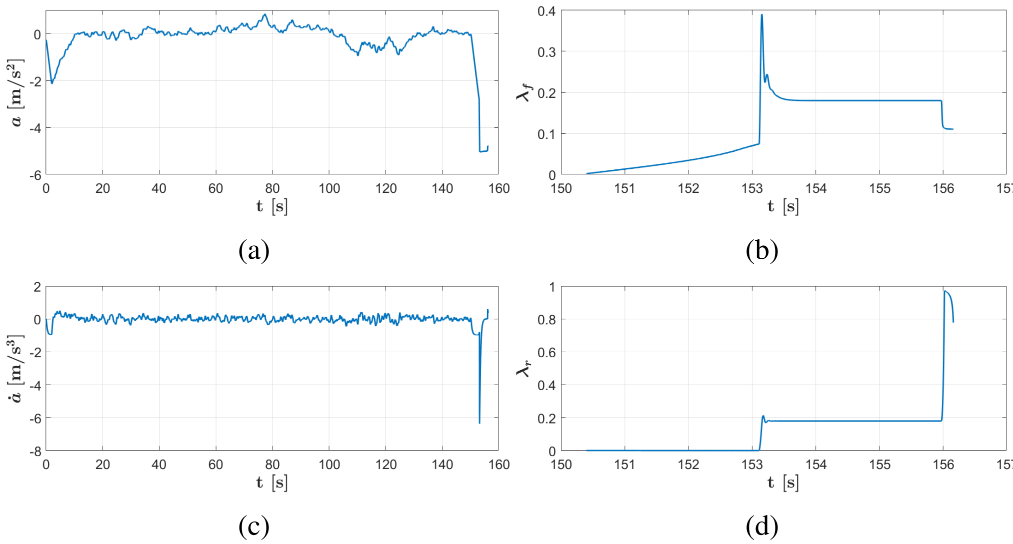

Fig. 5.8 Road-Grip aware Driving Functionalities: vehicle-following and hard emergency braking. Time-history of the ego-vehicle acceleration (**a**), jerk (**c**), front tyre (**b**) and rear tyre (**d**) longitudinal slip ratios.

In so doing, the collision is safely avoided (see Figure 5.7), but higher acceleration and jerk can be appreciated during the braking until the stop, as shown in Figure 5.8. It is also worth to note that, when the emergency braking maneuver is commanded from AEB, than the ABS is responsible ensuring that the longitudinal slips of the tyres are regulated to the optimal reference value λ^* returned by the friction estimator module as described in Section 5.3 (see Figure 5.8b–d).

In order to clearly appreciate the enhancement of the here proposed grip-aware driving functionalities with respect to classical ACC, AEB and ABS strategies, the above maneuver has been repeated without leveraging the knowledge of the actual road-grip.

Results in Figure 5.9 disclose that in this case the ACC is still capable of tracking the velocity references, while ensuring a desired gap that obviously depends only from the actual vehicle velocity, namely $d_{des}(t) = d_0 + \widetilde{\tau}_H v(t)$. However, when the leading vehicle performs the emergency hard brake, the safety distance results to be too small, the AEB is activated too late and it is impossible to avoid the collision that, hence, occurs at the time instant $t = 154$ s with a velocity of $v \simeq 10$ m/s = 36 km/h.

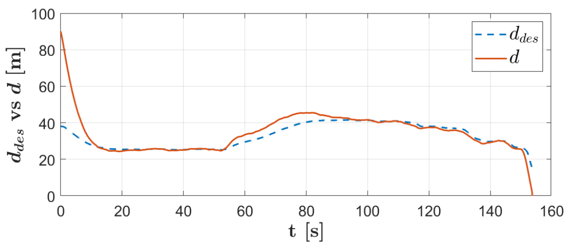

(a)

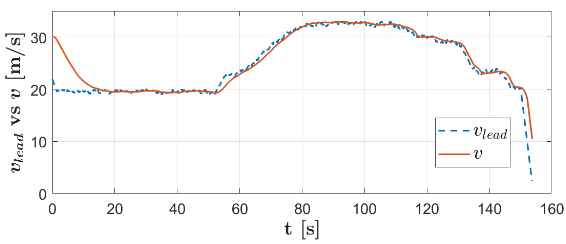

(b)

Fig. 5.9 Driving Functionalities without on-board road-grip estimate: vehicle-following and hard emergency braking. (**a**) Time-history of the current distance gap, d , and of the desired one, d_{des}. (**b**) Time-history of the ego velocity v and leader velocity v_{lead}.

A further investigation of the achievable performance has been performed in the case when vehicles are moving in variable environmental conditions, i.e., the actual grip changes in time due to different climatic condition that have to be faced during travelling. Specifically, vehicle drives from dry asphalt to wet road, i.e., the actual maximum road grip starts from $\mu = 1$ and than decreases, into two steps, until $\mu = 0.5$ (see Figure 5.10c). The initial dynamic condition of the vehicles match the ones chosen in the previous driving scenario.

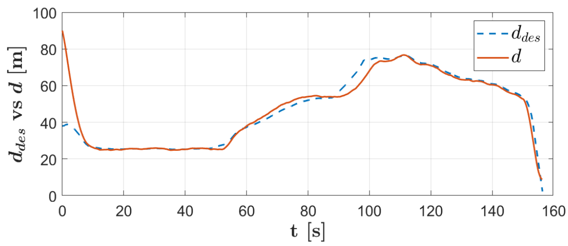

(a)

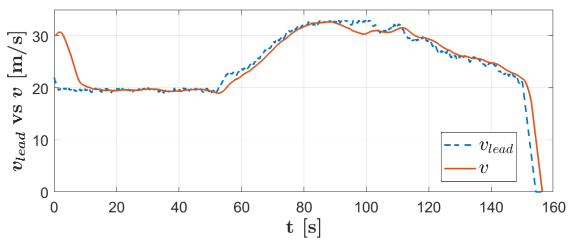

(b)

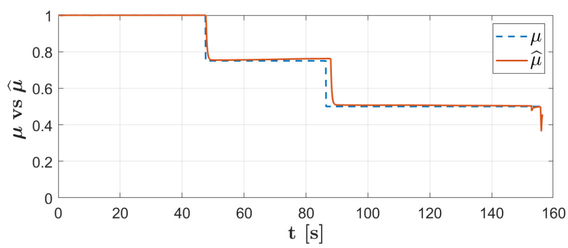

(c)

Fig. 5.10 Road-Grip aware Driving Functionalities in case of varying μ: vehicle-following and hard emergency braking. (**a**) Time-history of the current distance gap, d, and of the desired one, d_{des}. (**b**) Time-history of the ego velocity v and leader velocity v_{lead}. (**c**) On-board road-grip estimate, $\mu(t)$ vs. $\widehat{\mu}$.

Results depicted in Figure 5.10 show how the on-line road-grip estimate is performed with good precision (always below 1% at steady state). Furthermore, as the road grip decreases the safe distance is correctly adapted in order to provide a safer spacing with respect to the current adhesion (see Figure 5.10a) and the predictive ACC correctly tracks the reference values without any constraints violation. As in the previous driving scenario, at the time instant a $t = 150$ s an emergency situation emerges inducing the hard braking maneuver. Also in this case the combination of the grip-aware AEB and ABS is able of ensuring a safe stopping without collision.

Final exemplar results refer to a typical Stop & Go scenario where continuous smooth accelerations and decelerations occur due to traffic congestion. In order to better assess the collision risk and the safety margins during traffic jam, we leverage the following well-known non-dimensional collision-index $\gamma(t)$ [201]:

$$\gamma(t) = \frac{d(t) - d_{br}}{d_w - d_{br}}, \tag{5.48}$$

where $d(t)$ is the actual distance between the vehicles, d_{br} is the breaking critical distance and d_w is the warning critical distance. Note that the above index witnesses the possibility of an incoming crash due to the current driving situation. Specifically, when it is positive and greater than the unity a safe situation is detected, while, if it is below the unity, a possible dangerous scenario is signalized.

Results depicted in Figure 5.11 clearly confirm that, leveraging the road-aware driving control architecture, the safety index $\gamma(t)$ never goes below the unity, while, on the other hand, if the estimate of the road-grip is not exploited for the automated driving functionalities the collision index alerts for possible dangerous situations during the deceleration phases (see Figure 5.11), reducing the vehicle safety.

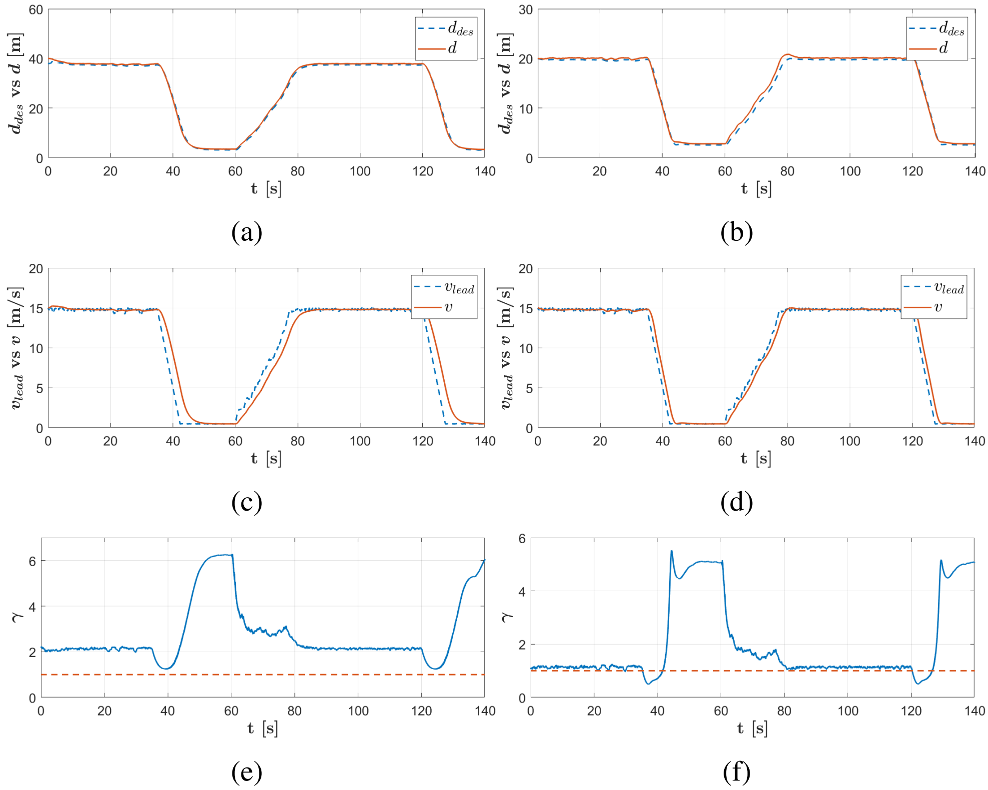

Fig. 5.11 Road-Grip aware Driving Functionalities during Stop&Go. Time-history of the current distance gap, d, and of the desired one, d_{des} (**a**) ego velocity v and leader velocity v_{lead} (**c**) safety index, γ (**e**) with road grip adaptation. Time-history of the current distance gap, d, and of the desired one, d_{des} (**b**) ego velocity v and leader velocity v_{lead} (**d**) safety index, γ (f) without road grip adaptation.

The effectiveness of the approach w.r.t. safety is finally summarized in Table 5.1. Here, results clearly disclose that, adapting in real-time the driving policy to the current road-grip, the overall automated driving performance can be enhanced with the minimal values assumed by the safety indexes [201] (i.e., time-to-collision, relative distance w.r.t. the predecessor and collision index γ as in Equation (5.48)) comparable with the ones required in the case of ideal road conditions.

Table 5.1 Summary of the minimal values assumed by the safety indexes in every described scenario.

Scenario	**min TTC**	**min λ**	**min d(t)**
Vehicle following with estimation	2.02	-0.15	10.30
Vehicle following w/o estimation	0	-1.08	0
Stop&Go with estimation	2.73	1.22	3.20
Stop&Go w/o estimation	2.13	0.48	2.70

Chapter 6

Design of advanced longitudinal control strategy with tyre thermal dynamics

6.1 Introduction

The dynamic behaviour of the vehicle can be deeply affected by the tyre operating conditions, including thermodynamic and wear effects. One of the biggest factors is tyre temperature itself, playing a fundamental role in high-performance motor sport applications [221]. Figure 2.21 shows the effect of tyre temperature on pure longitudinal grip. The tyre temperature also affects the cornering stiffness of the tyre, but the grip dependency is highly pronounced as shown in the Chapter 2 and [222].

In Formula 1, the drivers can see their tyre temperature on screen and make decisions based on their skill on how to control the car to extract maximum grip and manage tyre wear by optimizing the tyre temperature. Similar to a skilled race car driver, if a vehicle dynamics motion control system can assist an unskilled driver to make sure the tyres operate in a desirable window of temperature, it could be beneficial in race championships like FIA-WEC with gentlemen drivers, or an autonomous race car and possibly in an active safety application on road cars.

After explored and demonstrated in the Chapter 4 and 5, the existing widely accepted vehicle dynamics motion controllers like Anti-lock Braking System (ABS), Traction Control (TC), and Electronic Stability Control (ESC) are still sub-optimal in the sense that they don't consider the various multi-physical phenomena of the vehicle such as tyre temperature, tyre wear, possible variations in terms of tyre contact friction (as explored in the Chapter 5), etc. [223, 87], The focus of this Chapter is on the tyre temperature control.

Such systems, could be modified to explore the aforementioned idea. And, this can prove to be a good research foundation for future research into this domain of including multi-physical behaviour of sub-systems to improve the performance of these motion control systems.

A conventional vehicle dynamics motion control system that does not control tyre temperature won't be able to make sure that tyre temperatures are up to requirement whereas a controller that only regulates the tyre temperatures won't be able to ensure the adequate motion performance rather it will possibly disrupt the vehicle's performance, all while employing the wheel's longitudinal slip as input. Proposedly, a controller that optimizes the desired motion performance while making sure the tyre temperatures are also in the operating window, thus leading to a better performance, will inevitably need to prioritise its actions. This clearly points us to the problem of optimal control where a cost/objective function can help us specify relative priorities using weights, resulting in the best control inputs. In this project, the aforementioned motion control system is ABS.

To summarise, the chosen topic can possibly lay a foundation for the future research into autonomous control where, when the detailing of decision-making of the controllers will reach the level of multi-physics phenomenon of tyres, specifically tyre thermodynamic behaviour. One paper that addresses such an issue is [26], by taking into account the effect on the friction limits of the tyre due to temperature and eventually helping the Non-linear Model Predictive Control (NMPC) based controller take driver input decisions with the knowledge of those changing tyre friction limits deployed inside the prediction model.

6.1.1 Methodology and co-simulation platform

The modern computer technology has enabled us to solve complex non-linear problems numerically in finite time and great accuracy, where nowadays it is very common that organisations develop digital twins of products for prototyping. This approach has great benefits in the fact that testing variations are virtually infinite as compared to real world testing. Eventually, products can be developed quickly while being cost-effective. Of course, the former statement is true if at least the plant models being used are validated. But such an approach at least helps cut down a lot of possibilities that would have been tested in a real-life prototype with no fruitful results.

Such a method, is especially great for research studies where an exploration of the proposed idea is to be checked or the focus is at least not to develop the whole product but just the concept.

As the application is concerned with vehicle control related to tyre performance, existing control systems such as ABS and ESC instantly come to mind. ABS, in specific is chosen to be developed and tested. The focus is kept on high-level control and not the detailing of the low level hydraulic braking system, i.e. the actuator dynamics.

Concerning the optimal controllers, as stated in the literature survey, SDRE and NMPC were the two chosen options to test. Figure 6.1 shows the approach taken for the whole ABS development process. For each controller, first the quarter-car approach is used. In this system, the plant was modelled the same as the prediction model used inside the controllers.

After the quarter-car development, the full-car controller is developed only for the NMPC based controller as the SDRE controller did not provide

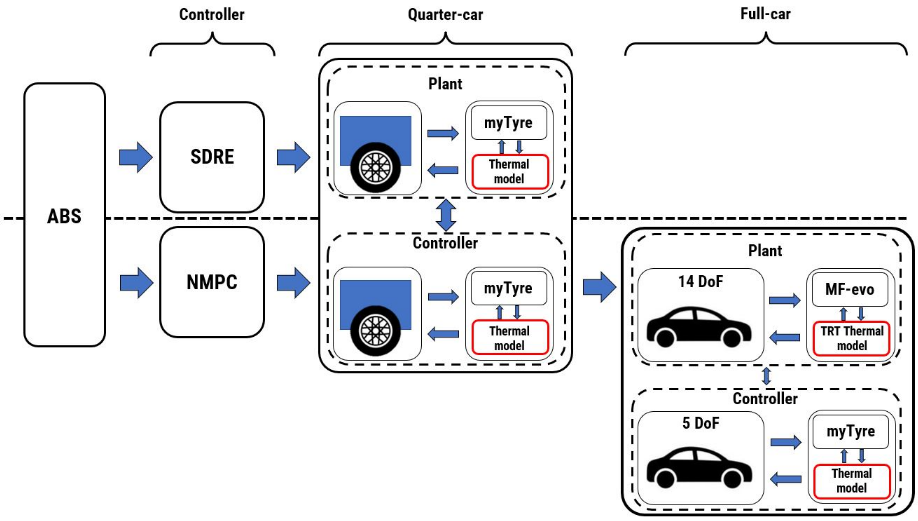

Fig. 6.1 ABS controller development schematic

much opportunity to tune and was very unstable at lower velocities. It is done using the co-simulation in Simulink environment. The Full-car model is the same described in the Chapter 4 and is coupled with the validated high-fidelity multi-physical tyre described in the Chapter 2 and thermal model described in [103] called "TRT: Thermo Racing Tyre", whereas the prediction model inside the controller includes a 5-DOF vehicle longitudinal model (6.4.1) coupled with the same myTyre as used in the case of quarter-car. The whole controller is modelled in Simulink, and the Simulink is the environment for the total simulations, with full-car model.

6.2 Tyre model

This section explains the tyre model developed for the prediction model inside the optimal controllers. It has been named 'myTyre' so that the reader can easily understand and pinpoint its exact usage. This model is a combination of the basic equations of Pacejka tyre model [224] and the tyre tread thermal model used to alter the stiffness and the peak force of the pacejka equations. The literature showed that using a steady-state tyre model (for the optimal controller predictions) should be good for ABS simulations and so, no transient effects (like relaxation length for the longitudinal force) were modelled. The following paragraphs will explain the details of the Pacejka force model, the thermal model and the connection between the two as shown in Figure 6.2.

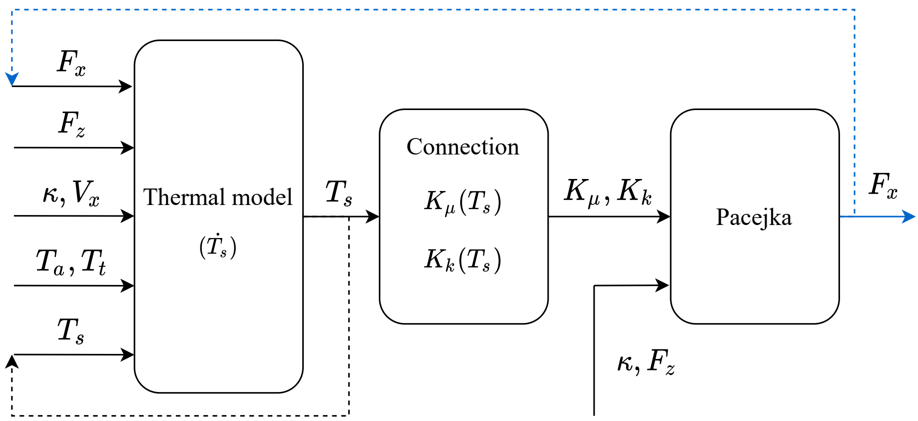

Fig. 6.2 Total thermal tyre model schematic with data flow

Tyre Force Model - Pacejka model based

The most famous empirical tyre model's equation, the Pacejka's MF Tyre model [224] described in the Chapter 1 and 2, has been used to represent the longitudinal tyre forces. It has been used in innumerable applications since its inception in 1990s. Based on the similarities concept, each parameter inside the equation is related to different characteristics of the tyre such as peak force, stiffness, etc. And the dependency of these parameters can be made a function of the desired variable, for example the tyre normal load. For high-level ABS controller testing, longitudinal tyre modelling proves sufficient, especially for the longitudinal tests where no lateral tyre slip is encountered. In this study, the focus is only kept on the performance of ABS in straight line tests with the same coefficient of friction for all the tyres, hence, a pure longitudinal model is sufficient. In the case of brake test cases involving cornering or split-μ conditions, the use of a combined-slip tyre is crucial.

6.2.1 Tyre thermal modelling

Much of the literature on tyre thermal modelling is related to the accuracy that it provides in the simulations in model-based development of vehicles [225–228, 17, 18]. These models range from simple empirical-lumped models to high fidelity Finite-element method (FEM)-based physical models. And because modern development also involves Driver in the Loop (DiL) simulations, so the numerical solutions of such models must also converge in real-time based on the current state-of-the-art financially viable computer technology. In the following paragraphs, the applicability of the aforementioned models is discussed.

A purely physical model with 3D FEM-based thermal and structural tyre model is presented by Calabrese [222], with major heat generation and heat exchange sources, clearly pointed out. He also presents a setup with force model based on MF-tyre model with empirical relations for the grip and stiffness dependency on the temperature. As pointed out by the author, the latter setup has lower computational cost. Anyways, both setups shows high accuracy and shows great applications in lap-time simulations or tyre development as well, being a physical model. Unquestionably, such a model can't be considered for the prediction model inside an optimal-controller, being computationally heavy, as it involves solving partial differential equations in 3 dimensions.

The physical model (1D-heatflow) presented by Rosa et al. [229] set the foundations for the 3D physical model later presented by Farroni et al. [221, 102] for motorsport applications "to estimate the temperature distribution even of the deepest tyre layers". As stated ny the authors, these models have shown great real-time applicability for DiL simulations. But the same reasoning as for the Calabrese's model [222] goes for it, not to be used as a prediction model for the controller.

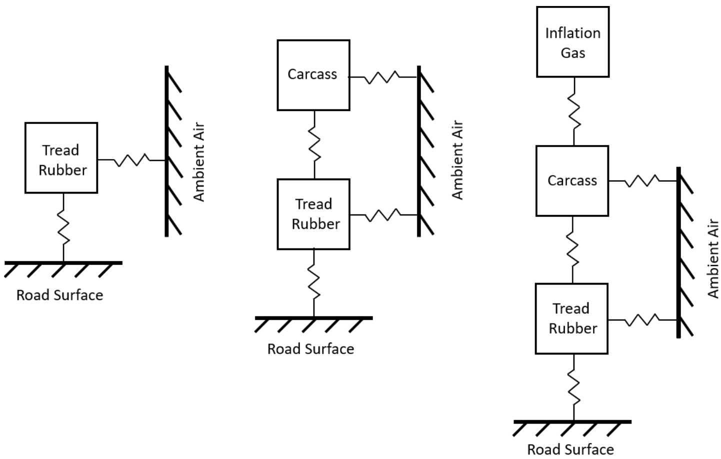

Fig. 6.3 1, 2 and 3 node lumped thermal model schematic, as presented in [17–19] respectively

The model presented by Tremlett [17] is a great example of a lumped-parameter model based on the heat flow equation formed using first law of thermodynamics with the assumption of an isotropic thermal tyre mass. They treat the tread of the tyre as a lumped mass with 4 dominant heat-flows viz. friction power, strain energy, air convection, and conduction in the non-sliding region of the patch. Not to mention that these individual heat flow terms are fit empirically with their individual efficiency terms. Such, a model involves a solution of a single Ordinary Differential Equation (ODE) to predict the tread temperature, which makes it suitable for a prediction model inside an optimal controller, as compared to a 3D model solved using FEM. As shown in Figure 6.3, a similarly lumped, 2-node (tread and carcass) thermal model by West and Limebeer [18], and a 3-node (tread, carcass and internal air) thermal model by Kelly and Sharp [19] can possibly accommodate bigger variations in boundary conditions, respectively, as compared to the aforementioned 1-node (tread) model. Thus, could also be used in the concerned future applications with an advantage of robustness.

Thermal Model

As was discussed in the literature survey, the thermal model developed by Tremlett [17] with some modifications related to the contact patch size related functions according to Hackl [227] was implemented.

The concerned model is an empirical lumped parameter model of the tyre tread based on the 1st law of thermodynamics. The tread mass is treated as an isotropic material. This tyre tread (1-node) model was an obvious starting choice for this problem not just from the need of a light and simple model but also the fact that the employed model-based controllers need full-state feedback. The tread temperature is know to be easily measured with the use of infrared sensors in the modern cars whereas in the case of a 2-node model with the additional temperature state of the carcass temperature, state estimation techniques would be necessary for the requirement of a full-state feedback.

The following 4 heat flows (Figure 6.4), being the dominant, are considered while radiation is neglected:

1. Q_1: Heat generated due to the friction power in the sliding region of the contact patch
2. Q_2: Heat generated due to the strain energy within the mass
3. Q_3: Heat exchange due to the forced convection with ambient air
4. Q_4: Heat exchange due to the conductive cooling at the non-sliding region of the contact patch

The homogeneous temperature of the tread mass (T_s) is given by the differential equation (6.1):

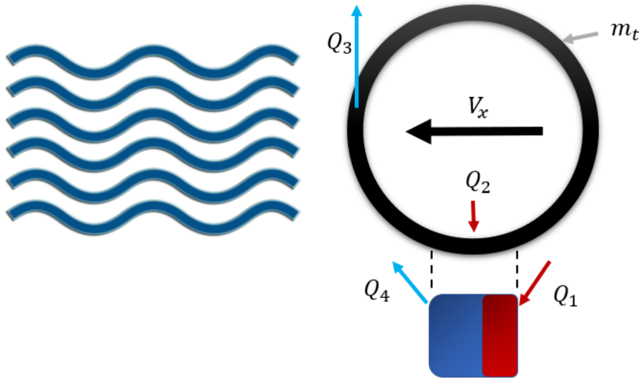

Fig. 6.4 Considered heat flows in the thermal model

$$m_t c_t \dot{T}_s = Q_1 + Q_2 - Q_3 - Q_4 \tag{6.1}$$

where m_t is the mass of the tyre tread and c_t its specific heat capacity. The heat generation due to friction power (Q_1) is represented as a sum of friction powers due to F_x (6.2) and the same heat due to F_y is neglected as we are using the pure longitudinal representation:

$$Q_1 = p_1 V_x |F_x \kappa| \tag{6.2}$$

where, V_x is the tyre ground velocity and p_1 represents the ratio of friction heat entering the tread. All the parameters (viz. p_i) in this model are fit empirically. The heat generation due to strain energy (Q_2) is represented as shown in equation (6.3) where the parameters here are the efficiencies related to each force i.e. F_x and F_z in this case. These efficiencies directly relate to the corresponding force's contribution to the strain energy losses:

$$Q_2 = V_x(p_2|F_x| + p_3|F_z|) \tag{6.3}$$

Next, the heat exchange due to forced convection around the tyre (Q_3) with the ambient air is represented using Newton's cooling law with an empirical formulation for the heat transfer coefficient, as seen in equation (6.4):

$$Q_3 = p_4 V_x^{p_5} (T_s - T_{amb}) \tag{6.4}$$

where T_{amb} is the ambient temperature and the heat coefficient is being represented as $p_4 V_x^{p_5}$ and is empirically fit. The formulation $p_4 V_x^{p_5}$ can very well represent the flow around a wheel in a car, once fit. Lastly, the heat exchange due to the conduction of the non-sliding region of the patch (Q_4) with the road is represented using the Fourier's law as shown in equation (6.5):

$$Q_4 = h_t A_{nsl} (T_s - T_{road}) \tag{6.5a}$$

where,

$$A_{nsl} = l_w l_{nsl} \tag{6.5b}$$

$$l_{nsl} = l_p (1 - c_s) \tag{6.5c}$$

$$l_p = a_{cp} F_z^{a_{cpp}} \tag{6.5d}$$

$$c_s = \left(\frac{c_{s2} - c_{s1}}{\kappa_{max}} \right) \kappa + c_{s1} \tag{6.5e}$$

For the non-sliding region area calculation, the whole patch is assumed as a rectangle with length l_p and width l_w where it was a safe choice to assume that the width remains fixed (being a radial tyre). The l_w is represented as a power function of the tyre normal load as shown in equation (6.5d), fit empirically using separate data. The non-sliding region's length l_{nsl} is calculated by first knowing the sliding length l_{sl} of the patch using the proportioning factor c_s as shown in equations (6.5c) and (6.5e). The c_s being a linear function of the longitudinal slip based on the values proposed by Hackl [227]. Here, c_{s2} and c_{s1} are the proportion of patch region that is sliding for the slip value at maximum force (κ_{max}) and zero slip, respectively. And the heat transfer coefficient h_t is taken as a constant.

Connection $K_\mu(T_s)$ and $K_k(T_s)$

As seen in Calabrese's work [222], the two main effects that the tyre temperature has on the tyre characteristics is on grip and stiffness, grip being a considerable change. Although in high-fidelity models like MFevo in Chapter(2), the grip and stiffness change is more precisely represented as a function of different internal tyre layer temperatures and also pressure as shown in [230, 231]. In myTyre, the grip and slip stiffness effect was included using the $K_\mu(T_s)$ and $K_k(T_s)$ functions by scaling the D_x and B_x, respectively. These scaling functions are shown in equation (6.6). Their degree of polynomial was based on the identification of the data from the reference tyre at a given pressure. It is safe to assume the pressure as constant for a given manoeuvre, but across the whole working range of environmental conditions in reality it is crucial to consider the pressure effect. In all the test performed in this work, the initial pressure was assumed to be the same ($1.4\,bar$) for all the different environmental conditions.

Although, the cornering stiffness of the tyre is more dependent on the carcass temperature than the tread temperature, but still because of some amount of correlation such a cubic polynomial (6.6) shows good enough empirical fit, at least in terms of the direction of trends:

$$K_\mu = K_{\mu,a}T_s^2 + K_{\mu,b}T_s + K_{\mu,c} \tag{6.6a}$$

$$K_\mu = K_{k,a}T_s^3 + K_{k,b}T_s^2 + K_{k,c}T_s + K_{k,d} \tag{6.6b}$$

where $K_{mu,i}$ and $K_{k,i}$ are the coefficients of respective polynomials ($i \in \{a,b,c,d\}$ here).

6.3 Vehicle model

6.4 Quarter-car

Quarter car is a model representing one corner of a car which includes the equivalent mass at that corner and the wheel. This leads to 3 main dynamics to be modelled viz. wheel slip dynamics, longitudinal velocity of the quarter-car, and the tread temperature dynamics. Not to mention, that here no load transfer effect (no moment balance) is considered due to the fact that there is only one tyre. Figure 6.5 shows us the quarter-car where only the longitudinal force balance between inertial force and tyre force, and the torque balance between inertial torque, brake torque and tyre force torque is taken into account. And the tyre normal load is simply equal to the weight of the quarter-car (mg).

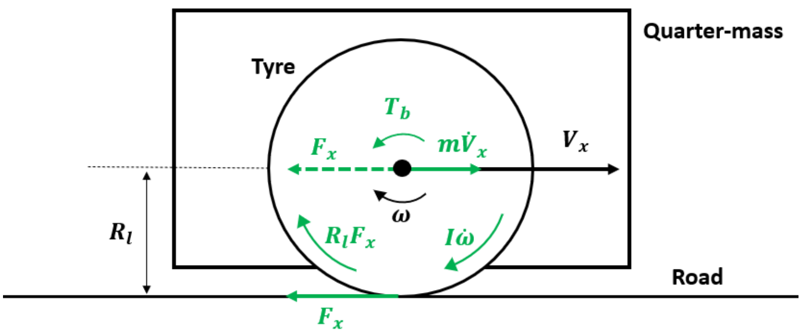

Fig. 6.5 Quarter-car forces and torques illustration

Such a simple model helps us understand the basics of the full-vehicle and also with better weight tuning for the full-car controller. This model coupled with myTyre was both used as the plant and prediction model. The following points state the assumptions in such a simplification:

- It moves in a straight line and thus, longitudinal dynamics of tyre must suffice
- No camber (γ) effects
- No suspension/load transfer effects considered
- Purely rigid longitudinal connections
- No coupling effects due to a chassis connecting the four wheels
- No variations in wheel radius

From the longitudinal slip definition in equation 1.4, has been possible get the following equation (6.7).

$$\dot{\kappa} = \frac{1}{V_x}\left[R_e\dot{\omega} - \dot{V}_x\left(1+\kappa\right)\right] \tag{6.7}$$

Balancing the torque around the wheel center, the wheel rotation dynamics ($\dot{\omega}$) has been evaluated as (6.8):

$$\dot{\omega} = \frac{T_b - R_l F_x}{I} \tag{6.8}$$

where, T_b is the braking torque applied to the wheel, R_l is the loaded radius of the tyre, F_x being the longitudinal tyre force and I being the wheel's total rotational inertia about the rotation axis.

A simple longitudinal equilibrium on the quarter-car brings us the equation (6.9):

$$\dot{V}_x = \frac{F_x}{m} \tag{6.9}$$

where m is the mass of the quarter-car.

Substituting the value of $\dot{\omega}$ from equation (6.8) and $\dot{V}_x$ from equation (6.9) in the equation (6.7), we get the following equation (6.10):

$$\dot{\kappa} = \frac{1}{V_x}\left[\frac{R_e T_b}{I} - F_x\left(\frac{R_e R_l}{I} + \frac{1+\kappa}{m}\right)\right] \tag{6.10}$$

In the tyre tests it was also seen unlike the loaded radius, the effective radius does not change much unless with larger values than the maximum force. So, a constant value was chosen and not modelled as dependent variable on factors like tyre load, speed, etc.

Finally, using the tread temperature dynamics definition $\dot{T}_s$ from equation (6.1) we get the quarter-car system's equation (6.11) in implicit form:

$$\begin{bmatrix} \dot{\kappa} - \frac{1}{V_x}\left[\frac{R_e T_b}{I} - F_x\left(\frac{R_e R_l}{I} + \frac{1+\kappa}{m}\right)\right] \\ \dot{V}_x - \frac{F_x}{m} \\ \dot{T}_s - \frac{1}{m_t c_t}\left(Q_1 + Q_2 - Q_3 - Q_4\right) \end{bmatrix} = \begin{bmatrix} 0 \\ 0 \\ 0 \end{bmatrix} \tag{6.11}$$

where the heat flows (Q_i) are represented as shown in equations (6.2)-(6.5) and have been omitted for spatial reasons. All the F_x terms are represented by the Pacejka tyre force equations.

6.4.1 Full-car

For the full-car analysis the plant and the prediction models have different fidelity. The plant is the 14-DOF vehicle model described in the Chapter 4 and the prediction model is a 5-DOF vehicle model used inside the controller.

5 DOF vehicle prediction model

The prediction model is much simpler than the plant model, and is used to depict the main dynamics of the system important for this controller application viz. wheel slip dynamics ($\dot{\kappa}$), and the vehicle's coupled longitudinal dynamics ($\dot{V}_x$). As our considered reference plant model has four wheels, which corresponds to 4 slip dynamic equations and a single equation representing the vehicle's longitudinal dynamics, leading to 5 degrees of freedom (Figure 6.6).

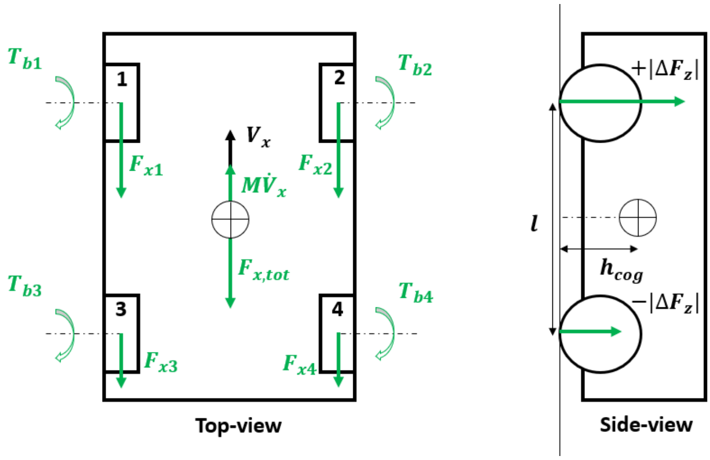

Fig. 6.6 Full-car 5 DoF Vehicle model - forces and torques illustration

Ideally, The load transfer can be included as a function of the vehicle longitudinal acceleration. This acceleration being a direct function of the tyre force, leads to a situation of algebraic loop for numerical simulations requiring special solver which is not a possibility in the case of Runge-Kutta solver used in side the NMPC prediction calculations. So, to avoid the issue of algebraic-loop the load transfer (ΔF_z) is modelled as first-order dynamics [232], as a function of the tyre longitudinal force as shown in (6.12) and (6.13). So, the load transfer becomes a state in the full-car dynamics, eventually increasing the DOF from 9 to 10 as seen in (6.15).

$$\dot{\Delta F}_z = \frac{1}{\tau}\left(\tilde{\Delta} - \Delta F_z\right) \tag{6.12}$$

where,

$$\tilde{\Delta} = \frac{F_{x,tot}\, h_{cog}}{2l} \tag{6.13}$$

Here, the τ represents the time constant of the first-order transfer function, h_{cog} is the height of the centre of gravity of the whole vehicle, l is the wheelbase and $F_{x,tot}$ is the summation of all four tyre longitudinal forces. The time constant is fit empirically based on one of the braking tests performed.

Finally, the load transfer is calculated by subtracting or adding the load transfer to the static front/rear wheel loads, respectively, as shown in equation (6.14).

$$F_{zi} = F_{z,static} \pm \Delta F_z \tag{6.14}$$

The equations for myVeh including the tyre tread dynamics (additional 4 degrees of freedom) are presented in implicit form in equation (6.15). The index of the variables corresponds to each wheel as shown in the Figure 6.6.

$$\begin{bmatrix} \dot{\kappa}_1 - \frac{1}{V_x}\left[\left(\frac{R_e}{I}\right)T_{b1} - \left(\frac{R_eR_l}{I}\right)F_{x1} - (1+\kappa_1)\frac{F_{x,tot}}{M}\right] \\ \dot{\kappa}_2 - \frac{1}{V_x}\left[\left(\frac{R_e}{I}\right)T_{b2} - \left(\frac{R_eR_l}{I}\right)F_{x2} - (1+\kappa_2)\frac{F_{x,tot}}{M}\right] \\ \dot{\kappa}_3 - \frac{1}{V_x}\left[\left(\frac{R_e}{I}\right)T_{b3} - \left(\frac{R_eR_l}{I}\right)F_{x3} - (1+\kappa_3)\frac{F_{x,tot}}{M}\right] \\ \dot{\kappa}_4 - \frac{1}{V_x}\left[\left(\frac{R_e}{I}\right)T_{b4} - \left(\frac{R_eR_l}{I}\right)F_{x4} - (1+\kappa_4)\frac{F_{x,tot}}{M}\right] \\ \dot{V}_x - \frac{F_{x,tot}}{M} \\ \dot{T}_{s1} - \frac{1}{m_{t1}c_{t1}}\left(Q_{11}+Q_{21}-Q_{31}-Q_{41}\right) \\ \dot{T}_{s2} - \frac{1}{m_{t2}c_{t2}}\left(Q_{12}+Q_{22}-Q_{32}-Q_{42}\right) \\ \dot{T}_{s3} - \frac{1}{m_{t3}c_{t3}}\left(Q_{13}+Q_{23}-Q_{33}-Q_{43}\right) \\ \dot{T}_{s4} - \frac{1}{m_{t4}c_{t4}}\left(Q_{14}+Q_{24}-Q_{34}-Q_{44}\right) \\ \dot{\Delta F}_z - \frac{1}{\tau}\left(\tilde{\Delta} - \Delta F_z\right) \end{bmatrix} = \begin{bmatrix} 0 \\ 0 \\ 0 \\ 0 \\ 0 \\ 0 \\ 0 \\ 0 \\ 0 \end{bmatrix} \tag{6.15}$$

where the indices for the variable κ_i, T_{bi}, F_{xi}, T_{si}, m_{ti}, c_{ti}, and Q_{ji} are defined as $i \in \{1,2,3,4\}$ representing each wheel (Figure 6.6) and $j \in \{1,2,3,4\}$ representing each heat flow for individual wheel (equations (6.2)-(6.5)). Similar to the quarter-car, the F_{xi} is represented by the Pacejka's tyre force equations. And the load transfer state equation is represented as shown in equation (6.12). M represents the mass of the full-car and $F_{x,tot}$ represents the sum of all F_{xi}. It can also be seen that the R_e, R_l, I, m_t, c_t, and other thermal parameters are assumed to be the same for all wheels, as all four tyres are represented using the same parameterisation.

6.4.2 Validation

This section talks about the parameterisation process used for each model while showing the validation plots for each. The reference tyre model (MFEvo, described in Chapter 2) used in the plant is a well-validated model and its validation plots will not be presented here for confidentiality reasons.

Specifically, the validation of the myVeh tyre model and the myVeh full-car model will be shown here. They are fit onto the data obtained from the tests performed with the full-car plant model and the MF-evo tyre with the TRT thermal model.

myTyre validation

The model is made up of 3 sub-models viz. Pacejka-based force equations, the thermal model, and the connecting equations.

The Pacejka force equation is fit onto the reference curve of MF-evo, which is present at the optimal temperature of $70°C$. First, the coefficients of $C_{f\alpha}$ and D_x relation were identified using separate tests for each. Based on the data, both are made linear functions of F_z. The 3 load values were chosen based on the average static load on each tyre of the reference vehicle and the maximum possible static load transfer based on the tyre peak coefficient of friction. Once, they are identified, C_x and E_x remain, which are identified using a non-linear numerical fitting routine. The validation plots are as shown in Figure 6.7. For ABS application, it is expected for the slip to not reach values much higher than the maximum force slip, so the fitting routine was kept between $[-0.15, 0]$ slip value, although it is evident from the figure that the fitting will also be good until locked wheel slip value of -1. The fitting is not expected to be perfect because the horizontal and vertical shift is not included in the Pacejka equation formulation used in this work. And, so, including the vertical and horizontal shifts, and also making E_x a function of load can improve the fit. But, such a fit didn't pose any problems related to stability because of plant-model mismatch.

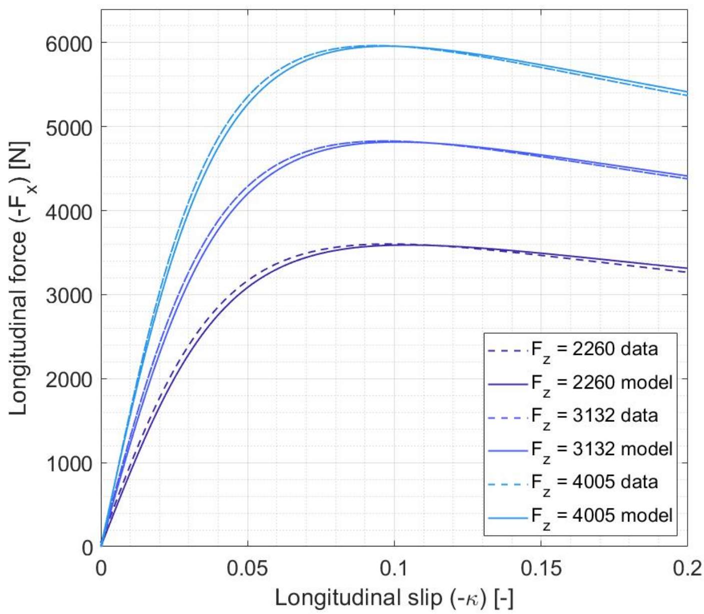

Fig. 6.7 Pacejka-based force equation validation at reference temperature

The next step is the parametrisation of the thermal model, which is done based on the data produced from the test on full plant coupled with the MF-evo tyre. The parameters for this model are divided into two categories viz.

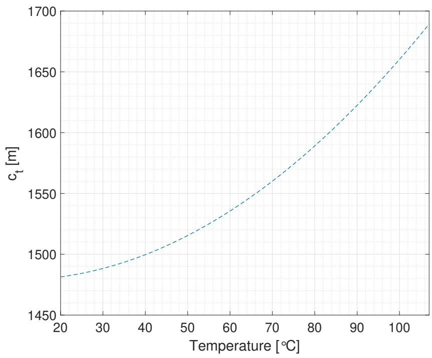

(a) $c_t(T_s)$

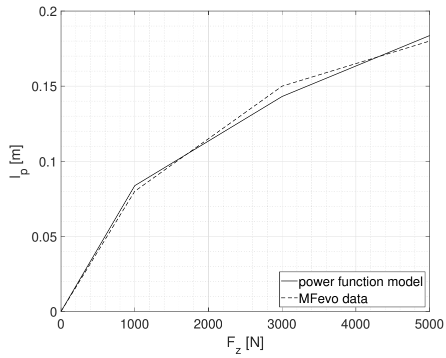

(b) $l_p(F_z)$

Fig. 6.8 MFevo specific heat capacity variation with tread temperature and patch length variation with tyre normal load

fixed and optimised. The fixed parameters are taken from the MFevo model. The specific heat capacity c_t is taken as constant in myTyre and so a value around the optimal temperature is used (Figure 6.8). And the heat transfer coefficient h_t is also taken to be a constant value. The power function for the patch's total length l_p is fit onto the available data for MF-evo as shown in Figure 6.8. All the final parameters are presented in the Table 6.1:

Table 6.1 Thermal model fixed coefficients

Coefficient description	Symbol	Value	Unit
Tread mass	m_t	2.54	kg
Tread specific heat capacity	c_t	1.6×10^3	$\frac{J}{K\,kg}$
Tread-road heat transfer coefficient	h_t	4.5×10^2	$\frac{W}{m^2 K}$
Contact patch width	l_w	2.9×10^{-1}	m
Contact patch length function coefficient	a_{cp}	2.9×10^{-3}	m
Contact patch length function power	a_{cpp}	4.9×10^{-1}	–
Fraction of contact patch in sliding at zero slip	c_{s1}	3×10^{-1}	–
Fraction of contact patch in sliding at F_{max} slip	c_{s2}	8×10^{-1}	–
F_{max} slip value (assumed fixed)	κ_{max}	1×10^{-1}	–

For the optimised parameter fitting routines, the various input variables (F_x, F_z, κ, V_x, T_t, T_a) are also taken from the test, whereas in the final compiled myTyre model, the F_x is fed from the simple Pacejka-based force model as shown in Figure 6.2. The parameters were identified using a non-linear least squares fitting routine for a brake test of the plant with the MFevo tyre, which involved changing tyre load F_z (due to load transfer), decreasing longitudinal velocity V_x and changing longitudinal slip κ. The test input and output values of a front tyre were chosen and used for both front and rear tyres.

Whereas the initial and boundary conditions for this test are stated in Table 6.2.

It is observed that the parameterisation for a given test (initial velocity and temperature, and boundary conditions) is able to reproduce the thermal behaviour for the similar conditions with a good accuracy, but fails to show good accuracy as these conditions change. But because the final selected value of the prediction horizon of the full-car NMPC controller is small enough, where the accuracy is always good for each prediction and the feedback of state helps update it each controller's sampling time. Hence, this same optimised paramter set is used for various tests with different initial and boundary conditions as described in Figure 6.16. Figure 6.9 shows the validation plot for the myTyre thermal model with the MFevo's thermal test data.

Table 6.2 myTyre thermal model validation test conditions

Initial conditions	Boundary conditions
$V_{x0} = 40m/s$	$T_a = 28°C$
$T_{s0} = 28°C$	$T_t = 35°C$

Finally, the last part of the myTyre, the connection between the Pacejka-based force model and the thermal model is parameterised. The MFevo tyre model modifies the tyre peak grip and stiffness based on complicated functions of the temperature of the tread's surface, core and base layer. But in

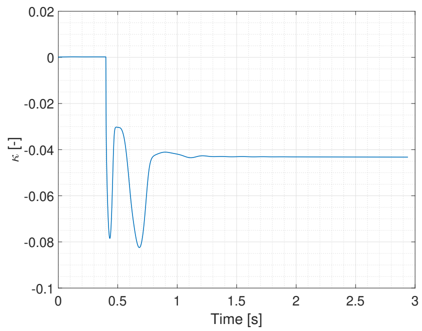

(a) Longitudinal slip input

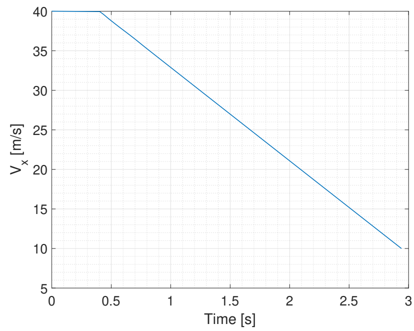

(b) Longitudinal velocity input

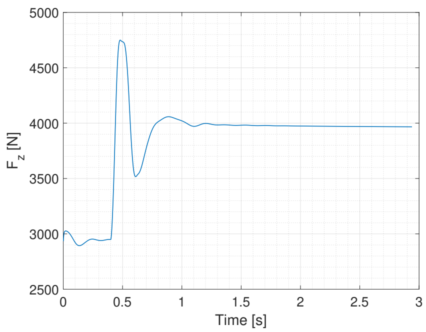

(c) Tyre normal load input

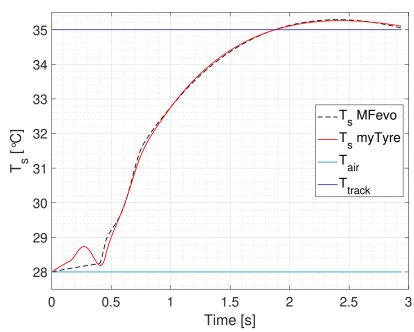

(d) Tread surface temperature output

Fig. 6.9 myTyre thermal model validation

the case of myTyre due to the availability of only the tread surface temperature, both the K_μ and K_k are a function of that (6.6). Multiple tests with different initial homogeneous tyre temperature are run to retrieve the values of K_μ and K_k. Final validation plots of the polynomial fitting of the functions are shown in Figure 6.10. The starting tyre pressure across the whole work is taken equal to $1.4bar$ and the impact due to its changing value is not taken into account because the pressure change is extremely small in a braking manoeuvre. In the real implementation, lookup tables can be setup to compensate for the impact of different inflation pressures on the grip and stiffness.

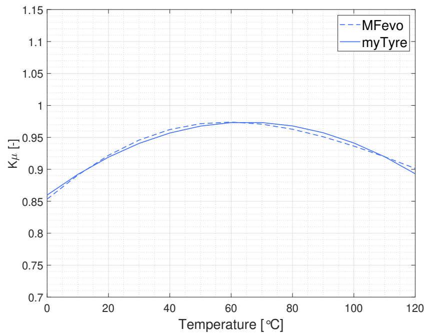

(a) $K_\mu(T_s)$

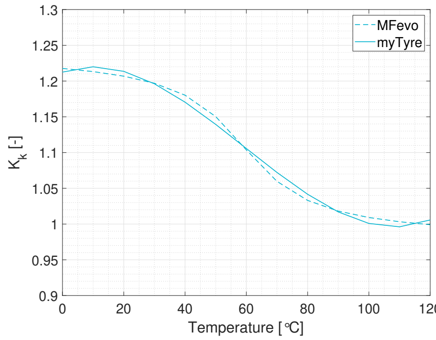

(b) $K_k(T_s)$

Fig. 6.10 myTyre - connection ($K_\mu(T_s)$ and $K_k(T_s)$) validation

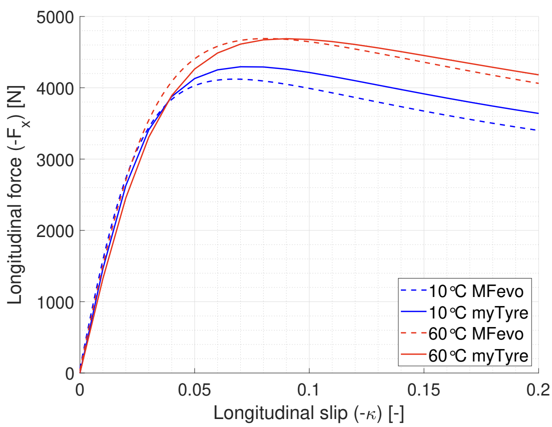

Fig. 6.11 Pacejka and connecting equation's combined performance - Longitudinal force with longitudinal slip ($F_z = 3132N$)

Figure 6.11 shows the performance of myTyre vs MFevo for 2 temperature values. Here the thermal model model is suppressed to check the performance of Pacejka equation combined with the connecting equation (6.6). The next section (6.4.2) will also show the performance of the myTyre in terms of inputs to the output longitudinal tyre force F_x as compared to the MFevo and also the pure Pacejka-based tyre model (at reference temperature of $70°C$) without temperature effects.

myVeh validation

Once the myTyre is validated, the full-car prediction model "myVeh" (6.4.1) is finally validated. The performance of the model is shown in Figure 6.12. In this model, all the tyres are the same manufacturer model, hence, are represented by the same parameterisation. Although, in the case of implementation, the rear tyres must definitely have a different thermal model parameterisation as compared to front because of the difference in air flow (being the biggest factor). It is also due to the fact that the one-node tread model presented in this work has limited capability, and needs a change in the optimised parameter set to accommodate for different air flows for front and rear tyres. So, it means that here it has been assumed that the front and rear tyres of the vehicle have same airflow around them.

In this test the same brake torque input is given to both the plant and the prediction model and outputs are validated. All the outputs show a good fit, especially the tyre normal load shows a good fit when made a state in the system as shown in 6.4.1. In the transient phase of the tyre normal load, the prediction model doesn't fit well because of the lack of suspension modelling within, as compared to the plant model. Due to this transient phase, the longitudinal slip and force transients also suffer. The tyre longitudinal force shows good fit overall, being the important output as it directly propagates to how much brake torque the controller will apply, which can also lead to under or over-braking than the required value. It is clear that the velocity propagation matches perfectly as is also important in a braking manoeuvre.

6.5 Controller and simulation

All the simulations were performed in Simulink environment. A general data flow of the controller with the plant is shown in Figure 6.13. In the controller simulations, it has been assumed that the ideal full-state information is available which could be either by the means of measurement or an

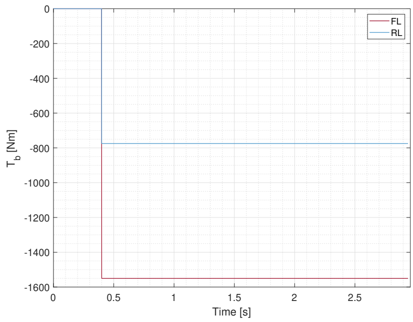

(a) Brake torque input

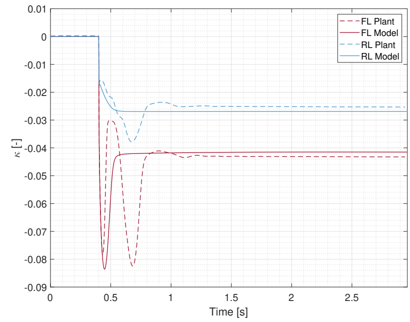

(b) Longitudinal slip

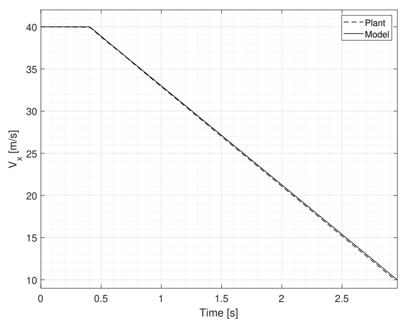

(c) Vehicle longitudinal velocity

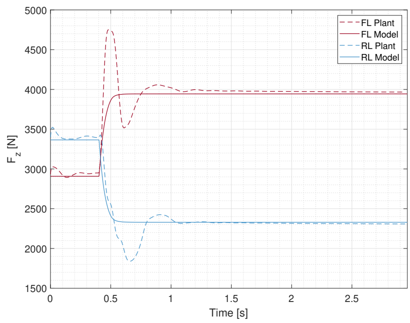

(d) Tyre normal load

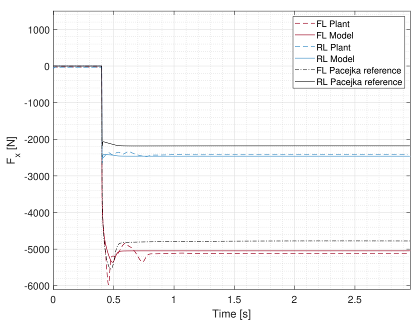

(e) Tyre longitudinal force

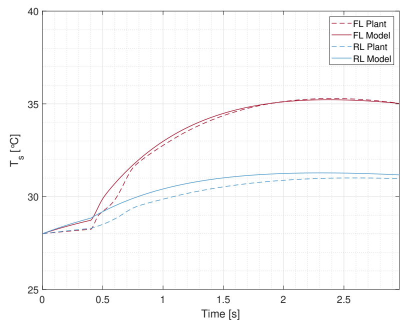

(f) Tread surface temperature

Fig. 6.12 Full-car model "myVeh" validation estimator. The whole simulation works on the assumption that everything is deterministic. The driver brake demand affects the reference for the controller whereas the controller weights can be made dependent on the state values. The controller's prediction model parameters can also be updated based on the different boundary conditions, as this model is not complex enough to represent the whole set of thermodynamics boundary conditions.

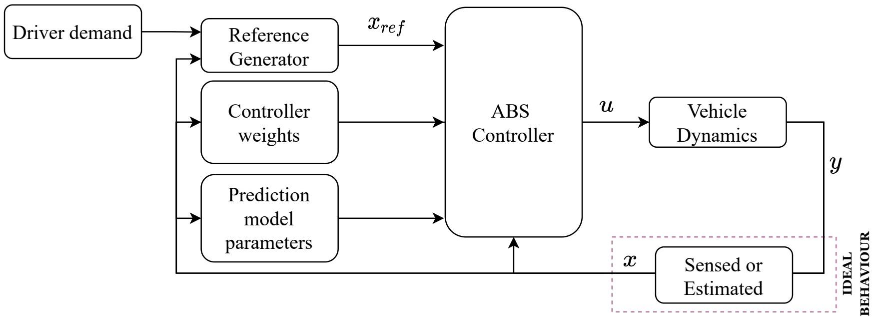

Fig. 6.13 Full-car simulation general setup

6.5.1 Quarter-car simulation

The quarter-car simulations are done to get an initial understanding of the response of the controllers, eventually helping mitigate complex problems in the full-car simulations. The plant and prediction models in this case were kept the same, such that pure plant-model match is achieved. This helps make sure the plant-mismatch instabilities are avoided and controller performance can be assessed. The model equations used are the ones shown in equation (6.11). These equations were treated differently based on the controller type - SDRE or NMPC. The next section goes into the detailing of the quarter-car model used in these simulations.

In these simulations, the reference and controller weighting for the controller is kept constant and not variable based on the state (as is done in the full-car simulations), to keep the analysis simple. Also, it is evident from the system equations that the κ dynamics become fast as the vehicle's longitudinal velocity V_x moves towards zero. This tells that the it will become difficult for the controller to stabilise the slip as the velocity decreases, as is also evident from the literature [233, 87]. Hence, a cut-off velocity ($V_{x,\text{cut-off}}$) is set to mitigate that.

As the plant and prediction model is the same here, the decription below fits both the models. Based on the model equation (6.11), it is seen that the state vector in this case is $[\kappa, V_x, T_s]^T$ whereas the input is simply the brake torque T_b. The quarter-car is clearly a Single Input Multi Output SIMO system when the weightage on both the longitudinal slip κ and the tread surface temperature T_s is non-zero, and it is expected that kappa being the first direct state (from T_b i.e. the only input) affecting the tread temp, would be used to quickly heat the tyre in case heating is required, as is also evident in the quarter-car simulations. A lower bound ($\kappa < 0$ in braking) on κ is important to ensure that the tyre lateral force producing capability doesn't deteriorate too much because of running a higher longitudinal slip κ than required to extract the maximum longitudinal force and vice-versa for the upper bound when tyre would be hotter than reference temperature (optimal, $70°C$ as can be seen in Figure 6.10 (a)). A lower bound on the brake torque is also set to ensure a realistic brake torque saturation. A T_b value a bit higher than the torque required to lock the tyre ($-2000Nm$).

The plant dynamics are simulated with a time step of $1 \times 10^{-3}s$ to capture the non-linearities of the longitudinal slip κ dynamics which fluctuate the fastest.

6.5.2 Quarter-car SDRE controller

This sections explains how the SDRE controller equations were setup including that of the prediction model. As mentioned before, there is a need to represent the non-linear system in a linear-like SDC form. The chosen SDC representation is then checked for stabilisability across the whole possible sets where states and inputs can propagate. The reader can refer to Appendix A for the detailing of SDC parameterisation.

In the SDRE, the pacejka-based tyre force equations are left out from the controller parameterisation and the tyre force is computed external to the SDC computation as is shown in Figure A.1. This technique is taken from [234, 235]. It helps to leave out the complicated pacejka-based tyre force function out of the SDC parameterisation and at the same time helps with including the state dependencies within the tyre force equation.

The MARE solution is implemented as shown in [236] which is based on the technique showed in [237]. The solution is based on the eigen-decomposition of the associated Hamiltonian matrix as stated in [85].

Reference generation

An important aspect in controllers is the definition of the reference. Here, the input for the plant is the product of the computed gain matrix and the error between the current state and the reference state (Figure 1.26):

$$\mathbf{u} = -\mathbf{K}\mathbf{e} \tag{6.16}$$

where

$$\mathbf{e} = \mathbf{x} - \mathbf{x_{ref}} \tag{6.17}$$

As seen before, the reference values in the case of quarter-car are kept constant. An obvious choice for the longitudinal velocity reference is 0 as it's a braking manoeuvre. But in the case of SDRE, it was seen that the gain computation was failing in such a case and so the reference velocity is set as follows by assuming a fixed deceleration a_{fixed} of the vehicle and the reference velocity being the result of achievable velocity change within the controller sampling time step Δt :

$$V_{x,ref} = V_x - a_{fixed}\Delta t \tag{6.18}$$

The reference for the longitudinal slip must be kept at the value where the maximum longitudinal force is achieved. For the given parameterisation, it is seen that -0.08 is good compromise across different temperature values and the given mass (tyre normal force, F_z) of the quarter-car ($3132N$ here as the nominal tyre load of full-car). But here, the reference for the longitudinal slip κ is kept equal to -0.1 as a fixed value. Because of the inevitable steady state error, -0.1 helped in achieving the steady state slip value of around -0.08. Finally, the reference value for the T_s is kept equal to the optimal temperature of the tyre i.e. $70°C$ for the tyre parameterisation used. But it was seen that when the state error for T_s is very high, the controller didn't perform well, so based on the initial condition of T_s a small initial error (by setting a lower $T_{s,ref}$ as compared to $70°C$) resulted in a better performance. For example, in the case of initial temperature of $30°C$ a $T_{s,ref} = 50°C$ performed much better as shown in Appendix B.

Tuning

The controller sampling frequency is checked and the value of $1000Hz$ is important to keep the system stable, otherwise the control of slip is very noisy (smaller controller frequencies). Even with a value of $1000Hz$ the controller oscillates to some extent when the vehicle velocity is lower than $14m/s$, but because of the cut-off velocity of $10m/s$, this is not a problem. There is no possibility of tuning the prediction horizon as it is set to infinity in the SDRE setup.

The tuning of weights in an optimal-control based controller is much simpler as compared to a conventional controller because the weights are directly connected to the state variables. For the start of tuning, the technique of setting the corresponding state weighting as a reciprocal of the square of its maximum achievable value $q_{ii} = 1/x_{i,max}^2$ [78] didn't help in terms of achieving a solution for gain computation but it gave an idea about where to start. Also, Mehmet et al. [238] show that the tuning of an SDRE controller is not a straightforward procedure and requires some hit and trial. Eventually, it is seen that the final weighting for κ is needed to be very large because of the fast dynamics. The weighting on the V_x doesn't show any performance benefit and the weighting on T_s is non-zero only in the case where optimising the tyre temperature is important. Any weighting on the control input T_b would result in suppressing the optimally calculated torque, so, it is kept equal to 0. All final weightings are stated in Table 6.3, where the first case is a pure control of κ only (while a feasible numerical solution of the gain is achieved with a non-zero weighting on V_x) and another case is where weighting is also given to control T_s which helps in optimising the tyre temperature that may achieve higher grip overall but at least heat the tyre faster which can help to simply heat the tyre quicker over multiple braking manoeuvres. The results of both these cases for a given set of initial and boundary conditions are shown in Appendix B.

Table 6.3 Quarter-car (QC) controller weights

		QC-SDRE		QC-NMPC	
State	Weight Variable	Value: κ - control	Value: κ and T_s - control	Value: κ - control	Value: κ and T_s - control
κ	q_κ	1×10^{10}	1×10^{10}	1×10^{4}	1×10^{4}
V_x	q_{V_x}	1×10^{-1}	1×10^{-1}	0	0
T_s	q_{T_s}	0	1×10^{6}	0	5

6.5.3 Quarter-car NMPC controller

This sections explains how the NMPC controller equations were setup including that of the prediction model. Here the prediction model is presented in the non-linear state-space format as shown in equation (6.11) in an implicit form. Here, the full non-linear model including the non-linear tyre equation is computed within the controller and not externally as seen in SDRE.

In NMPC it is also possible to set state and input bounds within the optimisation computation. In this work, mainly the bounds on κ and T_b are important and are implemented (as discussed in 6.5.1). The MATMPC toolbox requires multiple settings relevant to the numerical solution which are defined in Table 6.4.

In this work, for the objective function (1.52), the output vector $\mathbf{y}(t)$ and the the terminal output vector $\mathbf{y}(t_0 + T_P)$ are the same as the state vector $[\kappa.V_x, T_s]^T$.

Table 6.4 NMPC - MATMPC toolbox settings used

Setting parameter	Value
Hessian approximation	Gauss-Newton
Integrator-type	Implicit Runge-Kutta 3rd order
QP condensing	full
QP solver	qpOASES (full-condensed QP)
hotstart	no
RTI scheme	no

Reference generation

The reference for κ is kept the same as in the quarter-car SDRE as shown in the section 6.5.2. For V_x the reference is simply kept equal to 0 because it is a braking manoeuvre and the car aims to stop/slow down. And, the reference for T_s is kept equal to the optimal temperature value $70°C$ for the tyre as it was easy to achieve consistent performance across different conditions in the NMPC controller and a changing $T_{s,ref}$ was not needed like in SDRE. A non-uniform grid of references is also possible in the NMPC-based controller but currently is not available within the MATMPC toolbox. Although, the performance without that is satisfactory and it will only increase the amount of tuning variables, thus complicating the development.

Tuning

For the controller sampling time T_s selection, the fastest and unstable dynamics of the system are important to consider (here $\dot{\kappa}$). The κ dynamics are seen to be around 20-30 Hz, as is also seen in the literature. As a rule of thumb in control theory, the controller's sampling time must be 4-10 times faster than that of the process time constant. The faster the controller, the easier it will be to catch the changes in the states of the system, such that they can be controlled. Considering the 20 Hz of $\dot{\kappa}$, we see that at least 100 Hz (5 times) of controller frequency is necessary. Based on that, 3 values for the controller frequency are chosen $[100, 150, 200]Hz$, corresponding to $[10, 7, 5]ms$ of sampling time T_s. The difference between the rise time for a step change in κ is seen to be within $5ms$ and so the smallest value of $100Hz$ is chosen. In terms of settling time, it lags only by $10ms$ and has a negligible overshoot. For these tests, only the slip state is weighted (with a value of $1e04$) and the number of horizon steps (N) is kept constant at 2, corresponding to prediction horizons of $[20, 14, 10]ms$. Now comes the selection of the *prediction horizon* (T_P with N samples). Increasing N is costlier in terms of computation, on the other hand it helps the controller look into the future and improve stability. In this work, Increasing N also helps in controlling T_s (by running a higher $|\kappa|$ initially to heat the tyre quickly and then come back to zero error in slip. But the same effect is also seen by increasing the relative weight on the T_s. Between N and the weight on T_s, N is more costly as it has a direct positive correlation with the computation time of the controller. Although the computation time is out of scope of this thesis but in the future if this technique is implemented then computation time will become a big factor for real-time performance.

Once the controller settings (T_s and N) are selected, focus is shifted towards the weights set on the states and control input in the cost function (1.52). As NMPC is a model-based controller, this leads to the tuning being done based on the parameters directly connected with the states of the system model. Also, another benefit is the fact that the number of tuning parameters are less as compared to the industry standard rule-based controllers like the ABS in production cars [87].

As is seen in the quarter-car system model (6.11), there are 3 states, i.e. $\mathbf{x} = [\kappa, V_x, T_s]$ and the control input being $\mathbf{u} = T_b$. It is obvious not to put any non-zero weight on the control input T_b as that would lead to suppressing the optimal T_b value. In an ABS system, to meet the objective of generating the maximum longitudinal force (or maximum longitudinal acceleration) while maintaining steer ability is simply by following the reference set for the optimum longitudinal slip κ. If the reference longitudinal slip κ is maintained, it will automatically ensure that the desired velocity of 0 ($V_{des} = 0$) is met as soon as possible, so the weighting on it was set to zero. And the weight on κ is decided by using a range of values. It is seen that a weight of 1×10^4 is sufficient and increasing the weight beyond that didn't result in any reductions in rise time to a step response. Finally, the weight on T_s produces two cases, as seen in 6.5.2 and Table 6.3. For the case of only κ control (Case 1), the weight q_{T_s} is simply 0. And in the case of κ and T_s control (Case 2), the weight q_{T_s} is non-zero. Although the quarter-car is not tested extensively across a range of initial and boundary conditions, by some preliminary tests it was evident that varying the q_{T_s} with the initial conditions of T_s and V_x in a braking manoeuvre and also making it 0 when the velocity drops below a certain threshold ($V_{x,cut-off} = 20m/s$ here) helps with a consistent performance. It is seen that in a braking manoeuvre as the velocity drops, the heating of the tyre stagnates, thus, heating the tyre provides no benefit after that, so the weight on T_s is made 0 below this $V_{x,cut-off}$. Finally, this concept of variable weights is applied in the full-car NMPC controller. Table 6.3 states the chosen weights in the case of quarter-car NMPC, tested on a case with $T_{s0} = 30°C$, $V_{x0} = 40m/s$ and boundary conditions of $T_a = 28°C$ and $T_t = 35°C$. For the lower bound on κ, an arbitrary value of -0.12 is chosen. For real implementation, there can be a number of factors that can affect the choice. To name a few, drop in lateral grip, hydraulic system capability to stabilise slip beyond peak, gains in temperature, gains in braking distance performance, etc. can affect the choice.

6.6 Full-car simulation and NMPC controller

The quarter-car simulations already give a good idea on how the system will response without representing all the details of the full-car, but to see the real world applicability, the details like connection between the 4-wheels and load transfer are important to consider. The full-car simulation data-flow architecture which is representative of the setup in Simulink is shown in Figure 6.13. The plant used in these simulations is completely different than the prediction model inside the controller. The plant is composed of the full-car model coupled with the MF-evo. Whereas the prediction model is the "myVeh" as defined in 6.4.1.

For the full-car simulations it is chosen to move forward only with the NMPC based controller because the implementation of the SDRE based controller on quarter-car shows infeasibility in MARE solutions and would have become even more complicated to debug in the case of a full-car. Also, the instability of quarter-car SDRE controller is high as compared to NMPC (Figure B.1 and B.2). In this respect, the NMPC shows good robustness in terms of tuning the system.

The concerned states in the full-car case are simply based on the states that are modelled in the prediction model "myVeh", $\mathbf{x} = [\kappa_1, \kappa_2, \kappa_3, \kappa_4, V_x, T_{s1}, T_{s2},$-$T_{s3}, T_{s4}, \Delta F_z]^T$. These state variables are especially required as feedback from the plant as the NMPC-based control requires full-state feedback. The subscript numbers here are defined for each wheel as is also described in 6.4.1. Here, the control input is $\mathbf{u} = [T_{b1}, T_{b2}, T_{b3}, T_{b4}]^T$, i.e. the brake torques corresponding to each wheel. Here, as will be discussed below, the references are made variable based on the state feedback and some of the weights are also made a function of initial conditions and the state feedback. The lower bound on the κ belonging to the rear wheels is tighter as compared to the front wheels to ensure a stable behaviour ($\kappa_{1,bound} = -0.12$ and $\kappa_{3,bound} = -0.11$). An accurate quantification of these bounds must depend on the real application. Also, the torque bounds on the front and rear wheels are different (front higher than the rear - $T_{b1,bound} = -2200Nm$ and $T_{b3,bound} = -2000Nm$), set higher than the wheel locking limits, as is also discussed in 6.5.1. Lastly, the plant dynamics here are simulated with a time step of $1 \times 10^{-3}s$ to capture the non-linearities of the system.

The representation of the prediction model is done in the same way as described in 6.5.3. The optimisation at each controller sampling instant is done with the MATMPC toolbox with the settings as defined in Table 6.4. The cases of in-feasibility are not discovered in the work and so no such techniques like limiting the maximum iterations are applied. For the objective function (1.52), the output vector $\mathbf{y}(t)$ and the terminal output vector $\mathbf{y}(t_0 + T_P)$ are the same as the state vector $\mathbf{x} = [\kappa_1, \kappa_2, \kappa_3, \kappa_4, V_x, T_{s1}, T_{s2}, T_{s3}, T_{s4}, \Delta F_z]^T$ and the input vector is $\mathbf{u} = [T_{s1}, T_{s2}, T_{s3}, T_{s4}]^T$.

Reference generation

Here, the reference for the κ_i was especially required to be variable with the state as the peak of the F_x characteristic curve moves with changing load. In addition, the impact of the tread temperature is also included. The κ_{max} values as a function for the reference tyre model are as shown in Figure 6.14. As seen in quarter-car NMPC controller, the reference for V_x is set equal to 0. Also, for the load transfer state ΔF_z there is no concern about controlling it, so their reference and weight are set as 0. Finally, as seen in 6.5.3, the reference for the tread temperatures of all the tyres is set as $70°C$.

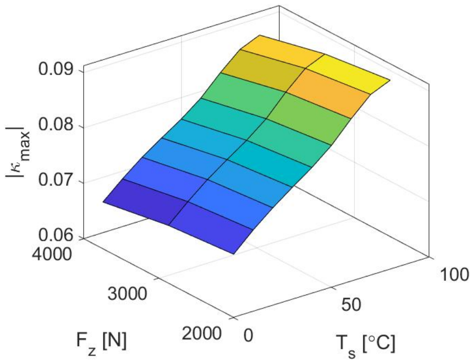

(a) Longitudinal slip κ reference for the controller - $\kappa_{max}(F_z, T_s)$

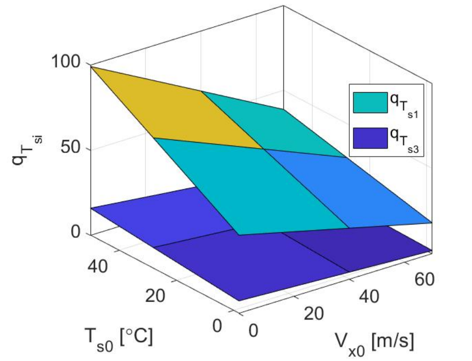

(b) Full-car variable controller weights - $q_{T_{s1}}$ and $q_{T_{s3}}$

Fig. 6.14 Variable reference as a function of T_s and F_z and variable weights on T_{si} for (κ & T_s)-control

Tuning

In a full-car simulation, the tyres experience changing loads especially because of the longitudinal load transfer in braking. This leads to a change in the sharpness of the peak of tyre characteristic curves, especially the tyres with higher loads have sharper F_x *vs* κ peaks. In a braking manoeuvre, the front tyres experience higher loads. Due to this reason, it becomes difficult for the controller to stabilise $\kappa_{1/2}$, as is seen in the preliminary tests, especially when the vehicle velocity is small. To mitigate this, it is seen that increasing the controller's sampling frequency makes a huge difference. So, the adequate controller sampling frequency is seen to be $1000Hz$, which still struggles to stabilise the $\kappa_{1/2}$ at the steady-state value with a zero error (as seen in the full-car controller results, Figures C.1 to C.6) Appendix C. The *prediction horizon* T_P is kept the same as $20ms$ which leads to $N = 20$, as seen in the case of quarter-car NMPC 6.5.3.

Coming to the weights in the cost function (1.52), first, the weights for the κ_i (q_{κ_i}) are finalised with higher weight given to the slip of the front wheels to ensure stability because of the reason of higher load as explained above. The weights related to V_x and ΔF_z (q_{V_x} and $q_{\Delta F_z}$) are kept equal to 0 as is explained in the reference generation section above.

As seen in the quarter-car weights tuning §6.5.3, the weights related to the tread temperature for the case of (κ and T_s) - control, are made a function of the initial conditions T_{s0} and V_{x0} including the zero value when $V_x < 20m/s$ (as shown for q_{T_s} in Table 6.3). Of course, the values for the weights on T_{si} in the full-car case are different but the dependencies are similar to the quarter-car case. This is achieved with the use of look-up table in Simulink, which is depicted in Figure 6.14. The variable weights for T_{si} ($q_{T_{si}}$) were chosen based on tests with different initial conditions and to achieve a consistent overall performance the weight values were tuned. Specifically, as the ($q_{T_{si}}$) values are non-zero only in the case of (κ and T_s) - control, it was made sure that the increase in braking distance didn't rise higher than 2% and the maximum temperature in the manoeuvre is at least greater than 5% as compared to the pure κ - control case. The final weights used are as shown in Table 6.5. As the vehicle model is symmetric, the left $(1,3)$ and right $(2,4)$ values are the same and so, only the values for the left are stated.

Table 6.5 Full-car NMPC controller weights

State	Weight variable	Value: κ - control	Value: κ and T_s - control
κ_1	q_{κ_1}	1×10^4	1×10^4
κ_3	q_{κ_3}	1×10^3	1×10^3
V_x	q_{V_x}	0	0
T_{s1}	$q_{T_{s1}}$	0	$f(T_{s0}, V_{x0})$ and 0 $\iff$ $(V_x{<}20 \vee \frac{dT_s}{dt}{<}0)$ **(Fig. 6.14 B)**
T_{s3}	$q_{T_{s3}}$	0	$f(T_{s0}, V_{x0})$ and 0 $\iff$ $(V_x{<}20 \vee \frac{dT_s}{dt}{<}0)$ **(Fig. 6.14 B)**
ΔF_z	$q_{\Delta F_z}$	0	0

6.6.1 Tests and Metrics

When all the simulation setups have been explained, there are 3 final full-car controller setups used for the final tests. These 3 setups are explained as follows:

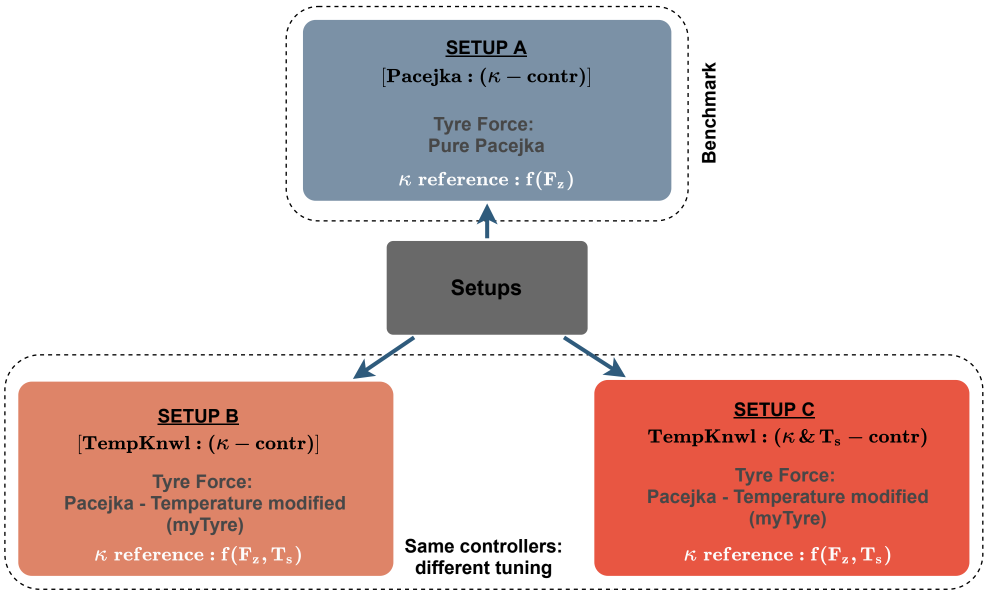

Fig. 6.15 Controller setups

Controller setups

- **Setup A [Pacejka:(κ-contr)]:** This controller setup's prediction model consists of "myVeh" (6.4.1) model with the reference Pacejka model (as used in "myTyre" (6.2) without any tread surface temperature dynamics (so, states $[T_{s1}, T_{s2}, T_{s3}, T_{s4}]^T$ are not available). Hence, the prediction model only consists of 6 states $[\kappa_1, \kappa_2, \kappa_3, \kappa_4, V_x, \Delta F_z]^T$. The parameterisation of this tyre model is taken as of the tyre operating at ($40°C$). Such a setup, to a good extent, replicates the controller as shown by Pretagostini et al. [87], which he shows performs much better than the state of the art rule-based controllers. The only difference here is that the first order torque rate dynamics haven't been considered inside the prediction model and the tyre force equations have been included inside the controller instead of feeding as inputs from wheel load sensors. Hence, this setup can be considered a benchmark for this work and results of the proposed controller setups (Setup B and C) can be compared relative to this setup. As regards the selection of tyre force model's parameterisation at $40°C$, it is like representing the tyre behaviour that acts like an average amongst the whole range of T_{s0} shown in Table 6.16. Even when a parameterisation at some other temperature is selected, the controller performance is expected to degrade at temperatures far above or below that. The reference generation being another important factor, Pretagostini et al. [87] use the slip reference input as a function of tyre load F_z for the the parameterisation used in their work. In this work, the reference is taken as the value that can perform well across the whole temperature range and maintain a stable behaviour (not go beyond the peak of F_x characteristic). And so, here, the reference generation is only a function of the tyre normal load (F_z). Such a setup of parameterisation and the reference slip values helps a controller with no knowledge of temperature to perform good enough across all the tests. The controller weights on the longitudinal slips (κ_i) are set as is shown in 6.6. For ease of readability, it is named **"Pacejka:(κ-contr)"** meaning that it's tyre model is only based on the Pacejka tyre force equation and has no temperature effects, and only tries to control the longitudinal slips i.e. κ_i.

- **Setup B [TempKnwl:(κ-contr)]:** This controller setup's prediction model consists of the full "myVeh" (6.4.1) model combined with the "myTyre" (6.2) i.e. with the tread surface temperature dynamics. Hence, this controller is able to also predict the change in tyre grip and stiffness with the changing temperature conditions throughout and between each test. This helps it control the tyre slip more precisely as compared to Setup A **Pacejka:(κ-contr)**. Here, the controller weights are non-zero only for the longitudinal slips (κ_i) and equal to the values used for Setup A (as defined for the case of κ - control in Table 6.5). For convenience, it is named **"TempKnwl:(κ-contr)"** meaning that it has the **Temp**erature **Kn**o**wl**edge (**TempKnwl**) and just controls the κ_i.

- **Setup C [TempKnwl:(κ & T_s-contr)]:** This controller setup is the same as described in Setup B with a slight difference being that, here the controller weights on tyre tread temperature states (T_{si}) are non-zero (as defined for the case of κ and T_s - control in Table 6.5). Especially, the weighting on T_s is kept non-zero to check how heating the tyre more towards the optimal temperature could help in terms of braking distance. For convenience, it is named **"TempKnwl:(κ & T_s-contr)"** meaning that it has the temperature knowledge the same as Setup B, and it tries to control the κ_i as well as the T_{si}. Hence, Setup B and Setup C only differ in terms of the weights (Figure 6.15).

The Setup B acts like a controller that has better knowledge of the plant dynamics as compared to the Setup A and so, these 2 are compared across the various tests. And, Setup C tries to optimise the tyre temperature while ensuring the slip dynamics are stable which can potentially lead to faster heating times or possible reduction in the braking distance as compared to both the other setups. Hence, for all the described tests, these 3 controllers will be compared while keeping the Setup A as the reference/benchmark.

Tests

The manoeuvre being performed here is a braking manoeuvre starting at some initial velocity V_{x0} and then a full brake demand is provided by the driver, which activates the NMPC-based ABS, eventually leading to optimally calculated brake torques going to each wheel. The road is assumed smooth and with a coefficient of friction of 1. As our main concern lies around thermodynamic boundary conditions, various tests with different track (T_t) and ambient (T_a) temperatures (fixed boundary conditions) are chosen, relating to the 3 different weather conditions, viz. Winter, Autumn/Spring, and Summer. For each of these boundary conditions, 3 initial condition temperatures are defined in the tests, viz. cold, warm, and hot. These tests are then performed with 2 different initial velocities viz. $40m/s$, and $70m/s$. Two initial velocities were chosen as the temperature behaviour linked to friction power and convection is highly dependent on the velocity. In each test, the simulation is stopped at $10m/s$ concerning the controller's instability at lower velocities (as can be seen in the $\dot{\kappa}$ equation (6.7) and is also discussed in 6.5.1). In total there are 18 tests per controller setup, as shown in Figure 6.16. In the results section, the test names (Test 1, Test 2, ...) as shown in this figure and the setups as previously mentioned will be used.

Initial Velocity [m/s]	Weather [deg. C]		Initial Temperature [deg. C]		
			Cold	Warm	Hot
40 m/s	Winter	T_t = 0 T_a = -2	Test 1 -2	Test 2 9	Test 3 18
	Autumn/Spring	T_t = 18 T_a = 12	Test 4 12	Test 5 30	Test 6 50
	Summer	T_t = 35 T_a = 28	Test 7 28	Test 8 50	Test 9 65
70 m/s	Winter	T_t = 0 T_a = -2	Test 10 -2	Test 11 9	Test 12 18
	Autumn/Spring	T_t = 18 T_a = 12	Test 13 12	Test 14 30	Test 15 50
	Summer	T_t = 35 T_a = 28	Test 16 28	Test 17 50	Test 18 65

Fig. 6.16 Test conditions

To assess the performance of each setup, there must be defined some metrics to quantify the time history of various state variables. As this work mainly focuses on high-level controller decision making, it is not relevant to include all the metrics that are in general used to assess ABS performance (like human related factors). Also, as the number of tests are large due to the various boundary conditions, it is better to choose a few important factors than a variety.

Here, for each test, 2 main metrics were chosen to assess the performance of the proposed controller setups:

1. **Braking distance** (s_{br}): This is defined as the distance the vehicle covers from the time the brake input is given to the time it reaches the set cut-off velocity ($V_{x,cut-off}$) of $10m/s$ as defined above. As, the main objective of ABS is to ensure the tyre deliver the maximum possible force, so, braking distance is the perfect metric for that. To assess the performance of this high-level controller, this metric is enough to show the difference in performance.

2. **Maximum tread temperature** ($T_{si,max}$): This is the maximum value of the tread surface temperature that is reached in each test. The subscript i refers to the wheel identity on the car (1, 2, 3, 4)≡(FL, FR, RL, RR). The higher its value the more the carcass of the tyre heats up using the heat coming from the tread, of course depending on the initial temperature of the carcass. In such a short braking manoeuvre, an increase in the maximum temperature value can easily depict that there is faster and overall more heating of the tread.

6.7 Results

6.7.1 Full-car results

The test results mentioned in 6.6.1 for the full-car are presented. As the total number of tests are 54 (18 tests for each setup), the results are presented in the form of a plot of the relative metrics, to keep things comprehensible. The variables' and inputs' trajectories over time are shown in Appendix C while for one of the tests (Test 5), is presented here for better understanding (Figure 6.21). For both the metrics, results are presented as percentage change with respect to the value of the Setup A (as discussed in 6.6.1). For the maximum temperature, only the results of the left side of the vehicle are provided as the differences between left and right tyres was insignificant due to the manoeuvre being symmetric (6.6.1).

Braking distance

In this section the braking distance performance is compared with respect to the chosen benchmark setup (Setup A [Pacejka:(κ-contr)]). As previously mentioned, all the values are in percentage change with respect to the Setup A. For absolute values, the reader can refer to Tables C.1 and C.2 in Appendix C.

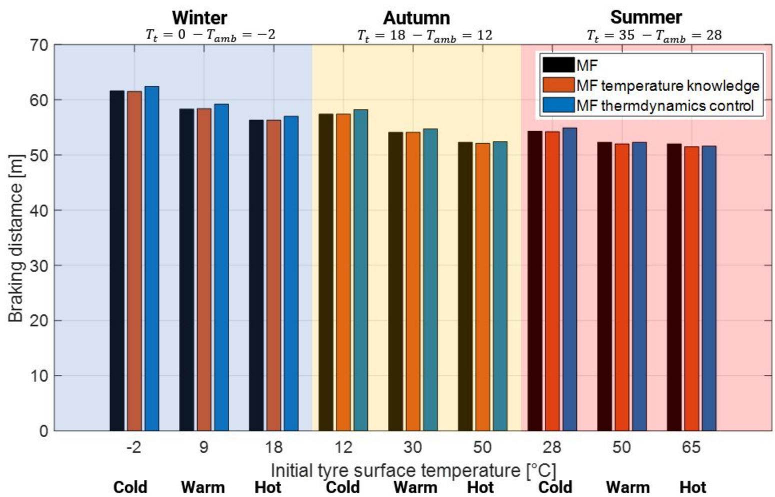

Fig. 6.17 Change in braking distance relative to standard MF starting at 40 m/s

The results are presented in 2 plots (Figure 6.17 and 6.18), for each initial velocity for the manoeuvre ($40m/s$ and $70m/s$). Now, comparing Setup B

[TempKnwl:(κ-contr)] to Setup A, it is seen that there is improvement in the braking distance as the boundary and initial conditions get hotter and hotter, with a maximum improvement of 1%. This clearly shows that giving the controller the knowledge of tyre temperature leads to better performance where the parameterisation of Setup A doesn't match well with the reality. Now, comparing Setup C [TempKnwl:(κ & T_s-contr)] to Setup B, it is seen that as the controller's energy is also spent in controlling the tyre temperature (making it closer to optimal temperature $70°C$ for better grip) there is no improvement in braking distance, although tyre temperature increases more (Figure 6.19), which could at least provide benefits in heating the tyres faster. A clear reasoning for this comes from the fact that an increase in temperature comes at the cost of running higher slip than the slip reference, which leads to a decrease in the tyre force (thus, the increase in braking distance) and the increase in grip is not enough to compensate for the lost tyre force. A clear reasoning why the temperature is controlled at the cost of slip is that the connection between the input brake torque T_b and the tyre temperature T_s is not direct, but via longitudinal slip κ. This behaviour is even easier to see in the quarter-car equations (6.11).

Now, similarly looking at the results of $70m/s$, comparing Setup B to Setup A similar improvements are seen as compared to the results of $40m/s$. And, comparing Setup C to Setup B, the loss in braking distance is less as compared to the results of $40m/s$ because at higher velocities (higher friction power) the tyre heating is higher which leads to more gains in grip due to temperature over the manoeuvre. But, still this increased grip is not enough to compensate for the lost braking force to heat the tyre.

And finally, comparing Setup C to Setup A, it is seen that braking distance performance is poor until the warm tyre conditions in Autumn/Spring (Test 5), and after that it shows improvements. But as will be seen in next section of temperature, the Setup C is heating the tyre more in all conditions as compared to Setup A and Setup B.

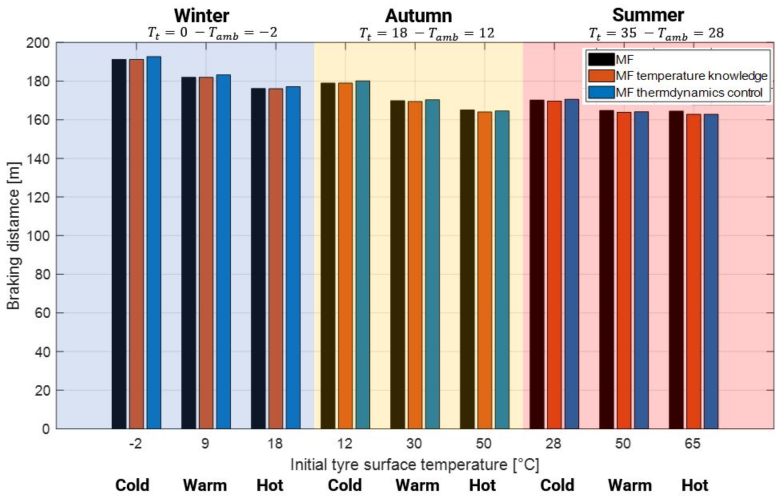

Fig. 6.18 Change in braking distance relative to standard MF starting at 70 m/s

Temperature behaviour

Now, looking at the thermal performance for both initial velocities (Figures 6.19 and 6.20), it is seen that both the Setup B and Setup C lead to more heating as compared to Setup A in all the weather conditions (test cases - Table 6.16). Although Setup A and Setup B have no consideration of optimising the tyre temperature, still the Setup B [TempKnwl:(κ-contr)] shows better performance as compared to Setup A.

Finally, comparing Setup C to Setup B where these two setups differ only in the sense that Setup C additionally tries to optimise the tyre temperature, a huge improvement is seen in terms of maximum temperature, whereas the maximum gain is $20-25\%$ as compared to Setup B. And, looking at the trend, it's clearly visible that the performance is much better in Winter conditions as compared to Summer. The reason being the fact that the difference between boundary conditions and tyre temperature is very large in Summer conditions, which leads to higher convective cooling and so, less heating gains.

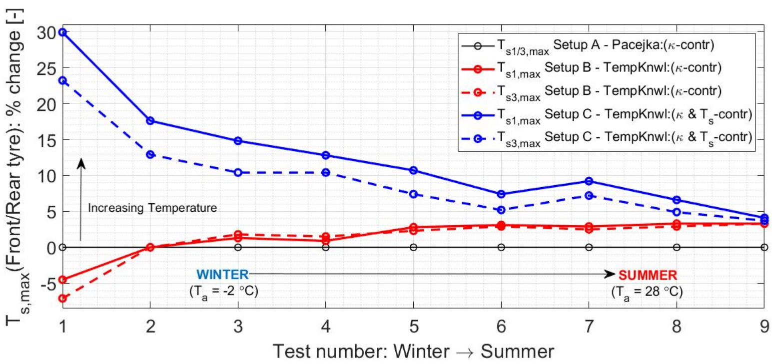

Fig. 6.19 Percentage change in maximum front and rear tyre tread temperature ($T_{s1/3,max}$) relative to Setup A starting at 40 m/s

6.8 Discussion

In a braking manoeuvre it was anyways expected that the temperature won't rise a lot due to the short duration of the manoeuvre, but for example in a lap on a race track, such small consistent efforts towards optimising the temp can lead to big improvements over the warm-up lap/race for a gentlemen driver.

Even if the Setup C is not able to provide decreased braking distance (and only gives an advantage in the increased tyre temperature, which can result in quicker tyre heating), it can at least work as a controller (Setup B) that is aware of the changing grip factor with the temperature (as seen in Chapter 2) and can take better decisions on torque input.

Another weight setting that is tested on the proposed controller (Temp-Knwl controller), is to set the weights on Longitudinal slip κ_i and T_s as zero and set a high weighting on the longitudinal velocity ($q_{V_x} = 1 \times 10^5$) of the vehicle. This setting is like telling the controller to optimise the slips and temperature by itself to achieve the quickest (optimal) drop in velocity. This setting is called Setup D for convenience and is explained better in Appendix C. Ideally, the prediction horizon must also be long enough to cover a considerable part of the braking manoeuvre, which would also enable it to see the

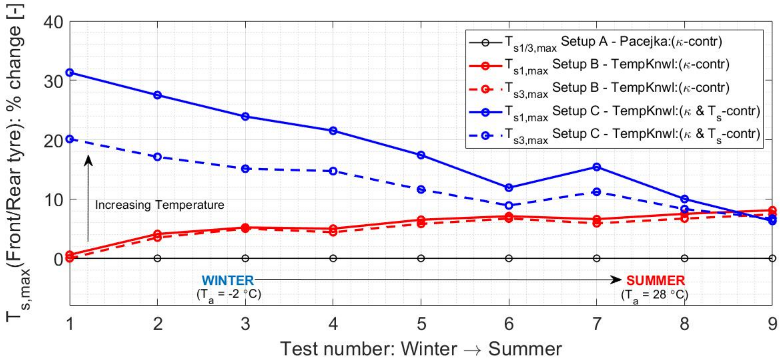

Fig. 6.20 Percentage change in maximum front and rear tyre tread temperature ($T_{s1/3,max}$) relative to Setup A starting at 70 m/s

slowly (relative to κ) varying tyre temperature effect on grip. But the SQP solution failed in that case. As a consequence of that, a smaller prediction horizon is tested ($N = 2$ and $T_s = 0.001s \rightarrow T_P = 0.002s$). In this latter case, the SQP solved successfully and the optimally calculated brake torques by the controller simply lead to longitudinal slips being the $\kappa_{i,max}$ for each tyre, which is simply the same as what is achieved in Setup B [TempKnwl:(κ-contr)]. Not to mention, the computation times of this controller are much longer than the Setup B, as the controller has to solve a heavier QP as compared to Setup B. And the computed solutions are very noisy, as is seen in Figure C.7

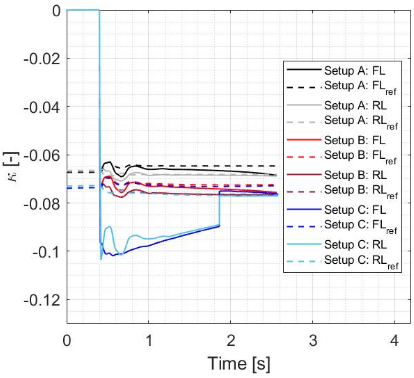

(a) Longitudinal slip $\kappa_{1/3}$

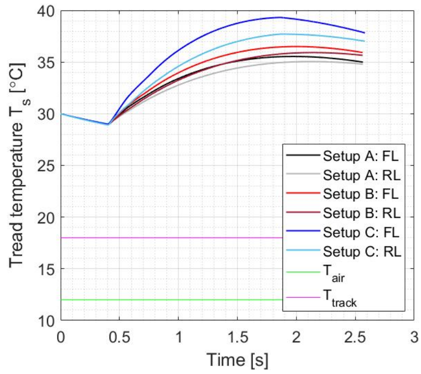

(b) Tread temperatures $T_{s1/3}$

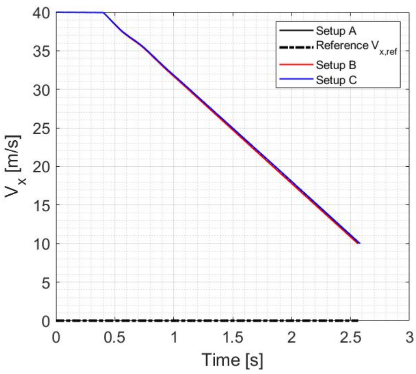

(c) Vehicle longitudinal velocity V_x

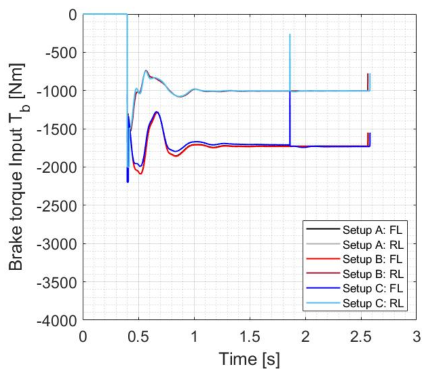

(d) Brake torque control input $T_{b1/3}$

Fig. 6.21 Time histories of variables and control inputs for the 3 setups of Full-car NMPC ABS controller in Test 5 (Table 6.16)

Conclusions and Further Developments

An innovative model-based control logic technique that take into account the multi-physical dependencies of the tyre properties on temperature, wear and aging effect and their variation during the entire life cycle, and the capability to understand the external environment and to correctly estimate the vehicle state in all the possible operating and environment conditions, in order to increase the vehicle performance and safety in critical scenario, has been presented. Therefore, an advanced procedure for a calibration of a multi-physical MF-based tyre model has been described. The identified set of MF-evo parameters has been compared to the experimental data acquired on track in a particularly demanding long-run motorsport application where both thermodynamic and wear effects can not be neglected, highlighting a good agreement between the model outputs and the dynamic behaviour of the real tyres. The co-simulation of the MF-evo model with additional tyre real-time thermal and wear models can represent a valuable instrument for the development of both safety and performance applications, in which tyre characteristics can vary significantly across the entire tyre life. Moreover, in order to correctly estimate the vehicle state the performance of different model-based state estimators (Extended Kalman Filters, Unscented Kalman Filters and Particle Filters) has been compared in terms of estimation accuracy and the computational cost for a chosen vehicle. Concerning the obtained results, the EKFs and the UKFs show a better state estimation using the vehicle model presented and the Pacejka macroparameters computed. Considering the mean value of the RMSE computed per each tests, the S-UKF exhibits the lowest value whereas the other UKFs exhibit a value which is about the 20% higher; the EKFs show the same mean value if compared one each other but this is about the 10% higher than the one reached by the S-UKF; Finally, the SYSTres-PF shows the lowest RMSE mean value if compared with the other implemented PFs, but if compared to the others the PFs exhibit the higher values, in particular the STRAres-PF shows the highest one. Concerning the computational burden required by each state estimator which can be considered as proportional to the time taken by the filter to estimate 1 second of real time, the FO-EKF is characterized by the lowest amount of time required, thanks to its simple algorithm. The other EKFs present a value which is about the 150% higher. Considering the UKFs, the SIMP-UKF and the SPHE-UKF require lower run-time than the S-UKF and the G-UKF, this latter is characterized by the highest one if considering only the Kalman-based filters, it is about the 340% higher than the lowest one. Considering the PFs, the time required is one order of magnitude higher than the Kalman-based one, they take about one-third of second to estimate 1 second of real time. However, the overall state estimate is not always accurate, this may be mitigated adopting a complete Magic Formula, with micro-parameters instead of macro-parameters. Moreover, it may be interesting to consider a tricycle vehicle model instead of a bicycle one in order to take into account the lateral load transfer effect. In order to improve the VSA estimation the tyre model may be a key factor, in this work the macro-parameters are fixed, but considering their update during filter execution, due to thermodynamics and wear effect, could lead to better results. An investigation on how accurate information regarding the state of the real system of the parameters concerning the controller model could affect the behavior of the real system, represented in the form of the high-fidelity validated plant model has been presented. The influence of the tyre thermal dynamics, the impact of the possible ageing effects and the contact with different road pavements have been examined. Wrong parameters in the definition of the internal model of the NMPC might compromise the control performance, especially when the vehicle is supposed to drive at the limit of handling conditions. Specifically, a controller characterized by an overestimation of the grip conditions is forced to compute too aggressive control actions that might bring the vehicle in unstable and unsafe conditions, that are very difficult to handle for the controller itself. On the contrary, an underestimation of the grip might reduce the performance of the controller, which is forced to compute too conservative control actions. Moreover, the parameters of the cost function play an important role in defining the level of performance that the controller is required to achieve. A high weight on the travel time forces the vehicle to drive fast along the path, hence requiring effective proper internal model parameters to describe the vehicle behavior at the limit of handling. Instead, a more conservative tuning (i.e., high weights on side-slip, lateral error, orientation error) can be effective with also less precise coefficients, as the vehicle is not supposed to travel at the limit of handling. Due to these statements, future development could include a real-time estimate of the tyre and the environment states, along with an adapting strategy for the weights of the cost function will be included in the whole analysis.

A new control architecture for vehicles, based on the estimation of the maximum achievable road friction coefficient in different environmental conditions, based on both bicycle model to evaluate the state of the vehicle and a tire Magic Formula model based on a slip-slope approach is presented. The introduction of the grip value in ADAS application, in particular for the longitudinal dynamics of the vehicle chassis, composed of Adaptive Cruise Control (ACC) and Autonomous Emergency Brake (AEB), and the Antilock Braking System (ABS), allows the vehicle to work at the maximum performance in all operating conditions. According to the results, the control system has been improved by the involvement of the current and potential friction coefficient evaluated in run-time. The improvement basically results from the development of a control system that is able to avoid collisions in any environmental condition. The potential grip has been therefore demonstrated to be crucial for the autonomous driving systems.

Finally an application of model-based optimal control based controller (NMPC) to a vehicle dynamics control system with the inclusion of tyre tread thermal dynamics. The chosen tyre tread thermal model for the full-car prediction model is chosen as the simplest possible (based on first order dynamics) that shows good performance in terms of the main effects that the tyre temperature has on the tyre performance i.e. grip and stiffness, in a braking manoeuvre. The proposed controller is developed into two setups, one that just controls the slip and the other that controls both slip and the tyre temperature, both fed with the reference slip state for maximum tyre longitudinal force. The test results show that when the slip-controller is given the knowledge of tyre temperature, it performs better across the whole range of temperature conditions from the Winter to Summer, whereas the biggest improvements in braking distance are seen to be 1%. Whereas, when the slip and temperature both are controlled, based on the tuning, so as to not lose a big chunk of braking distance, a maximum of $20-25\%$ improvements in maximum tyre temperature in the manoeuvre are seen.

Another solution that was expected, was that the controller would try to heat the tyre to increase the grip which would eventually lead to improvements in braking distance, in addition to the increased temperature.

The μ value is taken equal to 1 across all cases in this project to cut down on the possibilities of combinations. But it is recommended in the future research to take the variations of different μ conditions into account as it directly affects the friction power.

Future developments will also comprehend the lateral dynamics, the impact of the road bank angle and slope, the tire combined interaction characteristics, as well as, the variations of the vehicle dynamic behaviour due to the tire intrinsic multi-physics (i.e., wear effects).

References

[1] World Health Organization. *Global status report on road safety 2015*. World Health Organization, 2015.

[2] USDOT. Early estimate of motor vehicle traffic fatalities for the first 9 months of 2019, 2019.

[3] Khashayar Hojjati-Emami, Balbir Dhillon, and Kouroush Jenab. Reliability prediction for the vehicles equipped with advanced driver assistance systems (adas) and passive safety systems (pss). *International Journal of Industrial Engineering Computations*, 3(5):731–742, 2012.

[4] Salvatore Cafiso and Alessandro Di Graziano. Evaluation of the effectiveness of adas in reducing multi-vehicle collisions. *International journal of heavy vehicle systems*, 19(2):188–206, 2012.

[5] Sang Jin Park, Tae Yong Kim, Sung Min Kang, and Kyung Heon Koo. A novel signal processing technique for vehicle detection radar. In *IEEE MTT-S International Microwave Symposium Digest, 2003*, volume 1, pages 607–610. IEEE, 2003.

[6] Jaycil Z Varghese, Randy G Boone, et al. Overview of autonomous vehicle sensors and systems. In *International Conference on Operations Excellence and Service Engineering*, pages 178–191, 2015.

[7] Monte A Dickson, Noboru Noguchi, Qin Zhang, John F Reid, and Jeffrey D Will. Sensor-fusion navigator for automated guidance of off-road vehicles, September 3 2002. US Patent 6,445,983.

[8] Jelena Kocić, Nenad Jovičić, and Vujo Drndarević. Sensors and sensor fusion in autonomous vehicles. In *2018 26th Telecommunications Forum (TELFOR)*, pages 420–425. IEEE, 2018.

[9] SAE on Road Automated Driving Committee et al. Sae j3016. taxonomy and definitions for terms related to driving automation systems for on-road motor vehicles. Technical report, Technical Report.

[10] Mingyuan Bian, Long Chen, Yugong Luo, and Keqiang Li. A dynamic model for tire/road friction estimation under combined longitudinal/lateral slip situation. Technical report, SAE Technical Paper, 2014.

[11] H. B. Pacejka. *Tire and vehicle dynamics / Hans B. Pacejka.* Published on behalf of Society of Automotive Engineers, Warrendale, PA, 2002.

[12] Ondrej Mikulas. A Framework for Nonlinear Model Predictive Control. *Msc Thesis, Czech Technical University, Prague*, (January), 2016.

[13] Frank Allgöwer, Rolf Findeisen, and Zoltan K. Nagy. Nonlinear model predictive control: From theory to application. *Journal of the Chinese Institute of Chemical Engineers*, 35(3):299–315, 2004.

[14] HB Pacejka and IJM Besselink. Magic formula tyre model with transient properties. *Vehicle system dynamics*, 27(S1):234–249, 1997.

[15] S. J. Julier and J. K. Uhlmann. New extension of the kalman filter to nonlinear systems. *Signal Processing, Sensor Fusion, and Target Recognition*, 3068:182–193, 1997.

[16] Dan Simon. *Optimal State Estimation*. John Wiley & Sons, Inc., 2006.

[17] A. J. Tremlett and D. J.N. Limebeer. Optimal tyre usage for a Formula One car. *Vehicle System Dynamics*, 54(10):1448–1473, 2016.

[18] WJ West and DJN Limebeer. Optimal tyre management for a high-performance race car. *Vehicle System Dynamics*, pages 1–19, 2020.

[19] D. P. Kelly and R. S. Sharp. Time-optimal control of the race car: Influence of a thermodynamic tyre model. *Vehicle System Dynamics*, 50(4):641–662, 2012.

[20] World Health Organization et al. Global status report on road safety 2018: summary. Technical report, World Health Organization, 2018.

[21] Willie D Jones. Keeping cars from crashing. *IEEE spectrum*, 38(9):40–45, 2001.

[22] Santokh Singh. Critical reasons for crashes investigated in the national motor vehicle crash causation survey. Technical report, 2015.

[23] Paul A Pisano, Lynette C Goodwin, and Michael A Rossetti. Us highway crashes in adverse road weather conditions. In *24th conference on international interactive information and processing systems for meteorology, oceanography and hydrology, New Orleans, LA*, 2008.

[24] Derek Heraghty, Sidney Dekker, and Andrew Rae. Accident report interpretation. *Safety*, 4(4):46, 2018.

[25] Stefania Santini, Nicola Albarella, Vincenzo Maria Arricale, Renato Brancati, and Aleksandr Sakhnevych. On-board road friction estimation technique for autonomous driving vehicle-following maneuvers. *Applied Sciences*, 11(5):2197, 2021.

[26] Aleksandr Sakhnevych, Vincenzo Maria Arricale, Mattia Bruschetta, Andrea Censi, Enrico Mion, Enrico Picotti, and Emilio Frazzoli. Investigation on the model-based control performance in vehicle safety critical scenarios with varying tyre limits. *Sensors*, 21(16):5372, 2021.

[27] S Antonov, A Fehn, and A Kugi. Unscented kalman filter for vehicle state estimation. *Vehicle System Dynamics*, 49(9):1497–1520, 2011.

[28] Thomas A Wenzel, KJ Burnham, MV Blundell, and RA Williams. Dual extended kalman filter for vehicle state and parameter estimation. *Vehicle system dynamics*, 44(2):153–171, 2006.

[29] Wei Liu, Hongwen He, and Fengchun Sun. Vehicle state estimation based on minimum model error criterion combining with extended kalman filter. *Journal of the Franklin Institute*, 353(4):834–856, 2016.

[30] Juan M Collado, Cristina Hilario, Arturo De la Escalera, and José M Armingol. Model based vehicle detection for intelligent vehicles. In *IEEE Intelligent Vehicles Symposium, 2004*, pages 572–577. IEEE, 2004.

[31] Mandoye Ndoye, Virgil F Totten, James V Krogmeier, and Darcy M Bullock. Sensing and signal processing for vehicle reidentification and travel time estimation. *IEEE Transactions on Intelligent Transportation Systems*, 12(1):119–131, 2010.

[32] Valentin L Popov. *Contact mechanics and friction*. Springer, 2010.

[33] Hao Wang, Imad L Al-Qadi, and Ilinca Stanciulescu. Simulation of tyre–pavement interaction for predicting contact stresses at static and various rolling conditions. *International Journal of Pavement Engineering*, 13(4):310–321, 2012.

[34] Bo NJ Persson. Rubber friction: role of the flash temperature. *Journal of Physics: Condensed Matter*, 18(32):7789, 2006.

[35] F Farroni, A Sakhnevych, and F Timpone. Physical modelling of tire wear for the analysis of the influence of thermal and frictional effects on vehicle performance. *Proceedings of the Institution of Mechanical Engineers, Part L: Journal of Materials: Design and Applications*, 231(1-2):151–161, 2017.

[36] Alan Neville Gent and Joseph D Walter. *Pneumatic tire*. 2006.

[37] Massimo Guiggiani. The science of vehicle dynamics. *Pisa, Italy: Springer Netherlands*, 2014.

[38] Reza N Jazar. Road dynamics. In *Advanced Vehicle Dynamics*, pages 297–350. Springer, 2019.

[39] Francesco Calabrese, Flavio Farroni, and Francesco Timpone. A flexible ring tyre model for normal interaction. *complexity*, 7(9), 2013.

[40] C Allouis, F Farroni, A Sakhnevych, and F Timpone. Tire thermal characterization: test procedure and model parameters evaluation. In *Proceedings of the World Congress on engineering*, volume 2, 2016.

[41] Edwin W Hines. Indicator device for indicating tread wear and tire incorporating the indicator, December 30 1975. US Patent 3,929,179.

[42] Cx K Batchelor and GK Batchelor. *An introduction to fluid dynamics*. Cambridge university press, 2000.

[43] P Bosch, D Ammon, and F Klempau. Tyre models-desire and reality in respect of vehicle development. *Darmstdter Reifenkolloquium, October*, 2002.

[44] Flavio Farroni. Trick-tire/road interaction characterization & knowledge-a tool for the evaluation of tire and vehicle performances in outdoor test sessions. *Mechanical Systems and Signal Processing*, 72:808–831, 2016.

[45] Valentin L Popov. Thermal effects in contacts. In *Contact Mechanics and Friction*, pages 217–223. Springer, 2017.

[46] Bin Li, Xiaobo Yang, and James Yang. Tire model application and parameter identification-a literature review. *SAE International Journal of Passenger Cars-Mechanical Systems*, 7(2014-01-0872):231–243, 2014.

[47] Hans Pacejka. *Tire and vehicle dynamics*. Elsevier, 2005.

[48] Ernst Fiala. Seitenkraften am rollenden luftreifen. *VdI*, 96:973–979, 1954.

[49] Gwanghun Gim and Parviz E Nikravesh. An analytical model of pneumatic tyres for vehicle dynamic simulations. part 3: Validation against experimental data. *International Journal of Vehicle Design*, 12(2):217–228, 1991.

[50] MA Levin. Investigation of features of tyre rolling at non-small velocities on the basis of a simple tyre model with distributed mass periphery. *Vehicle system dynamics*, 23(1):441–466, 1994.

[51] Naoshi Miyashita and Kazuyuki Kabe. A study of the cornering force by use of the analytical tyre model. *Vehicle System Dynamics*, 43(sup1):123–134, 2005.

[52] IJM Besselink, AJC Schmeitz, and HB Pacejka. An improved magic formula/swift tyre model that can handle inflation pressure changes. *Vehicle System Dynamics*, 48(S1):337–352, 2010.

[53] AJC Schmeitz, IJM Besselink, and STH Jansen. Tno mf-swift. *Vehicle System Dynamics*, 45(S1):121–137, 2007.

[54] Wolfgang Hirschberg, Georg Rill, and Heinz Weinfurter. User-appropriate tyre-modelling for vehicle dynamics in standard and limit situations. *Vehicle System Dynamics*, 38(2):103–125, 2002.

[55] Jacob Svendenius and Magnus Gäfvert. A semi-empirical dynamic tire model for combined-slip forces. *Vehicle System Dynamics*, 44(2):189–208, 2006.

[56] L. Romano, A. Sakhnevych, S. Strano, and F. Timpone. A hybrid tyre model for in-plane dynamics. *Vehicle System Dynamics*, 58:1123–1145, 2020.

[57] M. Gipser. Ftire: a physically based application-oriented tyre model for use with detailed mbs and finite-element suspension models. *Vehicle System Dynamics*, 43:76–91, 2005.

[58] A. Gallrein and M. Bäcker. Cdtire: a tire model for comfort and durability applications. *Vehicle System Dynamics*, 45:69–77, 2007.

[59] Hans B Pacejka and Egbert Bakker. The magic formula tyre model. *Vehicle system dynamics*, 21(S1):1–18, 1992.

[60] P Bandel and C Monguzzi. Simulation model of the dynamic behavior of a tire running over an obstacle. *Tire Science and Technology*, 16(2):62–77, 1988.

[61] Masahiro Takayama and Koichi Yamagishi. Simulation model of tire vibration. *Tire Science and Technology*, 11(1):38–49, 1983.

[62] D Belluzzo, F Mancosu, R Sangalli, Fo Cheli, and S Bruni. New predictive model for the study of vertical forces (up to 250 hz) induced on the tire hub by road irregularities. *Tire Science and Technology*, 30(1):2–18, 2002.

[63] Seongho Kim, Parviz E Nikravesh, and Gwanghun Gim. A two-dimensional tire model on uneven roads for vehicle dynamic simulation. *Vehicle system dynamics*, 46(10):913–930, 2008.

[64] Shawky Hegazy and Corina Sandu. Evaluation of heavy truck ride comfort and stability. Technical report, SAE Technical Paper, 2010.

[65] PWA Zegelaar and HB Pacejka. The in-plane dynamics of tyres on uneven roads. *Vehicle System Dynamics*, 25(S1):714–730, 1996.

[66] L Walta, VAWJ Marchau, and K Brookhuis. Stakeholder preferences of advanced driver assistance systems (adas)—a literature review. In *Proceedings of the 13th World Congress and Exhibition on Intelligent Transport Systems and Service*, 2006.

[67] Jesse Levinson, Jake Askeland, Jan Becker, Jennifer Dolson, David Held, Soeren Kammel, J Zico Kolter, Dirk Langer, Oliver Pink, Vaughan Pratt, et al. Towards fully autonomous driving: Systems and algorithms. In *2011 IEEE Intelligent Vehicles Symposium (IV)*, pages 163–168. IEEE, 2011.

[68] M.C. Best, T.J. Gordon, and P.J. Dixon. An extended adaptive kalman filter for real-time state estimation of vehicle handling dynamics. *Vehicle System Dynamics*, 34(1):57–75, 2000.

[69] J. Dakhlallah, S. Glaser, S. Mammar, and Y. Sebsadji. Tire-road forces estimation using extended kalman filter and sideslip angle evaluation. In *2008 American Control Conference*, pages 4597–4602, 2008.

[70] T. A. Wenzel, K. J. Burnham, M. V. Blundell, and R. A. Williams. Dual extended kalman filter for vehicle state and parameter estimation. *Vehicle System Dynamics*, 44(2):153–171, 2006.

[71] M. Doumiati, A. Victorino, A. Charara, and D. Lechner. Unscented kalman filter for real-time vehicle lateral tire forces and sideslip angle estimation. In *2009 IEEE Intelligent Vehicles Symposium*, pages 901–906, 2009.

[72] S Antonov, A Fehn, and A Kugi. Unscented kalman filter for vehicle state estimation. *Vehicle System Dynamics*, 49(9):1497–1520, 2011.

[73] Ehsan Hashemi, Mohammad Pirani, Amir Khajepour, and Alireza Kasaiezadeh. A comprehensive study on the stability analysis of vehicle dynamics with pure/combined-slip tyre models. *Vehicle system dynamics*, 54(12):1736–1761, 2016.

[74] Massimo Guiggiani. *The Science of Vehicle Dynamics*. Springer International Publishing AG, 2018.

[75] Wei Liu, Hongwen He, and Fengchun Sun. Vehicle state estimation based on minimum model error criterion combining with extended kalman filter. *Journal of the Franklin Institute*, 353(4):834–856, 2016.

[76] X. Jin, G. Yin, and A. Hanif. Cubature kalman filter-based state estimation for distributed drive electric vehicles. In *2016 35th Chinese Control Conference (CCC)*, pages 9038–9042, 2016.

[77] Martin Haudum, Johannes Edelmann, Manfred Plöchl, and Manuel Höll. Vehicle side-slip angle estimation on a banked and low-friction road. *Proceedings of the Institution of Mechanical Engineers, Part D: Journal of automobile engineering*, 232(12):1584–1596, 2018.

[78] A.E. Bryson and Y.C. Ho. *Applied optimal control: optimization, estimation, and control*. Blaisdell Pub. Co., 1969.

[79] D.E. Kirk. *Optimal Control Theory: An Introduction*. Dover Books on Electrical Engineering Series. Dover Publications, 2004.

[80] Curtis P. Mracek and James R. Cloutier. Control designs for the nonlinear benchmark problem via the state-dependent Riccati equation method. *International Journal of Robust and Nonlinear Control*, 8(4-5):401–433, 1998.

[81] Tayfun Çimen. State-Dependent Riccati Equation (SDRE) control: A survey. In *IFAC Proceedings Volumes (IFAC-PapersOnline)*, volume 17, 2008.

[82] James R. Cloutier, Donald T. Stansbery, and Mario Sznaier. On the recoverability of nonlinear state feedback laws by extended linearization control techniques. *Proceedings of the 1999 American Control Conference (Cat. No. 99CH36251)*, 3:1515–1519 vol.3, 1999.

[83] R. M. Murray. Lecture notes in control and dynamics systems, January 2006.

[84] Radhakant Padhi. Lecture notes in optimal control, guidance and estimation, February 2013.

[85] Anil Kunnappillil Madhusudhanan, Matteo Corno, Bram Bonsen, and Edward Holweg. Solving algebraic riccati equation real time for integrated vehicle dynamics control. In *Proceedings of the American Control Conference*, pages 3593–3598, 2012.

[86] Francesco Borrelli, Alberto Bemporad, and Manfred Morari. *Predictive Control for Linear and Hybrid Systems*. Cambridge University Press, USA, 1st edition, 2017.

[87] Francesco Pretagostini, Laura Ferranti, Giovanni Berardo, Valentin Ivanov, and Barys Shyrokau. Survey on Wheel Slip Control Design Strategies, Evaluation and Application to Antilock Braking Systems. *IEEE Access*, 8:10951–10970, 2020.

[88] Yutao Chen, Mattia Bruschetta, Enrico Picotti, and Alessandro Beghi. Matmpc-A matlab based toolbox for real-time nonlinear model predictive control. *2019 18th European Control Conference, ECC 2019*, pages 3365–3370, 2019.

[89] Alexander Buchner, Holger Diedam, Hans Joachim Ferreau, Boris Houska, Dennis Janka, Manuel Kudruss, Aude Perrin, Andreas Potschka, Milan Vukov, Thomas Wiese, F Walter, and Leonard Wirsching. qpOASES User's Manual. 0(December):1–71, 2014.

[90] H. G. Bock and K. J. Plitt. Multiple Shooting Algorithm for Direct Solution of Optimal Control Problems. *IFAC Proceedings Series*, 17(2):1603–1608, 1985.

[91] H.G. Bock, M. Diehl, C. Kirches, K. Mombaur, and S. Sager. Lecture: Optimierung bei gewohnlichen differentialgleichungen. Technical report, Universitaet Heidelberg, 2014.

[92] Rajneesh Singh and Kevin Golsch. A downforce optimization study for a racing car shape. Technical report, SAE Technical Paper, 2005.

[93] Jorge Munoz, German Gutierrez, and Araceli Sanchis. Multi-objective evolution for car setup optimization. In *2010 UK Workshop on Computational Intelligence (UKCI)*, pages 1–5. IEEE, 2010.

[94] Hans B Pacejka. The tyre as a vehicle component. In *26th FISITA Congress, 16-13 June 1996, Prague, Czechoslovakia*, pages 112–125, 1996.

[95] Alex Eichberger and Marcus Schittenhelm. Implementations, applications and limits of tyre models in multibody simulation. *Vehicle System Dynamics*, 43(sup1):18–29, 2005.

[96] F Farroni. *Development of a grip & thermodynamics sensitive tyre/road interaction forces characterization procedure employed in high-performance vehicles simulation*. PhD thesis, PhD thesis, University of Naples" Federico II, 2014.

[97] A Sakhnevych. *Multi-Physical approach for tire contact and wear mechanisms modelling*. PhD thesis, Ph. D. thesis, Università degli Studi di Napoli Federico II, Naples, 2017.

[98] Hilding Elmqvist, Sven Erik Mattsson, Hans Olsson, Johan Andreasson, Martin Otter, Christian Schweiger, and Dag Brück. Real-time simulation of detailed automotive models. In *Proceedings of the 3rd International Modelica Conference, Linköping, Sweden*, pages 29–38, 2003.

[99] Muhammad Zohaib Iqbal, Andrea Arcuri, and Lionel Briand. Environment modeling and simulation for automated testing of soft real-time embedded software. *Software & Systems Modeling*, 14(1):483–524, 2015.

[100] A Vijay Alagappan, KV Narasimha Rao, and R Krishna Kumar. A comparison of various algorithms to extract magic formula tyre model coefficients for vehicle dynamics simulations. *Vehicle System Dynamics*, 53(2):154–178, 2015.

[101] Capra Damiano, Farroni Flavio, Sakhnevych Aleksandr, Salvato Gianluca, Sorrentino Antonio, and Timpone Francesco. On the implementation of an innovative temperature-sensitive version of pacejka's mf in vehicle dynamics simulations. In *Conference of the Italian Association of Theoretical and Applied Mechanics*, pages 1084–1092. Springer, 2019.

[102] Flavio Farroni, Aleksandr Sakhnevych, and Francesco Timpone. An evolved version of thermo racing tyre for real time applications. *Lecture Notes in Engineering and Computer Science*, 2218(July):1159–1164, 2015.

[103] Flavio Farroni, Michele Russo, Aleksandr Sakhnevych, and Francesco Timpone. Trt evo: advances in real-time thermodynamic tire modeling for vehicle dynamics simulations. *Proceedings of the Institution of Mechanical Engineers, Part D: Journal of Automobile Engineering*, 233(1):121–135, 2019.

[104] Haibo Huang, Yijui Chiu, Chen Wang, and Xiaoxiong Jin. Three-dimensional global pattern prediction for tyre tread wear. *Proceedings of the Institution of Mechanical Engineers, Part D: Journal of automobile engineering*, 229(2):197–213, 2015.

[105] Flavio Farroni, Michele Russo, Riccardo Russo, and Francesco Timpone. A physical-analytical model for a real-time local grip estimation of tyre rubber in sliding contact with road asperities. *Proceedings of the Institution of Mechanical Engineers, Part D: Journal of Automobile Engineering*, 228(8):955–969, 2014.

[106] James E Mark, Burak Erman, and Mike Roland. *The science and technology of rubber*. Academic press, 2013.

[107] Jin Haeng Lee, Taehyung Kim, and Hyungyil Lee. A study on robust indentation techniques to evaluate elastic–plastic properties of metals. *International Journal of Solids and Structures*, 47(5):647–664, 2010.

[108] John D Ferry. *Viscoelastic properties of polymers*. John Wiley & Sons, 1980.

[109] Meng-Jiao Wang. Effect of polymer-filler and filler-filler interactions on dynamic properties of filled vulcanizates. *Rubber chemistry and technology*, 71(3):520–589, 1998.

[110] Roderic Lakes and Roderic S Lakes. *Viscoelastic materials*. Cambridge university press, 2009.

[111] Tapas Kanungo, David M Mount, Nathan S Netanyahu, Christine D Piatko, Ruth Silverman, and Angela Y Wu. An efficient k-means clustering algorithm: Analysis and implementation. *IEEE transactions on pattern analysis and machine intelligence*, 24(7):881–892, 2002.

[112] Yvon Chevalier and Jean Vinh Tuong. *Mechanics of viscoelastic materials and wave dispersion*. Iste, 2010.

[113] Franck Renaud, Jean-Luc Dion, Gaël Chevallier, Imad Tawfiq, and Rémi Lemaire. A new identification method of viscoelastic behavior: Application to the generalized maxwell model. *Mechanical Systems and Signal Processing*, 25(3):991–1010, 2011.

[114] George Neville Greaves, AL Greer, Roderic S Lakes, and Tanguy Rouxel. Poisson's ratio and modern materials. *Nature materials*, 10(11):823–837, 2011.

[115] IH Sahputra and AT Echtermeyer. Effects of temperature and strain rate on the deformation of amorphous polyethylene: a comparison between molecular dynamics simulations and experimental results. *Modelling and Simulation in Materials Science and Engineering*, 21(6):065016, 2013.

[116] VG Geethamma, G Kalaprasad, Gabriël Groeninckx, and Sabu Thomas. Dynamic mechanical behavior of short coir fiber reinforced natural rubber composites. *Composites Part A: Applied Science and Manufacturing*, 36(11):1499–1506, 2005.

[117] Malcolm L Williams, Robert F Landel, and John D Ferry. The temperature dependence of relaxation mechanisms in amorphous polymers and other glass-forming liquids. *Journal of the American Chemical society*, 77(14):3701–3707, 1955.

[118] Roderic S Lakes. Viscoelastic measurement techniques. *Review of scientific instruments*, 75(4):797–810, 2004.

[119] Robert F Landel. A two-part tale: the wlf equation and beyond linear viscoelasticity. *Rubber chemistry and technology*, 79(3):381–401, 2006.

[120] Vincenzo Maria Arricale, Francesco Carputo, Flavio Farroni, Aleksandr Sakhnevych, and Francesco Timpone. Experimental investigations on tire/road friction dependence from thermal conditions carried out with real tread compounds in sliding contact with asphalt specimens. In *Key Engineering Materials*, volume 813, pages 261–266. Trans Tech Publ, 2019.

[121] Flavio Farroni, Raffaele Lamberti, Nicolò Mancinelli, and Francesco Timpone. Trip-id: A tool for a smart and interactive identification of magic formula tyre model parameters from experimental data acquired on track or test rig. *Mechanical Systems and Signal Processing*, 102:1–22, 2018.

[122] Irad Ben-Gal. Outlier detection. In *Data mining and knowledge discovery handbook*, pages 131–146. Springer, 2005.

[123] James MacQueen et al. Some methods for classification and analysis of multivariate observations. In *Proceedings of the fifth Berkeley symposium on mathematical statistics and probability*, volume 1, pages 281–297. Oakland, CA, USA, 1967.

[124] Sridhar Ramaswamy, Rajeev Rastogi, and Kyuseok Shim. Efficient algorithms for mining outliers from large data sets. In *Proceedings of the 2000 ACM SIGMOD international conference on Management of data*, pages 427–438, 2000.

[125] Eleazar Eskin, Andrew Arnold, Michael Prerau, Leonid Portnoy, and Sal Stolfo. A geometric framework for unsupervised anomaly detection. In *Applications of data mining in computer security*, pages 77–101. Springer, 2002.

[126] Varun Chandola, Arindam Banerjee, and Vipin Kumar. Outlier detection: A survey. *ACM Computing Surveys*, 14:15, 2007.

[127] Rajashree Dash, Rajib Lochan Paramguru, and Rasmita Dash. Comparative analysis of supervised and unsupervised discretization techniques. *International Journal of Advances in Science and Technology*, 2(3):29–37, 2011.

[128] Speed sensor hall-effect ha-m. https://www.bosch-motorsport.com/content/downloads/Raceparts/Resources/pdf/Data%20Sheet_69827851_Speed_Sensor_Hall-Effect_HA-M.pdf.

[129] Rt3000 v3. https://www.oxts.com/products/rt3000-v3/.

[130] Correvit s-motion dti. https://www.kistler.com/files/document/003-395e.pdf.

[131] Temperature sensor. https://www.mclaren.com/applied/catalogue/item/temperature-sensor-16x4-infra-red-array/.

[132] Tyre pressure measurement system. https://www.mclaren.com/applied/catalogue/item/tpms-ir-array/.

[133] Angus P. Andrews Mohinder S. Grewal. *Kalman filtering: Theory and practice using MATLAB*. Wiley-IEEE Press, 3 edition, 2008.

[134] Gary Bishop, Greg Welch, et al. An introduction to the kalman filter. *Proc of SIGGRAPH, Course*, 8(27599-23175):41, 2001.

[135] HENRIKSEN R. The truncated second-order nonlinear filter revisited. *IEEE TRANSACTIONS ON AUTOMATIC CONTROL*, AC-27(1), 1982.

[136] S. Julier, J. Uhlmann, and H. F. Durrant-Whyte. A new method for the nonlinear transformation of means and covariances in filters and estimators. *IEEE Transactions on Automatic Control*, 45(3):477–482, 2000.

[137] Simon J Julier and Jeffrey K Uhlmann. Unscented filtering and nonlinear estimation. *Proceedings of the IEEE*, 92(3):401–422, 2004.

[138] R. Van der Merwe and E.A. Wan. The square-root unscented kalman filter for state and parameter-estimation. In *2001 IEEE International Conference on Acoustics, Speech, and Signal Processing. Proceedings (Cat. No.01CH37221)*, volume 6, pages 3461–3464 vol.6, 2001.

[139] Simon J Julier. The spherical simplex unscented transformation. In *Proceedings of the 2003 American Control Conference, 2003.*, volume 3, pages 2430–2434. IEEE, 2003.

[140] M. Arulampalam, Simon Maskell, Neil Gordon, and Tim Clapp. A tutorial on particle filters for online nonlinear/ non-gaussian bayesian tracking. *Signal Processing, IEEE Transactions on*, 50:174 – 188, 03 2002.

[141] Tiancheng Li, Miodrag Bolic, and Petar M. Djuric. Resampling methods for particle filtering: Classification, implementation, and strategies. *IEEE Signal Processing Magazine*, 32(3):70–86, 2015.

[142] Pieter Abbeel, Adam Coates, Michael Montemerlo, and Andrew Ng. Discriminative training of kalman filters. pages 289–296, 06 2005.

[143] Julien Caroux, Christophe Lamy, Michel Basset, and Gérard-Léon Gissinger. Sideslip angle measurement, experimental characterization and evaluation of three different principles. *IFAC Proceedings Volumes*, 40(15):505–510, 2007. 6th IFAC Symposium on Intelligent Autonomous Vehicles.

[144] Juraj Kabzan, Miguel I Valls, Victor JF Reijgwart, Hubertus FC Hendrikx, Claas Ehmke, Manish Prajapat, Andreas Bühler, Nikhil Gosala, Mehak Gupta, Ramya Sivanesan, et al. Amz driverless: The full autonomous racing system. *Journal of Field Robotics*, 37(7):1267–1294, 2020.

[145] Saeid Niazi and Alireza Toloei. State estimation for target tracking problems with nonlinear kalman filter algorithms. *International Journal of Computer Applications*, 98, 07 2014.

[146] Alexander Wischnewski, Tim Stahl, Johannes Betz, and Boris Lohmann. Vehicle dynamics state estimation and localization for high performance race cars. *IFAC-PapersOnLine*, 52(8):154–161, 2019.

[147] S. Melzi and E. Sabbioni. On the vehicle sideslip angle estimation through neural networks: Numerical and experimental results. *Mechanical Systems and Signal Processing*, 25(6):2005–2019, 2011. Interdisciplinary Aspects of Vehicle Dynamics.

[148] Xiaoping Du, Huamei Sun, Kun Qian, Yun Li, and Liantao Lu. A prediction model for vehicle sideslip angle based on neural network. In

2010 2nd IEEE International Conference on Information and Financial Engineering, pages 451–455, 2010.

[149] Daniel Chindamo and Marco Gadola. Estimation of vehicle side-slip angle using an artificial neural network. *MATEC Web of Conferences*, 166:02001, 01 2018.

[150] Francesco Carputo, Danilo D'Andrea, Giacomo Risitano, Aleksandr Sakhnevych, Dario Santonocito, and Flavio Farroni. A neural-network-based methodology for the evaluation of the center of gravity of a motorcycle rider. *Vehicles*, 3:377–389, 07 2021.

[151] Danilo D'Andrea, Filippo Cucinotta, Flavio Farroni, Giacomo Risitano, Dario Santonocito, and Lorenzo Scappaticci. Development of machine learning algorithms for the determination of the centre of mass. *Symmetry*, 13:401, 02 2021.

[152] Cristiano Pieralice, Basilio Lenzo, Francesco Bucchi, and Marco Gabiccini. Vehicle sideslip angle estimation using kalman filters: modelling and validation. In *The International Conference of IFToMM Italy*, pages 114–122. Springer, 2018.

[153] Hongbin Ren, Sizhong Chen, Gang Liu, and Kaifeng Zheng. Vehicle state information estimation with the unscented kalman filter. *Advances in Mechanical Engineering*, 6:589397, 2014.

[154] Robust vehicle sideslip estimation based on kinematic considerations. *IFAC-PapersOnLine*, 50(1):14855–14860, 2017. 20th IFAC World Congress.

[155] Federico Cheli, Edoardo Sabbioni, M. Pesce, and Stefano Melzi. A methodology for vehicle sideslip angle identification: Comparison with experimental data. *Vehicle System Dynamics*, 45:549–563, 06 2007.

[156] Marco Gadola, Daniel Chindamo, Matteo Romano, and Fabrizio Padula. Development and validation of a kalman filter-based model for vehicle slip angle estimation. *Vehicle System Dynamics*, 52, 01 2014.

[157] Manuel Acosta Reche, Stratis Kanarachos, and Mike Blundell. Virtual tyre force sensors: An overview of tyre model-based and tyre model-less state estimation techniques. *Proceedings of the Institution of Mechanical Engineers Part D Journal of Automobile Engineering*, In press., 09 2017.

[158] Feliciano Di Biase, Basilio Lenzo, and Francesco Timpone. Vehicle sideslip angle estimation for a heavy-duty vehicle via extended kalman filter using a rational tyre model. *IEEE Access*, 8:142120–142130, 2020.

[159] Andrea Genovese, S Schiano, Salvatore Strano, Mario Terzo, M Iodice, Maurizio Indolfi, and G Coppola. Multiphysics design and optimization of a vibration-based energy harvester from pantograph-catenary interaction. *IOP Conference Series: Materials Science and Engineering*, 922:012012, 10 2020.

[160] Luigi Teodosio, Giuseppe Alferi, Andrea Genovese, Flavio Farroni, Benedetto Mele, Francesco Timpone, and Aleksandr Sakhnevych. A numerical methodology for thermo-fluid dynamic modelling of tyre inner chamber: towards real time applications. *IOP Conference Series: Materials Science and Engineering*, 922, 2021.

[161] Frank Naets, Sebastiaan van Aalst, Boulaid Boulkroune, Norddin El Ghouti, and Wim Desmet. Design and experimental validation of a stable two-stage estimator for automotive sideslip angle and tire parameters. *IEEE Transactions on Vehicular Technology*, 66(11):9727–9742, 2017.

[162] Arash Hosseinian and Selahattin Baslamisli. Adap-tyre: Dekf filtering for vehicle state estimation based on tyre parameter adaptation. *International Journal of Vehicle Design*, 12 2015.

[163] Edmo da Cunha Rodovalho and Giorgio de Tomi. Reducing environmental impacts via improved tyre wear management. *Journal of Cleaner Production*, 141:1419–1427, 2017.

[164] Kanwar Bharat Singh and Srikanth Sivaramakrishnan. An adaptive tire model for enhanced vehicle control systems. *SAE International Journal of Passenger Cars-Mechanical Systems*, 8(2015-01-1521):128–145, 2015.

[165] Janick V Frasch, Andrew Gray, Mario Zanon, Hans Joachim Ferreau, Sebastian Sager, Francesco Borrelli, and Moritz Diehl. An autogenerated nonlinear mpc algorithm for real-time obstacle avoidance of ground vehicles. In *2013 European Control Conference (ECC)*, pages 4136–4141. IEEE, 2013.

[166] B. Houska, H.J. Ferreau, and M. Diehl. ACADO Toolkit – An Open Source Framework for Automatic Control and Dynamic Optimization. *Optimal Control Applications and Methods*, 32(3):298–312, 2011.

[167] Karl Berntorp, Rien Quirynen, and Stefano Di Cairano. Friction adaptive vehicle control, September 17 2020. US Patent App. 16/299,285.

[168] Vincent A Laurense, Jonathan Y Goh, and J Christian Gerdes. Path-tracking for autonomous vehicles at the limit of friction. In *2017 American control conference (ACC)*, pages 5586–5591. IEEE, 2017.

[169] Jian Zhao, Jin Zhang, and Bing Zhu. Development and verification of the tire/road friction estimation algorithm for antilock braking system. *Mathematical problems in engineering*, 2014, 2014.

[170] Yiannis E Papelis, Ginger S Watson, and Timothy L Brown. An empirical study of the effectiveness of electronic stability control system in reducing loss of vehicle control. *Accident Analysis & Prevention*, 42(3):929–934, 2010.

[171] Vincenzo Punzo, Zuduo Zheng, and Marcello Montanino. About calibration of car-following dynamics of automated and human-driven vehicles: Methodology, guidelines and codes. *Transportation Research Part C: Emerging Technologies*, 128:103165, 2021.

[172] Allen Kim, Takuya Otani, and Valerie Leung. Model-based design for the development and system-level testing of adas. In *Energy Consumption and Autonomous Driving*, pages 39–48. Springer, 2016.

[173] Payman Shakouri, Jacek Czeczot, and Andrzej Ordys. Simulation validation of three nonlinear model-based controllers in the adaptive cruise control system. *Journal of Intelligent & Robotic Systems*, 80(2):207–229, 2015.

[174] Taehyun Shim and Chinar Ghike. Understanding the limitations of different vehicle models for roll dynamics studies. *Vehicle system dynamics*, 45(3):191–216, 2007.

[175] Yutao Chen. Algorithms and applications for nonlinear model predictive control with long prediction horizon. 2018.

[176] H Georg Bock, Moritz Diehl, Johannes P Schlöder, Frank Allgöwer, Rolf Findeisen, and Zoltan Nagy. Real-time optimization and nonlinear model predictive control of processes governed by differential-algebraic equations. *IFAC Proceedings Volumes*, 33(10):671–679, 2000.

[177] Shih-Ping Han. Superlinearly convergent variable metric algorithms for general nonlinear programming problems. *Mathematical Programming*, 11(1):263–282, 1976.

[178] Mattia Bruschetta, Enrico Picotti, Enrico Mion, Yutao Chen, Alessandro Beghi, and Diego Minen. A nonlinear model predictive control based virtual driver for high performance driving. In *2019 IEEE Conference on Control Technology and Applications (CCTA)*, pages 9–14, 2019.

[179] Vittore Cossalter, Mauro Da Lio, Roberto Lot, and Lucca Fabbri. A general method for the evaluation of vehicle manoeuvrability with special emphasis on motorcycles. *Vehicle system dynamics*, 31(2):113–135, 1999.

[180] Yiqi Gao, Andrew Gray, Janick V Frasch, Theresa Lin, Eric Tseng, J Karl Hedrick, and Francesco Borrelli. Spatial predictive control for agile semi-autonomous ground vehicles. In *Proceedings of the 11th international symposium on advanced vehicle control*, 2012.

[181] Thomas D Gillespie. Vehicle dynamics. *Warren dale*, 1997.

[182] Yutao Chen, Mattia Bruschetta, Davide Cuccato, and Alessandro Beghi. An adaptive partial sensitivity updating scheme for fast nonlinear model predictive control. *IEEE Transactions on Automatic Control*, 64(7):2712–2726, 2018.

[183] Yutao Chen, Davide Cuccato, Mattia Bruschetta, and Alessandro Beghi. An inexact sensitivity updating scheme for fast nonlinear model predictive control based on a curvature-like measure of nonlinearity. In *2017 IEEE 56th Annual Conference on Decision and Control (CDC)*, pages 4382–4387. IEEE, 2017.

[184] Hans Georg Bock and Karl-Josef Plitt. A multiple shooting algorithm for direct solution of optimal control problems. In *Proceedings of the IFAC World Congress*, 1984.

[185] Moritz Diehl, H Georg Bock, Johannes P Schlöder, Rolf Findeisen, Zoltan Nagy, and Frank Allgöwer. Real-time optimization and nonlinear model predictive control of processes governed by differential-algebraic equations. *Journal of Process Control*, 12(4):577–585, 2002.

[186] Yutao Chen, Nicolò Scarabottolo, Mattia Bruschetta, and Alessandro Beghi. Efficient move blocking strategy for multiple shooting-based non-linear model predictive control. *IET Control Theory & Applications*, 14(2):343–351, 2019.

[187] M. N. Zeilinger, C. N. Jones, and M. Morari. Robust stability properties of soft constrained mpc. In *49th IEEE Conference on Decision and Control (CDC)*, pages 5276–5282, 2010.

[188] Raymond Brach and Matthew Brach. The tire-force ellipse (friction ellipse) and tire characteristics. Technical report, SAE Technical Paper, 2011.

[189] Sadegh Arefnezhad, Ali Ghaffari, Alireza Khodayari, and Sina Nosoudi. Modeling of double lane change maneuver of vehicles. *International Journal of Automotive Technology*, 19(2):271–279, 2018.

[190] Julia Nilsson, Mattias Brännström, Erik Coelingh, and Jonas Fredriksson. Lane change maneuvers for automated vehicles. *IEEE Transactions on Intelligent Transportation Systems*, 18(5):1087–1096, 2016.

[191] Mattia Bruschetta, Enrico Picotti, Andrea De Simoi, Yutao Chen, Alessandro Beghi, Masatsugu Nishimura, Yoshitaka Tezuka, and Francesco Ambrogi. Real-time nonlinear model predictive control of a virtual motorcycle. *IEEE Transactions on Control Systems Technology*, 2020.

[192] Andreas Weißmann, Daniel Görges, and Xiaohai Lin. Energy-optimal adaptive cruise control based on model predictive control. *IFAC-PapersOnLine*, 50(1):12563–12568, 2017.

[193] Chengwei Sun, Liang Chu, Jianhua Guo, Dapai Shi, Tianjiao Li, and Yunsong Jiang. Research on adaptive cruise control strategy of pure electric vehicle with braking energy recovery. *Advances in Mechanical Engineering*, 9(11):1687814017734994, 2017.

[194] S. Zhang, Y. Luo, K. Li, and V. Li. Real-time energy-efficient control for fully electric vehicles based on an explicit model predictive control

method. *IEEE Transactions on Vehicular Technology*, 67(6):4693–4701, 2018.

[195] Sheng Zhang and Xiangtao Zhuan. Model-predictive optimization for pure electric vehicle during a vehicle-following process. *Mathematical Problems in Engineering*, 2019, 2019.

[196] D. Lee, S. Kim, Changseb Kim, and K. Huh. Development of an autonomous braking system using the predicted stopping distance. *International Journal of Automotive Technology*, 15:341–346, 03 2014.

[197] H. Xiong, Z. Ling, R. Yue, L. Yinong, Z. Zhenfei, L. Yusheng, Z. Qiang, and X. Zhoubing. Research on control strategy of automatic emergency brake system based on prescan. In *IET International Conference on Intelligent and Connected Vehicles (ICV 2016)*, pages 1–6, 2016.

[198] Seyed Naseralavi, Navid Nadimi, M. Saffarzadeh, and Amir Reza Mamdoohi. A general formulation for time-to-collision safety indicator. *Proceedings of the ICE - Transport*, 166:294–304, 10 2013.

[199] Umar Zakir Abdul Hamid, Fakhrul Razi Ahmad Zakuan, Khairul Zulkepli, Muhammad Zulfaqar Azmi, Hairi Zamzuri, Mohd Azizi Abdul Rahman, and Muhammad Zakaria. Autonomous emergency braking system with potential field risk assessment for frontal collision mitigation. In *2017 IEEE Conference on Systems, Process and Control (ICSPC)*, pages 71–76, 12 2017.

[200] I-Hsuan Lee and Bi-Cheng Luan. Design of autonomous emergency braking system based on impedance control for 3-car driving scenario. In *SAE Technical Paper*. SAE International, 04 2016.

[201] Seungwuk Moon, Ilki Moon, and Kyongsu Yi. Design, tuning, and evaluation of a full-range adaptive cruise control system with collision avoidance. *Control Engineering Practice*, 17:442–455, 04 2009.

[202] freddy a mullakkal babu, Meng Wang, B. Arem, and Riender Happee. Design and analysis of full range adaptive cruise control with integrated collision avoidance strategy. In *2016 IEEE 19th International Conference on Intelligent Transportation Systems (ITSC)*, 11 2016.

[203] Payman Shakouri, A. Ordys, and Mohamad Askari. Adaptive cruise control with stop&go function using the state-dependent nonlinear model predictive control approach. *ISA transactions*, 51:622–31, 06 2012.

[204] Dongbin Zhao, Zhaohui Hu, Zhongpu Xia, Cesare Alippi, Yuanheng Zhu, and Ding Wang. Full-range adaptive cruise control based on supervised adaptive dynamic programming. *Neurocomputing*, 125:57–67, 02 2014.

[205] Constantin Ilas. Electronic sensing technologies for autonomous ground vehicles: A review. In *2013 8th International Symposium on Advanced Topics in Electrical Engineering (ATEE)*, pages 1–6. IEEE, 2013.

[206] Seyedmeysam Khaleghian, Anahita Emami, and Saied Taheri. A technical survey on tire-road friction estimation. *Friction*, 5(2):123–146, 2017.

[207] Bo Leng, Da Jin, Lu Xiong, Xing Yang, and Zhuoping Yu. Estimation of tire-road peak adhesion coefficient for intelligent electric vehicles based on camera and tire dynamics information fusion. *Mechanical Systems and Signal Processing*, 150:107275.

[208] Juqi Hu, Subhash Rakheja, and Youmin Zhang. Tire-road friction coefficient estimation under constant vehicle speed control. *IFAC-PapersOnLine*, 52(8):136–141, 2019.

[209] Yan Chen and Junmin Wang. Adaptive vehicle speed control with input injections for longitudinal motion independent road frictional condition estimation. *IEEE Transactions on Vehicular Technology*, 60(3):839–848, 2011.

[210] Rajesh Rajamani, Neng Piyabongkarn, Jae Lew, Kyongsu Yi, and Gridsada Phanomchoeng. Tire-road friction-coefficient estimation. *IEEE Control Systems Magazine*, 30(4):54–69, 2010.

[211] Massimiliano De Martino, Flavio Farroni, Nicola Pasquino, Aleksandr Sakhnevych, and Francesco Timpone. Real-time estimation of the vehicle sideslip angle through regression based on principal component analysis and neural networks. In *2017 IEEE International Systems Engineering Symposium (ISSE)*, pages 1–6. IEEE, 2017.

[212] Guido Napolitano Dell'Annunziata, Basilio Lenzo, Flavio Farroni, Aleksandr Sakhnevych, and Francesco Timpone. A new approach for estimating tire-road longitudinal forces for a race car. In *IFToMM World Congress on Mechanism and Machine Science*, pages 3601–3610. Springer, 2019.

[213] WIM VAN WINSUM and Adriaan Heino. Choice of time-headway in car-following and the role of time-to-collision information in braking. *Ergonomics*, 39(4):579–592, 1996.

[214] John C. Hayward. Near-miss determination through use of a scale of danger. 1972.

[215] Gao Zhenhai, Wang Jun, Hu Hongyu, Yan Wei, Wang Dazhi, and Wang Lin. Multi-argument control mode switching strategy for adaptive cruise control system. *Procedia engineering*, 137:581–589, 2016.

[216] Rajesh Rajamani. *Vehicle dynamics and control*. Springer Science & Business Media, 2011.

[217] Julia B Edwards. The relationship between road accident severity and recorded weather. *Journal of Safety Research*, 29(4):249 – 262, 1998.

[218] Vadim Utkin, Jürgen Guldner, and Ma Shijun. *Sliding mode control in electro-mechanical systems*, volume 34. CRC press, 1999.

[219] William Pasillas-Lépine, Antonio Loría, and Mathieu Gerard. Design and experimental validation of a nonlinear wheel slip control algorithm. *Automatica*, 48(8):1852–1859, 2012.

[220] Jie Song, Yi Wu, Zhexin Xu, and Xiao Lin. Research on car-following model based on sumo. In *The 7th IEEE/International Conference on Advanced Infocomm Technology*, pages 47–55. IEEE, 2014.

[221] Flavio Farroni, Daniele Giordano, Michele Russo, and Francesco Timpone. Trt: thermo racing tyre a physical model to predict the tyre temperature distribution. *Meccanica*, pages 707–723, 3 2014.

[222] Francesco Calabrese, Manfred Baecker, Carlos Galbally, and Axel Gallrein. A Detailed Thermo-Mechanical Tire Model for Advanced Handling Applications. *SAE International Journal of Passenger Cars - Mechanical Systems*, 8(2):501–511, 2015.

[223] Konrad Reif Ed. *Brakes, Brake Control and Driver Assistance Systems*. 2014.

[224] H. Pacejka. *Tire and Vehicle Dynamics*. 01 2012.

[225] Diwakar Harsh and Barys Shyrokau. Tire model with temperature effects for formula SAE vehicle. *Applied Sciences (Switzerland)*, 9(24), 2019.

[226] Pierre Février, Oliver Blanco Hague, Bernhard Schick, and Charles Miquet. Advantages of a thermomechanical tire model for vehicle dynamics. *ATZ worldwide*, 112(7-8):33–37, 2010.

[227] Andreas Hackl. Enhanced Tyre Modelling for Vehicle Dynamics Control Systems. 4(3):182, 2019.

[228] Michal Maniowski. Optimisation of driver actions in RWD race car including tyre thermodynamics. *Vehicle System Dynamics*, 54(4):526–544, 2016.

[229] Raffaele De Rosa, Francesco Di Stazio, Daniele Giordano, Michele Russo, and Mario Terzo. ThermoTyre: Tyre temperature distribution during handling manoeuvres. *Vehicle System Dynamics*, 46(9):831–844, 2008.

[230] Damiano Capra, Flavio Farroni, Aleksandr Sakhnevych, Gianluca Salvato, Antonio Sorrentino, and Francesco Timpone. On the implementation of an innovative temperature-sensitive version of pacejka's mf in vehicle dynamics simulations. *Proceedings of XXIV AIMETA Conference 2019*, pages 1084–1092, 2019.

[231] Aleksandr Sakhnevych. Multiphysical mf-based tyre modelling and parametrisation for vehicle setup and control strategies optimisation. *Vehicle System Dynamics*, pages 1–22, 2021.

[232] Janick V. Frasch, Andrew Gray, Mario Zanon, Hans Joachim Ferreau, Sebastian Sager, Francesco Borrelli, and Moritz Diehl. An auto-generated nonlinear MPC algorithm for real-time obstacle avoidance of ground vehicles. *2013 European Control Conference, ECC 2013*, pages 4136–4141, 2013.

[233] Idar Petersen, Tor A. Johansen, Jens Kalkkuhl, and Jens Ludemann. Gain-scheduled wheel slip reset control in automotive brake systems. *2001 European Control Conference, ECC 2001 (2001) 606-611*, pages 606–611, 2001.

[234] M. Alirezaei, S. Kanarachos, B. Scheepers, and J. P. Maurice. Experimental evaluation of optimal Vehicle Dynamic Control based on the

State Dependent Riccati Equation technique. In *Proceedings of the American Control Conference*, pages 408–412. Institute of Electrical and Electronics Engineers Inc., 2013.

[235] Erik Wachter, Mohsen Alirezaei, Fredrik Bruzelius, and Antoine Schmeitz. Path control in limit handling and drifting conditions using State Dependent Riccati Equation technique. *Proceedings of the Institution of Mechanical Engineers, Part D: Journal of Automobile Engineering*, 234(2-3):783–791, 2020.

[236] PK Menon, T Lam, LS Crawford, and VHL Cheng. Real-time computational methods for sdre nonlinear control of missiles. In *Proceedings of the 2002 American Control Conference (IEEE Cat. No. CH37301)*, volume 1, pages 232–237. IEEE, 2002.

[237] William H Press, Saul A Teukolsky, William T Vetterling, and Brian P Flannery. *Numerical Recipes with Source Code CD-ROM 3rd Edition: The Art of Scientific Computing*. Cambridge University Press, 2007.

[238] Mehmet Itik, Metin Uymaz Salamci, and Stephen Paul Banks. SDRE optimal control of drug administration in cancer treatment. *Turkish Journal of Electrical Engineering and Computer Sciences*, 18(5):715–729, 2010.

[239] James R. Cloutier and Donald T. Stansbery. The capabilities and art of State-dependent Riccati equation-based design. *Proceedings of the American Control Conference*, 1:86–91, 2002.

Appendix A

SDC parameterisation - Quarter car

This section shows the quarter-car SDC paramterisation used for the controller. This parameterisation also passed the controllability/stabilisability test (as discussed in Chapter 5) as is described in the literature [82].

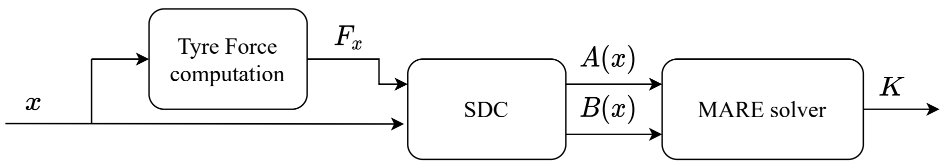

Fig. A.1 Tyre force computation done external to the SDC parameterisation

The quarter-car system is composed of 3 dynamic equations $[\dot{\kappa}, \dot{V}_x, \dot{T}_s]$. The reader can refer to Chapter 5 for the origin of these equations. Below, these equations (A.2,A.3 and A.4) are rearranged and shown in their final SDC parameterisation form, as were used within the controller. As is mentioned in 6.5.2, the tyre force F_x was used as input to the SDC paramaterisation and was represented as a linear parameterisation [234] of κ and T_s with the coefficients α_κ and α_{T_s}, as shown in equation A.1. This parameterisation of F_x is inserted into the 3 dynamic equations. In these equations, the R_e and

R_l were written as R, one can simply represent them with different values, if necessary. For easy readability, the states (not the ones belonging to the coefficients) are colored green and the input blue.

These parameterisation were done based on the rules defined by Cloutier and Stansbery [239]. In the tread surface dynamics, some terms had to be expanded to represent the appropriate state dependencies, which led to the origin of some free-parameters (ϕ_i). The value of the free parameters wasn't affecting the performance by large amounts so both their values were chosen to be equal to 0.5.

$$F_x = \alpha_\kappa \kappa + \alpha_{T_s} T_s \tag{A.1a}$$

$$\text{where} \quad \alpha_\kappa = F_x \tag{A.1b}$$

$$\alpha_{T_s} = F_x \left(\frac{1-\kappa}{T_s} \right) \tag{A.1c}$$

$$\begin{aligned} \dot{\kappa} = \frac{1}{V_x} \Bigg[&- \left(\frac{R^2}{I} \alpha_\kappa + \frac{1+\kappa}{m} \alpha_\kappa + \frac{\alpha_{T_s} T_s}{m} \right) \kappa + \\ &+ (0) V_x - \left(\frac{R^2}{I} \alpha_{T_s} + \frac{\alpha_{T_s}}{m} \right) T_s + \frac{R}{I} T_b \Bigg] \end{aligned} \tag{A.2}$$

$$\dot{V}_x = \frac{\alpha_\kappa}{m} \kappa + (0) V_x + \frac{\alpha_{T_s}}{m} \alpha_{T_s} T_s + (0) T_b \tag{A.3}$$

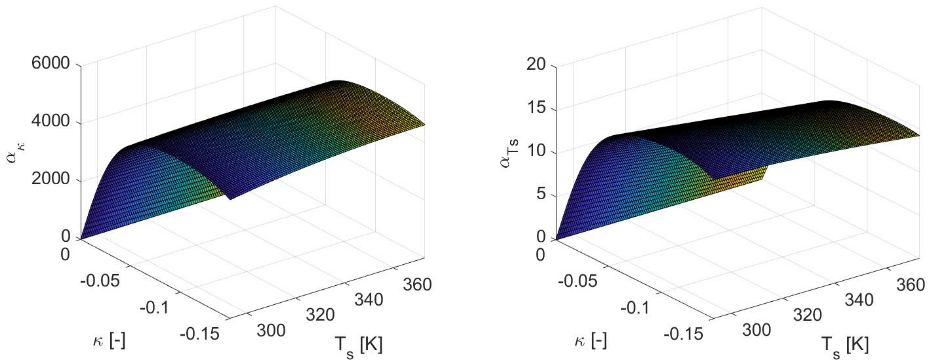

(a) α_κ (b) α_{T_s}

Fig. A.2 Tyre force paramterisation function - continuity over the domain

$$\begin{aligned}\dot{T}_s = \frac{1}{m_t c_t}\Bigg[&(\phi_1 p_1 \alpha_\kappa V_x \kappa - \phi_2 p_2 \alpha_\kappa V_x + \eta_1 \frac{\Delta c_s T_t}{\kappa_{max}})\kappa + \\ &+((1-\phi_1)p_1\alpha_\kappa \kappa^2 - (1-\phi_2) \\ &p_2 \alpha_\kappa \kappa + p_4 F_z + p_5 T_a {V_x}^{p_6-1})V_x + \\ &+(p_1 \alpha_{T_s} V_x \kappa - p_2 \alpha_{T_s} V_x - p_5 {V_x}^{p_6} - \\ &\eta_1 (1 + \frac{\Delta c_s \kappa}{\kappa_{max}} - c_{s1} + \frac{T_t(c_{s1}-1)}{T_s}))T_s + (0)T_b\Bigg]\end{aligned} \tag{A.4}$$

It is clearly seen that the coefficients of each state are state dependent (that become the elements of $\mathbf{A}(\mathbf{x})$ and $\mathbf{B}(\mathbf{x})$). In the implementation, the terms with the modulus are appropriately compensated with negative signs, as is seen in the temperature equation.

Another important thing with the tyre force parameterisation A.1 was that it must be continuous, which was true as can be seen in Figure A.2.

Appendix B

Quarter-car results

This appendix presents the results of the final tuned quarter-car SDRE and quarter-car NMPC based controllers for a given set of initial ($V_{x0} = 40m/s$) and boundary conditions ($T_a = 28°C$ and $T_t = 35°C$). The results are presented in the form of time history plots of the variable and the control input (Figures B.1 and B.2). For each controller type, two setups are shown, Setup A (κ-control) with only κ control and Setup B (κ & T_s-control) with κ and T_s control. Not to mention, the quarter car analysis consists of the "myTyre" tyre model within both the prediction model and the plant model.

We see that the steady state tracking of NMPC is perfect as compared to SDRE, the exact reason being that NMPC in each instant tries to stabilise the states to the terminal references, whereas SDRE is a regulator that calculates the gain values to reach the equilibrium (all states 0) as soon as possible in the optimal sense, and the gain is simply multiplied by the state error vector which no where guarantees steady state zero error. One solution to improve the steady state tracking in SDRE is is to introduce integral states for the desired states.

Another difference between the 2 controllers is the early onset of instability in the case of SDRE as compared to NMPC, with the longitudinal velocity V_x. Lastly, NMPC controller is able to achieve a stable behaviour with a sampling frequency of $100 Hz$ whereas the SDRE controller needs a sampling frequency of at least $1000 Hz$.

Table B.1 Results (metrics) of the 2 Setups (A and B) for both QC-SDRE and QC-NMPC controllers

Controller-type	Setup	s_{br} [m]	$T_{s,max}$ [$^{\circ}C$]
QC SDRE	A	54.34	46.0
	B	55.15	48.3
QC NMPC	A	54.23	45.2
	B	55.14	48.2

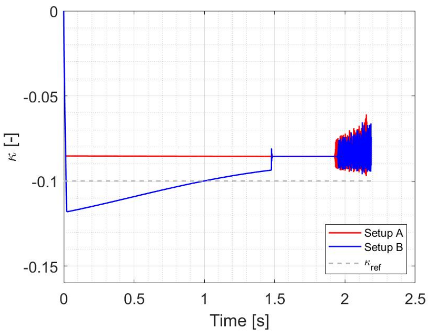

(a) Longitudinal slip κ

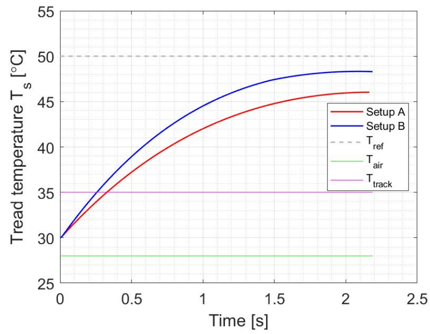

(b) Tread temperatures T_s

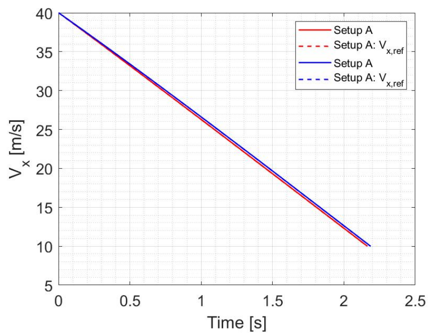

(c) Vehicle longitudinal velocity V_x

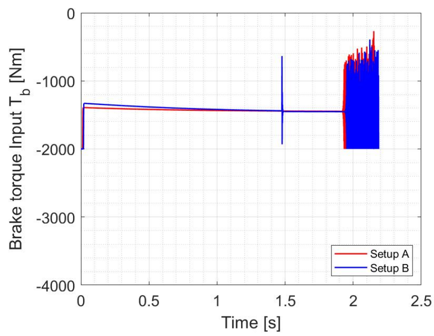

(d) Brake torque control input T_b

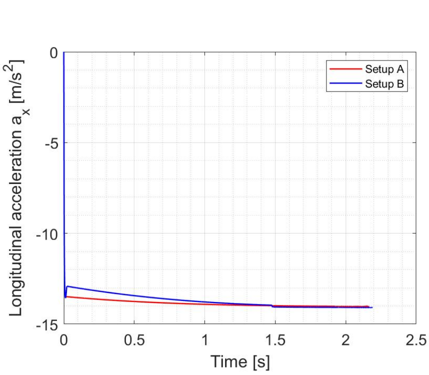

(e) Vehicle longitudinal acceleration

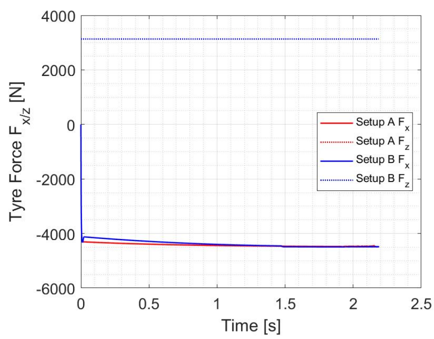

(f) Tyre longitudinal force F_x and Tyre vertical load F_z

Fig. B.1 Time histories of variables and control inputs for all the Setups (A and B) of quarter-car SDRE ABS controller with $T_a = 28°C$ and $T_t = 35°C$, starting at $40m/s$

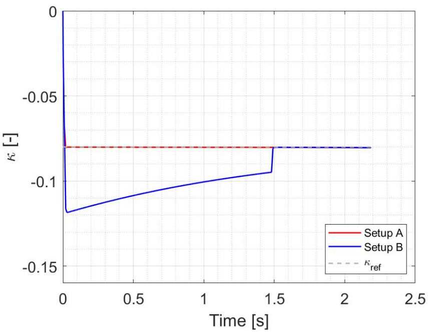

(a) Longitudinal slip κ

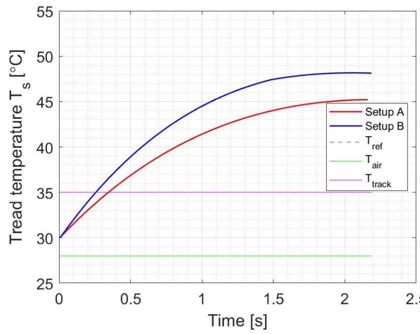

(b) Tread temperatures T_s

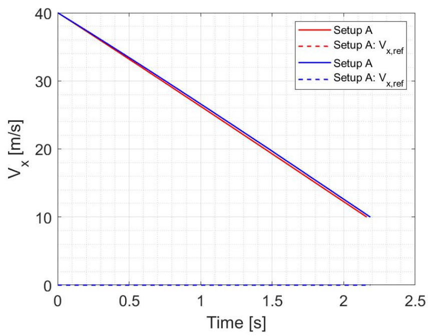

(c) Vehicle longitudinal velocity V_x

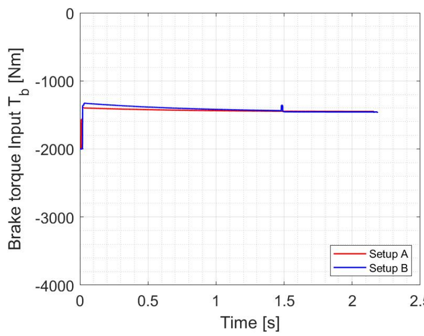

(d) Brake torque control input T_b

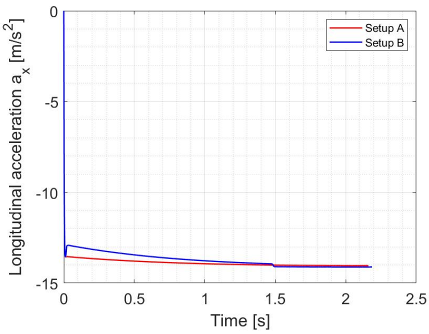

(e) Vehicle longitudinal acceleration

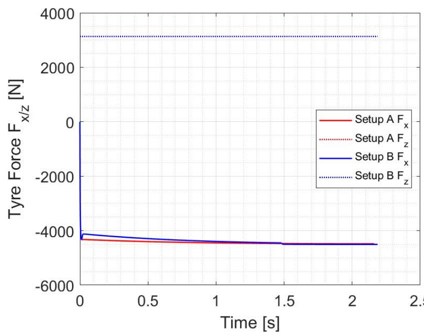

(f) Tyre longitudinal force F_x and Tyre vertical load F_z

Fig. B.2 Time histories of variables and control inputs for all the Setups (A and B) of quarter-car NMPC ABS controller with $T_a = 28°C$ and $T_t = 35°C$, starting at $40m/s$

Appendix C

Full-car results

This appendix presents the results of the different setups of the full-car NMPC setup in the form of Table and Time history plots. The reader may again refer to Table 6.16 to understand all the types of tests that are performed. The Tables C.1 and C.2 represent the values of the metrics defined in 6.6.1 for all the tests. All the percentage change of metrics are presented with respect to the benchmark i.e. Setup A [Pacejka:(κ-contr)].

For the time histories of the tests, due to spatial reasons it is chosen to present only the results of warm conditions of each weather for both the initial velocities (so, Tests 2, 5, 8, 11, 14, and 17). Anyway, the reader can easily predict the behaviour of the tests not presented here due to the continuous behaviour across all the tests.

Table C.1 Results of the 3 Setups (A, B, and C) for Test 1 to Test 9 (here $V_{x0} = 40 m/s$, Table 6.16)

	Setup	s_{br} [m]	% s_{br} w.r.t. A	$T_{s1,max}$ [$^\circ C$]	% $T_{s1,max}$ w.r.t. A	$T_{s3,max}$ [$^\circ C$]	% $T_{s3,max}$ w.r.t. A
Test 1	A	61.6	0.0	6.7	0.0	5.6	0.0
	B	61.5	-0.2	6.4	-4.5	5.2	-7.1
	C	62.4	1.3	8.7	29.9	6.9	23.2
Test 2	A	58.31	0.0	15.3	0.0	14.7	0.0
	B	58.4	0.2	15.3	0.0	14.7	0.0
	C	59.2	1.5	18	17.6	16.6	12.9
Test 3	A	56.3	0.0	22.3	0.0	22.2	0.0
	B	56.3	0.0	22.6	1.3	22.6	1.8
	C	57	1.2	25.6	14.8	24.5	10.4
Test 4	A	57.4	0.0	21.8	0.0	20.1	0.0
	B	57.4	0.0	22.0	0.9	20.4	1.5
	C	58.2	1.4	24.6	12.8	22.2	10.4
Test 5	A	54.1	0.0	35.5	0.0	35.1	0.0
	B	54.1	0.0	36.5	2.8	35.9	2.3
	C	54.7	1.1	39.3	10.7	37.7	7.4
Test 6	A	52.3	0.0	51.1	0.0	51.8	0.0
	B	52.1	-0.4	52.7	3.1	53.3	2.9
	C	52.4	0.2	54.9	7.4	54.5	5.2
Test 7	A	54.3	0.0	38.1	0.0	36.3	0.0
	B	54.2	-0.2	39.2	2.9	37.2	2.5
	C	54.9	1.1	41.6	9.2	38.9	7.2
Test 8	A	52.3	0.0	54.9	0.0	54.6	0.0
	B	52.0	-0.6	56.7	3.3	56.2	2.9
	C	52.3	0.0	58.5	6.6	57.3	4.9
Test 9	A	52	0.0	66.6	0.0	67.1	0.0
	B	51.5	-1.0	68.8	3.3	69.3	3.3
	C	51.6	-0.8	69.3	4.1	69.6	3.7

Table C.2 Results of the 3 Setups (A, B, and C) for Test 10 to Test 18 (here $V_{x0} = 70m/s$, Table 6.16)

	Setup	s_{br} [m]	% s_{br} w.r.t. A	$T_{s1,max}$ [$°C$]	% $T_{s1,max}$ w.r.t. A	$T_{s3,max}$ [$°C$]	% $T_{s3,max}$ w.r.t. A
Test 10	A	191.2	0.0	16.6	0.0	14.4	0.0
	B	191.2	0.0	16.7	0.6	14.4	0.0
	C	192.6	0.7	21.8	31.3	17.3	20.1
Test 11	A	182	0.0	24.4	0.0	22.8	0.0
	B	182	0.0	25.4	4.1	23.6	3.5
	C	183.2	0.7	31.1	27.5	26.7	17.1
Test 12	A	176.1	0.0	30.9	0.0	29.8	0.0
	B	176.0	-0.1	32.5	5.2	31.3	5.0
	C	177.1	0.6	38.3	23.9	34.3	15.1
Test 13	A	178.9	0.0	32.1	0.0	29.3	0.0
	B	178.9	0.0	33.7	5.0	30.6	4.4
	C	180.1	0.7	39	21.5	33.6	14.7
Test 14	A	169.83	0.0	44.7	0.0	43.1	0.0
	B	169.4	-0.3	47.6	6.5	45.6	5.8
	C	170.3	0.3	52.5	17.4	48.1	11.6
Test 15	A	165	0.0	58.8	0.0	58.6	0.0
	B	164.0	-0.6	63.0	7.1	62.5	6.7
	C	164.5	-0.3	65.8	11.9	63.8	8.9
Test 16	A	170.1	0.0	48.8	0.0	45.7	0.0
	B	169.6	-0.3	52.0	6.6	48.4	5.9
	C	170.5	0.2	56.3	15.4	50.8	11.2
Test 17	A	164.7	0.0	64	0.0	62.6	0.0
	B	163.8	-0.6	68.8	7.5	66.8	6.7
	C	164.1	-0.4	70.4	10.0	67.8	8.3
Test 18	A	164.4	0.0	74.4	0.0	74.1	0.0
	B	162.8	-1.0	80.4	8.1	79.6	7.4
	C	162.8	-1.0	79.1	6.3	79.1	6.7

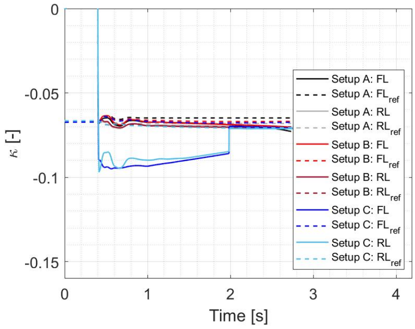

(a) Longitudinal slip $\kappa_{1/3}$

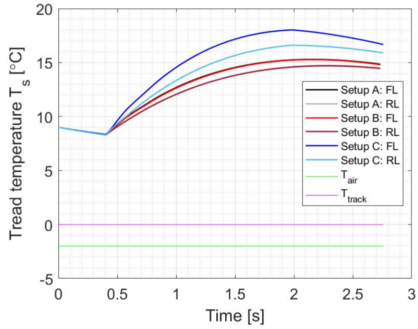

(b) Tread temperatures $T_{s1/3}$

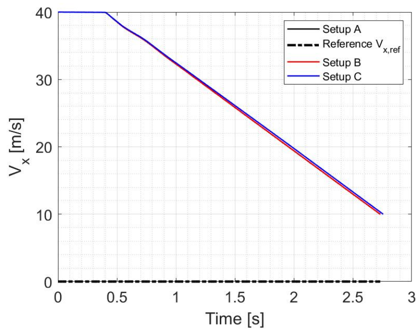

(c) Vehicle longitudinal velocity V_x

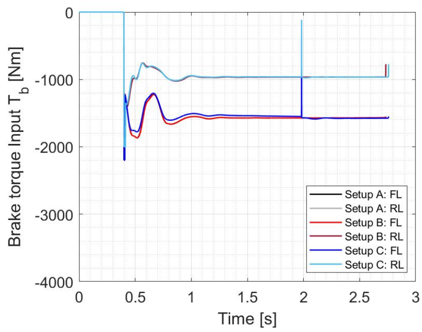

(d) Brake torque control input $T_{b1/3}$

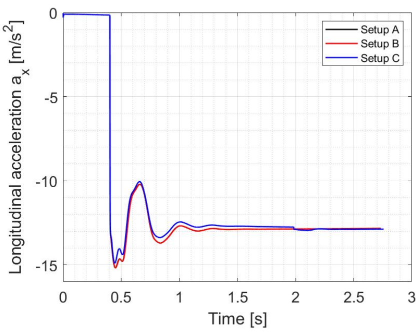

(e) Vehicle longitudinal acceleration

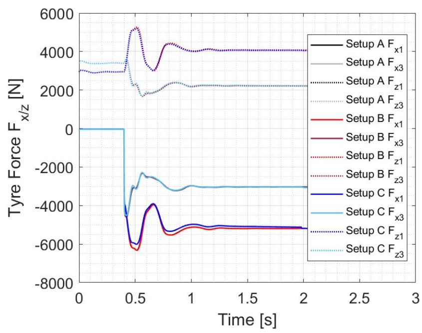

(f) Tyre longitudinal force $F_{x1/3}$ and Tyre vertical load $F_{z1/3}$

Fig. C.1 Time histories of variables and control inputs for all the Setups (A, B and C) of Full-car NMPC ABS controller in Test 2 (warm tyre in Winter starting at $40m/s$, Table 6.16)

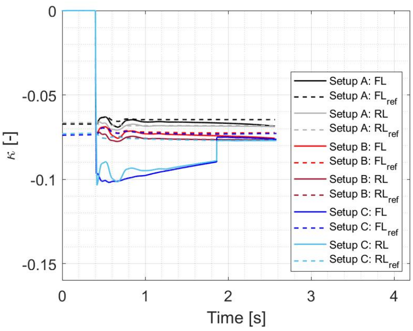

(a) Longitudinal slip $\kappa_{1/3}$

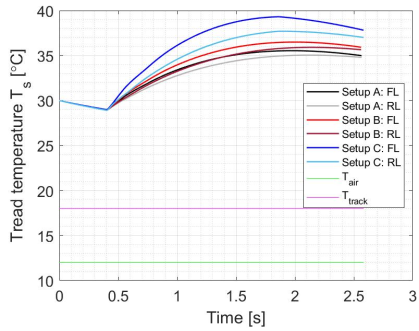

(b) Tread temperatures $T_{s1/3}$

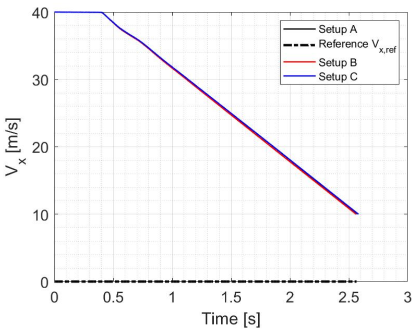

(c) Vehicle longitudinal velocity V_x

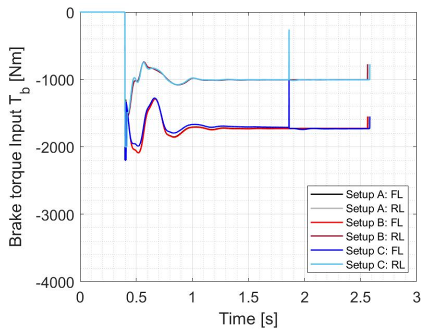

(d) Brake torque control input $T_{b1/3}$

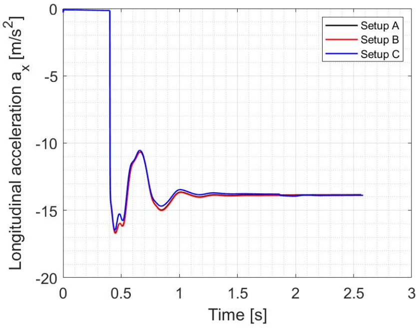

(e) Vehicle longitudinal acceleration

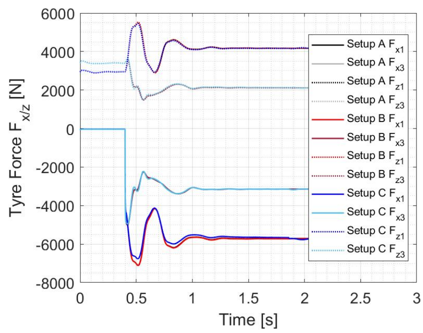

(f) Tyre longitudinal force $F_{x1/3}$ and Tyre vertical load $F_{z1/3}$

Fig. C.2 Time histories of variables and control inputs for all the Setups (A, B and C) of Full-car NMPC ABS controller in Test 5 (warm tyre in Autumn/Spring starting at $40 m/s$, Table 6.16)

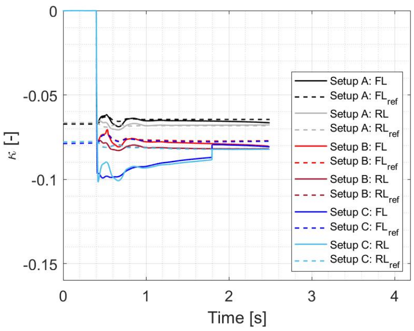

(a) Longitudinal slip $\kappa_{1/3}$

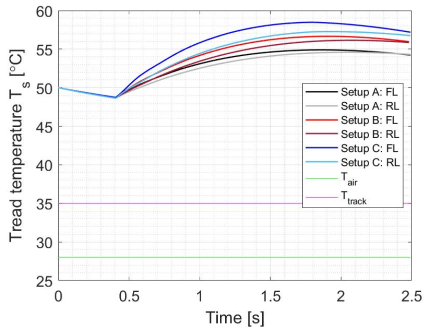

(b) Tread temperatures $T_{s1/3}$

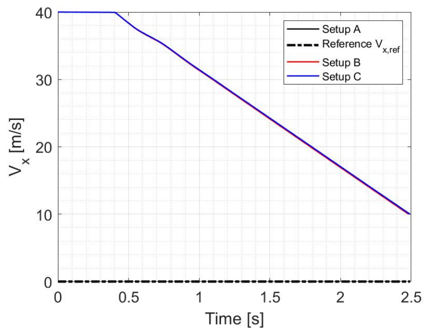

(c) Vehicle longitudinal velocity V_x

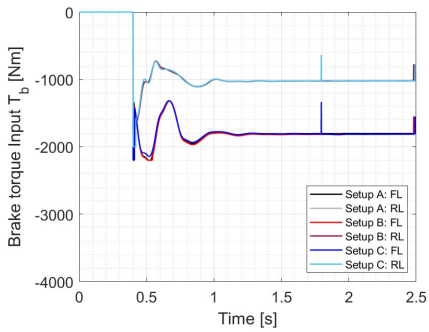

(d) Brake torque control input $T_{b1/3}$

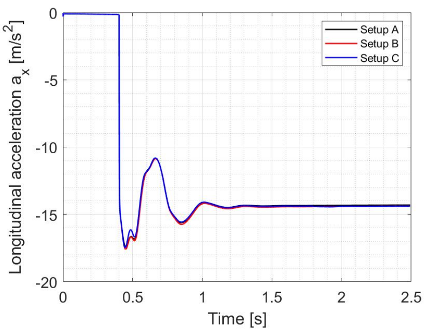

(e) Vehicle longitudinal acceleration

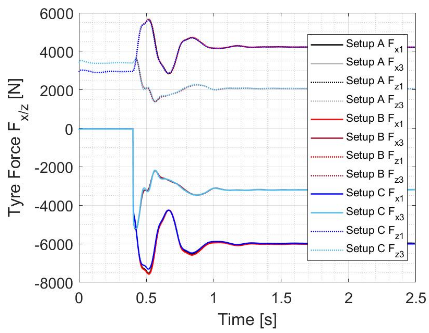

(f) Tyre longitudinal force $F_{x1/3}$ and Tyre vertical load $F_{z1/3}$

Fig. C.3 Time histories of variables and control inputs for all the Setups (A, B and C) of Full-car NMPC ABS controller in Test 8 (warm tyre in Summer starting at $40 m/s$, Table 6.16)

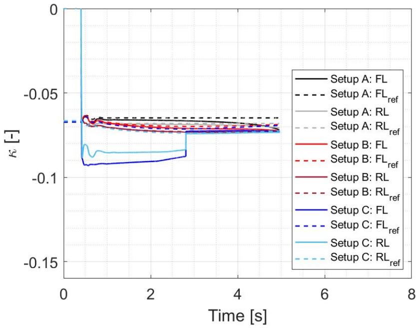

(a) Longitudinal slip $\kappa_{1/3}$

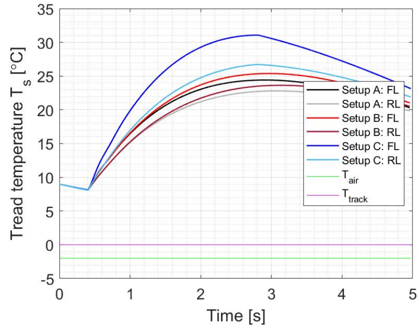

(b) Tread temperatures $T_{s1/3}$

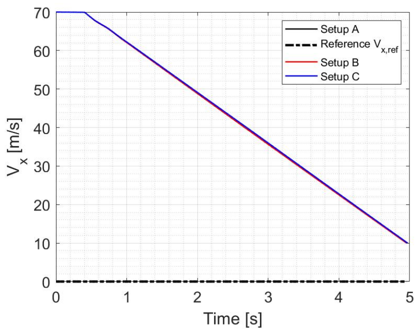

(c) Vehicle longitudinal velocity V_x

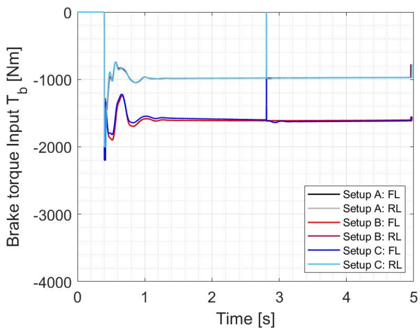

(d) Brake torque control input $T_{b1/3}$

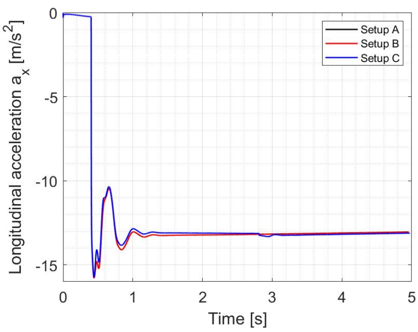

(e) Vehicle longitudinal acceleration

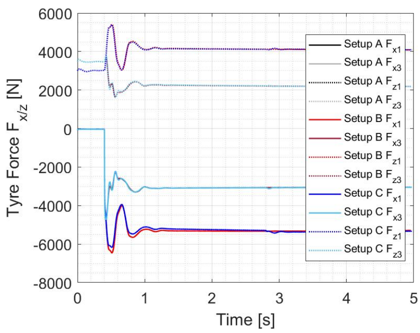

(f) Tyre longitudinal force $F_{x1/3}$ and Tyre vertical load $F_{z1/3}$

Fig. C.4 Time histories of variables and control inputs for all the Setups (A, B and C) of Full-car NMPC ABS controller in Test 11 (warm tyre in Winter starting at $70m/s$, Table 6.16)

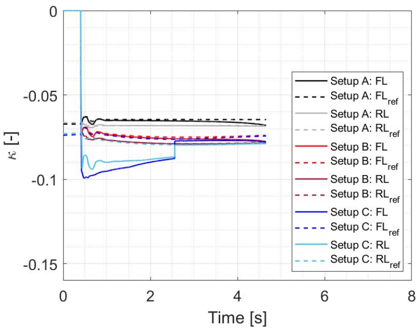

(a) Longitudinal slip $\kappa_{1/3}$

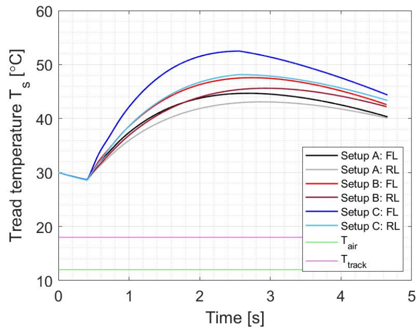

(b) Tread temperatures $T_{s1/3}$

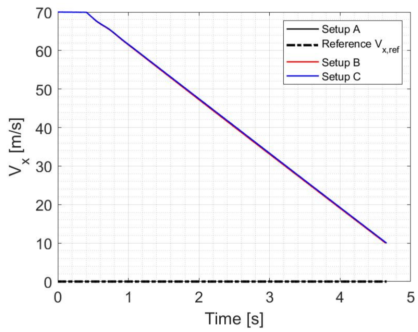

(c) Vehicle longitudinal velocity V_x

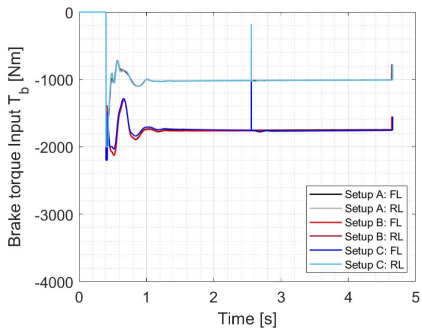

(d) Brake torque control input $T_{b1/3}$

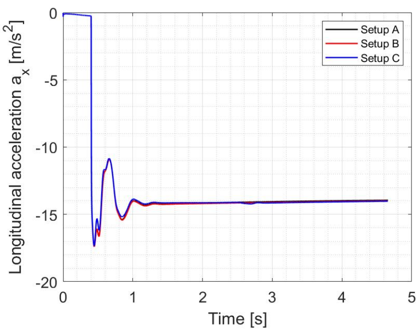

(e) Vehicle longitudinal acceleration

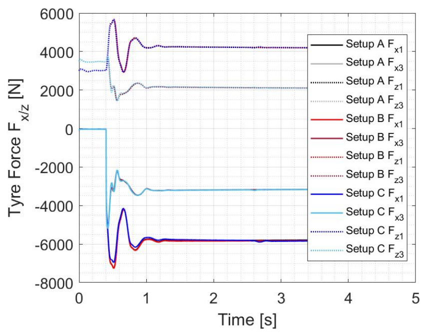

(f) Tyre longitudinal force $F_{x1/3}$ and Tyre vertical load $F_{z1/3}$

Fig. C.5 Time histories of variables and control inputs for all the Setups (A, B and C) of Full-car NMPC ABS controller in Test 14 (warm tyre in Autumn/Spring starting at $70 m/s$, Table 6.16)

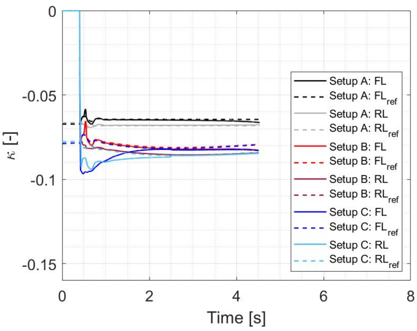

(a) Longitudinal slip $\kappa_{1/3}$

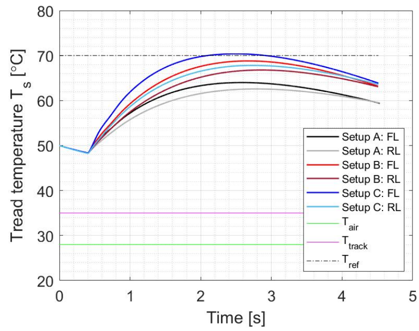

(b) Tread temperatures $T_{s1/3}$

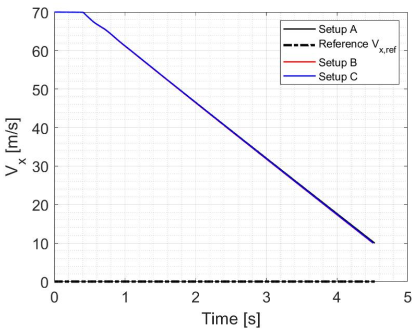

(c) Vehicle longitudinal velocity V_x

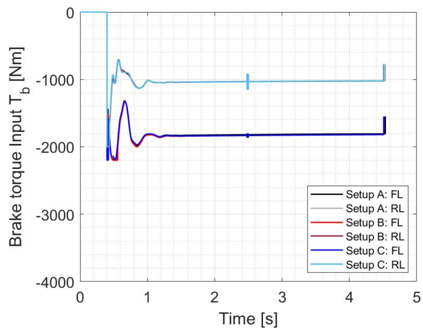

(d) Brake torque control input $T_{b1/3}$

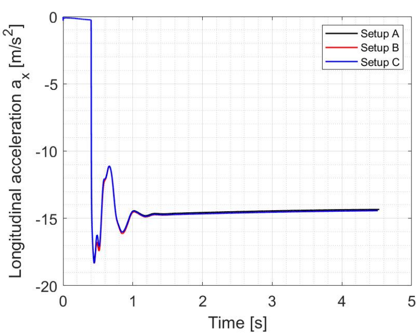

(e) Vehicle longitudinal acceleration

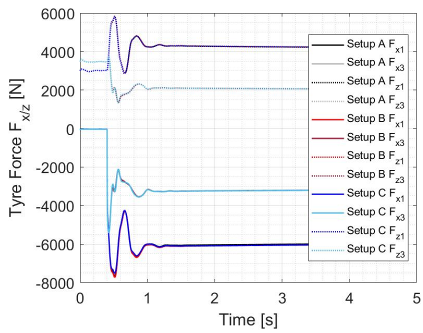

(f) Tyre longitudinal force $F_{x1/3}$ and Tyre vertical load $F_{z1/3}$

Fig. C.6 Time histories of variables and control inputs for all the Setups (A, B and C) of Full-car NMPC ABS controller in Test 17 (warm tyre in Summer starting at $70m/s$, Table 6.16)

As is discussed in the 6.8, a special setting of weights is tested. This setting is called Setup D for convenience. The controller setup here is the same as in Setup B and Setup C (TempKnwl) but the weights differ. That is, only V_x is weighted here (zero weights and no references are given for the κ_i and T_s) which makes the NMPC controller optimally compute by itself what brake torques must be given to achieve the quickest drop in the vehicle's longitudinal velocity V_x. As is already discussed, the QP solution failed when the prediction horizon is kept long, whereas it worked perfectly with a small prediction horizon. Also, the optimal results calculated in this case are very noisy. But the main discussion point for this results is the fact that this (Setup D) setup's performance is the same as that of Setup B, where the weighting is only set on the κ_i and optimal reference generation ($\kappa_{ref} = \kappa_{max} = f(F_z, T_s)$), such that the tyre longitudinal force F_x is always at maximum. Figure C.7 shows that the optimal state trajectories for κ_i and T_{si} are almost an overlay of each other. This only proves that, at least when the prediction horizon is small, the best strategy is not to heat the tyre but to only maintain the maximum longitudinal force (achieve κ_{max}) to achieve the quickest drop in vehicle longitudinal velocity. Although the solution in the case of bigger prediction horizon (equivalent to the total manoeuvre) failed, it is possible that by making some changes in the settings of the QP solver, one can achieve the right results. Due to the limited time for this work, it could not be achieved.

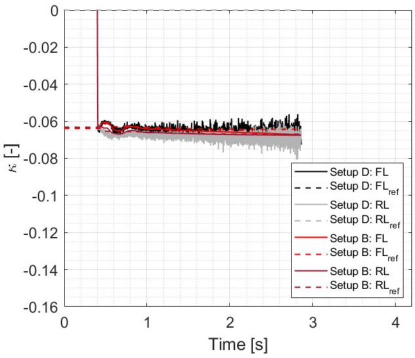

(a) Longitudinal slip $\kappa_{1/3}$

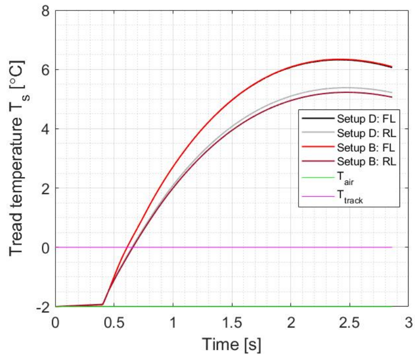

(b) Tread temperatures $T_{s1/3}$

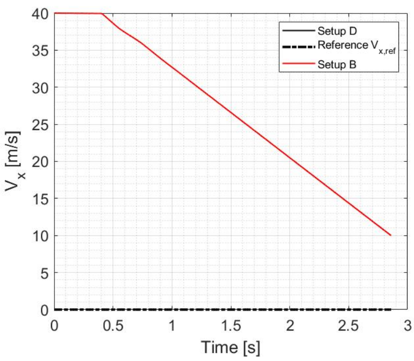

(c) Vehicle longitudinal velocity V_x

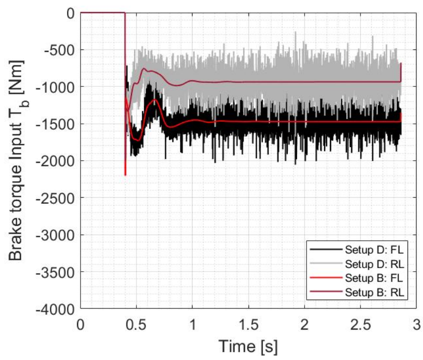

(d) Brake torque control input $T_{b1/3}$

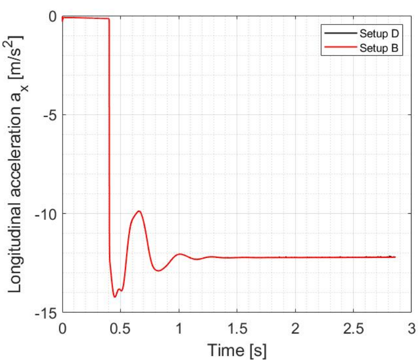

(e) Vehicle longitudinal acceleration

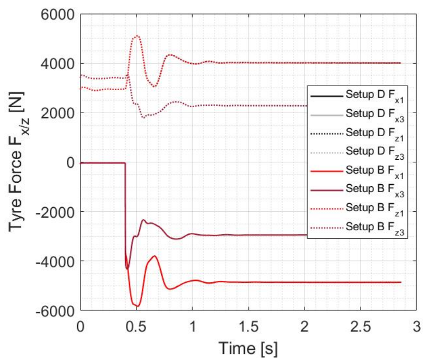

(f) Tyre longitudinal force $F_{x1/3}$ and Tyre vertical load $F_{z1/3}$

Fig. C.7 Time histories of variables and control inputs for the Setup B and Setup D of Full-car NMPC ABS controller in Test 1 (Table 6.16)